

THE OPTICAL PROPERTIES OF SPIKY GOLD NANOSHELLS

Simon P. Hastings

A DISSERTATION

in

Physics and Astronomy

Presented to the Faculties of the University of Pennsylvania

in

Partial Fulfillment of the Requirements for the

Degree of Doctor of Philosophy

2014

Supervisor of Dissertation

Signature _____

Zahra Fakhraai,

Assistant Professor of Chemistry

Graduate Group Chairperson

Marija Drndic, Professor of Physics and Astronomy

Co-Supervisor of Dissertation

Signature _____

Nader Engheta,

H. Nedwill Ramsey Professor of
Electrical and Systems Engineering

Dissertation Committee:

Philip Nelson, Professor of Physics and Astronomy

Alison Sweeney, Assistant Professor of Physics and Astronomy

Arjun Yodh, James M. Skinner Professor of Science, Director of LRSM

Acknowledgments

I would like to thank my parents for fostering my interest in science, and giving me the time and resources to pursue it. My supervisor Zahra Fakhraai and my co-supervisor Nader Engheta have my gratitude for providing their patience, insight and most importantly passion for this work. My collaborators and colleagues also have my gratitude: Brenda Sanchez-Gaytan, Zhaoxia Qian, Michael Reza, Chen Li, Brian Edwards, Christine McGinn, Pattanawit Swanglap, Ying Fang, So-Jung Park, and Stephan Link. I especially wish to thank Zhaoxia Qian for showing up with a mystery worth exploring every week and my fellow graduate students for their patience while I wrote this dissertation. Last, my good friend Elizabeth Patitsas, who has now provided support through three degrees and across both continents and oceans.

ABSTRACT

THE OPTICAL PROPERTIES OF SPIKY GOLD NANOSHELLS

Simon P. Hastings

Zahra Fakhraai

Nader Engheta

Plasmonic nanoparticles are a powerful and versatile tool for molecular sensing, drug delivery, and cancer treatment. When exposed to incident light, these nanoparticles have greatly increased far-field scattering and near-field enhancement. Spiky gold nanoshells are a recently developed class of nanoparticles composed of sharp gold spikes decorating a polystyrene core. Spiky nanoshells are synthesized using the templated surfactant-assisted seed growth method, which enables extensive control of the nanoparticle morphology. Here, it is shown that these particles have a tailorable far-field resonance, extremely uniform single-particle surface enhanced Raman scattering, and modal interference in dark-field microscopy measurements. Finite-difference time-domain simulations are performed to determine the morphological features which control these unusual behaviors. Additionally, a T-matrix method was developed to use finite-difference time-domain simulations to analyze mode mixing in these particles. These studies show that the lengths of spikes are critical in determining the far-field scattering peak. Additionally, simulation of the electric field near the particle surface show that the near-field Raman surface enhancement is dominated by the quadrupole modes, resulting in Quadrupole Enhanced Raman Scattering. Due to the large number of spikes, the near-field enhancement is relatively insensitive to variations in individual spikes, resulting in emergent homogeneity in optical properties due to heterogeneity in the structure. The disorder induced asymmetry of the spiky nanoshell enables mode-mixing between the dipole and quadrupole modes, which is

observed experimentally in dark-field measurements and predicted theoretically in a T-matrix analysis of finite-difference time-domain simulations. This mode mixing was found to be of the order of 5% between the quadrupole and dipole modes. Such mode mixing is responsible for the broadening of the quadrupole modes towards the infrared and for the activation of all six quadrupole moments, partially explaining how heterogeneity can result in reliable and robust near-field enhancement.

Contents

List of Figures	ix
1 Introduction	1
1.1 Scattering from Spherical Objects	2
1.2 The Development of Modern Nanoparticles	11
1.3 Surface Enhanced Raman Spectroscopy	20
1.4 Modal Interference	28
2 The Theory of Optical Scattering from Nanoparticles	36
2.0.1 Maxwell's Equations	36
2.1 Scattering Models	39
2.1.1 Expansion Definitions	41
2.1.2 General Cross Section Definitions in T-Matrix Theory	45
2.1.3 Determining the T-Matrix	50
3 Numeric Methods	57
3.1 Finite-Difference Time-Domain Simulations	57
3.2 Lumerical Solutions	60
3.3 Constructing the Nanostructure for FDTD Models	66

3.3.1	A Force Method for Spike Distributions	66
3.3.2	Molecular Dynamics Simulations for Raspberry-Like Metamolecule Particles (Raspberry-MMs)	68
3.4	Specific Data Analysis Topics	71
3.4.1	Calculating the Near-Field Enhancement	71
3.4.2	Determining the T-Matrix of a Particle	75
4	Modeling the Scattering	
	Properties of Spiky Nanoshells	78
4.1	Introduction	78
4.2	Context	79
4.3	Controlling the Topography and Surface Plasmon Resonance of Gold Nanoshells by a Templated Surfactant-Assisted Seed Growth Method	79
4.3.1	Abstract	79
4.3.2	Introduction	80
4.3.3	Experimental Methods	81
4.3.4	Results and Discussion	84
4.3.5	Conclusion	106
4.3.6	Acknowledgments	107
5	Quadrupole-Enhanced Raman Scattering in Spiky Nanoshells	108
5.1	Introduction	108
5.2	Context	109

5.3	Quadrupole-Enhanced Raman Scattering	109
5.3.1	Abstract	109
5.3.2	Introduction	110
5.3.3	Results and Discussions	112
5.3.4	Conclusion	142
5.3.5	Acknowledgments	143
5.3.6	Methods	143
5.4	Supporting Information	145
5.4.1	Particle Synthesis and Nanoparticle Characterization	145
5.4.2	Sample Preparation for Correlated Single Particle Optical and Electron Microscopy Studies	145
5.4.3	Single Particle Optical Studies	146
5.4.4	Finite-Difference Time-Domain (FDTD) Simulations	148
5.4.5	Scattering Mode Formalism	152
5.4.6	Spherical Harmonic Formalism	154
5.4.7	Calculations of the Scattering Cross section	155
6	Nanoparticle Modal interference	158
6.1	Introduction	158
6.2	Context	159
6.3	Modal Interference in Spiky Nanoshells	159
6.3.1	Abstract	159
6.3.2	Introduction	160
6.3.3	Methods	163
6.3.4	Results	174
6.3.5	Discussion	174

6.3.6	Conclusion	188
6.3.7	Appendix	189
6.3.8	Acknowledgments	191
6.3.9	Supplemental Information	191
7	Future Directions and Conclusion	200
7.1	Future Studies of the Spiky Nanoshell	200
7.2	Future Studies of the Raspberry-Like Metamolecules	202
7.3	Future Studies on Reconstructing the T-Matrix with FDTD	211
7.4	Summary and Conclusion	212
A	Glossary of Terms	215

List of Figures

1.1	Multipole Currents	5
1.2	Gold and Glass Spheres	10
1.3	Nanorod Tuneability	13
1.4	Silver Polyhedron Tunability	14
1.5	Gold Decahedra Multimodes	15
1.6	Shell to Core Size Dependence in Gold Nanoshells	16
1.7	SEM Images of Spiky Nanoshells	18
1.8	SERS with Gold Nanoshells	23
1.9	Plasmon-Sampled SERS	25
1.10	SERS Using Gold Trimers	27
1.11	Fanoshell Hybridization	30
1.12	Gold Decahedra Multimodes	34
2.1	Incident and Scattered Light Expansion	40
3.1	Yee Cell Diagram	59
3.2	FDTD Solutions Simulation Layout	61
3.3	FDTD Solutions Objects	62
3.4	FDTD Solutions Source Dialog	63
3.5	FDTD Solutions Material Dialog	65

3.6	Gold Cone Model	67
3.7	Spikey Nanoshell Model	68
3.8	Molecular Dynamics Forces	70
3.9	Raspberry-MM Shell Simulation	71
3.10	Determining the Sampled Shell	73
3.11	Shell Surface Coverage	74
3.12	Total-Field Scattered-Field Source	76
4.1	Rough and Spikey Gold Nanoshells	86
4.2	TEM and Extinction Spectra of Gold Nanostructures Without a Core	88
4.3	The Effect of Roughness on Gold Nanoshells	90
4.4	Far-field Tunability in Spikey Nanoshells	91
4.5	Scheme of the Effect of Halide Ions on the Spikey Nanoshell	93
4.6	TEM Images of Spikey Nanoshells	94
4.7	Nanoshells Synthesized with CTAC and NaI	95
4.8	The Effect of the Seed Solution to Growth Solution Ratio on Spikey Nanoshells	96
4.9	Simplified FDTD Models of Spikey Nanoshells	97
4.10	Supplemental Simplified FDTD Models of Spikey Nanoshells	99
4.11	Variations in Spikey Number in FDTD Simulations of Spikey Nanoshells	101
4.12	Agreement Between the Measured and Simulated Spikey Nanoshells .	104
4.13	Unnormalized Simulation Spectra of Various Nanoshells	105
5.1	Single Particle Dark-field Microscopy and SERS in Spikey Nanoshells .	113

5.2	Additional Single Particle Dark-field Microscopy and SERS in Spiky Nanoshells	114
5.3	Experimental Single Particle Dark-field Microscopy in Spiky Nanoshells	115
5.4	Correlations Between Dark-field Microscopy and SERS in Spiky Nanoshells	117
5.5	Far-Field and Moment Analysis of Simulation Spiky Nanoshells . . .	120
5.6	Simulated Far-Field Behavior of Spiky Nanoshells	121
5.7	Average and Individual Properties of Ten Disordered Nanoshells . . .	124
5.8	Simulated Polarization Currents in the Spiky Nanoshells	125
5.9	Far-Field and Near-Field Response of the Dipole and Quadrupole Modes	126
5.10	Projections of the Scattered Field into the Far-Field from the FDTD Simulations	129
5.11	Average Quadrupole Moment Strength of Ten Modeled Disordered Spiky Nanoshells	130
5.12	Simulated Near-Field Enhancement of Spiky Nanoshells	132
5.13	Enhancement Factors of the Ordered and Disordered Models	134
5.14	Relative Raman Enhancement Factors Including Both the Electrical and Wavelength Components	135
5.15	Average Electric Intensity at 634 and 784 nm	136
5.16	Spherical Harmonic Expansions Near Various Nanoshells	137
5.17	Projections of the Real Part of the Radial Component of the Electric Field onto a Sphere	138
5.18	A Simplified Donut-Like Model of the Spiky Nanoshell	139

5.19	Spectral Tunability of QERS	141
5.20	Dipole Scattering Cross Sections Estimated with Currents and Fields	157
6.1	Experimental and Theoretical Backscatter of Spiky Nanoshells	164
6.2	SEM Images of Spiky Nanoshells	165
6.3	A Dip in the Dark-Field Spectrum of Spiky Nanoshells	165
6.4	No Dip in the Dark-Field Spectrum of Spiky Nanoshells	166
6.5	Variation in Simulated Scattering Cross Sections of Spiky Nanoshells	168
6.6	The T-Matrix of a Spiky Nanoshell	173
6.7	Orientation Dependence of the Scattering Cross Section in Spiky Nanoshells	175
6.8	Diagonal and Full T-Matrix Solutions of Spiky Nanoshells	176
6.9	The Extinction Cross Section of a Spiky Nanoshell Under Different Models	178
6.10	Cross Sections of a Second Orientation of a Spiky Nanoshell Under Different Models	179
6.11	The Diagonal Components of the Total Scattering Cross Section in a Spiky Nanoshell	180
6.12	The Influence of Cross-Terms on the Cross Section of Spiky Nanoshells	183
6.13	The T-Matrix of an Ordered Nanoshell	186
6.14	The T-Matrix of a Gold Sphere	197
6.15	The Quadrupole Moments of a Spiky Nanoshell	199
7.1	Raspberry-MM SEM Image	203
7.2	Theoretical Raspberry-MM Scattering	204

7.3	Home Built 90 Degree Spectrometer	205
7.4	90 Degree Scattering Data	207
7.5	Angular Resolved Scattering Data	209

Chapter 1

Introduction

The study of the interaction of light with nanoparticles represents a critical step in achieving nanometer scale control of light. When light in the optical frequency range interacts with nanostructures composed of noble metals, it can lead to resonant charge oscillations in the particle resulting in enhanced near-fields and far-field peaks in scattering or absorption spectra. While enhanced light scattering allows effective bulk index sensing and optical tagging, the near-field properties of nanoparticles can be utilized in measurements at length scales dramatically smaller than the wavelength of light. This has enabled promising sensing techniques such as Surface Enhance Raman Spectroscopy (SERS) to become possible. Over the past century, progressively more sophisticated nanoparticle structures have been synthesized or fabricated, building the tool-set necessary for nanoscale interaction with light.

The goal of this work is to understand the optical properties of spiky nanoshells, a family of particles with a polystyrene core decorated with sharp gold spikes to form a shell. As a result of the random growth of spikes, spiky nanoshells have a highly disordered structure, yet possess surprisingly reproducible properties. This introductory chapter will examine the broader field in four parts. First, a general

overview of the theory of light scattering from particles will be presented. Second, as spiky nanoshells have a highly tuneable far-field extinction spectra, a brief overview of the context in which this tuneability sits is presented as background for chapter 4. In the third section, an overview of nanometer SERS substrates is presented for context to the highly reliable SERS measurements that are attributed to a higher order quadrupolar dark-mode in the spiky nanoshell, as presented in chapter 5. The final section discusses modal interference in nanoparticles in preparation for chapter 6, which examines modal interference between the dipole and quadrupole modes in the spiky nanoshell.

1.1 Scattering from Spherical Objects

Colloidal gold has been used to produce vibrant colors for thousands of years [112]. Purple of Cassius, a purple pigment made by reducing gold with tin, has been used to make ruby glass since at least the 1600s [48]. Modern interest began in 1857, when Faraday published his article “The Bakerian Lecture: Experimental relations of Gold (and other metals) to Light” in the *Philosophical Transactions of the Royal Society of London*. In 1908, Mie demonstrated that the origin of the scattering peak in spherical gold nanoparticles can be effectively explained with classical electromagnetism, establishing a theoretical framework still in use today [76]. The first of many modifications to this theory was provided in 1912 by Gans, who described the effects of elliptical geometry on the observed scattering peaks within gold nanoparticles and provided closed form approximations for the effect on the extinction of light [112].

In the far-field limit (where the observer is many wavelengths away from the scatterer), the most easily measurable optical property is the extinction coefficient. Extinction spectra can be measured by passing white light through a dilute solution of

nanoparticles and subtracting the resulting spectrum from the signal in the absence of the material. In this work, these will often be referred to as UV-vis-NIR (ultraviolet, visible, near-infrared) spectra, depending on the light range used in the measurement. The extinction cross section is defined as the power of light which is removed from a beam of unit intensity by each particle:

$$\sigma_{ext} = \frac{P_{removed}}{I_{Incident}} \quad (1.1.1)$$

Note that the cross section has units of area. Light which is not transmitted by a particle is either absorbed or scattered in another direction. The integral of scattered power per unit solid angle divided by the incident intensity is called the total scattering cross section:

$$\sigma_{scat} = \frac{\int \frac{dP(\theta,\phi)}{d\Omega} \sin\theta d\theta d\phi}{I_{Incident}} \quad (1.1.2)$$

The total power absorbed by the particle is the light which was removed from the incident beam but was not scattered:

$$\sigma_{abs} = \sigma_{ext} - \sigma_{scat} \quad (1.1.3)$$

The cross section definitions provide experimentally accessible characteristics for any given nanoparticle, however a theoretical framework for predicting their values is needed. Mie theory approaches this problem by expanding an incident plane wave with linear polarization into a series of vector spherical harmonic wave functions, which are also referred to as the electric and magnetic multipole modes. In Mie theory, the scattering object is assumed to have spherical symmetry, which results in each term of the expansion of the incident wave being independently scattered

as a scaled version of that term. The key result of Mie theory is that the ratio of the incoming to outgoing magnetic modes (b_n) and the ratio of the incoming to outgoing electric modes (a_n), can be used to produce the extinction and scattering cross sections for any given spherical particle [123]:

$$\sigma_{scat} = \frac{2\pi}{k^2} \sum_{n=1}^{\infty} (2n+1)(|a_n|^2 + |b_n|^2) \quad (1.1.4)$$

and the extinction cross section by [123]:

$$\sigma_{ext} = \frac{2\pi}{k^2} \sum_{n=1}^{\infty} (2n+1) \text{Re}(a_n + b_n) \quad (1.1.5)$$

For a sphere of radius a , matching boundary conditions give the ratio of the incoming and outgoing waves of each order multipole [123]:

$$a_n = \frac{k_p^2 a^2 j_n(k_p a) [ka j_n(ka)]' - k^2 a^2 j_n(ka) [k_p a j_n(k_p a)]'}{k_p^2 a^2 j_n(k_p a) [ka h_n(ka)]' - k^2 a^2 h_n(ka) [k_p a j_n(k_p a)]'} \quad (1.1.6)$$

and

$$b_n = \frac{j_n(k_p a) [ka j_n(ka)]' - j_n(ka) [k_p a j_n(k_p a)]'}{j_n(k_p a) [ka h_n(ka)]' - h_n(ka) [k_p a j_n(k_p a)]'} \quad (1.1.7)$$

Where k is the wave number, and a subscript ‘ p ’ indicates it is to be evaluated in the dielectric medium of the particle rather than in the medium surrounding the particle (usually air, water, or another dielectric material). The functions h_n and j_n are the n th order spherical Hankel functions of the first kind, and spherical Bessel functions of the first kind. As the particle becomes larger, more modes must be included in Eq. 1.1.4 to accurately model the particle’s cross section.

Rather than cross section, sometimes these will be referred to as efficiencies (denoted by Q), in which case they have been divided by the geometrical cross section

(the optical size of an object much larger than the wavelength of light), given for a sphere by:

$$\sigma_g = \pi a^2 \tag{1.1.8}$$

The electric and magnetic modes described above seem very abstract at first glance, however each has a straightforward physical interpretation. Terms with $n=1$ are referred to as dipoles, $n=2$ as quadrupoles, $n=3$ as octopoles, and so forth. As illustrated in Figure 1.1, the electric dipole term is the result (loosely) of currents moving between two poles at a given frequency. The electric quadrupole term is the result of two electric dipoles oriented in opposite directions such that current moves between four poles. The magnetic dipole is formed by a single loop of current circulating around the magnetic dipole vector at a given frequency, while the magnetic quadrupole has two such vectors oriented in opposite directions. Higher multipoles possess greater numbers of poles, but follow the same pattern.

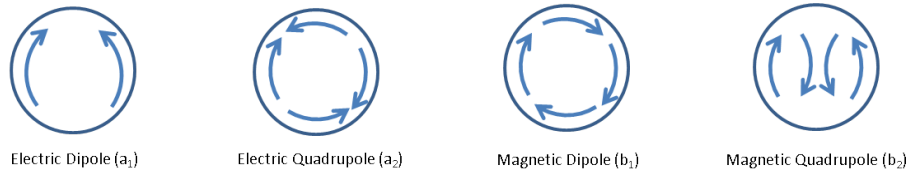


Figure 1.1: Schematic currents associated with the first two electric and magnetic modes for a spherical nanoparticle. Note that the electric dipole has one source/sync pair, while the electric quadrupole has two such pairs. Likewise, the magnetic dipole has a single center of current rotation, while the magnetic quadrupole has two such centres.

This approach works in principle for any spherically symmetric object made of linear, isotropic, and homogeneous materials. It is instructive to examine the case of the quasistatic limit, where the particle is much smaller than the wavelength of

light. In order to understand the behavior of a scattering object, it is also necessary to understand the electrical response of that object. The electric displacement in a homogeneous, isotropic, and linear medium is related to the electric field by:

$$\vec{D} = \epsilon \epsilon_0 \vec{E} \quad (1.1.9)$$

Where ϵ is the relative complex permittivity, and ϵ_0 is the permittivity of free space. The real component of permittivity, ϵ' , is the result of the polarizability of the material while the imaginary component, ϵ'' , is the result of the conductivity of the material and is associated with loss. For waves, it is often useful to describe material properties in terms of the refractive index, n , rather than the permittivity. The real part of the refractive index, n' , and the imaginary part of the refractive index, n'' , are related to the complex permittivity by:

$$\epsilon' = n'^2 - n''^2 \quad (1.1.10)$$

$$\epsilon'' = 2n'n'' \quad (1.1.11)$$

The wave vector in the medium is given by the wave vector in vacuum times the complex refractive index of the medium. For a wave vector oriented in direction \hat{k} , the complex wave vector in the medium is given by:

$$\vec{k}_p = \frac{2\pi n \hat{k}}{\lambda_0} \quad (1.1.12)$$

We will examine two simple but instructive cases of material properties here. First, in order to understand non-metallic materials in the optical region, we must examine the Lorentz model. In this case, the material is modeled as a set of oscillators with a

resonance frequency of ω_0 and loss γ , producing [16]:

$$\epsilon(\omega) = 1 + \frac{\omega_p^2}{\omega_0^2 - \omega^2 - i\gamma\omega} \quad (1.1.13)$$

Where ω_p is the plasma frequency of the material, and ω is the wavelength of the incident radiation.

Because most electronic transitions occur in the UV, and vibrational modes are in the IR, in the visible region materials described by Eq. 1.1.13 are far from the transition frequency (where $\omega = \omega_o$). As a result, these materials (called dielectrics) have a small imaginary part of ϵ in the optical regime, and the material is transparent.

Rayleigh scattering describes scattering of dielectric particles which are small compared to the wavelength. For a dielectric, ϵ is approximately real allowing the simplification of Eqs. 1.1.6 and 1.1.7. Examining Eqs. 1.1.6 and 1.1.7, $h_n(kr)$ (the spherical Hankel function of the first type) occurs in the denominator of both magnetic and electric coefficients. The asymptotic behavior of this function in the quasistatic limit ($r \rightarrow 0$ for constant k) dictates that [123]:

$$h_n(kr) \approx -i \frac{1 \cdot 3 \cdot 5 \dots (2n - 1)}{(kr)^{n+1}} + \frac{(kr)^n}{1 \cdot 3 \cdot 5 \dots (2n + 1)} \quad (1.1.14)$$

In this limit, the denominator will be multiplied by a factor of $1/kr$ for each increase in the order, n , and as a result only dipole term ($n = 1$) contributes to the far-field scattering of the particle. Additionally, $j_n(kr)$ (the spherical Bessel function of the first kind), has a small argument form given by:

$$j_n(kr) \approx \frac{(kr)^n}{1 \cdot 3 \cdot 5 \dots (2n + 1)} \quad (1.1.15)$$

As a result, the numerator in Eq. 1.1.7 is zero to first order, suppressing the

magnetic scattering for small particles. Therefore only the electric dipole terms are needed [123]:

$$h_1(kr) = -\left(1 + \frac{i}{kr}\right) \frac{e^{ikr}}{kr} \quad (1.1.16)$$

$$j_1(kr) = -\frac{\cos(kr)}{kr} + \frac{\sin(kr)}{(kr)^2} \quad (1.1.17)$$

Resulting in:

$$\lim_{r \rightarrow 0} (kr j_1(kr))' = \frac{2kr}{3} \quad (1.1.18)$$

$$\lim_{r \rightarrow 0} j_1(kr) = \frac{kr}{3} \quad (1.1.19)$$

$$\lim_{r \rightarrow 0} (kr h_1(kr))' = \frac{i}{(kr)^2} \quad (1.1.20)$$

$$\lim_{r \rightarrow 0} h_1(kr) = \frac{-i}{(kr)^2} \quad (1.1.21)$$

Here, for simplicity, we dropped the real part of the following expressions as it is asymptotically smaller than the imaginary part. In principle, to obey the optical theorem or to estimate the extinction cross section, both must be considered [123]. Combining expressions 1.1.6 and 1.1.18 to 1.1.21:

$$a_1 = \frac{k_p^2 a^2 \frac{k_p a}{3} \frac{2ka}{3} - k^2 a^2 \frac{ka}{3} \frac{2k_p a}{3}}{k_p^2 a^2 \frac{k_p a}{3} \frac{i}{(ka)^2} - k^2 a^2 \frac{-i}{(ka)^2} \frac{2k_p a}{3}} \quad (1.1.22)$$

And then simplifying:

$$a_1 = \frac{2}{3} \frac{k_p^2 k_p a k a - k^2 k a k_p a}{k_p^2 k_p a \frac{i}{(ka)^2} + k^2 \frac{i}{(ka)^2} 2k_p a} \quad (1.1.23)$$

$$a_1 = \frac{2(ka)^3}{3i} \frac{k_p^2 - k^2}{k_p^2 + 2k^2} \quad (1.1.24)$$

And then substituting in $k = 2\pi n/\lambda$ and $\epsilon = n^2$ where n and ϵ can be complex:

$$a_1 = \frac{-2i(ka)^3}{3} \frac{\epsilon_p - \epsilon}{\epsilon_p + 2\epsilon} \quad (1.1.25)$$

This formula, up until this point, made no assumptions about the nature of the particle except that it was small and spherical. From the discussions above, dielectric materials have a slowly varying, positive, real-valued ϵ in the visible region. As a result, to first order the entire wavelength dependence is encoded in k . When plugged into the total scattering cross section relation (Eq. 1.1.4), this results in the famous λ^{-4} Rayleigh scattering cross section shown in Figure 1.2:

$$\sigma_{scat} = \frac{2\pi}{k^2} (3) (|a_1|^2) = \frac{8\pi a^6 (2\pi)^4}{3\lambda^4} \left| \frac{\epsilon_p - \epsilon}{\epsilon_p + 2\epsilon} \right|^2 \quad (1.1.26)$$

For small spheres made of noble metals (such as gold, silver, aluminium, or copper) Eq. 1.1.26 still applies but ϵ is no longer constant as a function of frequency. In these cases the Lorentz model must be discarded because the materials possess substantial free charge. The material properties can instead be approximated by the Drude model, where the resonance frequency term from the Lorentz model is dropped entirely [16]:

$$\epsilon_p(\omega) = 1 - \frac{\omega_p^2}{\omega^2 + i\gamma\omega} \quad (1.1.27)$$

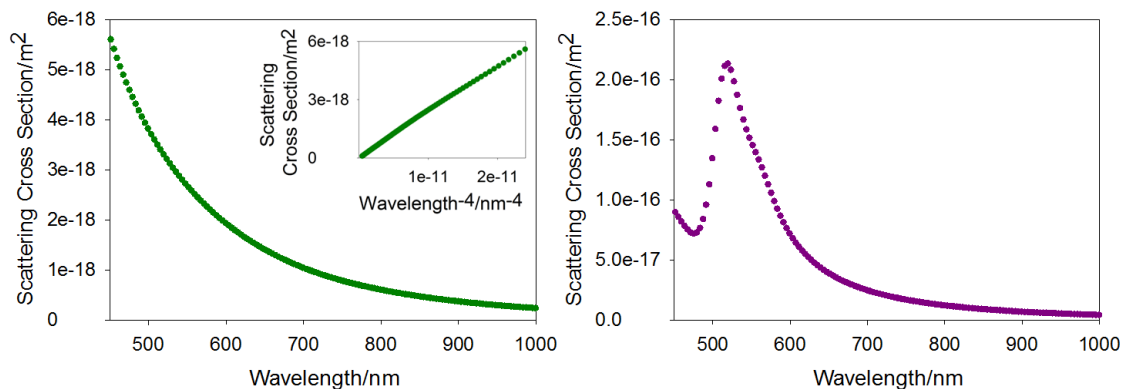


Figure 1.2: Scattering cross section for spheres made of a dielectric (glass, left) and a plasmonic material (gold, right). Inset-left is the same data plotted against λ^{-4} demonstrating the nearly linear relationship expected for Rayleigh scattering. The slight non-linearity observed is due to the wavelength becoming a non-trivial fraction of the total sphere size ($1/4$). Cross sections were calculated via numeric modeling, as discussed in the following chapters.

However, in most metals at room temperature, and in the visible and ultraviolet, γ is much smaller than ω_p and ω [16]. Hence, the real and imaginary parts of ϵ_p can be described by [16]:

$$\epsilon'_p(\omega) \approx 1 - \frac{\omega_p^2}{\omega^2} \quad (1.1.28)$$

$$\epsilon''_p(\omega) \approx \frac{\omega_p^2 \gamma}{\omega^3} \quad (1.1.29)$$

In this model, the real part of ϵ_p (labeled ϵ'_p) will be zero when $\omega_p = \omega$. In this approximation, when ω is below the plasma frequency (ω_p), ϵ' will continue to drop without limit. This approximation becomes invalid as ω approaches γ . In this case, Eq. 1.1.26 has very different behavior. In addition to the λ^{-4} dependence seen above, the material dependent term becomes important. For small spheres, the denominator

of Eq. 1.1.26 will approach zero when $\epsilon'_p = -2\epsilon'$, a condition which is satisfied by gold in air near 485 nm. However, due to the decreasing value of ϵ''_p in this range, the resulting resonance is slightly redshifted to about 520 nm, as seen in Figure 1.2. This resonance is often referred to as a localized surface plasmon resonance (LSPR).

Equation 1.1.26 made two assumptions which are often not the case. First, it assumed that the particle was much smaller than the wavelength of light. In addition to producing simplifying expansions, this limits the sum of multipoles to only the electric dipole. For larger spheres the higher order modes (including those shown in Figure 1.1) can also become resonant. The second assumption was made in Mie theory itself, which assumed that the particle is spherically symmetric. As described below, this is rarely the case in nanoparticles of interest.

1.2 The Development of Modern Nanoparticles

Despite the ease with which the above approach was applied to the scattering properties of spheres, very few structures are easily solvable. For finite particle sizes, no other shape has an exact solution for an arbitrary dielectric material. For a perfect electrical conductor (PEC), other shapes with symmetries such as ellipsoids and spheroids have been analytically solved as well [11]. This is only possible because the PEC simplifies these calculations by assuming an infinite conductivity (and hence ϵ''). Approximate solutions exist for certain cases, the most notable of which is an ellipsoid with dimensions much smaller than the wavelength of light. Solutions for more complicated shapes, including polyhedra, must be tackled with numeric methods such as the finite element method (FEM) or finite-difference time-domain (FDTD) simulations, which will be the subject of later chapters.

Since the development of a theoretical understanding of spherical and near spher-

ical particles, many different nanoparticles have been synthesized and characterized, with LSPR positions beyond those available from simple spheres. The goal is not only to produce a controlled LSPR position, but also to control width and intensity in both the near and far-field. This has been accomplished by not only inventing particles with a tuned dipole resonance, but also by introducing additional dipole and higher order resonances.

The simplest possible modification to the spherical geometry is the ellipsoid. As the aspect ratio of such a particle increases, it approximates a rod shaped particle. Rod shaped particles are valued for their ability to produce a wide range of LSPR resonances, which are tuneable based on the aspect ratio of the particle. Using synthetic methods to grow particles from seeds with the addition of a capping material composed of hexadecyltrimethylammonium bromide (CTAB) with or without benzyldimethylhexadecylammoniumchloride (BDAC), Nikoobakht *et al.* [92] demonstrated that rods with aspect ratios between 1.5 and 10 could be produced. These nanorods generated LSPR peaks ranging from under 600 nm to over 1200 nm in wavelength, as shown in Figure 1.3. While in that work only the dipole mode was strongly visible, it is possible to also excite higher order modes. Payne *et al.* [98] demonstrated that with an anodic aluminium oxide template technique, highly monodisperse nanorods (*i.e.*, having a narrow size distribution) can be fabricated with rod lengths ranging from 85 nm to 1175 nm with an 85 nm diameter (resulting in aspect ratios between 1 and 13.8). In addition to the transverse (across the short axis) and longitudinal (along the long axis) dipolar modes of the rods, the high level of monodispersity in these particles allowed higher order modes to become visible in the UV-vis spectrum. In this case, at least 7 modes were visible in the extinction spectra. These modes were labeled as odd or even based on the number of peaks and

troughs in the excited field. It is interesting to note that this included both odd and even modes, because while even modes are difficult to excite due to symmetry, angled illumination allows them to couple with the incident field.

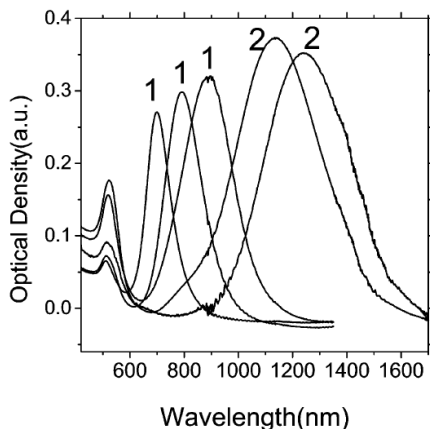


Figure 1.3: The Visible and NIR absorption spectra for gold nanorods prepared using either one or two surfactant mixtures (labeled with either a one or a two, respectively.) Reprinted with permission from Babak Nikoobakht and Mostafa A. El-Sayed. Preparation and Growth Mechanism of Gold Nanorods (NRs) Using Seed-Mediated Growth Method. *Chemistry of Materials*, 15(10):1957-1962, 2003. Copyright 2003 American Chemical Society.

Another well explored family of nanostructures is the silver polyhedron. A great deal of work has been performed on silver nanocubes. By synthetic manipulation of cubes, Tao *et al.* [121] showed that by introducing selective growth to the $\{111\}$ facet they can produce a family of structures between cube, cuboctahedron and octahedron with sizes between 80nm and 300nm. In UV-vis measurements and dark field measurements the spectra for the cube and octohedron were very monodisperse with multiple peaks corresponding to higher order modes, while the cuboctahedron varied due to incomplete growth along a face. Kumbhar *et al.* [59] studied silver icosohedrons as a function of synthesis time, producing a measurement of the extinction spectrum *via* UV-vis for a wide range of sizes up to 215 nm. This demonstrated the

expected result that as the size of the particle became larger, the number of multi-modes required to explain the extinction spectrum must also grow, as shown in the time series in Figure 1.4.

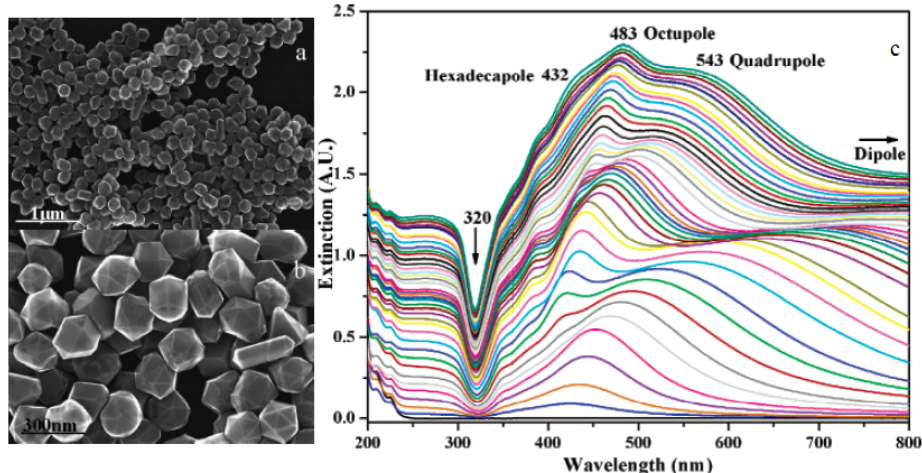


Figure 1.4: a and b. STEM (scanning transmission electron microscopy) images of silver polyhedron nanoparticles. c. UV-vis extinction measurements of the resulting particles, removed from the reactor in 15 minute intervals. Adapted with permission Amar S. Kumbhar, Mark K. Kinnan, and George Chumanov. Multipole Plasmon Resonances of Submicron Silver Particles. *Journal of the American Chemical Society*, 127(36):12444-5, September 2005. Copyright 2005 American Chemical Society.

Similar studies of gold polyhedrons have also been performed. Millstone *et al.* [79] demonstrated a gold seeded synthesis with cetyltrimethylammonium bromide (CTAB) as a capping agent to produce triangular nanoprisms with a size up to 250 nm. These particles possessed a bright dipole in the plane of the crystal as well as an in-plane quadrupole when the particle was large enough. Rodríguez-Fernández *et al.* [103] showed that in gold decahedra there are also in-plane quadrupoles and dipoles for sufficiently large particles ($>100\text{nm}$), as shown in Figure 1.5. Darkfield measurements showed that the far-field coupling to the quadrupole was orientation dependent. Additionally, on the short axis of the decahedra, there exists a dipole mode visible in UV-vis, but not in the dark field measurements. It is not clear

whether the dipole is absent due to lack of coupling from orientation in the substrate, or simply that the mode is too absorbent to be visible with darkfield measurements in air.

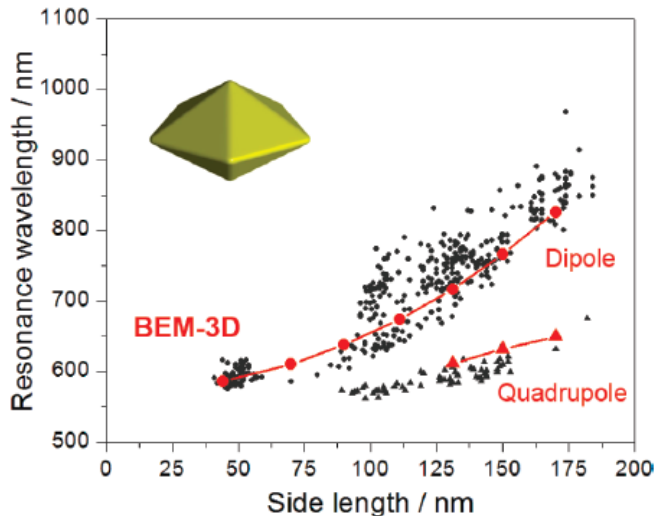


Figure 1.5: The measured single particle dipole and quadrupole positions as a function of side length for gold decahedra, compared with calculated positions from the BEM-3D software. Adapted with permission Jessica Rodríguez-Fernández, Carolina Novo, Viktor Myroshnychenko, Alison M. Funston, Ana Sánchez-Iglesias, Isabel Pastoriza-Santos, Jorge Pérez-Juste, F. Javier García de Abajo, Luis M. Liz-Marzán, and Paul Mulvaney. Spectroscopy, imaging, and modeling of individual gold decahedra. *The Journal of Physical Chemistry C*, 113(43):18623-18631, 2009. Copyright 2009 American Chemical Society.

Nanoshells, where a plasmonic shell surrounds a dielectric material, are especially interesting due to their highly tunable and spectrally versatile nature [93]. In order to create a gold nanoshell, gold seeds can be deposited on SiO_2 cores and allowed to act as nucleation sites in a growth medium [94, 93]. By varying the solution properties, it is possible to use gold seeds to deposit other metals as well, including silver [51] and copper [127]. In addition to the tuneability due to the different electrical properties of the metals, the position of the LSPR peak is exquisitely sensitive to the core diameter to shell thickness ratio [94]. As shown in Figure 1.6, as the gold shell

becomes thinner, the LSPR peak red shifts and increases in intensity and sharpness. It is also interesting to note that both gold nanoshells [94] and silver nanoshells [51] exhibit higher multimodes, including the quadrupole mode in their extinction spectrum. Prodan *et al.* [100] demonstrated that the modes in nanoshells can be viewed as hybridized versions of the components making up the particle, making an analogy to hybridization of molecular orbitals. In the case of the nanoshell, the hybridized modes are composed by combining a nanosphere with a smaller nanocavity (formed by creating a void in a bulk metal). Much like hybridized molecular orbitals, hybrid plasmonic modes are usually paired constructively and destructively to produce hybridized modes of lower and higher frequency than the original modes [100].

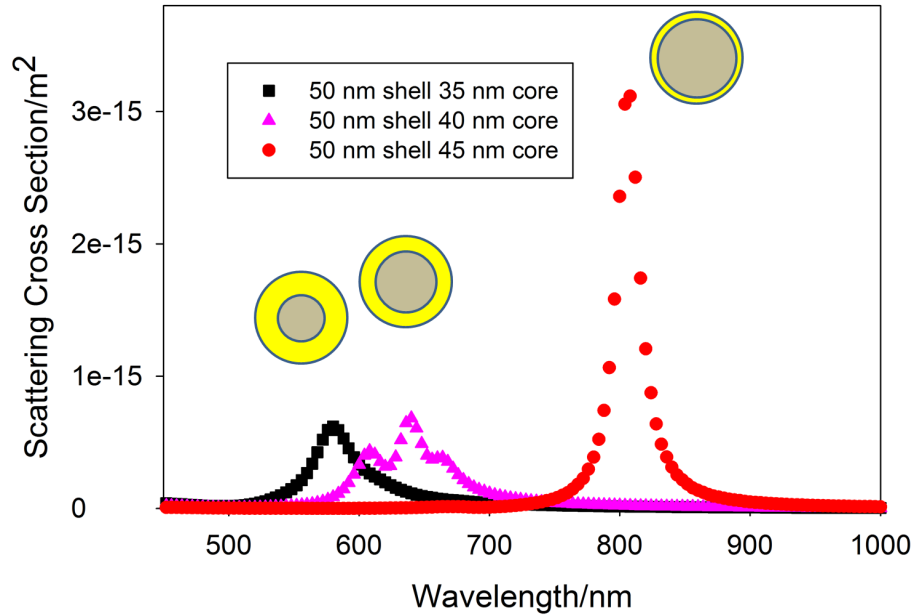


Figure 1.6: Scattering cross sections for shells with total diameter 50 nm, and interior diameter 35 nm (squares), 40 nm (triangles), and 45 nm (circles). Progressively thinner shells red shift as the total diameter stays constant in gold shells surrounding silica cores. The insets show schematic diagrams of the simulated models. Cross sections were calculated via FDTD simulation, as discussed in the following chapters.

Recently, attention has been paid to more complex nanoparticles supporting spike like substructures. Branched gold nanocrystals described by Hao *et al.* [34] grow spikes along the $\{111\}$ face of nanocrystals, with one, two, or three spikes. This selective growth is likely the result of including bis-(p-sulfonatophenyl) phenylphosphine dihydrate dipotassium (BSPP) in the synthesis. The far-field behavior of the particles is found to be sensitive to the length and sharpness of these spikes. It is understandable that the resonance wavelength should scale with the length of the object [34]. Gold nanostars [110] also have spikes, but are synthesized starting from preformed gold seeds and are subsequently grown along the $\{011\}$ face. From BEM (boundary element method) simulations, the extinction spectrum of the particles is understood to contain both a tip-mode, where fields occur predominantly around the spike tips and comes into resonance at about 750 nm, and a body-mode which is similar to a spherical mode on the body itself, and comes into resonance at about 530 nm. Further studies by Hao *et al.* [35] using an FDTD model show that the modes in these particles can be accurately described by bonding/anti-bonding hybridization between the spike modes in the absence of the core, and core modes in the absence of the spikes.

The two particle classes described above (shells and spiked particles) have been combined in order to produce a new class of nanoparticles, spiky nanoshells, which are the focus of this dissertation. Spiky nanoshells are formed by using silver seeds on the surface of a polystyrene substrate, and exposing the seeded cores to a growth solution which includes gold chloride and the surfactant CTAB. The gold almost completely replaces the silver when the spikes are grown, and the synthesis is highly efficient [106, 108]. The far-field properties of these particles, including tunability and higher order modes, are discussed in more detail in chapters 4 and 6. Similar

structures have been synthesized using silver octahedron cores and gold spikes [99], using poly-(vinylpyrrolidone) (PVP) in the growth solution with no CTAB. These bi-metallic particles were analyzed with EELS (electron energy-loss spectroscopy, a Transmission Electron Microscopy (TEM) technique which measures electron energy loss as a function of position around the particle). This study found that there are multiple modes associated with the core, the spikes, and hybridizations of plasmons between the two structures. Additionally, EELS shows that the shorter spikes are associated with higher energy modes, while longer spikes are associated with lower energy modes. This result is expected, as generally the wavelength required to excite an oscillator should scale with the length of the oscillator, as seen in the acoustics of drums and guitars or in the resonant frequency of a rectangular electromagnetic cavity. Similar structures have been constructed by growing spikes using different substrates (such as rods and wires) as cores [8].

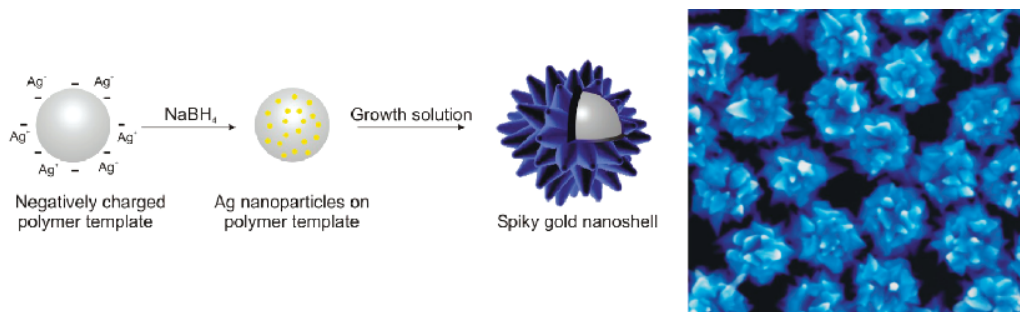


Figure 1.7: The synthesis of spiky gold nanoshells and an SEM image of the resulting particle around a 100 nm diameter polystyrene core. Adapted with permission from Brenda L. Sanchez-Gaytan, Pattanawit Swanglap, Thomas J. Lamkin, Robert J. Hickey, Zahra Fakhraai, Stephan Link, and So-Jung Park. Spiky Gold Nanoshells: Synthesis and Enhanced Scattering Properties. *The Journal of Physical Chemistry C*, 116(18):10318-10324, May 2012. Copyright 2012 American Chemical Society.

In addition to modifications of the growth parameters for nanoparticles as described above (so called ‘bottom up’ synthetic approaches), one can also act on an

existing substrate to produce a different structure. For example, it is possible to study the effects of surface roughness by modifying the structure of gold nanoshells and examining the optical activity of the resulting roughened nanoshells. For instance, Wang *et al.* [126] used a site specific etchant in order to modify prefabricated gold nanoshells. Site specificity was established by showing that in monocrystalline particles no roughening was observed although diameter decreased. Experimentally, this resulted in a progressively red-shifted spectrum as the nanoshell core thickness shrank. FDTD simulations indicated that in addition to a red shift in the dipole LSPR, the quadrupole mode is suppressed in the resulting structure based on observation of a decreased ratio of extinction efficiency between the two modes. A second approach to roughening nanoshells was shown by Wang *et al.* [124], where gold seeds were allowed to attach to the surface of a pre-existing complete nanoshell. As the shell became thicker, the dipole and quadrupole modes blue shifted and the quadrupole mode became more pronounced. These two effects are due to the thicker shell and larger overall size. Comparing rough and smooth shells with equal dipole resonances showed a broader extinction peak in the rough shells, but was otherwise very similar at both the dipole and quadrupole locations. Also performed was an Angle Dependent Light Scattering (ADLS) experiment where the intensity of the scattered light is measured as a function of angle. While the extinction spectra did not seem to be greatly affected by the roughness, at the quadrupole wavelength the ADSL distribution indicated a substantial difference in the quadrupole lobe of the scattered light, suggesting that there is indeed a measurable change in the far-field behavior.

In addition to the topology of a nanoparticle and the materials it is composed of, the environment surrounding it also plays a crucial role in determining its optical response. As mentioned earlier, for a spherical nanoparticle, Eqs. 1.1.6 and 1.1.7

depend on the wave-number in the environment. This has the effect of red-shifting the spectrum in general as the background index increases. Since the scattering response is dictated by the index of the environment, this method not only provides a powerful mechanism for controlling the interaction of light with the nanoparticle, but also provides a mechanism for sensing the environment itself. Sherry *et al.* [113] demonstrated that silver nanocubes have a single LSPR peak position when in an aqueous environment, but upon the introduction of a substrate, the dipole splits into two separate modes visible in backscatter measurements. They also introduced the concept of a ‘figure of merit’ for index sensing, defined as:

$$FOM = \frac{m}{FWHM} \quad (1.2.1)$$

Where m is the slope of the peak position shift as the index is changed and FWHM is the full-width half-maximum of the peak being examined. Numerous other nanoparticles have been characterized theoretically [78, 71] or experimentally [125] in this fashion.

1.3 Surface Enhanced Raman Spectroscopy

In Raman scattering, a monochromatic light source in the UV-vis-NIR region is used to excite a sample in order to characterize its vibrational modes [27]. Raman scattering, as opposed to Rayleigh scattering discussed above, is a type of inelastic scattering. The initial laser frequency, ν_0 , is scattered at frequency $\nu_s = \nu_0 \pm \nu_{vib}$, where ν_{vib} is the frequency of the molecular vibrational mode in the IR. The Stokes frequency scattered light, $\nu_s = \nu_0 - \nu_{vib}$, is the result of the scattered light leaving the molecule in an excited state. Conversely, the Anti-Stokes frequency scattered light, $\nu_{as} = \nu_0 + \nu_{vib}$,

is the result of the laser light acting on a molecule already in an excited state and relaxing it back to the ground state. As a result, in most circumstances the Stokes lines are used for Raman spectroscopy as they will be more intense under ordinary conditions. Raman scattering is governed by many different factors. The intensity of scattered light is given by [27]:

$$I_s = K(\nu) \times A(\nu) \times \nu_s^4 \times I_0 \times J(\nu) \times C \quad (1.3.1)$$

Where $K(\nu)$ is the overall spectral response, $A(\nu)$ describes the self-absorption for the medium, ν_s is the frequency of the scattered light, I_0 is the intensity of the exciting light, $J(\nu)$ is a molar scattering parameter and C is the concentration. The most important consequence of this equation is that high frequency light (*i.e.*, lasers closer to the UV) will usually provide higher Raman intensity than lasers in the IR. Another factor that is important to consider is whether the exciting laser frequency is near an electronic transition for the molecule. If this is not the case, then non-resonant Raman scattering is being performed. In Resonant Raman (RR), the excitation radiation excites the molecule's electronic state, which then decays to the excited vibrational state but in the electronic ground state. RR results in an enhancement of 10^3 to 10^5 in the scattered light intensity [27].

Surface enhanced Raman spectroscopy (SERS) is a powerful method for identifying, measuring, and characterizing chemicals. First observed on roughened silver metal [53, 7], SERS occurs when the local electric field around an analyte is enhanced. In SERS, the Raman process is enhanced both due to higher electric fields for the absorption process, and also due to a coupling of the molecular dipole to a macroscopic dipole in the enhancing structure [130]. It can be shown that the SERS electronic cross section enhancement factor, EF, is proportional to the near-field electric inten-

sity [85, 130]:

$$EF \propto \frac{|E(\nu_0)|^2 |E(\nu_s)|^2}{|E_0(\nu)|^2 |E_0(\nu_s)|^2} \quad (1.3.2)$$

Where the electric fields are due to the nearby plasmonic surface, measured at the excitation and emitting wavelengths. These are normalized to the field in the absence of the structure, E_0 . This can also be performed near an electronic transition and achieve several orders of magnitude of additional enhancement as in RR. This is called surface enhanced resonance Raman spectroscopy (SERRS).

In practice, this surface can be produced by a wide range of structures. Due to their utility as a model system, substantial attention has been paid to the enhancement of single spherical nanoparticles, which have analytical solutions for electric fields [119, 85]. Experimental studies of spherical gold nanoparticles have found maximum enhancement factors between 10^4 [54] and 10^6 are possible, with the largest enhancement factors at 50 nm diameter [45]. The variations in these numbers are the result of different particle size windows being tested, although the results may also not be comparable due to choice of analyte or differences in monodispersity of the particle samples.

Nanoshells have also been extensively studied due to their intrinsic tuneability. Talley *et al.* [120] showed that in nanoshell structures (monomers and dimers), the enhancement correlated with the predicted field from FDTD simulations. As shown in Figure 1.8, the enhancement from a smooth shell is much larger than that of a nanosphere, and can be further enhanced with the addition of roughness.

Higher enhancement is possible where the particle contains a sharp point or edge, such that the near-field is further enhanced by ‘lightning rod’ effects. These effects are seen near perturbations to smooth surfaces, as in the roughened shell in Figure 1.8.

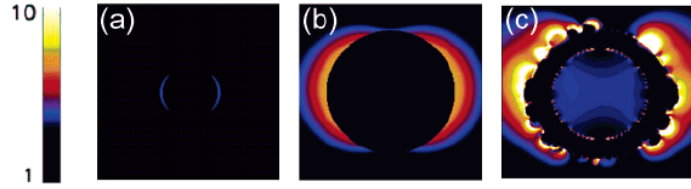


Figure 1.8: The electromagnetic field enhancement at $\lambda_0=633$ nm near a gold sphere ($r=30$ nm), shell ($r_1=49$ nm, $r_2=70$ nm) and roughened shell of the same size. Adapted with permission from Chad E. Talley, Joseph B. Jackson, Chris Oubre, Nathaniel K. Grady, Christopher W. Hollars, Stephen M. Lane, Thomas R. Huser, Peter Nordlander, and Naomi J. Halas. Surface-Enhanced Raman Scattering from Individual Au Nanoparticles and Nanoparticle Dimer Substrates. *Nano letters*, 5(8):1569-74, August 2005. Copyright 2005 American Chemical Society.

Many different nanoparticle systems have been developed to utilize these effects for SERS. Two groups have reported (different) flower like silver structures with rough or sharp surfaces. Most interesting is the work by Cathcart *et al.* [20], where silver particles with three or more sharp ‘petals’ are arranged around a common centre, producing maximum single particle enhancements factors of 4×10^8 . A second species going by the same name is actually a highly roughened sphere structure reported by Liang *et al.* [65] with polarization dependent hotspots on the particle. Due to their large size (up to approximately $2 \mu\text{m}$), dark field microscopy was reported to show a bright quadrupole peak at the SERS excitation wavelength. A similar meso-scale structure was produced in gold by Wang *et al.* [125]. These particles (called “meatballs”) possess high levels of monodispersity in size ($430 \text{ nm} \pm 38 \text{ nm} (\sigma)$). This allows the resolution of three peaks in the extinction spectrum, identified based on a smooth shell model as the dipole, quadrupole, and octopole. Additionally, these particles have substantial surface roughness, potentially increasing the SERS enhancement factor, which was found to be between 10^6 and 10^7 .

Optimizing the excitation wavelength dependence is of great interest in SERS.

Equation 1.3.2 suggests that one must maximize the enhancement at both the excitation and Stokes wavelengths. In particles where the near-field is dominated by the electric field due to a scattering mode, the strength of that mode in the far-field should provide an accurate guide for the location of maximum enhancement [40]. The simplest approach to confirming this is measurement of the enhancement factor as a function of the excitation wavelength. An early measurement of this effect was performed by Weitz *et al.* [131], where the absorption spectra was used to predict the SERS enhancement of silver-island films at many different excitation wavelengths. This approach is extremely difficult due to the large amount of equipment required when using traditional setups. Haynes *et al.* [40] avoided this issue by using triangle-like structures produced by nanosphere lithography. Due to the small intrinsic variation in LSPR position, the same measurement can be performed by keeping the wavelength fixed while the structure varies. As shown in Figure 1.9, the ‘plasmon-sampled’ measurement demonstrated that the peak enhancement occurs when the LSPR peak is approximately halfway between the excitation and Stokes wavelengths. This behavior is expected when the field enhancement is primarily due to the mode responsible for light scattering.

The highest known SERS enhancements have been observed in the study of nanoparticle aggregates (dimers, trimers, *etc.*) with gaps in the 1 nm range. This enhancement geometry has been studied in a number of materials, including gold and silver. In these aggregates (with resonant analytes), enhancements of up to 10^{15} have been observed [89]. This is sensitive enough to measure the signal of even a single molecule of analyte [58]. Kneipp *et al.* for instance used silver aggregates for the first time to measure single particles of crystal violet. This was accomplished by taking a time series and showing that the intensity of characteristic peaks for the analyte

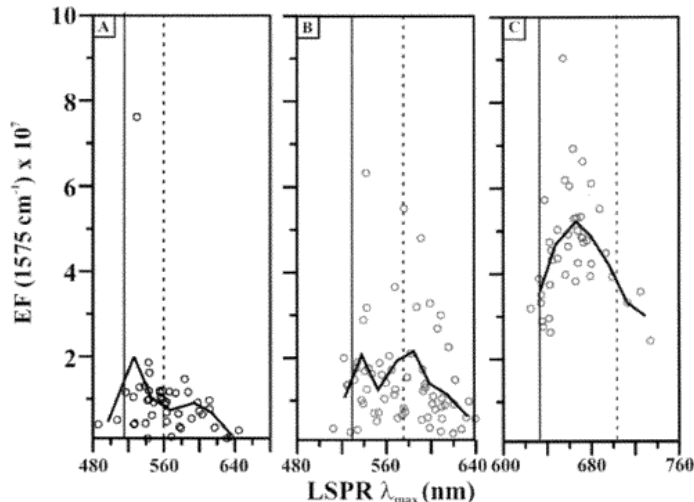


Figure 1.9: The enhancement as a function of LSPR position for the 1575 cm^{-1} benzoethiol line. Solid and dashed vertical lines present the excitation and Stokes wavelength positions, while the thick black line is the bin-averaged EF. Reprinted with permission from Christy L. Haynes and Richard P. Van Duyne. Plasmon-Sampled Surface-Enhanced Raman Excitation Spectroscopy. *The Journal of Physical Chemistry B*, 107(30):7426-7433, July 2003. Copyright 2003 American Chemical Society.

followed a Poisson distribution with clear discrete positions for zero, one, and two analyte molecules. Nie *et al.* [89] reported a similar single molecule result on what was claimed to be single Ag nanoparticles shortly thereafter, but this result has not been reproduced [19]. These aggregates are generally unreliable due to the random nature of the aggregation process. They therefore are sensitive to the polarization of the excitation source [134], as well as to the location of the analyte on the surface relative to the gap, and to the size of the gap itself [13].

There has been an active search for more reliable mechanisms of performing single molecule SERS so that applications can be more easily designed. Aggregate based methods are extremely prone to substrate unreliability as they are based on random aggregation of a few particles rather than an engineered structure [140]. One alternative method employs triangular nanopyramids created with nanosphere lithography.

Zrimsek *et al.* [140] utilized a dilute analyte solution of equal parts R6G-d₀ and R6G-d₆, such that each detection volume would have on average less than one particle present in the active volume at a time. By examining the statistics of how often signals from each analyte were found, as well as how often they are found together, it can be shown that single molecule measurements were occurring. In this case they found a 2.8:1:2.4 ratio of R6G-d₀:both:R6G-d₆ in agreement with an expected value of 2.5:1:2.5 for single molecule sensing.

A critical question surrounds the wavelength dependence of SERS in gap based structures. While in single particles the dipole LSPR mode was seen to dominate the enhancement, in this case the gap mode is a dark mode, and incapable of strong coupling to the far-field. Wustholz *et al.* [133] showed with FEM (the finite element method of electromagnetic simulation) that the enhancement in a gold nanosphere trimer structure coated in SiO₂ should have a broad plateau of enhancement across the visible and near-IR, and be largely uncorrelated with the LSPR position. On a sample size of 30 nano-antennas, they found the EF was largely unrelated to the number of cores in the aggregate, and that EF was largely uncorrelated with the LSPR position, particularly above 750 nm. A follow-up paper by Kleinman *et al.* [56] studied SERS at eight wavelengths distributed from green to the near-IR. As predicted in the earlier paper, such a plateau is indeed observed, with a striking agreement between the theoretical prediction and the average measured EF, as shown in Figure 1.10.

A number of promising applications of SERS have been explored. SERS sensing provides a powerful platform for chemical and biological weapons detection. For example, at least two groups have shown that X-Y scanned SERS can be used to identify specific pathogenic bacteria. Rule *et al.* [104] used two different resonant

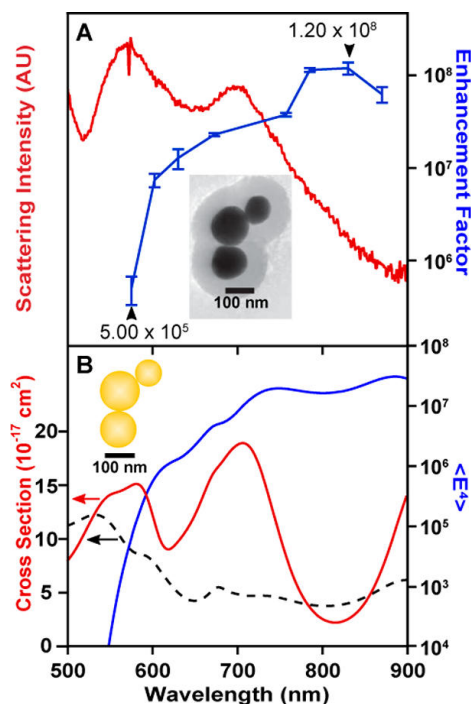


Figure 1.10: A: experimental backscatter (red) and SERS measurements (blue) of the encapsulated gold trimer (inset). B: FDTD simulations for a structure modeled based on the top TEM image including both the scattering cross section (red) absorption (dashed black) and the average E^4 (blue). Adapted with permission from Samuel L. Kleinman, Bhavya Sharma, Martin G. Blaber, Anne-Isabelle Henry, Nicholas Valley, R. Griffith Freeman, Michael J. Natan, George C. Schatz, and Richard P. Van Duyne. Structure Enhancement Factor Relationships in Single Gold Nanoantennas by Surface-Enhanced Raman Excitation Spectroscopy. *Journal of the American Chemical Society*, 135(1):301-8, January 2013. Copyright 2013 American Chemical Society.

dyes tagged on single gold nanospheres, each with a different antibody. The spatial distribution was then used to identify bacteria locations of different types. Huang *et al.* [46] performed similar work, but used an antibody with a very specific target in order to achieve high differentiation. Instead of using single gold nanoparticles for sensing purposes, they employed silica embedded gold aggregates with gap modes. This body of work, and others like it, show the tremendous promise SERS has for biomedical applications.

1.4 Modal Interference

In order to more finely control the electric near-field and the far-field scattering, as well as to understand the behavior of more complicated nanostructures, it is necessary to characterize interference between plasmonic modes. When two plasmonic modes overlap in space and frequency [70], their fields are able to interact and interfere both constructively and destructively, allowing the creation of sophisticated spectral features in plasmonic systems.

A number of different phenomena create interference features in the scattering spectrum of a nanostructure. Generally, there must be multiple resonances occurring with overlaps in both space and frequency for interference to occur. However, these resonances need not be on the same particle, or be of the same order. It is also possible for one part of a particle to interfere with another. For instance, in multi-layered shells, the dipole moment of one layer can cancel out the dipole moment of another, effectively cloaking the structure [83].

When two out of phase oscillators interfere with one another, they can dramatically reduce the scattering cross section. This is referred to as a sub-radiant mode. Alternatively, the two oscillators can be in-phase, resulting in the scattering cross section being greatly increased. This is referred to as a super-radiant mode. One common type of interference often observed in plasmonic nanostructures is the Fano-resonance. However, there appears to be some confusion in the literature on the exact definition of the term. Historically, a Fano-resonance described a phenomenon where a continuous background process interfered with a narrow resonance process, resulting in destructive interference on one side of the resonance frequency and constructive interference on the other due to the π phase change in the sharp resonance. In particular, this was originally used to describe inelastic electron scattering from

helium (a continuous processes) interfering with an autoionization process (a sharp resonant effect) [82]. While the term is applied fairly loosely in plasmonic systems, it usually is used to describe the interference of a narrow mode (usually a molecular resonance or higher order and perhaps dark mode) with a broad and bright dipolar mode [86].

Single particle systems which exhibit interference effects are particularly interesting as they are often produced synthetically rather than lithographically. The Fanoshell [86] is an excellent example of a single particle with interference. The Fanoshell is composed of an Au core surrounded by a SiO₂ shell with an additional Au shell on top of that. These have three characteristic interference patterns. A super-radiant mode is formed by the in-phase dipole oscillation of both the shell and core, exhibiting higher than usual scattering. Additionally, two Fano resonances occur, one due to the out of phase interference of the shell and the core, and one due to the interference of the core quadrupole mode and the shell dipole mode, as shown in the mode hybridization diagram in Figure 1.11.

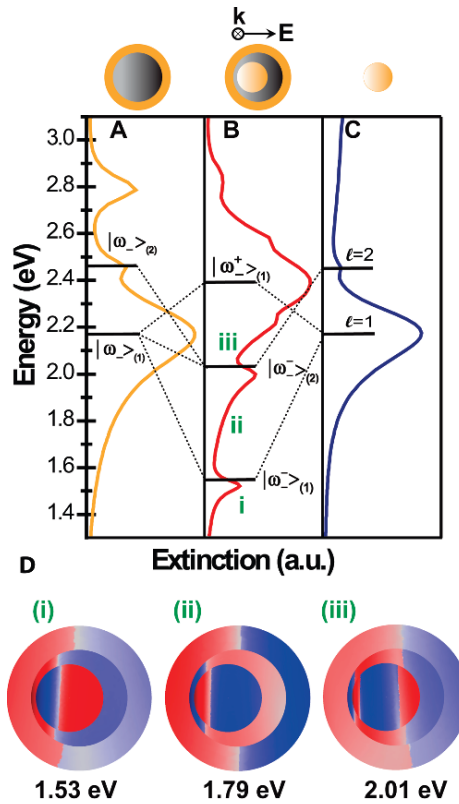


Figure 1.11: Hybridization diagram for a gold nanosphere and a gold nanoshell in silica to form a Fanoshell. The core, inner shell and outer shell have radius 35 nm, 50 nm, and 75 nm respectively, while the core is off-center by 10 nm. Results are the product of FEM simulations. Reprinted with permission from Shaunak Mukherjee, Heidar Sobhani, J. Britt Lassiter, Rizia Bardhan, Peter Nordlander, and Naomi J. Halas. Fanoshells: Nanoparticles with Built-in Fano Resonances. *Nano letters*, 10(7):2694-701, July 2010. Copyright 2010 American Chemical Society.

In single particle systems which obey Mie theory, it is only possible to induce an interference pattern between modes in angular scattering and in the extinction cross section. Recall that the total cross section efficiency is [72]:

$$Q_{scat} = \frac{2}{q^2} \sum_{n=1}^{\infty} (2n+1)(|a_n|^2 + |b_n|^2) \quad (1.4.1)$$

where $q = \omega a/c$, for the speed of light c and particle size a . As a result of the separate absolute value operations, interference between the dipole and quadrupole is impossible in such a system. In the Fano shell system, the interference between the core quadrupole mode and the shell dipole mode is possible due to a spatial offset on the core relative to the center of the shell, allowing the two modes to become non-orthogonal by violating the conditions of the above formulation. A second clear example of a Fano effect occurs in the spectra of silver nanorods [70] where the quadrupole mode is able to interfere with a dipole mode. In this case Mie theory's basic tenant of spherical symmetry has been clearly violated by the rod which possesses axial but not spherical symmetry.

However, in Mie theory this limitation is not shared with directional scattering [72, 122]. The radar backscatter efficiency for instance is [72]:

$$Q_{RBS} = \frac{1}{q^2} \left| \sum_{n=1}^{\infty} (2n+1)(-1)^n [a_n - b_n] \right|^2 \quad (1.4.2)$$

Here, it is explicitly possible for modes of different order (n) to interact. For a small plasmonic particle where $a_n \gg b_n$, the first interaction occurs between the dipole and the quadrupole [72]:

$$Q_{RBS} = \frac{1}{q^2} \left| a_1 - \frac{5}{3} a_2 \right|^2 \quad (1.4.3)$$

A number of theoretical and experimental studies have been performed on multi-layer shell structures [10, 83, 86], involving one or more layers of plasmonic material or dielectric material. In these structures, application of a dipolar transverse-magnetic (TM, an electric mode) wave can produce a Fano-like line shape with a characteristic peak and trough. In this case the interference is restricted to a single spherical harmonic mode, and represents different layers of the structure interfering rather than modes of different order interfering. For the case of a multilayer core shell system, we can still apply Mie theory because the structure is spherically symmetric, however we cannot apply Eqs. 1.1.6 and 1.1.7 because they were derived assuming a single boundary condition surface. In this case the n^{th} order TM (*i.e.*, an electric mode) scattering coefficient is instead given by [83]:

$$c_n^{TM} = -\frac{U_n^{TM}}{U_n^{TM} + iV_n^{TM}} \quad (1.4.4)$$

Here, the expressions for U_n^{TM} and V_n^{TM} are the determinants of matrices composed of the spherical bessel functions, their derivatives, and the size and material of the core and shell (and subsequent layers) [77]. The transverse-electric (TE, a magnetic mode) coefficients, labelled c_n^{TE} , are given by a similar expression. These variables serve the same purpose as a_n and b_n in Eqs. 1.1.6 and 1.1.7, but we will maintain the distinct naming convention to avoid confusion on how they are calculated. The total scattering cross section is given by the standard Mie theory result [83]:

$$\sigma_{scat} = \frac{\lambda_0^2}{2\pi} \sum_{n=1}^{\infty} (2n+1) (|c_n^{TM}|^2 + |c_n^{TE}|^2) \quad (1.4.5)$$

By tuning V very small, the coefficient can approach unity, while by tuning U small the coefficient can approach zero. For a (plasmonic core)-(dielectric shell)-(plasmonic shell) system like that of the Fanoshell, the former case will produce a super-radiant

mode. In this case, both the shell dipole mode and the core dipole mode are in-phase and the combination of multiple scatters results in an increased scattering cross section. In the latter case, the two modes are out of phase, and they will effectively cloak the structure reducing its total scattering cross section significantly. This occurs due to cancellation of the fields from multiple dipoles located in different layers. A Fano-like spectral line shape can be created when the super-radiant mode is next to a sub-radiant mode. This can be fabricated in a controlled fashion by tuning the layer thicknesses in the nanostructure [10, 83]. For a simple dielectric coated in Ag, Alù *et al.* [83] showed that two distinct types of cloaking modes occur. In one mode the incident wave is virtually unperturbed, while it is also kept nearly zero within the structure. However, at a second cloaking resonance point, while the incident field was still unperturbed, the interior field was very large. The former case is useful as it protects the interior of the particle from damage, while the later presents an opportunity for sensing applications where high fields are useful.

Lithographically printed structures have been a versatile way to study the Fano resonance in a controlled fashion. One such system is a gold ring cavity containing a disk [36]. These are effectively the two-dimensional analog of the core-shell models discussed previously. This results in two cases: a symmetric case, where the disk is concentric with the ring, and an asymmetric case where the disk is on a shifted axis. For the concentric case, the structure is known to support a super-radiant mode with anti-bonding between a primitive dipole excitation in the ring and a dipole pattern in the disk. Additionally, a sub-radiant mode with bonding dipole excitations in both structures is also possible. With the addition of asymmetry, a quadrupole mode in the ring can couple with the dipole mode in the disk. This produces a Fano-resonance, which has been experimentally observed [118]. Theoretical models from Sonnefraud

et al. are shown in Figure 1.12.

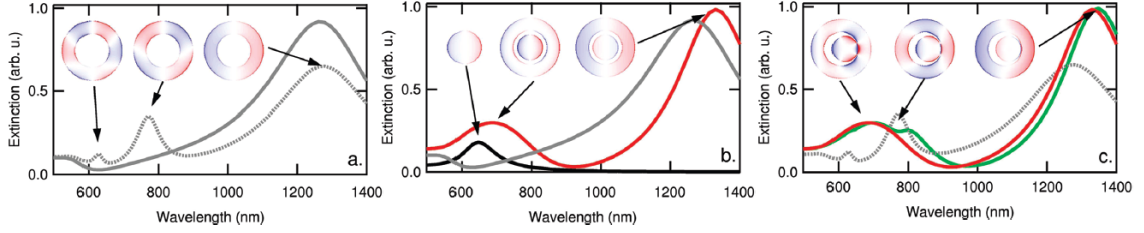


Figure 1.12: Simulated extinction cross sections for concentric disk/ring cavities with charge distributions inset. a. Extinction for an isolated ring. Different modes are available with normal incidence (gray) compared to grazing incidence (dotted gray). b. The disk (black) and ring (gray) are compared to the combined concentric (symmetric) system (red). c. The ring at grazing incidence (dotted gray) compared to the concentric (red) and non-symmetric (green) curves. Diameter of the disk was 150 nm, while the interior and exterior diameters of the ring were 200 nm and 350 nm respectively. The non-symmetric cavity has a gap of only 8 nm. Adapted with permission from Yannick Sonnefraud, Niels Verellen, Heidar Sobhani, Guy A.E. Vandenbosch, Victor V. Moshchalkov, Pol Van Dorpe, Peter Nordlander, and Stefan A. Maier. Experimental Realization of Subradiant, Superradiant, and Fano Resonances in Ring/Disk Plasmonic Nanocavities. *ACS Nano*, 4(3):1664-1670, 2010. Copyright 2010 American Chemical Society.

Exciting applications have been proposed by mixing Fano-like interference with non-linear materials. Argyropoulos *et al.* showed that by employing a non-linear Kerr material as a core with relative permittivity $\epsilon_c = \epsilon_L + \chi^{(3)}|\vec{E}|^2$, where $\epsilon_L = 2.2$ and $\chi^{(3)} = 4.4 \times 10^{-20} m^2/V^2$, an optical switching effect could be achieved [10]. In this work, the sharp Fano-like resonance will drop the scattering cross section by approximately 40 dB when the wavelength changes by a fraction of a nanometer. As a result of the non-linear material, the intensity of incident light can act as a trigger for this optical switch, where a slight increase of intensity will induce a drastic drop in scattered light. Additionally, such a system possesses hysteresis, meaning that it could also be used to potentially construct an optical memory device [10].

By layering a shell several times with staggered ϵ values, one can also construct

a comb-like pattern of Fano-like resonances. Monticone *et al.* [84] showed that in the limit of thin shells, the cloaking and super-radiant resonance points are described by the same equations, and are robust. In particular, in the lossless limit, each layer is equally capable of inducing a super-radiant or cloaking mode, regardless of position within the layers. Monticone *et al.* further describe a scheme for using such a plasmonic comb structure for optical tagging, where the peak positions could be used to uniquely identify an object.

In addition to the cloaking, optical tagging and super-radiant/sub-radiant applications discussed above, there is substantial potential for modal interference to play a role in sensing applications. In these cases, it is often possible to induce very large near-fields near Fano and Fano-like features [135, 83]. For instance, many studies have discussed the possibility of SERS enhancement being increased in a ring/disk cavity or other nanostructure with a built in Fano resonance [36, 118]. This has been tested by Ye *et al.* [135], who showed a moderate increase in enhancement factors.

Another potential sensing application specific to Fano systems is index sensing. Hao *et al.* [37] showed for instance that the Fano resonance in ring-disk cavities are unusually sensitive to the local index of refraction of the media, with a figure of merit (FOM) as high as 8.34, as defined by Eq. 1.2.1. López-Tejiera *et al.* [71] showed that using the Fano resonance in silver nanorice, a substantially higher FOM of between 8.7 and 18.9 could be achieved, where they also included the effect of disorder and size dispersion explicitly in their calculations. In the same work, they demonstrated that lithographically produced gold nanobelts could also be used for index sensing, which would in principle not suffer from the same level of size dispersion. Additionally, control of the angle of exposure and light collection could in principle enhance the signal from the Fano resonance.

Chapter 2

The Theory of Optical Scattering from Nanoparticles

2.0.1 Maxwell's Equations

Maxwell's equations provide the relationship of the electric and magnetic fields, \vec{E} and \vec{H} , to the charge and current density, ρ and \vec{J} . In a linear, homogeneous, and isotropic medium with permittivity ε and permeability μ , these are given by [97]:

$$\nabla \cdot \vec{H}(\vec{r}, t) = 0 \quad (2.0.1)$$

$$\nabla \cdot \vec{E}(\vec{r}, t) = \frac{\rho(\vec{r}, t)}{\varepsilon} \quad (2.0.2)$$

$$\nabla \times \vec{E}(\vec{r}, t) = -\mu \frac{\partial \vec{H}(\vec{r}, t)}{\partial t} \quad (2.0.3)$$

$$\nabla \times \vec{H}(\vec{r}, t) = \varepsilon \frac{\partial \vec{E}(\vec{r}, t)}{\partial t} + \vec{J}(\vec{r}, t) \quad (2.0.4)$$

The auxiliary fields are defined as:

$$\begin{aligned}\vec{D} &= \varepsilon_0 \vec{E} + \vec{P} = \varepsilon_0 \vec{E} + \varepsilon_0 \chi_e \vec{E} \\ &= \varepsilon_0 (1 + \chi_e) \vec{E} = \varepsilon \varepsilon_0 \vec{E} = \varepsilon \vec{E}\end{aligned}\tag{2.0.5}$$

$$\vec{H} = \frac{\vec{B}}{\mu_0} - \vec{M} = \frac{\vec{B}}{\mu}\tag{2.0.6}$$

For electric and magnetic polarizations \vec{P} and \vec{M} . The permittivity of the material is referred to as ε . The relative permittivity (or dielectric constant) is given by $\epsilon = 1 + \chi_e = \frac{\varepsilon}{\varepsilon_0}$. Here, the electric susceptibility, χ_e , describes the degree of polarization a material acquires in response to an applied electric field.

Additionally, conservation of charge requires the continuity equation. This is a differential statement of the fact that in any infinitesimal piece of space the net change in charge over time must equal the current flow out of that space.

$$\nabla \cdot \vec{J} = -\frac{\partial \rho}{\partial t}\tag{2.0.7}$$

Because Maxwell's equations support wave solutions, we can re-express them in frequency space as complex fields. In general, this is done with the Fourier transform:

$$\vec{E}(\omega, \vec{r}) = \int \vec{E}(t, \vec{r}) e^{i\omega t} dt\tag{2.0.8}$$

Fields (and other real functions of space and time) are usually worked with in the frequency domain. The complex coefficients (which we will refer to as 'phasors') can be converted back to the time domain by reintroducing the time dependence and taking the real part [97]:

$$\vec{E}(\vec{r}, t) = \text{Re}\{\vec{E}_\omega(\vec{r})e^{-i\omega t}\} \quad (2.0.9)$$

In phasor form, using the convention $e^{-i\omega t}$, Eqs. 2.0.1 to 2.0.4 transform into the monochromatic Maxwell's equations [97]:

$$\nabla \cdot \vec{H}(\vec{r}, \omega) = 0 \quad (2.0.10)$$

$$\nabla \cdot \vec{E}(\vec{r}, \omega) = \frac{\rho(\vec{r}, \omega)}{\epsilon} \quad (2.0.11)$$

$$\nabla \times \vec{E}(\vec{r}, \omega) = i\omega\mu\vec{H}(\vec{r}, \omega) \quad (2.0.12)$$

$$\nabla \times \vec{H}(\vec{r}, \omega) = \vec{J}(\vec{r}, \omega) - i\epsilon\omega\vec{E}(\vec{r}, \omega) \quad (2.0.13)$$

It is often necessary to consider the energy transported by an electromagnetic wave. The intensity and direction of energy flow at any time and point in space is determined (in W/m²) by the instantaneous Poynting vector:

$$\vec{S}(t, \vec{r}) = \vec{E}(t, \vec{r}) \times \vec{H}(t, \vec{r}) \quad (2.0.14)$$

And the time-averaged Poynting vector (which notably does not follow the rule for phasors above) is:

$$\langle \vec{S} \rangle = \frac{1}{2} \text{Re}\{\vec{E} \times \vec{H}^*\} \quad (2.0.15)$$

2.1 Scattering Models

The study of the optical properties of nanoparticles focuses on the problem of how an incident plane wave will be distorted in passing through a nanoparticle. Because a particle is effectively point-like in the far-field, it is easiest to express the fields in a spherical coordinate system. Since the particle may not be spherical, it is necessary to define a spherical region surrounding it, V_0 . The rest of space will be referred to as V_1 [123]. Strictly speaking, V_0 is the smallest inscribing sphere which can contain the particle, as shown in Figure 2.1. We now can project the electric field of the incident plane wave in region V_0 onto an orthogonal Vector Spherical Harmonic Wave Function basis (VSHWF) [123]:

$$\vec{E}^I(\vec{r}) = \sum_{m,n} \left[a_{mn}^{I(M)} Rg\vec{M}_{mn}(kr, \theta, \phi) + a_{mn}^{I(N)} Rg\vec{N}_{mn}(kr, \theta, \phi) \right] \quad (2.1.1)$$

Here, $Rg\vec{M}_{mn}$ and $Rg\vec{N}_{mn}$ are the electric fields associated with the incoming m^{th} magnetic and electric modes of order n (defined below), while $a_{mn}^{I(M)}$ and $a_{mn}^{I(N)}$ are the expansion coefficients. The vector spherical harmonic wave functions ($Rg\vec{M}_{mn}$ and $Rg\vec{N}_{mn}$) form a complete orthogonal basis for describing the scattered radiation field. The index variables take values $n = 1, 2, \dots, \infty$, $m = -n, -n + 1, \dots, n - 1, n$.

The outgoing scattered waves can be described by a similar expansion in region V_1 [123]:

$$\vec{E}^S(\vec{r}) = \sum_{m,n} \left[a_{mn}^{S(M)} \vec{M}_{mn}(kr, \theta, \phi) + a_{mn}^{S(N)} \vec{N}_{mn}(kr, \theta, \phi) \right] \quad (2.1.2)$$

Where where \vec{M}_{mn} and \vec{N}_{mn} are the electric fields associated with the electric and magnetic outgoing modes. Each of these modes represents the light scattered in a particular multipole ($n = 1$ terms correspond to dipolar scattering, *etc.*). In a

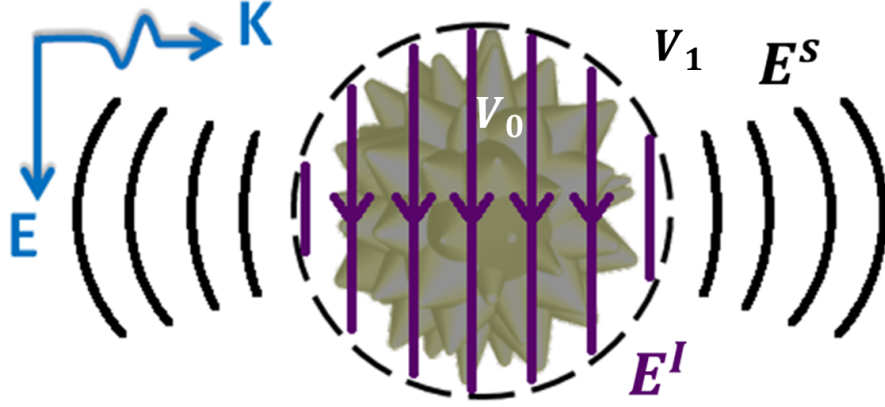


Figure 2.1: In the T-matrix theory the scattered field is expanded outside of a circumscribing sphere around the particle, while the incident field is expanded inside the sphere.

linear system, when using complete basis functions for the scattered and excitation fields, it is possible to relate all incoming modes to all outgoing modes by a matrix of coefficients. This is referred to as the T-matrix [123]:

$$\begin{bmatrix} \vec{a}^{S(M)} \\ \vec{a}^{S(N)} \end{bmatrix} = \begin{bmatrix} \mathbf{T}^{(11)} & \mathbf{T}^{(12)} \\ \mathbf{T}^{(21)} & \mathbf{T}^{(22)} \end{bmatrix} \times \begin{bmatrix} \vec{a}^{I(M)} \\ \vec{a}^{I(N)} \end{bmatrix}$$

Or simply:

$$\vec{a}^S = \mathbf{T}\vec{a}^I \quad (2.1.3)$$

Where the T-matrix is simply the set of coefficients linking these two equations [123]:

$$a_{mn}^{S(M)} = \sum_{m'n'} \left[T_{mnm'n'}^{(11)} a_{m'n'}^{I(M)} + T_{mnm'n'}^{(12)} a_{m'n'}^{I(N)} \right] \quad (2.1.4)$$

$$a_{mn}^{S(N)} = \sum_{m'n'} \left[T_{mnm'n'}^{(21)} a_{m'n'}^{I(M)} + T_{mnm'n'}^{(22)} a_{m'n'}^{I(N)} \right] \quad (2.1.5)$$

This approach allows a great deal more theoretical flexibility than traditional Mie theory, but introduces many new parameters to be determined.

2.1.1 Expansion Definitions

There are three types of VSHWFs: outgoing waves (referred to here as $\vec{N}^{(1)}$ and $\vec{M}^{(1)}$, or simply as \vec{N} and \vec{M}), incoming waves (labeled as $\vec{N}^{(2)}$ and $\vec{M}^{(2)}$), and regularized waves (labeled as $Rg\vec{N}$ and $Rg\vec{M}$). The formulation of T-matrix theory employed here only uses the outgoing and regularized wave functions. The outgoing wave functions represent the scattered waves, while the regularized wave functions represent the incident field in region V_0 near the particle. These have been ‘regularized’ to have a finite value at the origin, while the other wave functions have not been regularized. There is a third vector spherical harmonic wave, \vec{L} , but generally it is not used to represent a mode in this theory as it does not satisfy the vector wave equation. These functions are constructed from several simpler basis functions, described below.

The spherical harmonic functions provide a complete basis set for describing arbitrary scalar functions on a sphere. These are defined in this context as [123]:

$$Y_n^m(\theta, \phi) = P_n^m(\cos\theta)e^{im\phi} \quad (2.1.6)$$

Where we have introduced the associated Legendre polynomial function, P_n^m . These can be viewed as a Fourier transform on a spherical surface. In order to expand a field, three such functions are required in order to describe all vector components. These are given by the vector spherical harmonic functions [123]:

$$\vec{V}_{mn}^{(1)}(\theta, \phi) = \vec{P}_{mn}(\theta, \phi) = \hat{r}Y_n^m(\theta, \phi) \quad (2.1.7)$$

$$\begin{aligned} \vec{V}_{mn}^{(2)}(\theta, \phi) &= \vec{B}_{mn}(\theta, \phi) = r\nabla[Y_n^m(\theta, \phi)] = \\ &\left(\hat{\theta}\frac{dP_n^m(\cos(\theta))}{d\theta} + \hat{\phi}\frac{im}{\sin(\theta)}P_n^m(\cos(\theta))\right)e^{im\phi} \end{aligned} \quad (2.1.8)$$

$$\begin{aligned} \vec{V}_{mn}^{(3)}(\theta, \phi) &= \vec{C}_{mn}(\theta, \phi) = \nabla \times [\vec{r}Y_n^m(\theta, \phi)] = \\ &\left(\hat{\theta}\frac{im}{\sin(\theta)}P_n^m(\cos(\theta)) - \hat{\phi}\frac{dP_n^m(\cos(\theta))}{d\theta}\right)e^{im\phi} \end{aligned} \quad (2.1.9)$$

The regularized VSHWF can now be defined [123]:

$$Rg\vec{L}_{mn}(kr, \theta, \phi) = \gamma'_{mn} \left\{ j'_n(kr)\vec{P}_{mn}(\theta, \phi) + \frac{j_n(kr)}{kr}\vec{B}_{mn}(\theta, \phi) \right\} \quad (2.1.10)$$

$$Rg\vec{M}_{mn}(kr, \theta, \phi) = \gamma_{mn}j_n(kr)\vec{C}_{mn}(\theta, \phi) \quad (2.1.11)$$

$$\begin{aligned} Rg\vec{N}_{mn}(kr, \theta, \phi) &= \gamma_{mn} \left\{ \frac{n(n+1)j_n(kr)}{kr}\vec{P}_{mn}(\theta, \phi) + \right. \\ &\quad \left. \frac{(krj_n(kr))'}{kr}\vec{B}_{mn}(\theta, \phi) \right\} \end{aligned} \quad (2.1.12)$$

Where j_n is the n^{th} spherical Bessel function of the first kind. To calculate the outgoing waves outside the scatterer (denoted by \vec{N} and \vec{M}), replace j_n with $h_n^{(1)}$, the spherical Hankel function of the first kind. Although not employed within the formulation used in this dissertation, substituting j_n with $h_n^{(2)}$ will produce the incoming waves outside the scatterer if needed. For this formulation of T-matrix theory,

only the outgoing waves are needed, and as a result the superscript in $h_n^{(1)}$ will be dropped from here on. Various normalizations are common in this theory, and it is important to note that the ones applied in these equations do not fully match those used in the software packages employed later in this work. These equations follow the normalizations used in Tsang *et al.* [123]:

$$\gamma'_{mn} = \sqrt{\frac{(2n+1)(n-m)!}{4\pi(n+m)!}} \quad (2.1.13)$$

$$\gamma_{mn} = \sqrt{\frac{(2n+1)(n-m)!}{4n\pi(n+1)(n+m)!}} \quad (2.1.14)$$

Upon integration, these functions obey the orthogonality relation:

$$\int_0^\pi d\theta \sin(\theta) \int_0^{2\pi} d\phi \vec{V}_{mn}^{(\alpha)}(\theta, \phi) \cdot \vec{V}_{-m'n'}^{(\beta)}(\theta, \phi) = \delta_{\alpha\beta} \delta_{mm'} \delta_{nn'} z_{\alpha mn} \quad (2.1.15)$$

Where the normalization constants are:

$$z_{1mn} = (-1)^m \frac{4\pi}{2n+1} \quad (2.1.16)$$

$$z_{2mn} = z_{3mn} = (-1)^m \frac{4\pi n(n+1)}{2n+1} \quad (2.1.17)$$

For the work in the following chapters, it is necessary to determine the scattering coefficients from the total scattered field. The r dependence given in the P function provides a method to calculate $a_{nm}^{S(N)}$ using orthogonality. The scattered field of order n, m in the radial direction is given by:

$$\vec{E}_{m,n,r}^S = \vec{N}_{r,nm} = \gamma_{mn} \frac{n(n+1)h_n(kr)}{kr} Y_n^m(\theta, \phi) \hat{r} \quad (2.1.18)$$

So that the radial component of the total scattered field is:

$$\begin{aligned}\vec{r} \cdot \vec{E}^S &= \sum_{m,n} \left[a_{mn}^{S(N)} r \hat{r} \cdot \vec{N}_{mn}(kr, \theta, \phi) \right] \\ &= \sum_{m,n} \left[a_{mn}^{S(N)} r \gamma_{mn} \frac{n(n+1)h_n(kr)}{kr} Y_n^m(\theta, \phi) \right]\end{aligned}\quad (2.1.19)$$

Upon multiplying by the conjugate spherical harmonic and then integrating across a spherical surface of radius r_0 :

$$\begin{aligned}\oint \vec{r}_0 \cdot \vec{E}^S Y_{n'}^{m'*} r_0^2 \sin\theta d\theta d\phi &= \\ \oint \sum_{m,n} \left[a_{mn}^{S(N)} \gamma_{mn} \frac{n(n+1)h_n(kr_0)}{kr_0} Y_n^m Y_{n'}^{m'*} \right] r_0^3 \sin\theta d\theta d\phi &= \end{aligned}\quad (2.1.20)$$

Where $Y_{n'}^{m'*} = Y_{n'}^{-m'}$ and the normalization constant is given by:

$$\oint Y_n^m Y_{n'}^{-m'} \sin\theta d\theta d\phi = (-1)^m \frac{4\pi}{2n+1} \delta_{mm'} \delta_{nn'} \quad (2.1.21)$$

Or:

$$\begin{aligned}\oint \vec{r}_0 \cdot \vec{E}^S Y_n^{m*} r_0^2 \sin\theta d\theta d\phi &= \\ a_{mn}^{S(N)} \left[\gamma_{mn} \frac{n(n+1)h_n(kr)}{k} (-1)^m \frac{4\pi}{2n+1} \right] r_0^2 &= \end{aligned}\quad (2.1.22)$$

Thus, we can determine the $a_{mn}^{S(N)}$ terms as:

$$a_{mn}^{S(N)} = \frac{\left[\oint (\vec{r} \cdot \vec{E}^S) Y_n^{-m} dA \right] k(2n+1)}{r_0^2 \gamma_{mn} h_n(kr) 4\pi (-1)^m n(n+1)} \quad (2.1.23)$$

One can also determine the magnetic modes in the same way, using H rather than E . Note that in this case, the coefficients are scaled by a complex constant which is media dependent.

2.1.2 General Cross Section Definitions in T-Matrix Theory

It is useful to relate the scattering coefficients obtained from the T-matrix to measurable far-field parameters. In this work, the scattering polarization can be either horizontal or vertical for the incident electric field (E_s) and scattered electric field (E_i) k vectors [123]. The scatterer can be characterized by a dyad, \mathbf{F} , which for a given input and output wave vector, relates the horizontally and vertically polarized components of the electric field, *i.e.* [123]:

$$\begin{bmatrix} E_s^v \\ E_s^h \end{bmatrix} = \begin{bmatrix} F^{(vv)} & F^{(vh)} \\ F^{(hv)} & F^{(hh)} \end{bmatrix} \times \begin{bmatrix} E_i^v \\ E_i^h \end{bmatrix}$$

Here we are concerned with electric fields perpendicular to the wave vector only. This is because the component of the electric field parallel with the wave vector does not transport energy away from the origin, and \mathbf{F} is defined in the far-field limit. This expression therefore provides a complete description of the far-field. The scattering Dyad can then be expressed as a function of the T-matrix [123]:

$$\begin{aligned}
\mathbf{F}(\theta, \phi; \theta', \phi') = & \frac{4\pi}{k} \sum_{n,m,n',m'} (-1)^{m'} i^{n'-n-1} \times \\
& \left\{ \left[T_{mnm'n'}^{(11)} \gamma_{mn} \vec{C}_{mn}(\theta, \phi) + T_{mnm'n'}^{(21)} i \gamma_{mn} \vec{B}_{mn}(\theta, \phi) \right] \right. \\
& \quad \cdot \gamma_{-m'n'} \vec{C}_{-m'n'}(\theta', \phi') \\
& + \left[T_{mnm'n'}^{(12)} \gamma_{mn} \vec{C}_{mn}(\theta, \phi) + T_{mnm'n'}^{(22)} i \gamma_{mn} \vec{B}_{mn}(\theta, \phi) \right] \\
& \quad \left. \cdot \gamma_{-m'n'} \frac{\vec{B}_{-m'n'}(\theta', \phi')}{i} \right\}
\end{aligned} \tag{2.1.24}$$

Where θ and ϕ are the direction of the scattered light, and θ' and ϕ' are the direction of the incident light. Here we will examine three useful scattering properties. First, the total scattering cross section for an incident wave with polarization $\hat{\beta}$ in direction θ_i and ϕ_i is defined as the total light scattered in all directions:

$$\begin{aligned}
\sigma_{s\beta}(\phi_i, \theta_i) = & \int_{4\pi} d\Omega \left[|\mathbf{F}(\theta, \phi; \theta_i, \phi_i) \cdot \hat{\beta}|^2 \right] \\
= & \int_{4\pi} d\Omega \left[|f_{hh}(\theta, \phi; \theta_i, \phi_i) \beta_h + f_{hv}(\theta, \phi; \theta_i, \phi_i) \beta_v|^2 \right. \\
& \quad \left. + |f_{vh}(\theta, \phi; \theta_i, \phi_i) \beta_h + f_{vv}(\theta, \phi; \theta_i, \phi_i) \beta_v|^2 \right]
\end{aligned} \tag{2.1.25}$$

By using the orthogonality of \vec{B}_{mn} and \vec{C}_{mn} , in addition to applying the orthogonality between different orders of \vec{B}_{mn} and \vec{C}_{mn} , terms can be dropped and reorganized [123]:

$$\sigma_{s\beta}(\theta_i, \phi_i) = \frac{16\pi^2}{k^2} \sum_{m,n} \quad (2.1.26)$$

$$\left\{ \left| \sum_{m'n'} i^{n'} (-1)^{m'} \gamma_{-m'n'} \left[T_{mnm'n'}^{(11)} \vec{C}_{-m'n'}(\theta_i, \phi_i) \cdot \hat{\beta} + T_{mnm'n'}^{(12)} \frac{\vec{B}_{-m'n'}(\theta_i, \phi_i)}{i} \cdot \hat{\beta} \right] \right|^2 + \left| \sum_{m'n'} i^{n'} (-1)^{m'} \gamma_{-m'n'} \left[T_{mnm'n'}^{(21)} \vec{C}_{-m'n'}(\theta_i, \phi_i) \cdot \hat{\beta} + T_{mnm'n'}^{(22)} \frac{\vec{B}_{-m'n'}(\theta_i, \phi_i)}{i} \cdot \hat{\beta} \right] \right|^2 \right\} \quad (2.1.27)$$

Second, the extinction cross section can be derived using the optical theorem. According to the optical theorem, light which has been forward scattered is related to the extinction cross section by the relation [123]:

$$\sigma_{e\beta} = \frac{4\pi}{k} \text{Im} [\hat{\beta} \cdot \mathbf{F}(\theta_i, \phi_i, \theta_i, \phi_i) \cdot \hat{\beta}] \quad (2.1.28)$$

Expanding this simple expression results in a complete extinction cross section for an arbitrary particle:

$$\sigma_{e\beta} = \frac{16\pi^2}{k^2} \text{Im} \left[\sum_{nmm'n'} (-1)^{m'} i^{n'-n-1} \gamma_{mn} \gamma_{-m'n'} \left\{ \begin{aligned} & [\hat{\beta} \cdot \vec{C}_{mn}(\theta_i, \phi_i)] T_{mnm'n'}^{(11)} [\vec{C}_{-m'n'}(\theta_i, \phi_i) \cdot \hat{\beta}] - \\ & i [\hat{\beta} \cdot \vec{C}_{mn}(\theta_i, \phi_i)] T_{mnm'n'}^{(12)} [\vec{B}_{-m'n'}(\theta_i, \phi_i) \cdot \hat{\beta}] + \\ & i [\hat{\beta} \cdot \vec{B}_{mn}(\theta_i, \phi_i)] T_{mnm'n'}^{(21)} [\vec{C}_{-m'n'}(\theta_i, \phi_i) \cdot \hat{\beta}] + \\ & [\hat{\beta} \cdot \vec{B}_{mn}(\theta_i, \phi_i)] T_{mnm'n'}^{(22)} [\vec{B}_{-m'n'}(\theta_i, \phi_i) \cdot \hat{\beta}] \end{aligned} \right\} \right] \quad (2.1.29)$$

Last, a frequently used metric is the differential backscattering cross section - the light scattered exactly by 180 degrees. This is particularly useful in experimental dark-field microscopy where light is reflected back from a particle. This is often used as a cross section by rescaling it by 4π [16]. For ease of calculation, we consider the case where the electric and magnetic modes do not mix (*i.e.*, the T-matrix is block diagonal with the top right, and bottom left quadrants zero). Backscattered light is described in terms of the scattering Dyad as:

$$\frac{\sigma_{bs,\beta}(\phi_i, \theta_i)}{d\Omega} = \left| \mathbf{F}(\pi - \theta_i, \pi + \phi_i, \theta_i, \phi_i) \cdot \hat{\beta} \right|^2 \quad (2.1.30)$$

This includes light of either polarization. This expression can be simplified by applying the symmetry relations for the vector spherical harmonics [123]:

$$\vec{C}_{mn}(\pi - \theta, \pi + \phi) = (-1)^n \vec{C}_{mn}(\theta, \phi) \quad (2.1.31)$$

$$\vec{B}_{mn}(\pi - \theta, \pi + \phi) = (-1)^{n+1} \vec{B}_{mn}(\theta, \phi) \quad (2.1.32)$$

Applying these relations results in:

$$\begin{aligned} \frac{\sigma_{bs,\beta}(\phi_i, \theta_i)}{d\Omega} = \frac{16\pi^2}{k^2} \left| \sum_{nmm'n'} (-1)^{m'+n} i^{n'-n-1} \gamma_{mn} \gamma_{-m'n'} \left\{ \right. \right. \\ \left. \left. \begin{aligned} &\vec{C}_{mn}(\theta_i, \phi_i) T_{mnm'n'}^{(11)} \left[\vec{C}_{-m'n'}(\theta_i, \phi_i) \cdot \hat{\beta} \right] \\ &- \vec{B}_{mn}(\theta_i, \phi_i) T_{mnm'n'}^{(22)} \left[\vec{B}_{-m'n'}(\theta_i, \phi_i) \cdot \hat{\beta} \right] \end{aligned} \right\} \right|^2 \quad (2.1.33) \end{aligned}$$

These results implicitly depend on the assumption that the particle has been illuminated with a plane wave, as expressed by the scattering dyad. For a plane wave

of amplitude E_0 and polarization $\hat{\beta}$, the expansion coefficients are [123]:

$$a_{mn}^{i(M)} = (-1)^m \frac{1}{\gamma_{m,n}} \frac{(2n+1)}{n(n+1)} i^n \left[E_0 \hat{\beta} \cdot \vec{C}_{-mn}(\theta_i, \phi_i) \right] \quad (2.1.34)$$

$$a_{mn}^{i(N)} = (-1)^m \frac{1}{\gamma_{m,n}} \frac{(2n+1)}{n(n+1)} i^n \left[E_0 \hat{\beta} \cdot (-i \vec{B}_{-mn}(\theta_i, \phi_i)) \right] \quad (2.1.35)$$

The T-matrix method can be applied more generally than just to plane waves, when given the knowledge of the expansion coefficients of the incident field. This is useful when there are many interacting scatterers, such as in a particle composed of many sub-particles. This idea is applied in the discrete dipole approximation (DDA) method discussed below, where each spherical scatterer not only scatters light from the incident field but also from the combined scattered fields of the other particles.

The T-matrix method simplifies to the Mie solution for spherically symmetric particles. For a spherical particle, the T-matrix is given by the negative of Eqs. 1.1.6 and 1.1.7 [123]:

$$T_n^N = -a_n = (-1) \frac{k_p^2 a^2 j_n(k_p a) [k a j_n(k a)]' - k^2 a^2 j_n(k a) [k_p a j_n(k_p a)]'}{k_p^2 a^2 j_n(k_p a) [k a h_n(k a)]' - k^2 a^2 h_n(k a) [k_p a j_n(k_p a)]'} \quad (2.1.36)$$

and

$$T_n^M = -b_n = (-1) \frac{j_n(k_p a) [k a j_n(k a)]' - j_n(k a) [k_p a j_n(k_p a)]'}{j_n(k_p a) [k a h_n(k a)]' - h_n(k a) [k_p a j_n(k_p a)]'} \quad (2.1.37)$$

Where T_n^N and T_n^M are the diagonal entries for the n th order electric and magnetic modes. Due to spherical symmetry, all m values are identical. Additionally, spherical symmetry also means that there can be no mixing between the modes, so all off-

diagonal positions in the T-matrix are zero.

2.1.3 Determining the T-Matrix

The T-matrix method allows a great deal more theoretical flexibility than traditional Mie theory, but introduces many new parameters. The amount of mixing which occurs between N_{max} modes is now given by $(N_{max})^2$ coefficients instead of the N_{max} coefficients used in Mie theory. Determining those coefficients is very challenging. While integral expressions for the coefficients in the T-matrix exist, they generally must be integrated numerically. In addition to the existing approaches to determining these coefficients discussed below, chapter 6 will introduce a versatile general purpose simulation method for this task.

The above equations do not provide a method to calculate the T-Matrix, but instead, how to utilize it if you have it. Mie theory provides equations to determine the scattering coefficients, but only for spherically symmetric particles. For general particles, it is possible to apply the Extended Boundary Condition Method (EBCM) [129] to determine the mixing of various components. In particular, Tsang *et al.* defines a set of J matrices as follows [123]:

$$\begin{bmatrix} J_{mnmnl}^{(11)} \\ J_{mnmnl}^{(12)} \\ J_{mnmnl}^{(21)} \\ J_{mnmnl}^{(22)} \end{bmatrix} = (-1)^m \int_s dS \hat{n}(\vec{r}) \cdot \begin{bmatrix} RgM_{mnl}(k_s r) \times M_{-mn}(kr) \\ RgM_{mnl}(k_s r) \times N_{-mn}(kr) \\ RgN_{mnl}(k_s r) \times M_{-mn}(kr) \\ RgN_{mnl}(k_s r) \times N_{-mn}(kr) \end{bmatrix}$$

And:

$$\begin{bmatrix} RgJ_{mnmtnl}^{(11)} \\ RgJ_{mnmtnl}^{(12)} \\ RgJ_{mnmtnl}^{(21)} \\ RgJ_{mnmtnl}^{(22)} \end{bmatrix} = (-1)^m \int_s dS \hat{n}(\vec{r}) \cdot \begin{bmatrix} RgM_{mtnl}(k_s r) \times RgM_{-mn}(kr) \\ RgM_{mtnl}(k_s r) \times RgN_{-mn}(kr) \\ RgN_{mtnl}(k_s r) \times RgM_{-mn}(kr) \\ RgN_{mtnl}(k_s r) \times RgN_{-mn}(kr) \end{bmatrix} \quad (2.1.38)$$

Where we have suppressed the θ and ϕ dependence to save space, k is the wavevector in the medium and k_s is the wavevector in the particle. These are then combined:

$$\begin{bmatrix} P_{mnmtnl} \\ R_{mnmtnl} \\ S_{mnmtnl} \\ U_{mnmtnl} \end{bmatrix} = -ikk_s \begin{bmatrix} J_{mnmtnl}^{(21)} \\ J_{mnmtnl}^{(11)} \\ J_{mnmtnl}^{(22)} \\ J_{mnmtnl}^{(12)} \end{bmatrix} - ik^2 \begin{bmatrix} J_{mnmtnl}^{(12)} \\ J_{mnmtnl}^{(22)} \\ J_{mnmtnl}^{(11)} \\ J_{mnmtnl}^{(21)} \end{bmatrix} \quad (2.1.39)$$

And likewise \mathbf{RgP} , \mathbf{RgR} , \mathbf{RgS} and \mathbf{RgU} only with \mathbf{RgJ} instead of \mathbf{J} . These then form two matrices:

$$\mathbf{Q} = \begin{bmatrix} \mathbf{P} & \mathbf{R} \\ \mathbf{S} & \mathbf{U} \end{bmatrix} \quad (2.1.40)$$

$$\mathbf{RgQ} = \begin{bmatrix} \mathbf{RgP} & \mathbf{RgR} \\ \mathbf{RgS} & \mathbf{RgU} \end{bmatrix} \quad (2.1.41)$$

The T-matrix is then determined by a simple linear algebra expression [123]:

$$\mathbf{T} = -\mathbf{RgQ}(\mathbf{Q}^{-1}) \quad (2.1.42)$$

This nominally means that one can evaluate the cross-product integrals above

to calculate multipole cross sections for any arbitrary shape defined by a surface separating one medium from another. However, these matrices can be ill-conditioned, meaning that numerical inversion may be unstable. Additionally, this method is only exact for an infinite number of terms in the expansion and there is an implicit approximation from the finite term length which affects all output terms.

It is instructive to examine the case of spherical symmetry. For this situation, $J_{mnm/nl}^{(22)}$ and $J_{mnm/nl}^{(11)}$ are zero, because at all positions on the surface the \vec{M} and $Rg\vec{M}$ functions will be parallel, and for \vec{N} and $Rg\vec{N}$ the non-orthogonal component is parallel with the surface and does not contribute to the integral. This restriction immediately removes the possibility of electric/magnetic mode mixing. Additionally, the ϕ dependence in the \vec{N} and \vec{M} functions immediately requires that $m = m'$ for a non-zero result, and the orthogonality of the associated Legendre polynomials enforces the requirement that $n = n'$ [123], resulting in the expected diagonal matrix.

A number of different approaches exist for this integration problem. The goal is to maintain high levels of accuracy while decreasing the processor time required. One area of concern is how to approach shapes with sharp edges or points. Kahnert *et al.* [55] implemented and compared two approaches from the literature for solving a cubic geometry. Geometries which can be described by a surface of distance $r(\theta, \phi)$ are referred to as star shaped. In this case, one can perform an expansion of this function in order to produce a series approximation of the shape. By only using continuous functions, this expansion results in an arbitrarily good approximation to the cubic geometry which does not suffer from a singularity in the curvature [55]:

$$r(\theta, \phi) \approx a_{00} + \sum_{n=1}^N \sum_{m=0}^n a_{n,m} d_{0,m}^n(\theta) \cos m\phi \quad (2.1.43)$$

Where $d_{l,m}^n(\theta)$ represents the Wigner d functions, and the approximation is trun-

cated after order N . The other approach explored in the work of Kahnert *et al.* [55] required the use of a Gauss-Legendre quadrature scheme where numerical integration points were selected along the boundary of the shape. With knowledge of the exact geometry of the surface (in this case a cube), an even distribution of points between faces with a higher density of points near corners was possible. This ultimately results in more accurate results.

Iskander *et al.* [50] demonstrated another interesting approach to this problem for high aspect ratio objects. In this method, called the Iterative Extended Boundary Condition Method (IEBCM), the scattering object is replaced with a PEC version of itself and the scattering problem is solved for this new object. Using the surface currents from the PEC model, the electric and magnetic fields inside the structure are solved for, where the structure has been divided up into overlapping regions. These solutions are combined to generate new estimates of the surface current density. This process is repeated until convergence. This approach has the advantage that it can handle high aspect ratio objects, but does so with substantial added complexity to the problem. Additionally, it depends on the PEC initial estimate being somewhat close to the true object, so the method breaks down if the object is not sufficiently conductive.

The point matching method (PMM) [90] is another approach to determining the T-matrix. It is similar to the EBCM in that it matches boundary conditions on a particle's surface. However, the expansion chosen is slightly different. In particular, the incident wave is decomposed into incoming wave functions using spherical Hankel functions of the second type. The boundary conditions are then given by [90]:

$$\hat{n} \times (\vec{E}_{inc}(r) + \vec{E}_{scat}(r)) = \hat{n} \times \vec{E}_{int}(r) \quad (2.1.44)$$

$$\hat{n} \times (\vec{H}_{inc}(r) + \vec{H}_{scat}(r)) = \hat{n} \times \vec{H}_{int}(r) \quad (2.1.45)$$

This produces $4N_{max}(N_{max} + 2)$ unknown values, corresponding to the expansion coefficients of the scattered and internal fields truncated after N_{max} entries. A grid of $2N_{max}(N_{max} + 2)$ points is then sampled, giving $8N_{max}(N_{max} + 2)$ total independent equations to be solved for [90].

The integration based methods described above have the disadvantage that they depend on surface integration. As a result, they cannot easily deal with particles with multiple layers, and are incapable of solving inhomogeneous or anisotropic particles. In these cases, volume methods of calculating scattering such as the discrete dipole approximation (DDA), finite-difference frequency-domain (FDFD) or finite-difference time-domain (FDTD) must be used. A hybrid FDFD/T-matrix method was developed by Loke *et al.* [68]. This approach results in an over determined linear algebra problem for each incident mode. By cycling through all incident modes of interest, the T-matrix can be filled in one row at a time. The FDTD approach, to the author's knowledge, has only ever been completed in the work in chapter 6, where it will be discussed in detail.

The last volume based approach discussed in this chapter uses the DDA to determine the T-matrix. Mackowski [73] demonstrated that there is a fairly straightforward connection between the DDA method and the T-matrix. In the DDA method, the scattering particle is decomposed into a large number of small pieces, each of which only supports a dipole mode. In this formulation, the boundary conditions require that [73]:

$$\frac{1}{\alpha} a_m^i - \sum_{j \neq i} \sum_{k=-1}^{N_d} H_{mk}^{ij} a_k^j \equiv \sum_{j=1}^{N_d} \sum_{k=-1}^{N_d} A_{mk}^{ij} a_k^j = p_m^i \quad (2.1.46)$$

Where the outgoing dipole spherical harmonics of order m of dipole i are denoted by a_m^i (as determined at the origin of each dipole), there are N_d total dipoles in the particle, p_m^i is the total VSHWF, and H_{mk}^{ij} is a matrix which used the VSHWF addition theorem to translate the expansion coefficients due to the dipole j at position j to the coefficients due to dipole j at position i . Once the outgoing VSHWF is known from each dipole, the VSHWF addition theorem can be used to sum all of the dipoles up, generating an overall response, including modes higher than dipole. By solving for a single value of p_m^i at a time, this method will generate a single row of the T-matrix on each application. Because of the large number of dipoles involved in this method, it can become difficult to numerically solve. It is possible to express this problem as a matrix inversion problem in much the same way the EBCM method above is a matrix inversion problem. This avoids generating the polarizations of each individual dipole but introduces numeric instability [73]. This method is referred to as the discrete dipole moment method (DDMM). The DDA approach can also be combined with the point matching approach above, including substantial simplifications to take advantage of particle symmetry [67].

The methods described in this chapter suffer from a number of difficulties. All the methods discussed are performed in the frequency domain, and as a result must be independently used at every frequency of interest. Depending on the method and structure, this can mean days (or more) of calculation to achieve sampling rates similar to those that the finite-difference time-domain (FDTD) produces for optical parameters. The surface integration methods in principle might be modified to handle multi-layer structures, however the complexity would be substantial. The volume based methods (either DDA-based or FDFD-based) are the most promising in this light. To resolve these difficulties, an FDTD method for calculating the T-matrix was

developed, and is presented in chapter 6.

Chapter 3

Numeric Methods

3.1 Finite-Difference Time-Domain Simulations

The application of the T-matrix method discussed in chapter 2 is generally limited due to the difficulty in numerically determining the T-matrix. Even when methods for determining the T-matrix do exist, they generally need to be applied separately at each frequency of interest. Additionally, it is difficult to solve the T-matrix for non-isotropic materials or complex multi-material shapes using this method. The T-matrix is often not necessary to understand a particle's behavior, and simpler time domain simulation methods such as the finite-difference time-domain (FDTD) method can be used to predict a particle's optical properties over a broadband window. In chapters 4 and 5 this method is used to study spiky nanoshells. To circumvent the above difficulties, in chapter 6 the author develops a method of determining the T-matrix using the FDTD method.

The Finite-difference time-domain method is a powerful approach to predict the interaction of light with complex nanoparticles. In this approach, described by Yee in 1966 [136], the magnetic and electric fields are discretized in both space and time,

and are then integrated forward in time. In a typical simulation, a plane wave will be injected into a simulation region where it will interact with the object of interest. At the boundaries, or at points of interest, the fields will be recorded as a function of time. In most cases, these values are Fourier transformed to produce solutions for a wide spectral window. This simultaneously determines many optical properties over a range of wavelengths, including both far-field cross sections and near-field enhancement of light.

FDTD Equations

Although the work in this dissertation is performed using a commercial FDTD engine (FDTD Solutions from Lumerical Solutions, Inc. [2]), it is worthwhile to examine the physical basis of the method. For simplicity, we will focus on free space. The FDTD method uses Ampere's law and Faraday's law to provide equations for the time evolution of the fields:

$$\nabla \times \vec{B} = \mu_0 \epsilon_0 \frac{\partial \vec{E}}{\partial t} + \mu_0 \vec{J}(t) \quad (3.1.1)$$

$$\nabla \times \vec{E} = -\frac{\partial \vec{B}}{\partial t} \quad (3.1.2)$$

As Yee described, these equations can be discretized to provide an update equation for a finite time difference [136]:

$$\nabla \times \vec{B} = \mu_0 \epsilon_0 \frac{\vec{E}(t + \Delta t) - \vec{E}(t)}{\Delta t} + \mu_0 \vec{J}(t) \quad (3.1.3)$$

$$\nabla \times \vec{E}(t) = -\frac{\vec{B}(t + \Delta t) - \vec{B}(t)}{\Delta t} \quad (3.1.4)$$

By rearranging these equations, we arrive at an integration formula for the electric and magnetic fields:

$$\vec{E}(t + \Delta t) = \vec{E}(t) + \frac{(\nabla \times \vec{B}(t) - \mu_0 \vec{J}(t)) \Delta t}{\mu_0 \epsilon_0} \quad (3.1.5)$$

$$\vec{B}(t + \Delta t) = \vec{B}(t) - (\nabla \times \vec{E}(t)) \Delta t \quad (3.1.6)$$

Given the knowledge of the electric and magnetic fields at any given time t , one can infer the electric and magnetic fields at any future time using the discrete forms of the curl operator. However, the above equations are numerically unstable. Yee improved this method using a so-called ‘leapfrog’ approach in two places. First, the electric and magnetic fields are not calculated at the same positions, but rather staggered half a grid step from each other, as shown in Figure 3.1. Second, the fields are not calculated simultaneously, but rather if electric fields are calculated at times $t, t + \Delta t, t + 2\Delta t, \text{ etc.}$, then the magnetic fields are calculated at times $t + 1/2\Delta t, t + 3/2\Delta t, t + 5/2\Delta t, \text{ etc.}$

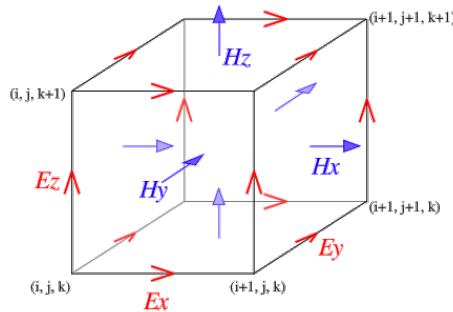


Figure 3.1: The electric and magnetic fields are staggered half a bin width apart. “Yee-cube”. Licensed under Creative Commons Attribution-Share Alike 3.0 via Wikimedia Commons - <http://commons.wikimedia.org/wiki/File:Yee-cube.svg#mediaviewer/File:Yee-cube.svg>

For uniform materials, this results in a simple stability criterion, given for a region with maximum speed of light c_{max} as [136]:

$$\sqrt{(\Delta x)^2 + (\Delta y)^2 + (\Delta z)^2} > c_{max} \Delta t \quad (3.1.7)$$

Generally the Δt used in a simulation is a few percent smaller than the maximum stable Δt value.

3.2 Lumerical Solutions

The work described in chapters 4 through 7 was performed using Lumerical Inc.’s FDTD Solutions [2] (version 8.6 and 8.7), a commercial FDTD engine. In this section, the details of these simulations will be discussed. A simple simulation layout for a gold sphere illuminated with a plane-wave is shown in Figure 3.2.

In this simulation there are a number of simulation objects that control the behavior of the simulation or the information recorded for later analysis. Figure 3.3 shows a list of the objects used in this simulation. This list includes objects which specify the structure (the ‘sphere’), control the grid spacing (‘mesh’), control the source (‘field’), and record the power, index, and electric field (‘ind_mon’, ‘monitor’, ‘scatter’, and ‘absorb’).

The three other important variables in constructing a simulation are the boundary conditions of the simulation, the parameters of the source injected into the simulation and the material properties used. In all the work discussed here, the boundary conditions were set as Perfectly Matched Layers (PML). In a PML boundary condition, a series of impedance matched layers are added to the boundary of the simulation with material parameters tuned to minimize reflection and maximize absorption [49].

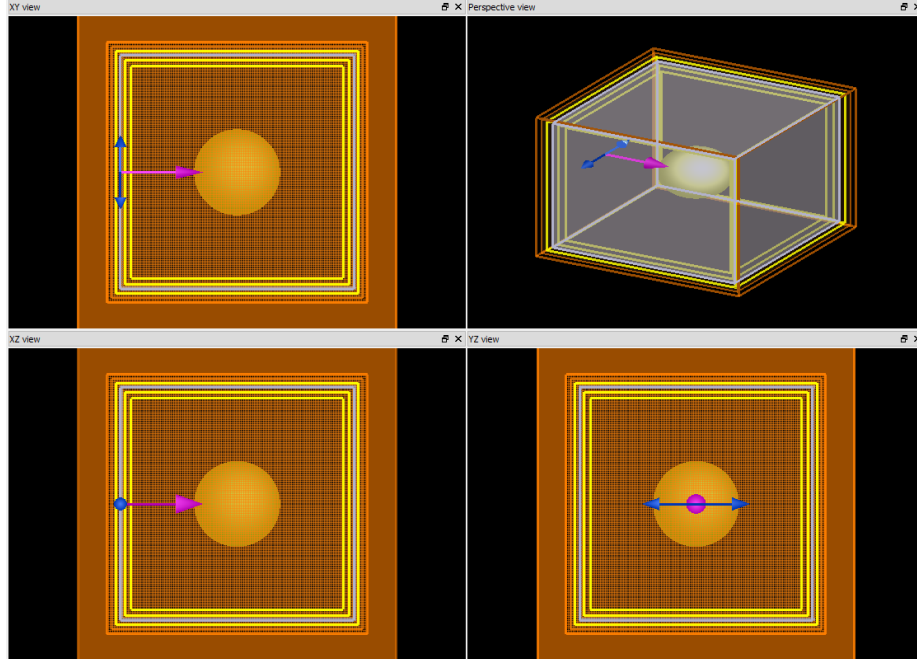


Figure 3.2: A simulation layout for a simple gold sphere exposed to a plane wave along x with polarization along y .

In Lumerical Solutions, the boundary conditions are controlled by the FDTD object. The PML boundary conditions in the above simulation were set to contain 16 layers with a maximum reflection of $1e-4$, but these can be tuned higher depending on the needs of the simulation.

Light is injected into the simulation by a total-field scattered-field (TFSF) source. The TFSF source specifies a volume entirely enclosing the particle into which a plane wave will be injected. The software will then subtract the incident wave at the edges of that volume. Outside the source region, the only fields present are scattered from inside the volume, and therefore, were not subtracted from the original wave. Using this object, the phase, polarization, and injection direction can be controlled. This allows illumination from any direction (although angular dispersion effects will occur if the injection \vec{k} vector is not one of \hat{x} , \hat{y} or \hat{z}). It should be noted that the phase is

	model	Model
	FDTD	FDTD
	mesh	Mesh
	Field	TFSFSource
	scatter	AnalysisGroup
	absorb	AnalysisGroup
	sphere	Sphere
	ind_mon	IndexMonitor
	monitor	DFTMonitor

Figure 3.3: A collection of the objects created to run the simulation shown in Figure 3.2.

generally defined based on the location of the injection plane rather than the origin of the simulation. Figure 3.4 shows the main options for the TFSF source.

Since the FDTD method is in the time domain, the source must be specified as a function of time. In practice, a plane wave is injected as a wave packet, as shown by the signal vs. time graph in 3.4. This means that the source has a finite width in time which specifies a minimum total simulation time. The width of this packet is determined by the width of the spectrum vs. frequency graph (left-middle panel Figure 3.4), while the central frequency will approximately correspond to the frequency of the injected pulse. In practice this is important for two reasons. First, results from Lumerical have the option to be normalized to the spectral amplitude of the incident pulse (this is described in great detail in their online documentation [2]). In general, the work performed here always employs continuous wave normalization. In this case, the output of the simulation is Fourier transformed, and the frequency domain data is normalized according to the spectral amplitude distribution of the source. This produces optical properties which would result from a unit monochromatic exposure. However, this may not always be the correct normalization for the task at hand, so caution should be employed. For example, in cross section calculations, it is sometimes preferable to normalize to the spectral power rather than the spectral

amplitude. Second, the simulation is the most sensitive (has highest signal to digital noise) at the peak of the source frequency distribution. It is therefore important to insert a source with a wide enough distribution to encompass the range of interest, but not so wide that the injected time domain pulse becomes too short to simulate accurately.

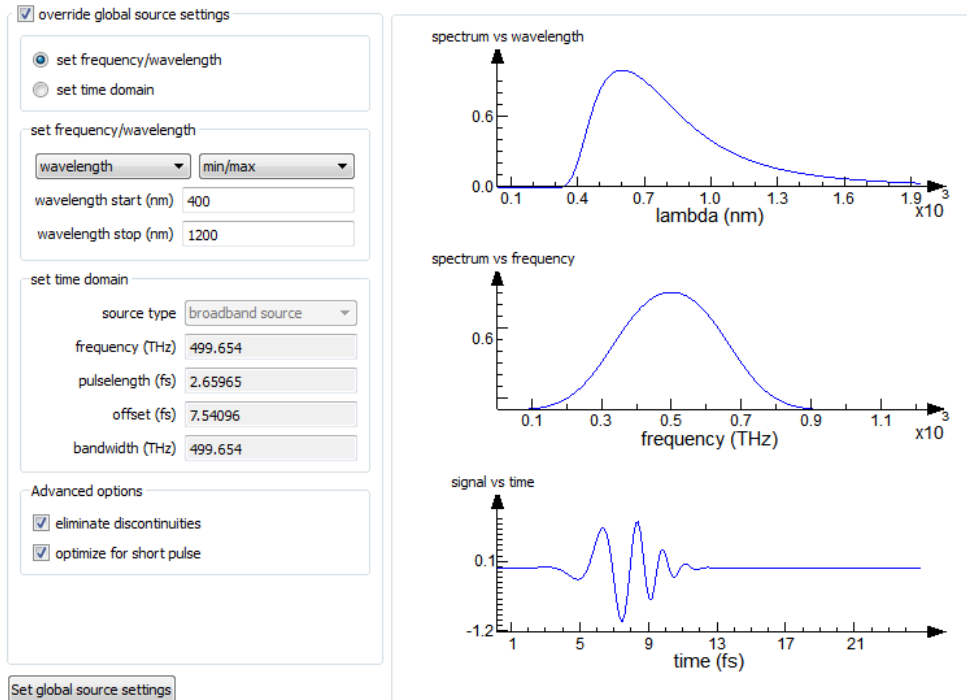


Figure 3.4: The source parameter control document specifying the behaviour of the TFSS source, as described in the text.

Material properties are specified using measurements of the real and imaginary parts of the index of refraction as a function of frequency. In addition to the library of material properties which come with the software (as with CRC data [41] employed in Figure 3.5), it is also possible to import data from another source, such as ellipsometry measurements (as with the polystyrene material used in chapters 4-6). Because the data in Figure 3.5 is in the frequency domain and the simulations are performed

the time domain, it is necessary to transform the data to the time domain. The constitutive equation is given by a convolution integral [49]:

$$\vec{D}(r, t) = \epsilon_0 \epsilon_\infty \vec{E}(r, t) + \epsilon_0 \int_0^t \vec{E}(r, (t - \tau)) \chi_e(r, \tau) d\tau \quad (3.2.1)$$

Where the electric susceptibility, $\chi_e(r, \tau)$ is given by the inverse Laplace transform of $\chi_e(r, \omega)$, and ϵ_∞ is the relative permittivity at very high frequency. This convolution means that in theory, $\vec{D}(r, t)$ depends on the value of $\vec{E}(r, t)$ at all previous times, which is a serious problem as the simulation would have prohibitively high memory costs. In practice there are several methods of solving this problem. For example, one can introduce an additional field to the update equation [49] that stores the information needed to generate these values at each iteration based only on the values in the previous iteration.

A second issue is that the data points in frequency space are not continuous, and in some regions may be quite sparse. It is therefore necessary to generate a parametrized curve for performing these calculations. In FDTD Solutions, the specific methods being employed to solve these two issues are proprietary. However, the user is given a certain level of control over the accuracy of the parametrization, and the opportunity to verify that it is sufficiently accurate, as shown in Figure 3.5. It is important to note that an FDTD simulation will never be more accurate than the data used to generate these material parameters, or than the accuracy of the fit used to interpolate the material parameters.

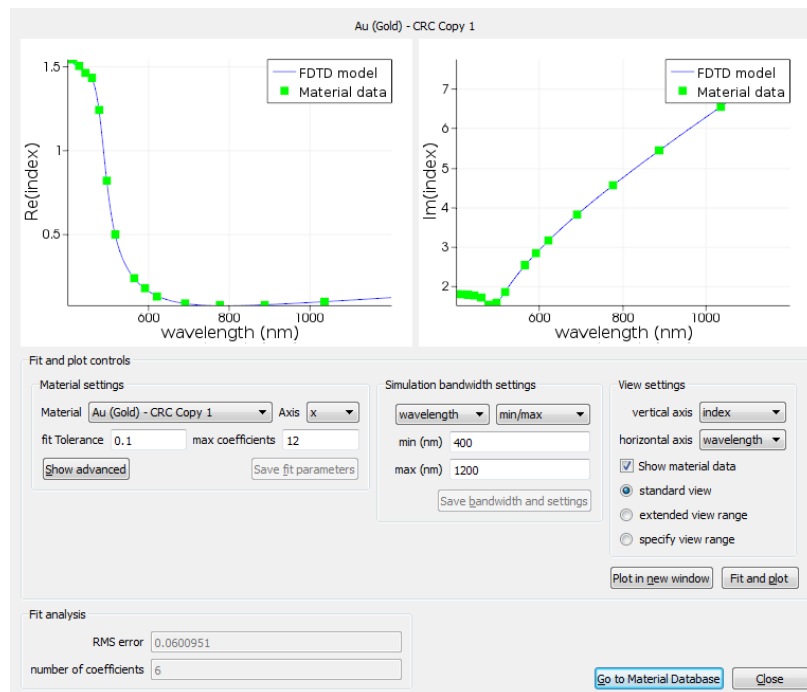


Figure 3.5: The material explorer dialogue for material parameters in FDTD Solutions, as described in the text.

3.3 Constructing the Nanostructure for FDTD Models

In order to produce realistic models for the complicated shapes of the particles used in this dissertation, two molecular dynamics simulation methods were employed. The structural data was then imported into FDTD Solutions for numerical modeling of the electric field.

3.3.1 A Force Method for Spike Distributions

Spiky nanoshells were modeled as a set of cones placed on the surface of a polystyrene core. Each cone was modeled as an ‘rd_tip_cone’ object in FDTD Solutions. This simulation object has three free parameters (as shown in Figure 3.6): Tip radius, cone-angle, and spike length. A fourth non-free parameter is the cladding-radius, which can be derived from the other three. In practice, the exact definitions of these parameters in FDTD Solutions are a bit unclear due to a bug in the default cone generation code. Despite this bug, the code works well in this application and the deviation from the length shown in Figure 3.6 are substantially less than the tip radius. An important practical point when using this simulation object is that cladding radius should be set much larger than is necessary, in order to avoid the shape being truncated to a cylinder.

In order to construct a realistic model of the spiky nanoshell, it is necessary to place as many as two hundred spikes on the surface of the core. It is important to place the spikes using an efficient and unbiased method. More specifically, the mathematical problem here is to generate a series of coordinates for spikes on the surface of a sphere of unit radius such that each spike is, on average, an equal distance

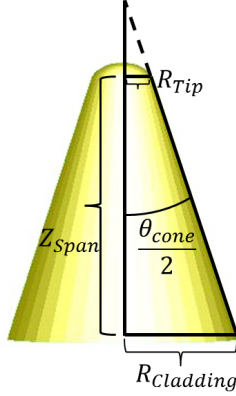


Figure 3.6: Parameters in the gold cone model.

from each of its nearest neighbors. For arbitrarily large numbers of particles, an exact solution with equal distances does not exist. In practice this problem needs to only be solved approximately [15]. In this work, a force algorithm was used to produce a miniature simulation which generates a set of coordinates that are in a locally optimized configuration. Each point (which later becomes the center of the base of a spike) is modeled as a unit point charge confined on the surface of the sphere. The force on the i^{th} charge of N total charges is given by:

$$\vec{F}_i = \sum_{j \neq i}^N \frac{-\hat{r}_{i,j}}{|\vec{r}_{i,j}|^2} \quad (3.3.1)$$

Where $\vec{r}_{i,j}$ is the vector connecting point charge i to point charge j . This approach is physically justified, as the positively charged seeds are strongly attracted to the negatively charged core by the electrostatic force, and repelled from each other due to charge similarity. The algorithm pseudocode is:

While not converged:

Calculate force vectors

Normalize and apply force vectors

Project positions back onto sphere

The code used here was borrowed from Reference [3]. The result of this algorithm is shown in Figure 3.7A. Figure 3.7B and 3.7C show spiky nanoparticles with equal or randomized parameter values. For the randomized structure, each spike's length, cone angle, and tip radius are chosen from a uniform distribution. The equal parameter models were predominately used in chapter 4, while the randomized structures were used to study disorder in spiky nanoshells, which plays an important role in the studies presented in chapters 5 and 6.

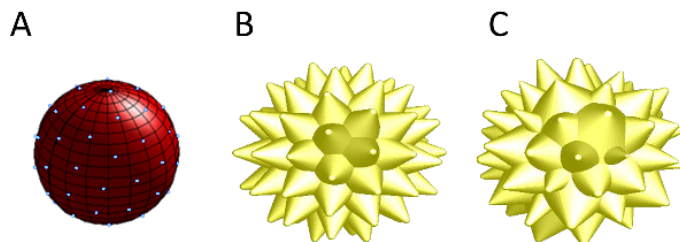


Figure 3.7: A. A converged point simulation where each point represents the base of a spike. B. 60 cones with equal parameters: Z_{span} 57 nm, θ_{cone} 47 degrees, and R_{tip} 4 nm. C. 60 cones with uniformly distributed parameters: Z_{span} between 50 nm and 65 nm, θ_{cone} from 30 to 75 degrees, and R_{tip} 2 nm to 6 nm.

3.3.2 Molecular Dynamics Simulations for Raspberry-Like Metamolecule Particles (Raspberry-MMs)

A second class of nanoparticles, the Raspberry-like metamolecule (Raspberry-MM), was simulated as part of future work discussed in chapter 7. Similar to the spiky

nanoshells, the raspberry-MMs produced by a surfactant-assisted seed growth method on a polystyrene core. While the spiky nanoshells discussed above are well modeled by a single layer of spikes, raspberry-MMs can have many layers of tightly packed spherical gold beads. In order to generate realistic models for these nanoshells, it is necessary to both model several layers of stacked nanoparticles and to tightly pack these beads in a distance of a few nanometers. This is accomplished using a molecular dynamics simulation, which, similar to the model above described for spiky nanoshells, depends on generating forces between the beads. However, the beads are no longer confined to the surface of a sphere representing the core. Additionally, the simulation must take the finite size of each bead into account by maintaining a minimum distance between the bead centers. This is done by generating three forces that act on each bead, as shown in Figure 3.8:

- An asymmetric harmonic force between the surface of the core and each bead (\mathbf{F}_{core})
- A one-sided (repulsive) harmonic force between each pair of beads, where the force is only active when the beads are touching (\mathbf{F}_{bead})
- A damping force applied to each bead, proportional to, but oriented in the opposite direction of the velocity of the beads (\mathbf{F}_{damp})

The asymmetric nature of the forces is critical to ensuring the correct behavior of the simulation. The force acting on the i th bead due to the core takes the form:

$$F_{i,core} = -k_c \hat{r} (|\vec{r}_c - \vec{r}_i| - (R_{core} + R_{bead})) \quad (3.3.2)$$

Where R_{core} and R_{bead} are the radii of the core and bead, respectively, and k_c is the force constant. In practice, \vec{r}_c is always at the origin, so the force is central as

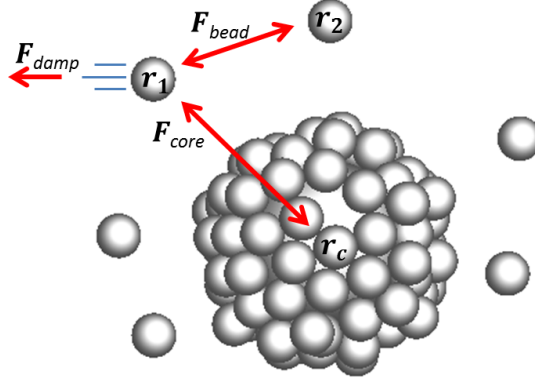


Figure 3.8: Illustration of the molecular dynamics scheme used to generate raspberry-MM positions. The three forces, as explained in the text, are responsible for damping the motion of the beads, repelling beads which are already in contact, and weakly attracting beads to the core surface but strongly repelling them once inside the core.

shown above. If the number of layers is too high, the beads are forced into the core by the force from the beads of the outer layers. This is mitigated by the force used to attract the beads to the core being much weaker than the same force when applied to repel them. This asymmetric potential will force the beads to equilibrate outside the core rather than inside it. This is controlled by setting k_c to be much larger when $(|\vec{r}_c - \vec{r}_i| - (R_{core} + R_{bead}))$ is negative.

Likewise, a very stiff repulsion force must be present between the beads, but only when they are in contact. The form of the force is essentially identical as the above. The force acting on the i th bead due to the j th bead takes the form:

$$F_{i,j \text{ bead}} = -k_b \widehat{r}_{j,i} (|\vec{r}_j - \vec{r}_i| - 2R_{bead}) \quad (3.3.3)$$

Where $\widehat{r}_{j,i}$ is the unit vector from the j th to the i th bead. In this case, there should be no attraction between the beads when they are not touching, so k_b is set

to zero when $(|\vec{r}_j - \vec{r}_i| - 2R_{bead})$ is positive. For completeness, the force on the i th bead due to the damping force is simply:

$$F_{i,damp} = -\gamma\vec{v}_i \quad (3.3.4)$$

Where γ is the positive damping constant and \vec{v}_i is the velocity of the i th bead. An example of a resulting model is shown in Figure 3.9.

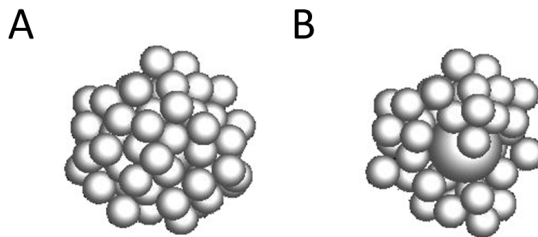


Figure 3.9: A. Raspberry-MM with 75 gold beads of 12 nm radius. B. The same perspective but with the core exposed.

3.4 Specific Data Analysis Topics

In this section, specific data analysis tasks performed in later chapters will be explained in detail.

3.4.1 Calculating the Near-Field Enhancement

In chapter 5, spiky nanoshells are analyzed with FDTD to determine the origin of their unusually high SERS efficiency. This section will discuss how that calculation was performed. The main approach is to identify a thin shell surrounding the particle and perform the averaging only inside that shell. The specific steps required were:

1. Load position, index, and electric field for each pixel in the simulation into Matlab™.
2. Adjust the positions so the center of the particle coincides with the zero coordinate.
3. Increase the index of refraction of the core to ensure only the exterior surface is included in the analysis.
4. Calculate an isosurface based on the absolute value of the index with a threshold of 1.4. This will generate a surface which divides the simulation volume into regions filled with gold and regions filled with air. Step 3 above insures that the core is treated as part of the particle rather than as air in this calculation.
5. Compose a Delaunay triangulation [1] for the set of points defining the surface. This divides the simulation space into volumes based on proximity to the surface points, and is required to perform an efficient nearest-neighbor search of the simulation volume.
6. For each point in the field, find the closest surface point using the triangulation.
7. Classify each point as interior or exterior by comparing the radial surface position of the closest surface point and the radial field position (see Figure 3.10).
8. Calculate the distance from each exterior point to the surface and keep any between 0 and 2.1 nm (the thickness of the shell).
9. Perform the desired analysis at each point locally and then average. *e.g.*, multiply the field intensity at two different wavelengths and then average over the shell to calculate the SERS enhancement.

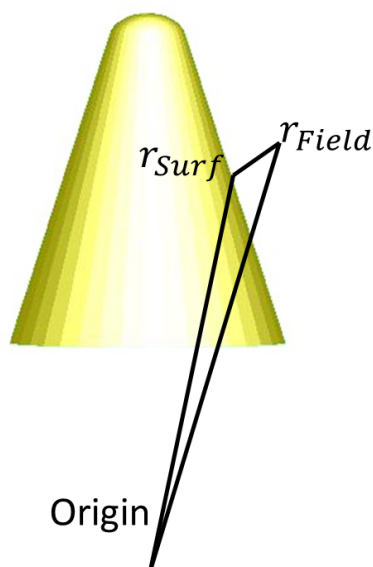


Figure 3.10: The distance from origin of the surface point r_{surf} , and the field point, r_{field} , are compared to determine whether the field position in question is inside or outside the gold surface. If $r_{surf} < r_{field}$, the point is classified as exterior.

In step 6 it was assumed that any point outside the particle would have a radial position greater than the nearest point on the surface. This assumption works well for many structures such as cubes or spheres. In the highly structured spiky nanoshell, with high levels of discretization and small angles, this algorithm may identify fewer sample points. In particular, as shown in Figure 3.11, on a few spikes there are small poorly sampled patches. However, the most important areas, the spike tips, usually have a large number of sample points, and the overall effect on the calculation is negligible. It is possible to tune the algorithm to avoid this by integrating a larger shell, but the resulting field spectra will remain the same, and it will likely introduce patches which are over sampled rather than under sampled.

A simple approach that was not used here but may be applied in the future is to use a neighbor based approach, where the simulation space is divided into areas

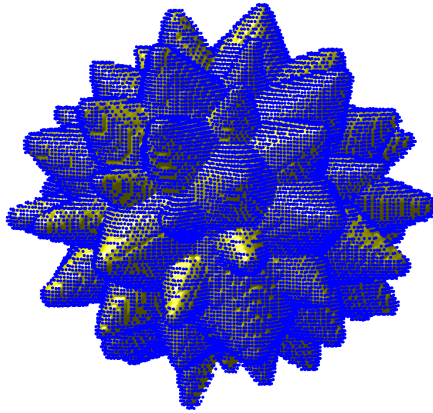


Figure 3.11: Field points included within the shell sample are indicated with blue dots on top of the nanostructure. Although there are patches of under sampled points, they only occur on the sides of spikes and make up a small portion of the total surface area.

labeled as gold or dielectric. A shell could then be constructed by examining each dielectric position, and identifying if any of its 26 neighboring sites are gold, and if so, include that entry in the shell. The thickness of the shell is less well defined in this method, and the result may introduce additional bias due to discretization at certain angles, but it will include all neighboring points.

3.4.2 Determining the T-Matrix of a Particle

Another important data analysis task is determining the T-matrix of a given particle. Once the T-matrix has been determined, the cross sections can be calculated as described in chapter 2. Two different approaches to this task were taken in the course of the work described in this dissertation. The simpler method will be discussed here, while a more general method will be discussed in chapter 6. In general, the T-matrix maps the incident vector spherical harmonic wave functions (VSHWFs) to the scattered VSHWFs:

$$\vec{a}^S = \mathbf{T}\vec{a}^I \quad (3.4.1)$$

In order to determine the T-matrix from a simulation, we must know the incident and scattered VSHWF coefficients for that simulation. Given the polarization and direction of the incident plane wave, Eq. 2.1.34 (repeated here) equips us with the values of a^I for that simulation:

$$a_{mn}^{I(M)} = (-1)^m \frac{1}{\gamma_{m,n}} \frac{(2n+1)}{n(n+1)} i^n \left[E_0 \hat{\beta} \cdot \vec{C}_{-mn}(\theta_i, \phi_i) \right] \quad (3.4.2)$$

$$a_{mn}^{I(N)} = (-1)^m \frac{1}{\gamma_{m,n}} \frac{(2n+1)}{n(n+1)} i^n \left[E_0 \hat{\beta} \cdot (-i\vec{B}_{-mn}(\theta_i, \phi_i)) \right] \quad (3.4.3)$$

Determining the \vec{a}^S terms is more difficult. By employing a total-field scattered-field (TFSF) source, independent access to the purely scattered field is possible. As shown in Figure 3.12, the simulation is constructed so that a mathematical spherical surface could be placed between the boundary of the TFSF source and the edge of the simulation. A field monitor is then constructed which fully encompasses this (mathematical) sphere. The field monitor must therefore have a width which is at

least $\sqrt{3}W$, where W is the width of the source.

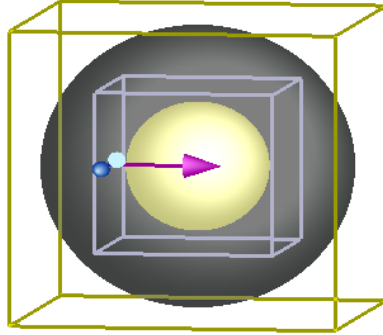


Figure 3.12: To generate the VSHWF expansion coefficients for the scattered field, a mathematical sphere is sampled from the data points (shown here in gray - note that no literal structure is created in the simulation). It is important that this surface be entirely outside the TFSF source, or it will include some of the incident light as well by mistake. A field monitor which fully encompasses the sampling sphere is added. Unlike in the surface sampling above, this sphere can have relatively low spatial resolution.

It is then possible to numerically integrate Eq. 2.1.23 (repeated here) over the sphere in Figure 3.12 to capture the information in a^S using the radial component of the electric and magnetic fields:

$$a_{mn}^{S(N)} = \frac{\left[\oint (\vec{r} \cdot \vec{E}^S) Y_n^{-m} dA \right] k(2n+1)}{r_0^2 \gamma_{mn} h_n(kr) 4\pi (-1)^m n(n+1)} \quad (3.4.4)$$

While two vectors are not sufficient to solve matrix equation 3.4.1 in general, it is possible to solve the T-matrix under some specific assumptions. In particular, there is no clear preferred direction in Raspberry-MMs. As a result, the nanoshells should act isotropically in space, and the T-matrix should be mostly diagonal. Making this assumption, it is straight forward to calculate the T-matrix:

$$T_{n,m} = \frac{a_{n,m}^S}{a_{n,m}^I} \quad (3.4.5)$$

The approximate T-matrix derived in this fashion is only usable with the original illumination direction and polarization because for typical illuminations a^I will contain several zero values, and so those entries in the T-matrix will be set to *NaN* ('not a number'), and as a result were set to 0. This decomposition is useful to determine the cross sections of different scattering modes in a single simulation, as used in chapters 5 and 7. A more general method of determining the T-matrix is discussed in chapter 6.

Chapter 4

Modeling the Scattering

Properties of Spiky Nanoshells

4.1 Introduction

The far-field scattering properties of spiky nanoshells are controlled by the surface topography. A major advantage of spiky nanoshells over regular gold nanoshells is the ease with which it is possible to tune the extinction peak from the mid-visible to the near-infrared. In the studies in this chapter, published in Reference [107], a range of spiky nanoshells are synthesized by modifications to the synthesis method. The resulting particles were modeled in FDTD Solutions as a set of spikes surrounding a polystyrene core. By tuning the parameters of the spikes, the extinction spectrum of different types of spiky nanoshells were reproduced. It was also shown that the models require a complete core-shell structure with a continuous conducting outer shell in order to correctly predict the experimental data. This establishes that FDTD simulations are capable of explaining and guiding the design of these nanoshells.

4.2 Context

The text and figures in this section of the dissertation are taken with permission from Reference [107]. The author's contribution was in constructing the models and simulations. This work was done in collaboration with a number of other researchers. In particular, the UV-vis measurements and particle synthesis were performed by Brenda L. Sanchez-Gaytan and Zhaoxia Qian, supervised by So-Jung Park, while the FDTD simulations were performed by the author with the assistance of Michael L. Reca and supervised by Zahra Fakhraai.

4.3 Controlling the Topography and Surface Plasmon Resonance of Gold Nanoshells by a Templated Surfactant-Assisted Seed Growth Method

Reprinted with permission from Brenda L. Sanchez-Gaytan, Zhaoxia Qian, Simon P. Hastings, Michael L. Reca, Zahra Fakhraai, and So-Jung Park. Controlling the Topography and Surface Plasmon Resonance of Gold Nanoshells by a Templated Surfactant-Assisted Seed Growth Method. *The Journal of Physical Chemistry C*, 117(17):8916-8923, May 2013. Copyright 2013 American Chemical Society.

4.3.1 Abstract

Gold nanoshells with varying surface topographies and tunable SPR bands were synthesized in high yields by the templated surfactant-assisted seed growth method. By

changing the types and amounts of surfactants and ionic additives in the growth solution, the nanoshell topography was controlled from smooth shells to highly structured nanoshells composed of spherical nanoparticles or sharp spikes of varying aspect ratios. The SPR band of the nanoshells could be tuned over a wide range of wavelengths by varying the nanoshell topography, without significantly changing the amount of gold. Finite-difference time-domain (FDTD) modeling was used to predict and understand the optical properties of nanoshells composed of various subparticles, providing insight into the origins of the tunable SPR band.

4.3.2 Introduction

Controlled synthesis of metal nanoparticles is an important area of study because of the unique size and shape dependent properties of such nanoparticles [22, 109, 81, 32]. For example, gold and silver nanoparticles show distinct surface plasmon resonance (SPR) bands varying with the size and shape of the nanoparticles. Among many different types of metal nanoparticles, nanoshells are of great interest for their tunable SPR in the near-IR region and their hollow architecture, which have led to a number of applications ranging from spectroscopy to cancer diagnosis and therapy [64, 14, 95].

In addition to size and shape, surface topography provides another way to significantly influence the properties of polycrystalline metal nanostructures. For macroscopic metal thin films, surface defects are known to affect the excitation of surface plasmon waves [63]. Wang *et al.* showed that the introduction of surface roughness on gold nanoshells can cause interesting changes in their scattering properties [126, 124]. Similar spectral changes have been found for solid gold nanoparticles as well [103]. To understand and harness the properties resulting from topology control, it is necessary to develop a synthetic method to generate a series of metal

nanoshells with controllable and well-defined surface topographies beyond the simple introduction of surface roughness and texturing.

Recently, we reported that gold nanoshells covered with spikes, called spiky nanoshells [106, 108], can be synthesized by merging templated nanoshell synthesis [44] and the surfactant assisted seed growth method [52]. In this approach, polymer beads decorated with small silver seed particles were used as templates to grow gold nanoshells packed with sharp spikeshaped particles. Owing to the highly structured surface, spiky nanoshells showed strong far-field and near-field scattering compared to smooth shells [108]. Herein, we show that the templated surfactant-assisted seed growth method can be used to synthesize gold nanoshells with varying surface topographies by changing the type of surfactants and ions in the growth solution. The SPR position of the nanoshells could be controlled over a wide wavelength range by varying the surface topography. Finite-difference time-domain (FDTD) modeling was used to elucidate the origin of the tunable SPR band of various nanoshells. Given the versatility of the surfactant assisted seed growth method demonstrated for homogeneous syntheses with isolated seed particles [109], we believe that our approach provides a powerful platform that allows for the synthesis of a range of different types of hollow particles with interesting optical properties.

4.3.3 Experimental Methods

Materials and Instrumentation.

Cetyltrimethylammonium bromide (CTAB), cetyltrimethylammonium chloride (CTAC), chloroauric acid (HAuCl_4), sodium borohydride (NaBH_4), silver nitrate (AgNO_3), and ascorbic acid were purchased from Sigma-Aldrich. Sodium bromide, sodium iodide, and ammonium hydroxide were purchased from Fisher Scientific.

Carboxylate-modified FluoSpheres (diameter = 100 nm, 2% solids) were purchased from Invitrogen. The average diameter of the PS beads was determined to be 94.5 ± 7.2 nm by transmission electron microscopy (TEM). TEM images were recorded with a Tecnai G212 TWIN instrument operating at 120 kV accelerating voltage. Scanning electron microscopy (SEM) images were recorded with a Quanta 600 FEG Mark II instrument at 20 kV accelerating voltage. Extinction spectra were measured with an Agilent 8453 UV-visible spectrophotometer. The gold concentration was determined using inductively coupled plasma-atomic emission spectroscopy (ICP-AES) (Spectro Genesis).

Preparation of Seed-Decorated Polymer Beads.

Carboxylate-modified FluoSpheres (diameter = 100 nm, 2% solids, 100 μ L) with a charge density of 0.3207 mequiv/g were mixed with an aqueous solution of $\text{Ag}(\text{NH}_3)_2^+$ (0.01 M, 100 μ L), which was prepared by mixing AgNO_3 (2 mL, 1 M) and NH_4OH (14.8 N, one droplet). After 30 min, 1 mL of purified water (18.0 M Ω) was added to the solution, and the mixture was centrifuged at 18000 rpm for 30 min. Supernatant was discarded, and the same washing procedure was repeated one more time. The supernatant was then replaced with 500 μ L of water. To form silver seed particles on the polymer beads, an aqueous solution of freshly prepared NaBH_4 (0.01 M, 100 μ L) was added to the solution with vigorous mixing. To allow for the decomposition of unreacted NaBH_4 , the seed solution was aged overnight before use. Finally, the seed-decorated PS beads were purified by centrifuging the solution at 18000 rpm for 30 min and replacing the supernatant with 5 mL of water.

Synthesis of Spiky CTAB Nanoshells.

The growth solution was prepared by mixing the following solutions: CTAB (0.1 M, 10 mL), H_{Au}Cl₄ (0.01 M, 421 μ L), AgNO₃ (0.01 M, 64 μ L), and ascorbic acid (0.1 M, 67 μ L) in that order. Throughout this article, the concentrations of surfactants are reported as the concentrations of the surfactant stock solutions added to the growth solution, unless otherwise specified. For the synthesis of spiky shells, 10-40 μ L of the seed-decorated bead solution described in the preceding section was added to the growth solution (10 mL), and the resulting solution was mixed gently for a few seconds. Red color started developing in approximately 5 min after mixing, and the reaction was completed in 1-2 h.

Synthesis of Smooth CTAC Nanoshells.

The growth solution was prepared by mixing aqueous solutions of CTAC (0.1 M, 10 mL), H_{Au}Cl₄ (0.01 M, 421 μ L), AgNO₃ (0.01 M, 64 μ L), and ascorbic acid (0.1 M, 67 μ L). For nanoshell synthesis, the seed-decorated bead solution (10-80 μ L) described earlier was added to the growth solution (10 mL), and the resulting solution was mixed gently for a few seconds. Red color started developing after approximately 1-2 min, and the reaction was completed in less than 1 h.

Synthesis of Superspiky CTAC/Br Nanoshells.

The growth solution was prepared by adding varying amounts of NaBr (1 M, from 100 μ L to 1 mL) to the CTAC-based growth solution. A CTAC solution and a NaBr solution were mixed first before the addition of other reagents. All other reaction conditions were the same as those used for regular spiky nanoshells. The optimal NaBr concentration for producing superspiky nanoshells was found to be 50 mM.

4.3.4 Results and Discussion

In typical syntheses of nanoshells, numerous small silver seed particles (2-5 nm in diameter) were first synthesized on negatively charged carboxylate-modified polystyrene (PS) beads (94.5 ± 7.2 nm in diameter). Subsequently, the seed-decorated polymer particles were added to a growth solution containing HAuCl_4 , ascorbic acid, AgNO_3 , and cationic surfactants. Because the standard reduction potentials [versus the standard hydrogen electrode (SHE)] of $\text{Ag}^+(\text{aq})/\text{Ag}(\text{s})$ and $\text{AuBr}_2^-(\text{aq})/\text{Au}(\text{s})$ are 0.962 and 1.11 V, respectively [96, 12], gold precursors should be reduced on polymer beads through both galvanic replacement [114] and catalytic reduction, forming gold nanoshells. We previously reported that growth solution containing cetyltrimethylammonium bromide (CTAB) as the surfactant generates gold nanoshells that are densely covered with sharp spikes called spiky nanoshells (Figure 4.1A,C) [106]. To understand the role of the surfactant in controlling the surface topography, we replaced CTAB in the growth solution with cetyltrimethylammonium chloride (CTAC). In the CTAC growth solution, continuous gold nanoshells with a relatively smooth surface were synthesized (Figure 4.1B,D), in contrast to the spiky shells formed in CTAB growth solution (Figure 4.1A,C). This structure is hereafter referred to as smooth CTAC nanoshells to emphasize the smoother surface texture of the nanoshells synthesized in the CTAC growth solution compared to spiky CTAB shells. In homogeneous nanoparticle synthesis with isolated gold seed particles, the CTAB growth solution produces rod-shaped particles, whereas the CTAC growth solution generates quasispherical particles [33, 25], as also confirmed in our control experiment (Figure 4.2). The preferential binding of bromide ions to selective facets of gold particles has been found to promote the growth of anisotropic particles in the presence of CTAB [128, 29]. In essence, a similar behavior was observed in the heterogeneous syntheses

reported here; when CTAB was replaced by CTAC, quasispherical particles continued to grow from seed particles until neighboring particles on a polymer bead fused together to form a relatively smooth gold nanoshell (Figure 4.1B,E). The smooth CTAC nanoshells showed an SPR band at 710 nm, which is blue-shifted from that of typical spiky shells (Figure 4.1E) and close to that expected for perfectly smooth shells (*vide infra*).

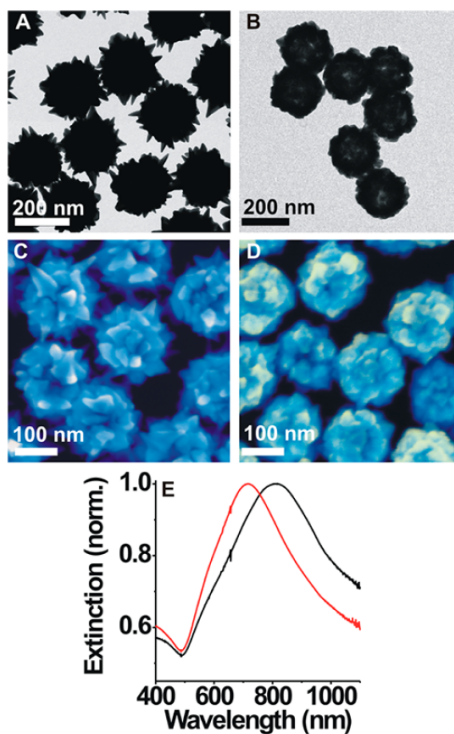


Figure 4.1: (A,B) TEM images of nanoshells synthesized in (A) CTAB and (B) CTAC. (C,D) SEM images of nanoshells synthesized in (C) CTAB and (D) CTAC. (E) Extinction spectra of nanoshells synthesized in CTAB (black) and CTAC (red). Reprinted with permission from Brenda L. Sanchez-Gaytan, Zhaoxia Qian, Simon P. Hastings, Michael L. Reza, Zahra Fakhraai, and So-Jung Park. Controlling the Topography and Surface Plasmon Resonance of Gold Nanoshells by a Templated Surfactant-Assisted Seed Growth Method. *The Journal of Physical Chemistry C*, 117(17):8916-8923, May 2013. Copyright 2013 American Chemical Society.

Although the surface topography of the nanoshells studied here is consistent with the findings in homogeneous syntheses with isolated seed particles as described previously, the nanoparticle growth on a polymer template was somewhat different from that in homogeneous syntheses. Because the templated syntheses reported here utilized silver seed particles instead of commonly used gold seed particles, another set of control experiments of homogeneous syntheses was performed with silver seed particles (Figure 4.2). When silver particles were used as the seeds, slightly elongated

gold particles were observed in CTAB growth solution, whereas spherical gold particles were formed in CTAC growth solution. These results are generally consistent with those obtained using gold seed particles, which generated nanorods with CTAB and nanospheres with CTAC. However, the aspect ratio of gold particles grown from silver seed particles in CTAB growth solution is significantly smaller than that obtained with gold seed particles. On the other hand, in templated syntheses, gold spikes of high aspect ratios were formed even from silver seed particles, presumably because of the slow and directional diffusion of gold precursors to the PS beads.

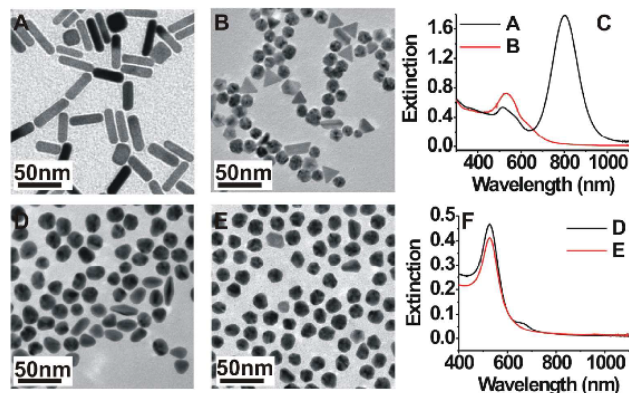


Figure 4.2: TEM and extinction spectra of gold nanostructures synthesized using gold (A, B, C) or silver (D, E, F) seed particles without polymer templates. Gold seed particles (2~5 nm) were synthesized by mixing 0.250 mL of 0.01M HAuCl_4 solution with 7.5 mL of 0.10 M CTAB solution followed by a quick injection of 0.600 mL of 0.01M ice-cold NaBH_4 solution while vigorously stirring. The solution was kept at 25° C for a couple of hours before using. Silver seed particles were prepared by mixing 0.250 mL of 0.01 M AgNO_3 solution with 7.5 mL of 0.10 M CTAB (D) or CTAC (E) solution followed by quick injection of 0.01 M ice-cold NaBH_4 during vigorous stirring. Because Ag seed particles tend to aggregate in solution over time, it was used one hour after the preparation. The growth solution was prepared by adding 0.200 mL of 0.01 M HAuCl_4 , 0.030 mL of 0.01 M AgNO_3 and 0.032 mL of 0.10 M L-ascorbic acid solutions into 4.75 mL 0.01 M surfactant solution (CTAB for samples in A and D, CTAC for samples in B and E). For all samples, 10 μL seed solution was added to the growth solution with vigorous stirring. After two hours, the final product was collected by centrifugation (12,000 rpm, 30 min). Reprinted with permission from Brenda L. Sanchez-Gaytan, Zhaoxia Qian, Simon P. Hastings, Michael L. Reza, Zahra Fakhraai, and So-Jung Park. Controlling the Topography and Surface Plasmon Resonance of Gold Nanoshells by a Templated Surfactant-Assisted Seed Growth Method. *The Journal of Physical Chemistry C*, 117(17):8916-8923, May 2013. Copyright 2013 American Chemical Society.

Finite-difference time-domain (FDTD) simulations were used to model gold nanoshells with varying surface topographies. Relatively smooth CTAC shells were modeled with gold nanospheres distributed at equally spaced random positions on the surface of a PS bead, whereas spiky CTAB shells were modeled by replacing the gold spheres with gold cones. The positions of the gold nanoparticles were chosen using a force algorithm [15, 3]. In a typical force algorithm, equally distanced points on the surface of a sphere were obtained by randomly placing a fixed number of charged particles on the sphere, with the assumption that the charged particles repel each other with a force described by a r^{-2} potential. The number of charges was chosen to match the experimental number of spikes or spheres. Once the forces on each charged particle are balanced by the repulsion of other charged particles, they do not move any further. Lumerical FDTD software was used to place gold spheres or cones of varying sizes and shapes on the predefined equilibrium positions of nanoparticles to calculate their absorption and scattering spectra. The details of the FDTD model, including materials properties and boundary conditions, were described in an earlier publication [108]. All reported values of length scales are accurate within the mesh size of ± 2 nm.

Figure 4.3 presents models for smooth CTAC nanoshells produced by placing 26-nm gold spheres on a PS bead with a diameter of 95 nm. The diameter of the gold spheres was chosen to match the experimentally determined thickness of CTAC shells (26.6 ± 4.7 nm) shown in Figure 4.1D. The FDTD simulation was carried out with varying number of particles on the polymer bead from 100 to 180 particles (Figure 4.3A). This approach of overlapping spheres to form nanoshells provides a way to systematically vary the roughness of the nanoshells. As the number of spheres decreased and the surface roughness increased (Figure 4.3A), the extinction spectrum

red shifted and became sharper and more intense (Figure 4.3B). This result is consistent with the previous report by Wang *et al.*, which predicted that the introduction of surface roughness on nanoshells causes a red shift of the SPR bands and dampening of higher-mode plasmon resonances, as well as increases in scattering intensity [126].

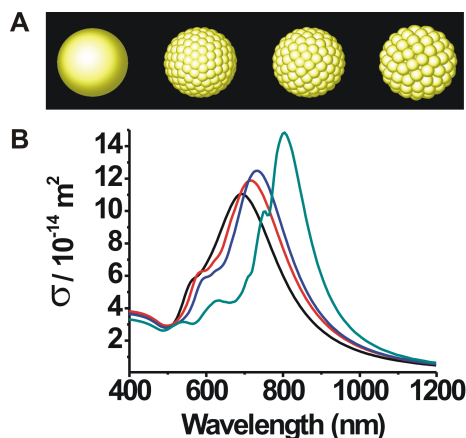


Figure 4.3: (A) Models of gold nanoshells arranged in order of increasing surface roughness. (B) Calculated extinction spectra of a smooth nanoshell (black) and three different gold nanoshells generated by placing varying numbers of 26-nm gold spheres on a PS bead (red, 180 spheres; blue, 140 spheres; dark cyan, 100 spheres) shown in panel A. A PS core with a diameter of 95 nm was used for all models. The thickness of the perfectly smooth nanoshell was set to 23 nm to match the amount of gold in the CTAC shell model constructed with 180 gold spheres. Reprinted with permission from Brenda L. Sanchez-Gaytan, Zhaoxia Qian, Simon P. Hastings, Michael L. Reza, Zahra Fakhraai, and So-Jung Park. Controlling the Topography and Surface Plasmon Resonance of Gold Nanoshells by a Templated Surfactant-Assisted Seed Growth Method. *The Journal of Physical Chemistry C*, 117(17):8916-8923, May 2013. Copyright 2013 American Chemical Society.

The peak position of the extinction spectrum of CTAC shells was reproduced when 180 nanoparticles were placed on the PS bead (Figure 4.3A, red). In this case, the gold spheres significantly overlap each other to form continuous nanoshell structures (Figure 4.3A, second model). For comparison, the extinction spectrum of a perfectly smooth nanoshell on the same size PS bead (Figure 4.3A, first model) was also calculated and is plotted in Figure 4.3B (black). The same amount of gold was

used to model the CTAC shell (Figure 4.3A, second model) and the perfectly smooth shell (Figure 4.3A, first model). The comparison of the two spectra reveals that CTAC shells show an SPR band that is slightly more intense and red-shifted than that of perfectly smooth gold nanoshells, demonstrating that the surfactant-assisted synthesis reported here offers a high yield synthetic method to prepare roughened nanoshells with scattering properties resembling those of widely studied smooth gold nanoshells. Although gold nanoshells with roughened surfaces were previously synthesized by chemically etching the surface of presynthesized nanoshells [126], the postsynthesis chemical etching approach is not ideal as a synthetic method because chemical etching can destabilize the nanoparticles and it is difficult to control the surface topography beyond surface roughening using such a method.

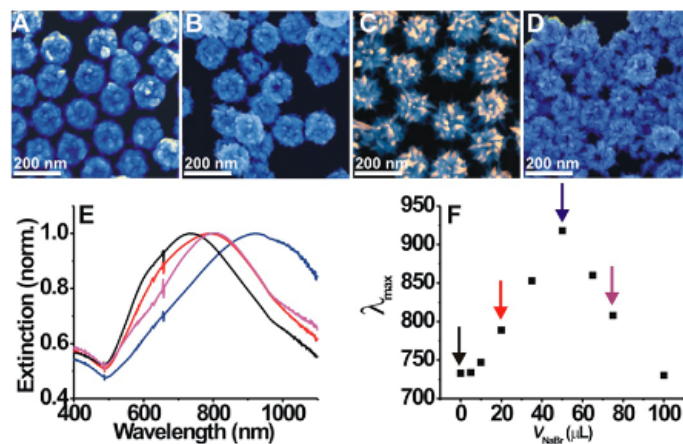


Figure 4.4: (A-D) SEM images of nanoshells grown in CTAC/Br growth solutions with varying amounts of NaBr: (A) 0, (B) 20, (C) 50, and (D) 75 mM. (E) Extinction spectra of samples shown in panels A, black; B, red; C, blue; and D, magenta. (F) Plot of maximum extinction positions as a function of the volume of 1 M NaBr solution added to 1 mL of CTAC-based growth solution. Reprinted with permission from Brenda L. Sanchez-Gaytan, Zhaoxia Qian, Simon P. Hastings, Michael L. Reza, Zahra Fakhraai, and So-Jung Park. Controlling the Topography and Surface Plasmon Resonance of Gold Nanoshells by a Templated Surfactant-Assisted Seed Growth Method. *The Journal of Physical Chemistry C*, 117(17):8916-8923, May 2013. Copyright 2013 American Chemical Society.

To examine the role of halides in the metal reduction and nanoshell growth, sodium bromide was added to the CTAC growth solution for nanoshell synthesis (Figure 4.4). As expected, the growth solution containing CTAC and NaBr (CTAC/Br growth solution) resulted in gold nanoshells covered with spikes, confirming that the halide ions play an important role in regulating the shell morphology [80]. Figure 4.4 shows SEM images of gold nanoshells formed at a series of different concentrations of NaBr in CTAC/Br growth solution. The morphology of the nanoshells changes sensitively with the concentration of bromide ions, and the sharpness and density of the spikes on the nanoshells become higher with increasing NaBr concentration, reaching the maximum aspect ratio at about 50 mM concentration (Figure 4.4C). A further increase of bromide concentration led to nanoshells with shorter rods with patches of voids on the PS bead surface (Figure 4.4D). This observation can be explained by the concentration-dependent facet selectivity of bromide ion binding. When the concentration of bromide ions exceeds a certain value, the ions can adsorb on more stable surfaces as well as less stable facets. Therefore, nanoshells synthesized at excessively high bromide concentrations present smaller-aspect-ratio spikes on the surface. A similar phenomenon was previously observed in the synthesis of copper nanoparticles [28], where the aspect ratio of copper particles was controlled by the concentration of chloride ions. Note that the combination of CTAC and NaBr offers a means to adjust the concentrations of the two different additives (cationic surfactants and halide ions) separately to fine-tune the structure. Therefore, gold nanoshells composed of much sharper and denser spikes can be formed using an appropriate CTAC/Br growth solution, as depicted in Figure 4.5. The sharp spiky nanoshells synthesized in CTAC/Br growth solution (Figure 4.4C, Figure 4.6B) are hereafter referred to as superspiky shells.

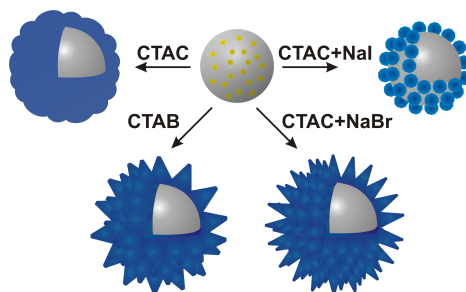


Figure 4.5: Pictorial Representation of the Effects of Surfactants and Halide Ions on the Morphology of Gold Nanoshells. Reprinted with permission from Brenda L. Sanchez-Gaytan, Zhaoxia Qian, Simon P. Hastings, Michael L. Reza, Zahra Fakhraai, and So-Jung Park. Controlling the Topography and Surface Plasmon Resonance of Gold Nanoshells by a Templated Surfactant-Assisted Seed Growth Method. *The Journal of Physical Chemistry C*, 117(17):8916-8923, May 2013. Copyright 2013 American Chemical Society.

The SPR band position of the gold nanoshells was found to vary with the surface topography (Figure 4.4E,F). With increasing NaBr concentration, the SPR band exhibited gradual red shifts from 710 to 930 nm (Figure 4.4E). Under the conditions used in the set of experiments (Figure 4.4F), the nanoshells with the highest-aspect-ratio spikes were obtained at a CTAC and NaBr concentration ratio ($[CTAC]/[Br^-]$) of 2. A further increase in NaBr concentration caused blue shifts in the extinction spectrum, reflecting the blunt shape of the spikes synthesized under these conditions (Figure 4.4F). Eventually, at NaBr concentrations over 75 mM, the SPR position of nanoshells became similar to that of CTAC shells. Therefore, the NaBr concentration needs to be adjusted to obtain nanoshells with desired morphologies and optical properties. When additional NaBr was added to the CTAB-based growth solutions, similar blue-shifts were observed with a loss of spike sharpness.

To further elucidate the effect of halides on nanoshell growth, we used a growth solution containing CTAC and sodium iodide for nanoshell synthesis. The concentration of NaI was kept below 4 mM to avoid the precipitation of surfactants. Figure

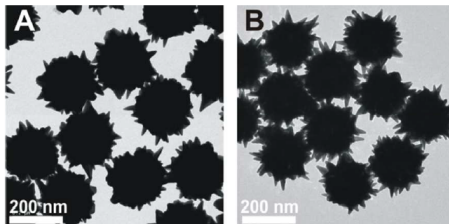


Figure 4.6: TEM images of nanoshells synthesized in CTAB-based growth solution (A) and CTA C/Br-growth solution with 50 mM NaBr (B). For both syntheses, $20\mu\text{L}$ of seed was used for 10 mL of corresponding growth solution. Reprinted with permission from Brenda L. Sanchez-Gaytan, Zhaoxia Qian, Simon P. Hastings, Michael L. Reza, Zahra Fakhraai, and So-Jung Park. Controlling the Topography and Surface Plasmon Resonance of Gold Nanoshells by a Templated Surfactant-Assisted Seed Growth Method. *The Journal of Physical Chemistry C*, 117(17):8916-8923, May 2013. Copyright 2013 American Chemical Society.

4.7 presents a typical TEM image and extinction spectrum of nanoshells synthesized in a growth solution containing CTAC and NaI (CTAC/I growth solution). Unlike the continuous nanoshells synthesized in a CTAC growth solution or spiky nanoshells formed in CTAB growth solution, the CTAC/I growth solution generated discrete quasispherical nanoparticles on PS beads, resulting in incomplete shells (Figure 4.7A). We attribute this behavior to the strong binding of iodide ions to the gold surface [25, 74, 116]. In nanorod synthesis, the presence of iodide impurities in CTAB is reported to result in the formation of spherical particles instead of nanorods [116]. In the templated synthesis studied here, the strong iodide-gold interaction leads to discrete quasispherical particles on the PS beads instead of anisotropic spikes formed with the addition of NaBr. In addition, the densely packed surfactant layer on growing gold particles slows the gold reduction and protects the particles from fusing together and forming a continuous shell. The effects of various additives in the growth solution are summarized in Figure 4.5. The particles synthesized in CTAC/I growth solution showed a complex extinction spectrum with multiple peaks originating from coupling

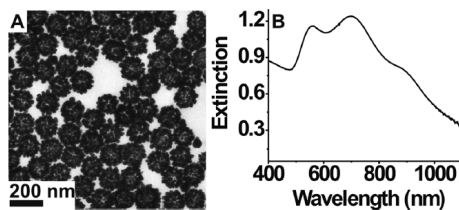


Figure 4.7: (A) TEM image and (B) UV-vis spectrum of nanoshells synthesized using a growth solution containing 0.10 M CTAC and 2 mM NaI. For the synthesis, 10 mL of growth solution and 20 μ L of seed solution were used. Reprinted with permission from Brenda L. Sanchez-Gaytan, Zhaoxia Qian, Simon P. Hastings, Michael L. Reza, Zahra Fakhraai, and So-Jung Park. Controlling the Topography and Surface Plasmon Resonance of Gold Nanoshells by a Templated Surfactant-Assisted Seed Growth Method. *The Journal of Physical Chemistry C*, 117(17):8916-8923, May 2013. Copyright 2013 American Chemical Society.

between many discrete particles decorating the PS beads (Figure 4.7B) instead of a broad shell dipole SPR shown in continuous CTAC shells. This result demonstrates that a continuous shell is necessary to obtain a controllable SPR band in the near-IR range.

The SPR position of superspiky nanoshells could be further controlled by changing the amount of growth solution relative to the amount of seed-decorated polymer beads. Figure 4.8 presents SEM images and extinction spectra of nanoshells synthesized at varying ratios of the growth solution and seed solution, which show that a larger amount of growth solution results in longer spikes decorating the beads. This morphology change caused red shifts of the SPR band from 785 to >1100 nm. Nanoshells synthesized using CTAB growth solution showed similar red shifts with the relative amount of growth solution [108]. However, when CTAB was used as the surfactant, the SPR band maximized at around 900 nm, and a further increase in the amount of CTAB growth solution relative to the amount of seed-decorated beads resulted in the formation of nanostar side products. On the other hand, the SPR of

nanoshells synthesized in CTAC/Br growth solution could be tuned farther into the near-IR region without the appearance of nanostars. Therefore, the growth solution of CTAC and NaBr mixture provides much better control over the morphology and optical properties of spiky nanoshells.

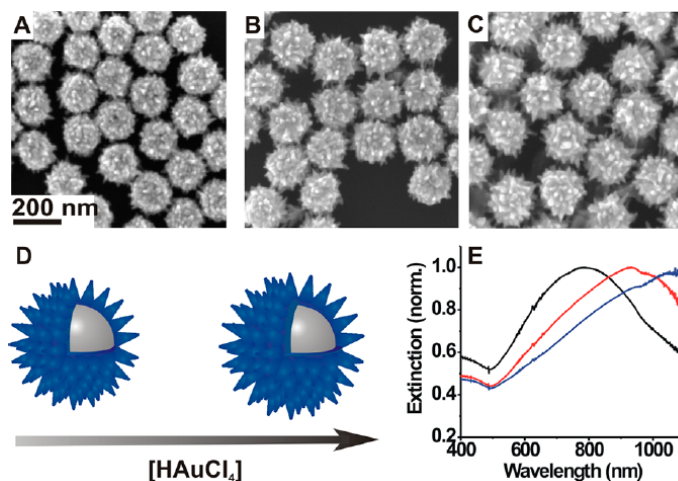


Figure 4.8: (A-C) SEM images of nanoshells synthesized in the presence of CTAC and NaBr (50 mM) at varying seed-to-growth solution ratios. For the syntheses, 10 mL of growth solution was mixed with (A) 45, (b) 25, and (C) 15 μL of seed solutions. (D) Scheme showing how the morphology changes with the relative amount of growth solution. (E) Extinction spectra of nanoshells shown in panels A, black; B, red; and C, blue. Average tip-to-tip diameters of the nanoshells shown in panels A-C were measured to be (A) 171 ± 11 , (B) 197 ± 14 , and (C) 212 ± 12 nm. Reprinted with permission from Brenda L. Sanchez-Gaytan, Zhaoxia Qian, Simon P. Hastings, Michael L. Reza, Zahra Fakhraai, and So-Jung Park. Controlling the Topography and Surface Plasmon Resonance of Gold Nanoshells by a Templated Surfactant-Assisted Seed Growth Method. *The Journal of Physical Chemistry C*, 117(17):8916-8923, May 2013. Copyright 2013 American Chemical Society.

To elucidate the origin of the broad SPR band of spiky nanoshells in the near-IR region, extinction spectra of a series of simplified models were calculated by FDTD modeling (Figures 4.9, Figures 4.10, and 4.11). Figure 4.9 presents a set of structures evolving from a smooth nanoshell (Figure 4.9A) and two isolated spikes (Figure 4.9B) on a PS bead to a complete spiky shell on a PS bead. In this set of modeling, a spiky

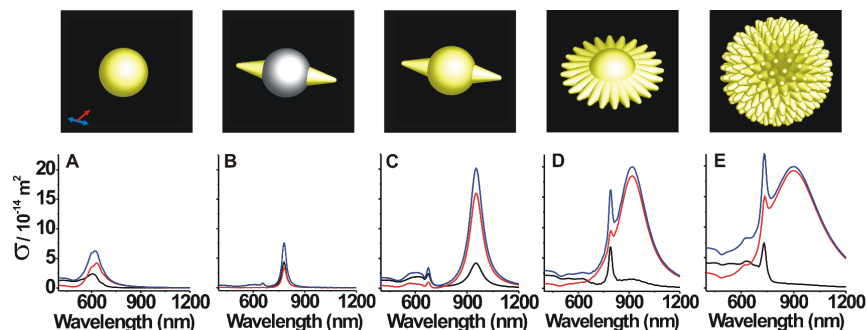


Figure 4.9: Absorption (black), scattering (red), and extinction (blue) spectra of various nanostructures. In all cases, the direction of polarization is along the blue arrow, and the propagation direction is along the red arrow. All spectra are plotted on the same scale. (A) Smooth gold nanoshell with a thickness of 20 nm on a PS core with the diameter of 56 nm. (B) Two gold cones with a base diameter of 38 nm, a height of 52 nm, and a tip diameter of 10 nm on a PS bead with a diameter of 95 nm. The polarization of light was along the long axis of the cone. (C) Gold nanoshell decorated with two gold cones. (D) Gold nanoshell decorated with 16 gold cones. All cones are arranged in the plane formed by the propagation and polarization vectors. (E) Gold nanoshell decorated with 240 randomly oriented gold cones. The shell and cone dimensions used in panels C-E are identical to those used in panels A and B. The SPR peak positions were (A) 624, (B) 780, (C) 952, (D) 920, and (E) 900 nm. Reprinted with permission from Brenda L. Sanchez-Gaytan, Zhaoxia Qian, Simon P. Hastings, Michael L. Reza, Zahra Fakhraai, and So-Jung Park. Controlling the Topography and Surface Plasmon Resonance of Gold Nanoshells by a Templated Surfactant-Assisted Seed Growth Method. *The Journal of Physical Chemistry C*, 117(17):8916-8923, May 2013. Copyright 2013 American Chemical Society.

nanoshell is viewed as a combination of a smooth shell and spikes. The scattering spectra calculated for the polarization direction along the long axis of the spikes (Figure 4.9A,B) reveal that neither a smooth nanoshell nor isolated spikes alone can describe the broad near-IR band observed for spiky nanoshells. When two spikes are located on the surface of a PS bead, the spikes do not significantly interact because of the large size of the PS bead, and the SPR peak position of the structure is the same as that of one spike. When a thin gold shell is added to the structure, the two spikes are connected and generate a dipole mode that oscillates along the long axis

of the nanoparticle, as shown in Figure 4.9C. This dipole resonance is red-shifted compared to the SPR of isolated spikes (Figure 4.9B) and smooth nanoshells (Figure 4.9A). Again, we note that a simple nanoshell structure cannot produce such a red-shifted near-IR band and the addition of elongated particles is necessary to shift the oscillation to lower frequencies. This mode of resonance is attributed to the primary SPR mode observed in spiky nanoshells. Adding more spikes to the same structure either in one plane (Figure 4.9D) or in random orientations (Figure 4.9E) did not significantly shift the plasmon resonance frequency. Instead, the addition of more spikes contributed to the broadening of the peak. Note that the scattering intensity of two spikes connected by a shell in the middle (Figure 4.9C) is significantly larger than the simple addition of the scattering intensities of the two components [*i.e.*, a shell (Figure 4.9A) and two isolated spikes (Figure 4.9B)]. Compared to two gold spikes attached at the base, two spikes connected by a shell (Figure 4.9C) showed a significantly red-shifted spectrum, indicating that the SPR band can be tuned by changing the shell dimensions as well as the dimensions of the spikes (See Figure 4.10).

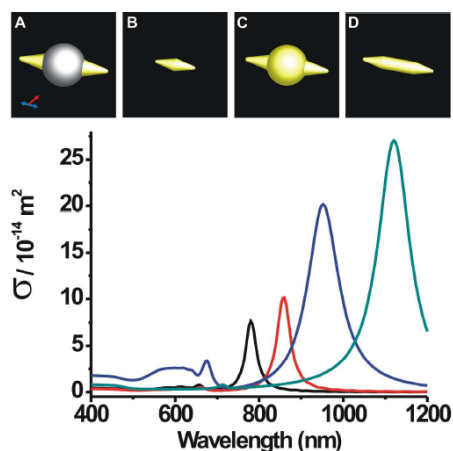


Figure 4.10: Extinction spectra of spiky nanoshells and related structures. The direction of polarization is along the blue arrow and the propagation direction is along the red arrow. (A) Two spikes oriented along the polarization on a PS bead as in Figure 4.9B. (B) Two spikes attached to each other. (C) Two spikes oriented along the polarization on a smooth nanoshell on a PS core. (D) Two spikes oriented along the polarization attached at two ends of a gold nanorod. The base diameter and the height of the spike in all models are 38 nm and 51 nm, respectively. The nanorod in (D) is 209 nm long with a 38 nm base diameter. Reprinted with permission from Brenda L. Sanchez-Gaytan, Zhaoxia Qian, Simon P. Hastings, Michael L. Reza, Zahra Fakhraai, and So-Jung Park. Controlling the Topography and Surface Plasmon Resonance of Gold Nanoshells by a Templated Surfactant-Assisted Seed Growth Method. *The Journal of Physical Chemistry C*, 117(17):8916-8923, May 2013. Copyright 2013 American Chemical Society.

In a spiky nanoshell, the overlap of many spikes generates the effective shell that is needed to produce a tunable near-IR SPR band. This effect can be visualized by adding more spikes to the structure presented in Figure 4.11A. As shown in Figure 4.11B,C, the addition of more spikes does not significantly shift the SPR position from that of two isolated spikes (Figure 4.11A) until the spikes are close enough to interact and generate hot spots (Figure 4.11C). A further addition of spikes generates enough overlap between spikes to produce a thin shell on the PS surface, at which point the spectrum becomes smooth and resembles that of a spiky nanoshell (Figure 4.11D). Although the localized fields between spikes are important in surface-enhanced Raman scattering, as reported earlier [108], these simulation results show that the main SPR band originates from the shell dipole mode.

The surface-topology-dependent SPR of nanoshells synthesized in this study is summarized in Figure 4.12, which shows that the SPR band of the nanoshells can be tuned from about 700 nm to beyond 1100 nm by varying the surface morphology of the gold nanoshells. The introduction of anisotropic substructures on the nanoshells (Figure 4.12B, top, blue) leads to a red shift of the SPR from that of smooth nanoshells (Figure 4.12B, top, red). The comparison of the spiky nanoshells (Figure 4.12B, top, blue) and the superspiky nanoshells (Figure 4.12B, top, green) clearly shows that the nanoshells formed using the combination of CTAC and NaBr exhibit much sharper and denser spikes on the surface, which leads to a red shift of the SPR band. This result is consistent with our previously reported FDTD modeling [108], and it was achieved experimentally here by adjusting the bromide concentration in the growth solution. The gold conversions for the syntheses were determined to be $(82.6 \pm 2.3)\%$, $(80.4 \pm 1.9)\%$, and $(77.8 \pm 3.2)\%$ for smooth CTAC, spiky CTAB, and superspiky CTAC/Br nanoshells, respectively (Figure 4.12B, top, red, blue, and green, respec-

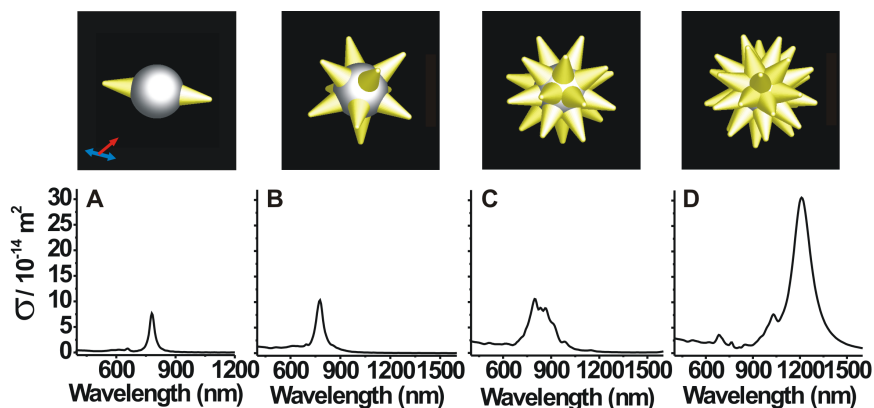


Figure 4.11: Extinction spectra of a PS bead decorated with varying numbers of evenly spaced gold cones: (A) 2, (B) 10, (C) 20, and (D) 30. The polarization direction is aligned with the long axis of two cones in panel A. The SPR band positions were found at (A) 780, (B) 778, (C) 796, and (D) 1210 nm. The extinction spectrum in panel B is close to that in panel A despite the additional cones, as the cones are still noninteracting. In panel C, some cones are close enough to make local contact, but the overlap is not sufficient to form a full shell, resulting in a structured and only moderately shifted spectrum. In panel D, the spikes are completely connected to form a shell, resulting in a dipole mode through the shell formed by overlapping cones at the base. Reprinted with permission from Brenda L. Sanchez-Gaytan, Zhaoxia Qian, Simon P. Hastings, Michael L. Reza, Zahra Fakhraai, and So-Jung Park. Controlling the Topography and Surface Plasmon Resonance of Gold Nanoshells by a Templated Surfactant-Assisted Seed Growth Method. *The Journal of Physical Chemistry C*, 117(17):8916-8923, May 2013. Copyright 2013 American Chemical Society.

tively) by ICP-AES, indicating that the three different types of nanoshells are made of similar amounts of gold. The SPR band can be further shifted to longer wavelengths by increasing the length of spikes on the superspiky nanoshells (Figure 4.12B, top, magenta). The optical properties of metal nanoshells have been extensively studied using smooth gold nanoshells on silica cores ($\text{SiO}_2@Au$) [17]. It is well-known that the SPR position of smooth shells can be readily controlled by changing the ratio between the core diameter and shell thickness and that the increased core/shell ratio results in red shifts of the SPR band [94]. However, large cores are often not desirable, as they significantly increase the overall particle diameter. Although the shell thickness

can be reduced to obtain SPR bands far in the near-IR region, it can be challenging to prepare uniform shells with very small thicknesses (<5 nm). For example, to achieve an SPR band at a wavelength beyond 1000 nm, the shell thickness should be less than 5 nm for a 100-nm-diameter PS core, whereas the thinnest shell reported thus far had a thickness of around 6 nm [17]. In our system that couples a shell and spikes (Figure 4.9), one can readily tune the SPR band over a wide range without significantly changing the size of the nanoshells or the amount of gold.

Finite-difference time-domain (FDTD) simulations were used to model gold nanoshells with varying surface topographies with experimentally relevant structural parameters. In all cases, the amount of gold on the modeled particles was kept consistent with experimental values. As shown in Figure 4.12B (bottom), the position of the broad SPR dipole band depends on the shape, density, and dimensions of the substructure (spheres or spikes) composing the shell. The spiky CTAB shell model (Figure 4.12B, blue) shows a spectrum that is red-shifted from that of the CTAC shell model (Figure 4.12B, red) because of the increased aspect ratio of the substructure and surface roughness. For the same reason, the increase in the spike length and sharpness results in red shifts in the scattering spectra (Figure 4.12B, blue, green, and magenta), as discussed in our previous publication [108]. Increasing the spike density without changing its shape slightly blue shifts the SPR band as a result of the spike overlap and the reduced surface roughness (data not shown). The calculated spectra were generally sharper and had more fine features than the experimental spectra, which is not surprising given the fact that the experimental nanoshells were more heterogeneous in size and shape and were ensemble-averaged over many individual particles. Nonetheless, the simulated SPR positions in Figure 4.12B (bottom) match well with the experimental peak positions in Figure 4.12B (top), using the

amount of gold and the geometry found in the synthesized nanoshells. The scattering intensity of the nanoshells increased with the surface roughness, demonstrating an important advantage of the structured nanoshells synthesized here (See Figure 4.13 for unnormalized spectra).

Compared to the nanostar synthesis using large ($\sim 10\text{-}15$ nm) gold nanoparticle seeds [32, 88], the templated surfactant assisted seed growth method reported here produces uniform spiky nanostructures in nearly 100% yield whereas the nanostar synthesis generates a mixture of nanostars with different numbers of arms. The hollow architecture of nanoshells is also advantageous because it adds another control characteristic (*i.e.*, core size) to tune the SPR position. In addition, other functional materials and molecules can be incorporated into the core to fabricate multifunctional nanoshells.

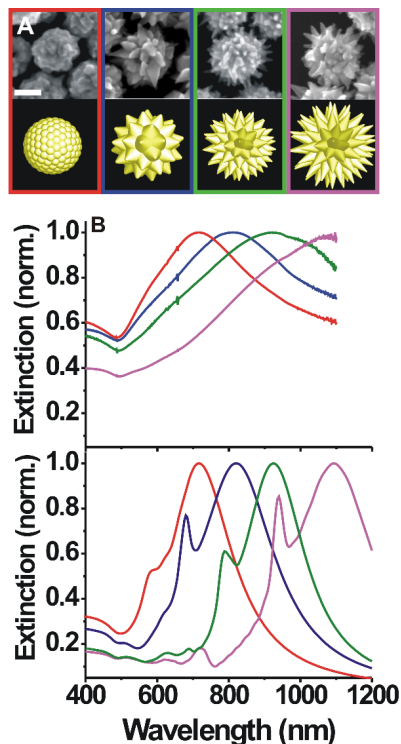


Figure 4.12: (A) (Top) SEM images of various nanoshells synthesized in CTAC (red), CTAB (blue), and CTACBr (green and magenta) growth solutions. Scale bar = 100 nm. (Bottom) Corresponding models used for FDTD simulations. (B) (Top) Extinction spectra of nanoshells shown in panel A: smooth CTAC shell (red), spiky CTAB shell (blue), and superspiky CTAC/Br shells (green and magenta). For the syntheses, 10 mL of growth solution was mixed with 20 μL (red, blue, green) or 10 μL (magenta) of seed solution. (Bottom) Calculated extinction spectra of various nanoshells: nanoshell model resembling the smooth CTAC nanoshell composed of 180 nanospheres with a 26-nm diameter (red); spiky CTAB nanoshell model composed of 40 spikes with a base diameter of 60 nm, height of 45 nm, and tip diameter of 10 nm (blue); superspiky CTAC/Br nanoshell model constructed using a larger number of sharper spikes (80 spikes with a base diameter of 38 nm, height of 45 nm, and tip diameter of 4 nm) (green); and superspiky nanoshell model constructed by placing 80 spikes with a base diameter of 38 nm, height of 65 nm, and tip diameter of 4 nm (magenta). In all cases, gold nanostructures were placed on the surface of a 95-nm PS core. Reprinted with permission from Brenda L. Sanchez-Gaytan, Zhaoxia Qian, Simon P. Hastings, Michael L. Reza, Zahra Fakhraai, and So-Jung Park. Controlling the Topography and Surface Plasmon Resonance of Gold Nanoshells by a Templated Surfactant-Assisted Seed Growth Method. *The Journal of Physical Chemistry C*, 117(17):8916-8923, May 2013. Copyright 2013 American Chemical Society.

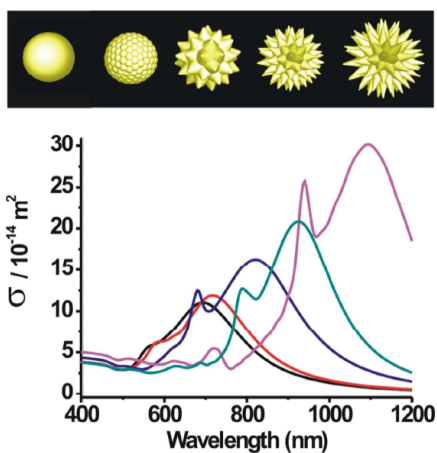


Figure 4.13: Unnormalized extinction spectra of four models (red, blue, green, magenta) presented in Figure 4.12. The extinction spectra of the smooth nanoshell (black) presented in Figure 4.3 is also presented here for comparison. Reprinted with permission from Brenda L. Sanchez-Gaytan, Zhaoxia Qian, Simon P. Hastings, Michael L. Reza, Zahra Fakhraai, and So-Jung Park. Controlling the Topography and Surface Plasmon Resonance of Gold Nanoshells by a Templated Surfactant-Assisted Seed Growth Method. *The Journal of Physical Chemistry C*, 117(17):8916-8923, May 2013. Copyright 2013 American Chemical Society.

4.3.5 Conclusion

In summary, the templated surfactant-assisted seed growth method provides a robust synthetic method to synthesize gold nanoshells with controllable fine structure and SPR position. When CTAC was used as the surfactant instead of CTAB, the isotropic nanoparticles on polymer templates continued to grow and fused together into relatively smooth nanoshells. The addition of bromide ions to the CTAC-based growth solution yielded spiky nanoshells having sharper and denser spikes decorating the shell surface, compared to the nanoshells prepared using a CTAB growth solution. The concentration of bromide was found to control the aspect ratio and surface coverage of spikes on the surface. On the other hand, the addition of iodide ions to the growth solution resulted in incomplete shells composed of discrete gold spheres decorating PS beads because of the strong binding of iodide ions on gold surface. The surface topography significantly changed the characteristics of the SPR band of nanoshells, and we were able to tune the SPR position over a wide wavelength range by changing the shape, size, density, and degree of overlap of subparticles decorating the polymer core. The highly structured nanoshells contain many hot spots, which should be useful for a number of scattering-based applications of nanoshells including surface-enhanced spectroscopy [101] and photothermal therapy [61, 47]. In addition, the structured nanoshells reported here mimic the topographies of many biological and environmental particles such as dendritic cells and pollen grains, providing opportunities to systematically investigate the effects of particle surface topology on the interactions with living systems. Based on the capability of the surfactant-assisted seed growth method to generate a wide range of different shapes of nanoparticles, the templated surfactant-assisted seed growth method reported here should provide new opportunities in the synthesis and application of metal nanoparticles.

4.3.6 Acknowledgments

S.-J.P. acknowledges financial support from an NSF Career Award and a Camille Dreyfus Teacher-Scholar Award. Z.F. acknowledges funding from the Department of Chemistry and School of Arts and Sciences of the University of Pennsylvania. TEM and SEM measurements were carried out at the Electron Microscopy Resource Laboratory and the Penn Regional Nanotechnology Facility. The authors thank Professor Nader Engheta for insightful discussions.

Chapter 5

Quadrupole-Enhanced Raman Scattering in Spiky Nanoshells

5.1 Introduction

The near-field of a nanostructure can have very different behavior from the far-field. Sensing applications such as surface enhanced Raman spectroscopy (SERS) depend on the ability to locally enhance the electric field. As a result, they are best performed with highly localized fields in the gaps and near sharp tips of metallic objects. Spiky nanoshells possess many such tips, which can be excited by hybridization to the main multipole scattering moments. In the studies in this chapter, published in Reference [38], it is determined that the majority of the enhancement in these particles is the result of coupling of the spikes to the dark quadrupole mode, rather than the bright dipole mode. As shown in this chapter, the disorder in these particles induces many different quadrupole modes, which collectively couple strongly to the tips generating a reliable average enhancement factor as seen experimentally.

5.2 Context

The text and figures in this section of the dissertation are taken with permission from Reference [38]. This work was done in collaboration with a number of other researchers: the particle synthesis and the UV-vis measurements were performed by Zhaoxia Qian supervised by So-Jung Park, the dark field and SERS measurements were performed by Pattanawit Swanglap and Ying Fang, supervised by Stephan Link. The author was responsible for the structural modeling, FDTD simulation, near-field analysis, scattering analysis and (collaboratively) writing the manuscript, supervised by Zahra Fakhraai and co-supervised by Nader Engheta.

5.3 Quadrupole-Enhanced Raman Scattering

Reprinted with permission from Simon P. Hastings, Pattanawit Swanglap, Zhaoxia Qian, Ying Fang, So-Jung Park, Stephan Link, Nader Engheta, and Zahra Fakhraai. Quadrupole-Enhanced Raman Scattering. *ACS Nano*. 2014 8 (9), 9025-9034. Copyright 2014 American Chemical Society.

5.3.1 Abstract

Dark, nonradiating plasmonic modes are important in the Raman enhancement efficiency of nanostructures. However, it is challenging to engineer such hotspots with predictable enhancement efficiency through synthesis routes. Here, we demonstrate that spiky nanoshells have designable quadrupole resonances that efficiently enhance Raman scattering with unprecedented reproducibility on the single particle level. The efficiency and reproducibility of Quadrupole Enhanced Raman Scattering (QERS) is due to their heterogeneous structure, which broadens the quadrupole resonance both

spatially and spectrally. This spectral breadth allows for simultaneous enhancement of both the excitation and Stokes frequencies. The quadrupole resonance can be tuned by simple modifications of the nanoshell geometry. The combination of tunability, high efficiency, and reproducibility makes these nanoshells an excellent candidate for applications such as biosensing, nanoantennas and photovoltaics.

5.3.2 Introduction

Surface enhanced Raman spectroscopy (SERS) [39] has been widely studied for its diverse potential applications ranging from chemical [58, 24, 21, 30] and biological [104, 105, 46] detection to intracellular imaging [57] and medicine [102]. When a Raman analyte is placed in the near-field of a plasmonic nanostructure, the vibrational modes of the analyte couple to the local electric field, and the Raman scattering cross section scales with the local electric field to the fourth power [119]. As such, SERS substrates are often designed to generate hotspots at sharp corners or small gaps, either between nanostructures [24, 43, 120, 56, 133] or engineered into single nanoparticles [20, 65, 66]. While hotspots in particle junctions can be used to achieve extremely high SERS cross sections, they are difficult to engineer [13], and it is challenging to precisely place the analyte in the right position and orientation for maximum coupling. Furthermore, the enhancement is extremely sensitive to small changes in the local structure including the size of the gap [13], the polarization of the incident light [134], and the direction of detection [5]. These factors lead to extremely large variations of SERS intensity in hotspot-based SERS substrates.

In contrast, in simple single nanoparticles such as isolated spheres and rods, the near-field intensity is usually dominated by the dipolar resonance of the localized surface plasmon resonance (LSPR) [40]. Thus, SERS enhancement on these simple

nanoparticles usually correlates well with far-field plasmon resonances. However, the enhancement factor on these simple nanoparticles is much lower than hotspot based substrates. In nonspherical or large nanostructures, a higher order resonance called the quadrupole resonance can occur and can lead to SERS enhancement due to bright quadrupole resonances [65, 125]. In smaller nanoparticles, the quadrupole resonances are dark and their electric fields decay rapidly with distance from the particle. However, they can still have a significant contribution to the near-field intensity [75, 139, 42].

Here, we demonstrate both experimentally and theoretically that dark quadrupole resonances can play an important role in the SERS cross section, and thereby achieve highly efficient and uniform SERS enhancement. We have recently developed a new method of synthesis to produce highly structured metal nanoshells composed of numerous sharp spikes called spiky nanoshells [106, 108, 107]. These nanoshells were shown to be remarkably effective SERS substrates with exceptionally reproducible Raman scattering signals on the single particle level [108]. In this manuscript, we demonstrate that Raman scattering with even larger cross section and narrower distribution can be achieved by excitation at the quadrupole resonance, and that the remarkable reproducibility results from the disorder in the spiky nanoshells that broadens the quadrupole resonance. The disorder in the structure results in the formation of spatially delocalized hotspots on the tip of many spikes that can enhance the Raman cross section of randomly placed analyte molecules. This is in sharp contrast with other observations of SERS enhancement in hotspots, where the direction of the detection and the exact position of the analyte are extremely important and with particular detection methods such as directivity enhanced Raman scattering (DERS) where the plasmonic structure itself has a preferred direction to its Raman cross section [5].

5.3.3 Results and Discussions

For this study, spiky gold nanoshells were synthesized by surfactant-assisted seed growth method [106, 108, 107] and characterized by UV-vis absorption spectroscopy, transmission electron microscopy (TEM), and scanning electron microscopy (SEM). Figure 5.1a shows an SEM image of the spiky nanoshells used in this study. Single particle dark field backscattering (Figure 5.1d,f) and Raman spectroscopy (Figure 5.1g) were performed on individual spiky nanoshells immobilized on a glass substrate and coated with 4-mercaptopbenzoic acid (Figure 5.1b). They were then studied with an inverted microscope (Figure 5.1c) to examine how far field backscattering characteristics correlate with the Raman scattering cross section. Ensemble averaged spectra and histograms of these data are shown in Figure 5.2, with additional backscattering spectra in Figure 5.3. SERS spectra were collected at 633 nm and 785 nm excitation wavelengths. After all optical measurements, the nanoshell samples were imaged by SEM (Figure 5.1e) to make sure that only single particle data are included in the data analyses, as the variable shape of the backscattering spectra did not allow for conclusive identifications of isolated nanoshells. Representative SERS spectra are shown in Figure 5.1g. More details of the sample preparation and Raman experiments can be found in the Supporting Information (SI).

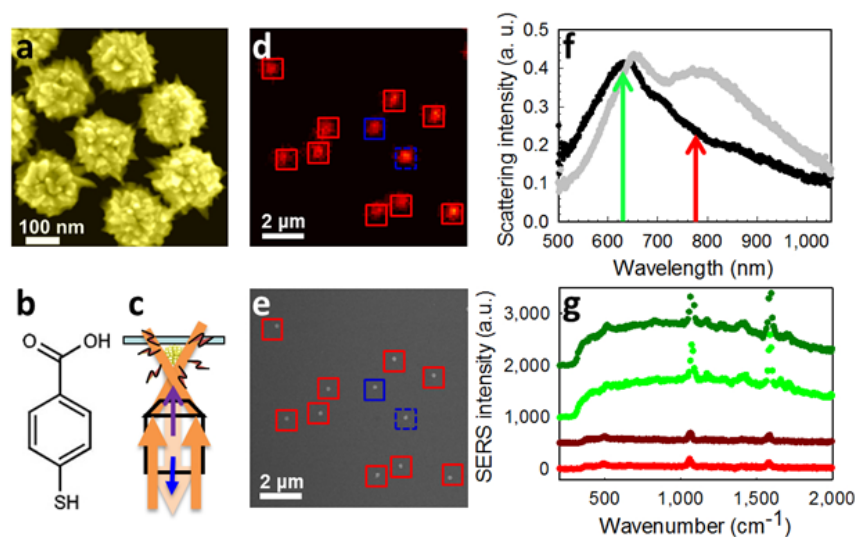


Figure 5.1: SERS and dark-field scattering measurements and apparatus. (a) An SEM image of a collection of spiky nanoshells. (b) The structure of 4-mercaptobenzoic acid that was used as the Raman analyte. (c), Schematic of the single particle backscattering and Raman scattering measurements. Orange arrows show the direction of incident and backscattered white light, while the purple and blue arrows indicate the orientation of the laser excitation and the Stokes lines, respectively. (d) Dark-field backscattering image of spiky nanoshells. (e) SEM image of the same area as (d) used to ensure that only single particle spectra were collected. Boxes are added to individual spiky nanoshells to aid in the comparison of the images. (f) Representative examples of typical dark-field scattering spectra from the two particles highlighted with blue boxes. Green and red arrows show the excitation wavelengths used for Raman scattering. (g) SERS spectra at 633 nm (green), and 785 nm (red) excitations. The dark green and dark red SERS spectra represent spectra obtained from the particle with the solid black far-field scattering spectrum in (f), and highlighted by the solid blue boxes in (d) and (e), and the light green and light red SERS spectra correspond to the single particle spectrum given by the gray far-field scattering spectrum, shown in the dashed blue boxes in (d) and (e). The dark red, light green, and dark green spectra are shifted vertically by 500, 1000 and 2000 intensity units, respectively, for better visualization. Reprinted with permission from Simon P. Hastings, Pattanawit Swanglap, Zhaoxia Qian, Ying Fang, So-Jung Park, Stephan Link, Nader Engheta, and Zahra Fakhraei. Quadrupole-Enhanced Raman Scattering. *ACS Nano*. 2014 8 (9), 9025-9034. Copyright 2014 American Chemical Society.

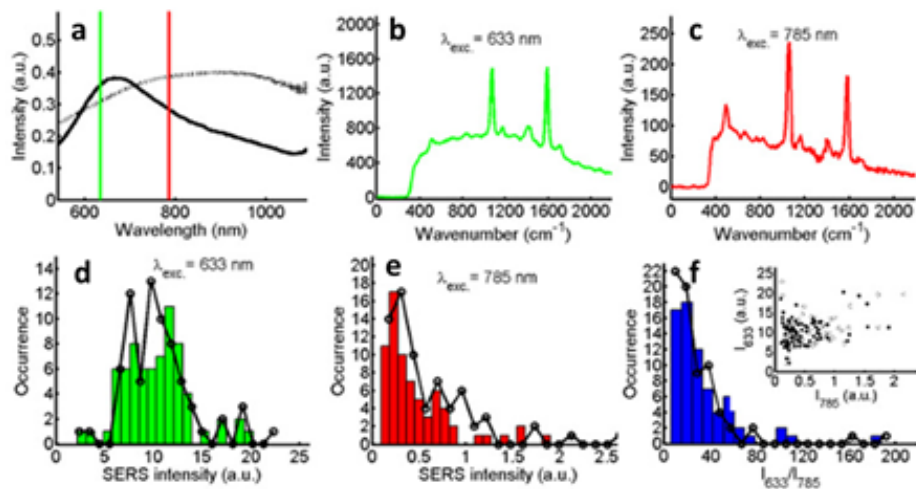


Figure 5.2: Single particle SERS distributions. Ensemble averaged spectra of dark-field scattering (a, solid line), 633 nm excited (b), and 785 nm excited (c) SERS. The spectrum represented by the dashed line in (a) is the solution phase extinction spectrum of the spiky nanoshells. Histograms of SERS intensities for 633 nm (d, $\langle 10.4 \rangle_{1585} \pm 3.5$; $\langle 10.5 \rangle_{1077} \pm 3.6$) and 785 nm (e, $\langle 0.48 \rangle_{1585} \pm 0.38$; $\langle 0.60 \rangle_{1077} \pm 0.48$) excitation and the ratio of SERS intensities (I_{633}/I_{785}) for the two excitation wavelengths (f). The bars correspond to the SERS intensities evaluated at the 1585 cm^{-1} peak, while the black data points and line represent SERS intensities for the 1077 cm^{-1} peak. The inset in (f) plots the SERS intensity for 633 nm excitation vs. the corresponding SERS intensity measured with 785 nm excitation for the same individual spiky nanoshell (solid circles: 1585 cm^{-1} , open circles: 1077 cm^{-1}). The green and red lines in a indicate the excitation wavelengths of 633 nm and 785 nm used in the SERS measurements. Reprinted with permission from Simon P. Hastings, Pattanawit Swanglap, Zhaoxia Qian, Ying Fang, So-Jung Park, Stephan Link, Nader Engheta, and Zahra Fakhraei. Quadrupole-Enhanced Raman Scattering. *ACS Nano*. 2014 8 (9), 9025-9034. Copyright 2014 American Chemical Society.

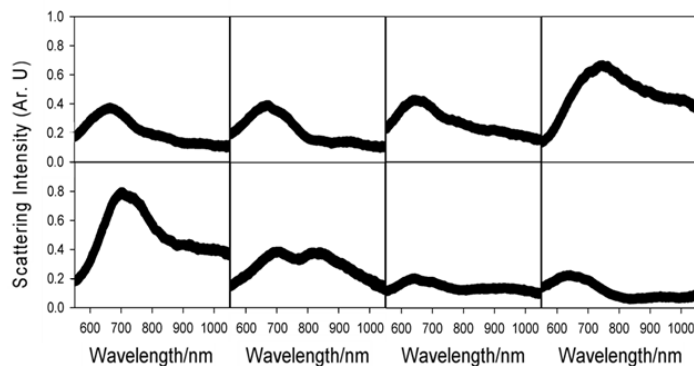


Figure 5.3: Comparison of eight experimental dark-field spectra representing single spiky nanoparticles. Reprinted with permission from Simon P. Hastings, Pattanawit Swanglap, Zhaoxia Qian, Ying Fang, So-Jung Park, Stephan Link, Nader Engheta, and Zahra Fakhraai. Quadrupole-Enhanced Raman Scattering. *ACS Nano*. 2014 8 (9), 9025-9034. Copyright 2014 American Chemical Society.

SERS intensity changes significantly with the excitation wavelength. As shown in Figure 5.4, for all 71 particles examined, the Raman intensity at 633 nm was about a factor of 20 higher compared to the 785 nm excitation for both 1585 cm^{-1} and 1077 cm^{-1} peaks. In addition, at 633 nm excitation the Raman signals show significantly lower intensity variations compared to 785 nm, with 34% and 80% standard deviations, respectively. Note that the signal is remarkably more reproducible for both wavelengths when compared to intensity variations found for nanoparticle dimers, in which the enhancement factor can vary by 4 orders of magnitude depending on the inter-particle distance [133].

Figure 5.4 shows the intensity of each Raman line of the analyte, measured at both excitations as a function of peak far-field wavelength (λ_{max}) and the calculated enhancement factor as described below. The correlation plots in Figure 5.4 show that the measured SERS intensity is neither correlated with the far-field scattering peak of the nanoshells (Figure 5.4a), nor with the enhancement factor calculated based on the far-field spectrum (Figure 5.4b). Single particle measurements also

show that the presence of an apparent dip, which was sometimes observed at longer wavelengths (gray spectrum in Figure 5.1f), did not visibly affect the SERS intensities on a single particle level. As the SEM image in Figure 5.1e shows, the particles are well separated and the backscattering feature shown in Figures 5.1f and 5.3 cannot be the result of interference between two near-by particles. The origin of this behavior will be discussed in a future manuscript. Therefore, far-field spectral features can neither explain the origin of the strong enhancement factors at 633 nm excitation compared to the 785 nm excitation, nor its exceptional reproducibility. Therefore, specific near-field effects must be considered in order to explain these experimental observations.

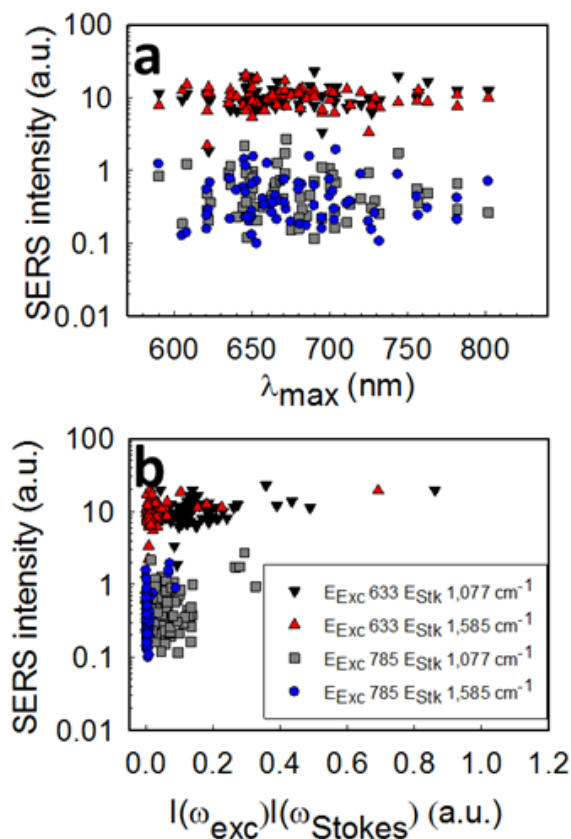


Figure 5.4: Single particle SERS and dark-field scattering correlations. (a) Correlation between the measured SERS intensity and the peak backscattering wavelength (λ_{max}) for 633 excitation with 1077 cm^{-1} Stokes scattering (black downward triangles), 1585 cm^{-1} Stokes scattering (red upward triangles), 785 excitation with 1077 cm^{-1} Stokes scattering (gray squares), and 1585 cm^{-1} Stokes scattering (blue circles). (b) Correlation between Raman signal intensity and the calculated enhancement factors based on the far-field scattering spectrum for the same data in (a). Reprinted with permission from Simon P. Hastings, Pattanawit Swanglap, Zhaoxia Qian, Ying Fang, So-Jung Park, Stephan Link, Nader Engheta, and Zahra Fakhraai. Quadrupole-Enhanced Raman Scattering. *ACS Nano*. 2014 8 (9), 9025-9034. Copyright 2014 American Chemical Society.

To explore the origin of the strong relative Raman enhancement at 633 nm, it is necessary to examine the underlying mechanisms of SERS. The Raman scattering dipole of an analyte, μ_α , placed in an electrical field can be described as [18]:

$$\mu_\alpha = \alpha_{\alpha\beta}E_\beta + \frac{1}{3}A_{\alpha\beta\gamma}E_{\beta\gamma} + \dots \quad (5.3.1)$$

In this equation $\alpha_{\alpha\beta}$ and $A_{\alpha\beta\gamma}$ are the dipole and quadrupole polarizability tensors of the molecule, E_β is the electric field, and $E_{\beta\gamma}$ is the electric field gradient with respect to γ , where α , β , and γ denote the coordinates. Higher order terms are assumed to be small and are ignored. The analyte used in this study, 4-mercaptobenzoic acid, has two vibrational bands in the experimental window as shown in Figure 5.1g. Both vibrational bands are dipolar in nature, and therefore the second term in Eq. 5.3.1 is negligible (details provided in the Supporting Information). Under these conditions, the non-resonant SERS enhancement factor (EF) can be described by [119, 69, 130]:

$$EF = \frac{I_{Exc}I_{Stokes}}{I_0^2} \quad (5.3.2)$$

where I_{Exc} is the electric field intensity at the excitation wavelength, I_{Stokes} is the near-field electric field intensity at the Stokes wavelength, and I_0^2 is the near-field electric field intensity of the incident wave to the power of two.

As mentioned above, in simple nanoparticles, where both near-field and far-field electric fields can be described by a dipole moment, the far-field spectrum provides a reasonable guide for predicting and optimizing the Raman enhancement factor [119]. However, in nanostructures containing hotspots [56, 133] the enhancement factors are often uncorrelated with the far-field spectral features. Wustholz *et al.* [133] showed that in these cases the optimum frequency for SERS enhancement can be predicted through detailed understanding, *via* simulation, of the near-field around

the nanoparticle.

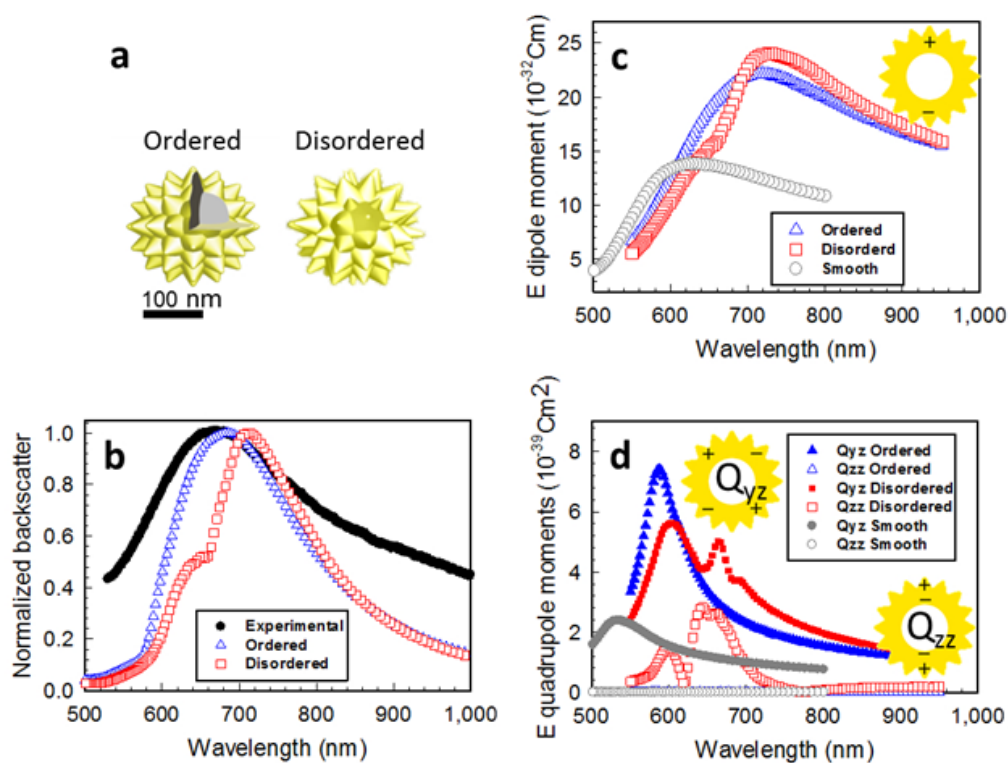


Figure 5.5: Simulated far field and multipole spectra for spiky nanoshells. (a) Modeled structures of spiky nanoshells. The simplified ordered nanoshell is shown on the left, and the disordered structure is shown on the right. A scale bar indicates the approximate scale of the nanoshells. Part of the ordered nanoshell is removed to show the polystyrene core present in both models. Please see the methods and SI for more details. (b) Ensemble averaged experimental dark-field backscattering spectrum (black) compared with the simulated far-field backscattering spectra of the ordered (blue) and disordered (red) model nanoshells. (c) Electric dipole moment of the ordered (blue) and disordered (red) nanoshells compared with a smooth nanoshell (gray) with the same amount of gold as the disordered nanoshells and the same core size. (d) Electric quadrupole moments of the ordered (blue), disordered (red), and smooth (gray) nanoshells. Solid symbols indicate the quadrupole moment in the yz direction, while the open symbols show the quadrupole moment in the zz direction. The y and z directions denote the direction of propagation and polarization vectors of the incident wave in the Cartesian coordinates. All higher moments are orders of magnitude weaker. Adapted with permission from Simon P. Hastings, Pattanawit Swanglap, Zhaoxia Qian, Ying Fang, So-Jung Park, Stephan Link, Nader Engheta, and Zahra Fakhraei. Quadrupole-Enhanced Raman Scattering. *ACS Nano*. 2014 8 (9), 9025-9034. Copyright 2014 American Chemical Society.

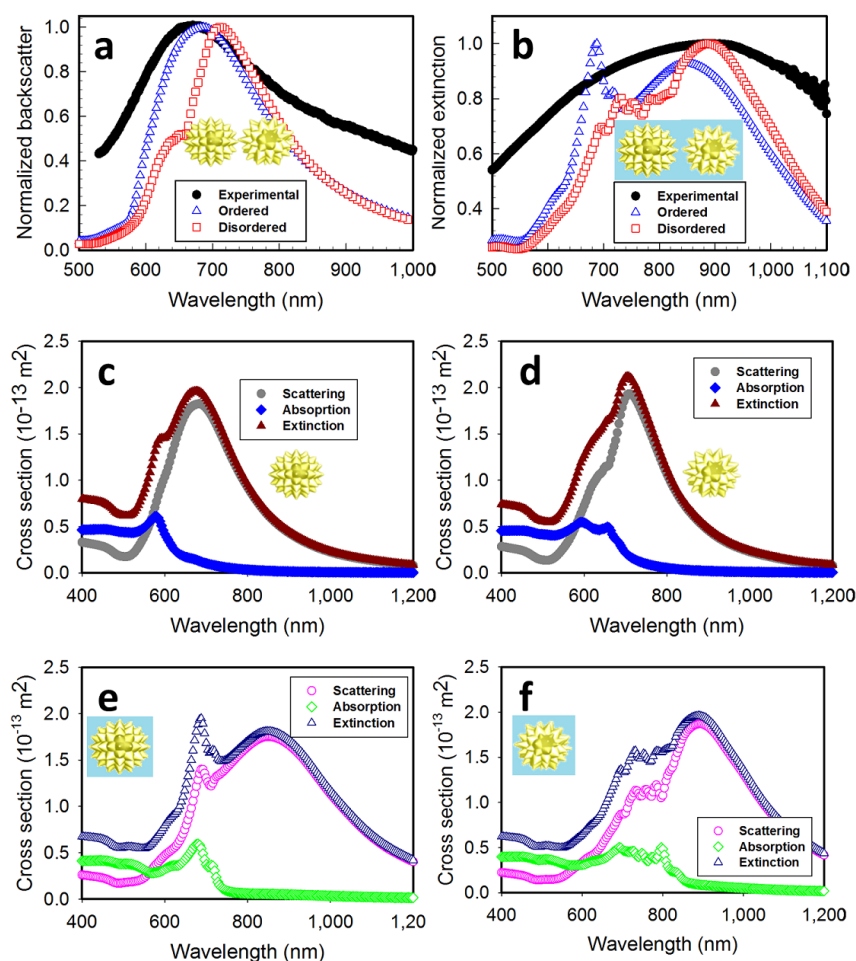


Figure 5.6: Comparison of the far-field properties of the modeled nanoshells to the experimentally measured ones. a, The average experimental backscattering spectrum from 71 spiky nanoshells (black) compared to the theoretical disordered (red) and ordered (blue) models backscattering spectra in a uniform background index of refraction $n=1$. b, The experimental extinction in water compared to the extinction spectra of the disordered and ordered models in a uniform background index of refraction of $n=1.333$. Far field scattering, absorption and extinction is also shown for the ordered particles (c and e), and for the disordered particles (d and f). Middle figures (c and d) are in an air-like constant dielectric ($n=1$), while the bottom figures (e and f) are in a constant water-like dielectric ($n=1.333$). Reprinted with permission from Simon P. Hastings, Pattanawit Swanglap, Zhaoxia Qian, Ying Fang, So-Jung Park, Stephan Link, Nader Engheta, and Zahra Fakhraei. Quadrupole-Enhanced Raman Scattering. *ACS Nano*. 2014 8 (9), 9025-9034. Copyright 2014 American Chemical Society.

Near-field profiles of spiky nanoshells were obtained by Finite-Difference Time Domain (FDTD) simulations using the two models shown in Figure 5.5a. As in previous studies [108, 107], these models were built based on experimentally relevant parameters (see Supporting Information) in order to elucidate the structural origin of the unusual excitation wavelength dependence of the SERS intensities. Ordered and disordered structures were created to explore the heterogeneity of the actual nanoshells, which was found to play an important role in the uniform SERS intensity (*vide infra*). The calculated backscattering (Figure 5.5b) and extinction (Figure 5.6) spectra of these models match well with the experimentally measured spectra (see Supporting Information). This provides confidence that the modelled structures are good representations of typical spiky nanoshells. In order to avoid bias from the randomization, ten additional re-randomized structures were studied as shown in Figure 5.7. The dipole and quadrupole moments of these model nanoshells were calculated from the polarization currents, using the following equations [97]:

$$\vec{P} = \frac{i}{\omega} \int \vec{J}(\vec{r}') dV' \quad (5.3.3)$$

$$Q_{\alpha\beta} = \frac{i}{\omega} \int \vec{J}_{\alpha}(\vec{r}') \vec{r}'_{\beta} + \vec{J}_{\beta}(\vec{r}') \vec{r}'_{\alpha} dV' \quad (5.3.4)$$

In these equations \vec{P} is the dipole moment vector, Q is the quadrupole moment tensor, \vec{J} is the polarization current volume density, \vec{r} is the position vector, and ω is the angular frequency of excitation where the time harmonic wave, $exp(-i\omega t)$, has been considered. α and β each denote x , y or z depending on which quadrupole moment is calculated. Here y denotes the direction of propagation and z corresponds to the direction of polarization of the incident field. The integral is over the entire simulation space. Calculated spectral shapes of the dipole and quadrupole mo-

ments for the two structures are presented in Figures 5.5c and 5.5d, exhibiting strong quadrupole resonances. For comparison, we provide the same results for a smooth shell with gold volume equal to the disordered model. The polarization current maps at the Q_{yz} quadrupole and the dipole resonances are shown in Figures 5.9a and 5.9b respectively for the disordered model, and in Figure 5.8 for the ordered model. These current maps show that despite significant disorder and numerous sharp points in the nanoshell structure, the polarization current, and the local electric fields are primarily dominated by the particular quadrupole or dipole resonance at a given frequency.

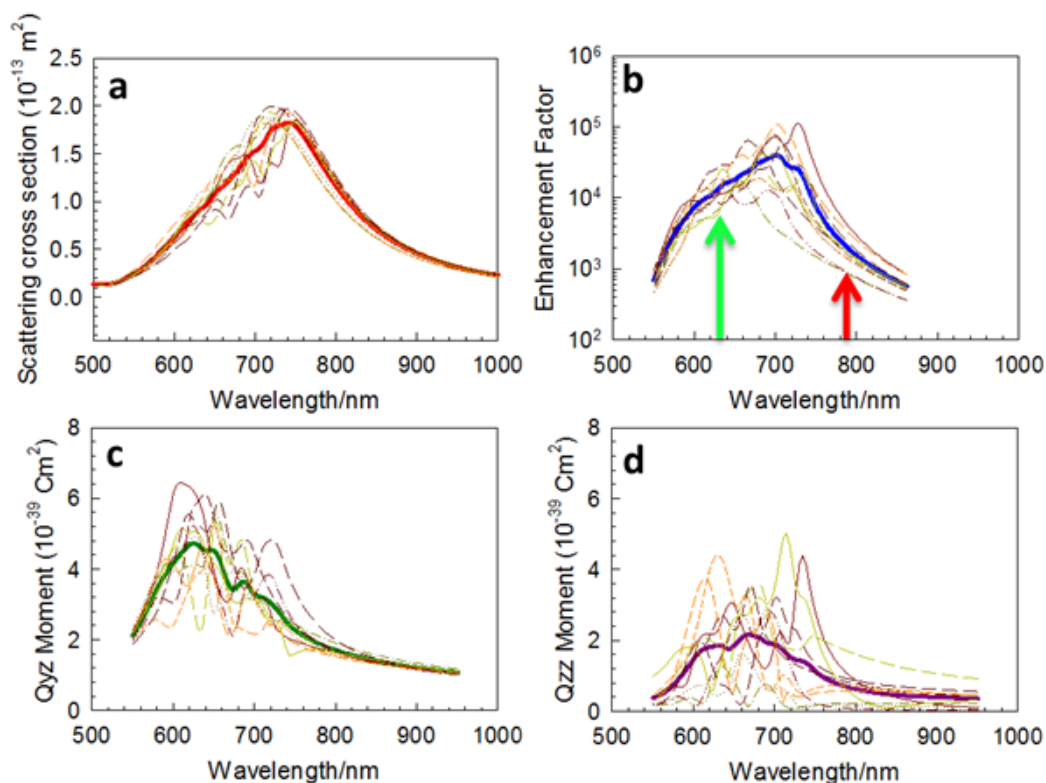


Figure 5.7: Average and individual properties of a set of ten re-randomized model disordered nanoshells. The ensemble averages are presented in figure 5.19 of the main manuscript. a, Scattering cross sections with the average cross section (thick red). b, Enhancement factor calculated based on the procedure explained in the manuscript as well as the average enhancement factor at 1077 cm^{-1} (thick blue). The enhancement factor at 785 nm excitation is substantially smaller than the corresponding value at 633 nm in all 10 models. The variations from mean are also smaller at 633 nm compared to 785 nm. c, Q_{yz} quadrupole along with the ensemble average Q_{yz} quadrupole (thick green). d, Q_{zz} quadrupole along with the ensemble average Q_{zz} quadrupole (thick purple). Panels c and d demonstrate the high levels of disorder in the individual quadrupole modes. Reprinted with permission from Simon P. Hastings, Pattanawit Swanglap, Zhaoxia Qian, Ying Fang, So-Jung Park, Stephan Link, Nader Engheta, and Zahra Fakhraei. Quadrupole-Enhanced Raman Scattering. *ACS Nano*. 2014 8 (9), 9025-9034. Copyright 2014 American Chemical Society.

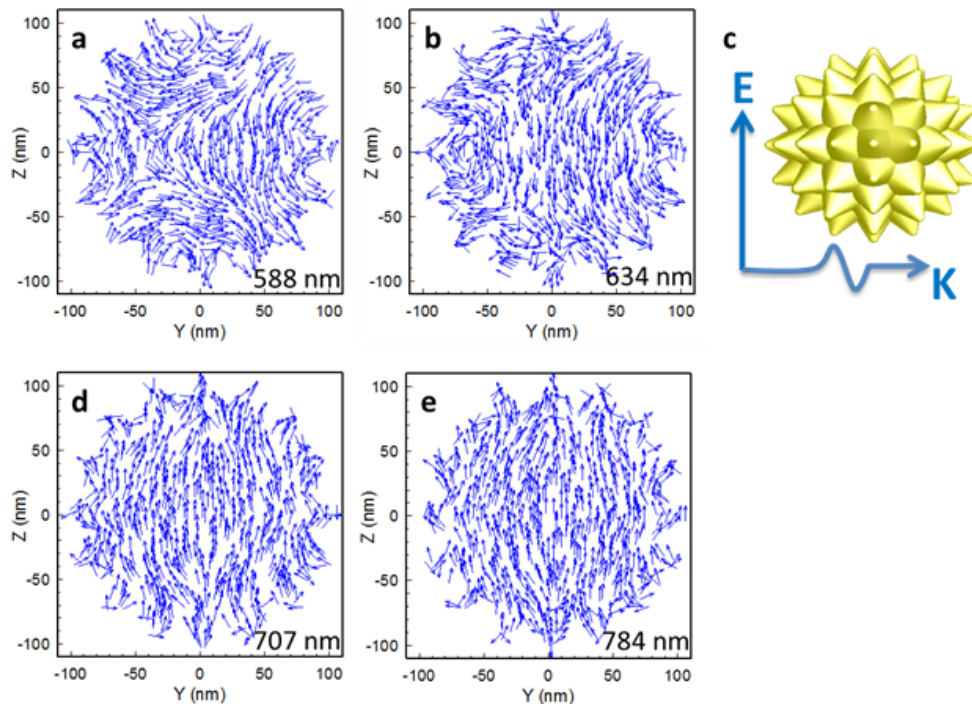


Figure 5.8: Polarization currents in the spiky nanoshell from the FDTD simulation of the ordered structure, projected onto the yz plane. Magnitude was removed to produce uniform vector lengths. a, Polarization currents of the ordered structure at 588 nm (the Q_{yz} quadrupole resonance). b, Polarization currents of the ordered structure at 634 nm (the short wavelength Raman excitation line). c, The structure of the ordered nanoshell along with the orientation of the incident wave and polarization of the electric field. d, Polarization currents of the ordered structure at 707 nm (the dipole resonance). e, Polarization currents of the ordered structure at 784 nm (the long wavelength Raman excitation line). Reprinted with permission from Simon P. Hastings, Pattanawit Swanglap, Zhaoxia Qian, Ying Fang, So-Jung Park, Stephan Link, Nader Engheta, and Zahra Fakhraei. Quadrupole-Enhanced Raman Scattering. *ACS Nano*. 2014 8 (9), 9025-9034. Copyright 2014 American Chemical Society.

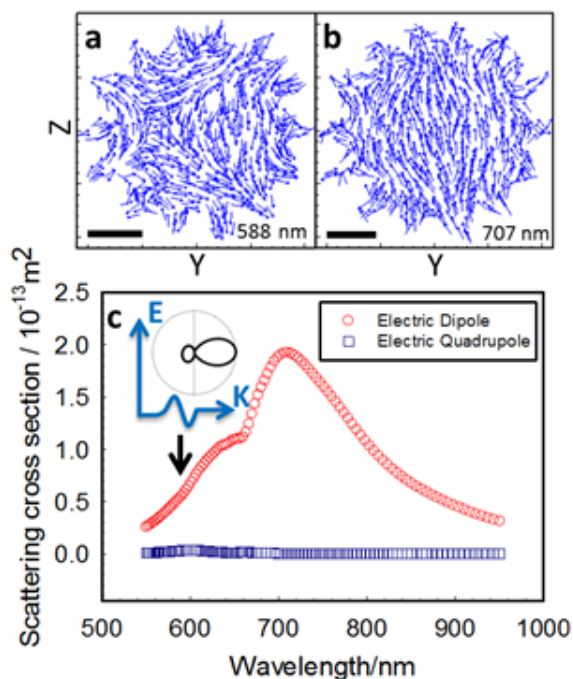


Figure 5.9: Far-field and near-field response of the dipole and quadrupole modes. (a) Polarization currents in the disordered spiky nanoshell obtained from the FDTD simulation at 588 nm (the Q_{yz} quadrupole resonance), projected onto the yz plane. Magnitude was removed to produce uniform vector lengths. (b) Polarization currents of the same structure at 707 nm (the dipole resonance). The scale bars are 50 nm in length for both a and b. (c) Calculated scattering cross section of the dipole (red) and quadrupole (blue) modes. Inset shows the far-field angular distribution at the yz quadrupole peak (588 nm), which is clearly dipolar in nature. The y and z directions denote the direction of propagation and polarization vectors of the incident wave in the Cartesian coordinates. Reprinted with permission from Simon P. Hastings, Pattanawit Swanglap, Zhaoxia Qian, Ying Fang, So-Jung Park, Stephan Link, Nader Engheta, and Zahra Fakhraei. Quadrupole-Enhanced Raman Scattering. *ACS Nano*. 2014 8 (9), 9025-9034. Copyright 2014 American Chemical Society.

To demonstrate that the quadrupole mode can be considered a dark mode in the far-field, the scattering cross section of the dipole and quadrupole modes were calculated for the disordered nanoshell. This is performed assuming that there was no mixing or interference between the modes. We note that given the fine features in the far-field scattering spectrum as shown in Figure 5.5b and in the experimental data of Figures 5.1f and 5.3, modal interference is possible. The details of this phenomenon are beyond the scope of this paper and will be discussed in a separate publication, where we show the coupling is less than about 5% and can be ignored for the purposes of this paper. Figure 5.9c shows that the quadrupole mode is indeed a dark mode in the far-field and does not significantly contribute to the far-field scattering cross section (see SI for details of the calculation). The inset of Figure 5.9c and additional polar plots presented in Figure 5.10 also confirm that the angular distribution of the far-field scattering follows the dipolar angular distribution at both the dipole and quadrupole resonance wavelengths with no additional lobes or substantial changes to the nodal plane as seen in directional emission [23]. Furthermore, the addition of disorder to the structure does not significantly change the far-field LSPR peak (Figure 5.5b) or the dipole resonance (Figure 5.5c) except for potential interference between the Q_{zz} quadrupole and the dipole, which results in a small apparent shift in the dipole resonance peak.

While the addition of disorder to the structure does not significantly change the far-field LSPR peak or the dipole resonance, it strongly affects the quadrupole resonances (Figure 5.5d). In the smooth nanoshell and in the ordered structure, the only nonzero quadrupole moment is in the yz plane (Q_{yz}), where y and z denote the direction of propagation and the polarization of the incident wave, respectively. In contrast, in the disordered structure, which more closely represents the imperfect

structure of the synthesized spiky nanoshells, nonuniform spike lengths generate additional nonzero quadrupoles with the strongest in the polarization direction (Q_{zz}). In comparison to the smooth shells, the quadrupole resonances are nearly a factor of four stronger and are spectrally much broader.

As shown in Figure 5.5d, compared to the ordered nanoshell, the disordered nanoshell has spectrally broadened quadrupole resonances with more spectral features (examples from more nanoshell realizations are shown in Figure 5.7 and averages in 5.11). This is achieved without a significant change in the peak amplitude or the quality factor ($QF = f/\delta f$, where f is the frequency). The spectral breadth of the quadrupole resonance in the disordered structure enables efficient enhancement of the electric field both at the excitation and the Stokes scattering frequencies and is crucial to the experimental observation of Quadrupole Enhanced Raman Scattering (QERS). We note that the fine features in the disordered structure depend on the details of the randomization and vary from one model to another. Figure 5.7 and 5.11 show that despite these variations the conclusions stated here remain valid for an ensemble of disordered nanoshells.

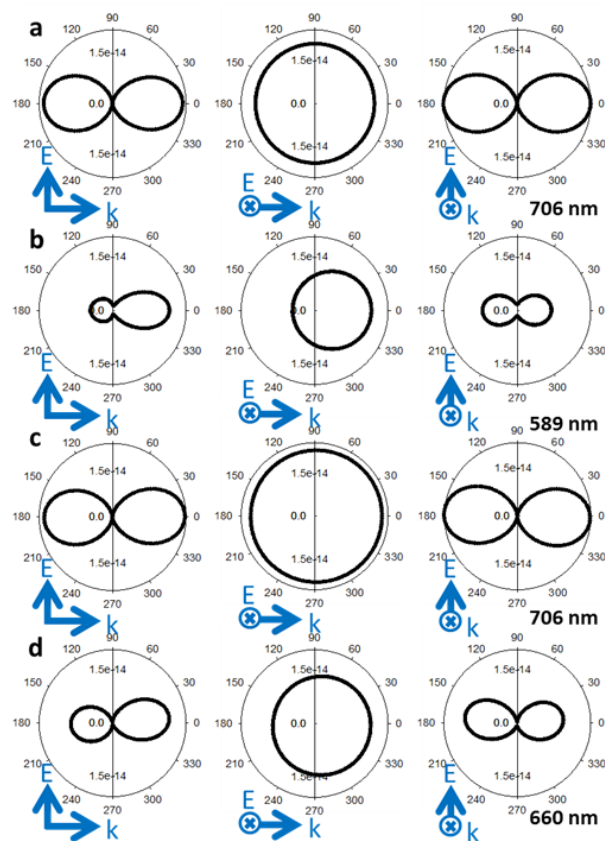


Figure 5.10: Projections of the scattered field into the far field from the FDTD simulations. Each projection is set on a plane (either yz , xy , or xz from left to right). Polarization is oriented along z and propagation along y . a, The far field scattering of the ordered particle at the dipole wavelength (706 nm). b, The far field scattering of the ordered particle at the yz quadrupole wavelength (589 nm), which is also the peak field enhancement position. c, The far field scattering of the disordered particle at the dipole wavelength (706 nm). d, The far field scattering of the disordered particle at the zz quadrupole wavelength (660 nm), which is also the peak field enhancement position. In each plot, arrows indicate the directions of propagation and polarization of the incident wave. Small mismatches in the wavelength of the quadrupole and dipole listed here to the above sample frequencies are due to simulation frequency discretization. The asymmetry in b and d is due to forward scattering of the dipole at those wavelengths. Reprinted with permission from Simon P. Hastings, Pattanawit Swanglap, Zhaoxia Qian, Ying Fang, So-Jung Park, Stephan Link, Nader Engheta, and Zahra Fakhraai. Quadrupole-Enhanced Raman Scattering. *ACS Nano*. 2014 8 (9), 9025-9034. Copyright 2014 American Chemical Society.

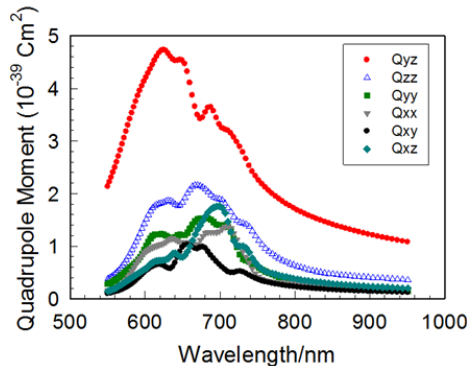


Figure 5.11: Average quadrupole moment strength of ten modeled disordered spiky nanoshells. All 6 non-redundant quadrupole moments are shown for the set of the ten medium sized disordered models. The yz quadrupole, shown in the main text, is strongest as is expected given that it is capable of coupling to the incident wave without even for the smooth structure. The zz quadrupole, also shown in the main text, is the second strongest. This is likely due to the ease with which a small shape perturbation in along the e-field axis can induce this mode. All other modes are smaller and approximately equal. Reprinted with permission from Simon P. Hastings, Pattanawit Swanglap, Zhaoxia Qian, Ying Fang, So-Jung Park, Stephan Link, Nader Engheta, and Zahra Fakhraei. Quadrupole-Enhanced Raman Scattering. *ACS Nano*. 2014 8 (9), 9025-9034. Copyright 2014 American Chemical Society.

The electric field intensity and the corresponding near-field enhancement factors (based on Eq. 5.3.2) can be directly calculated using the results of the FDTD simulations. To perform these calculations, the electric field intensity and the enhancement factors were integrated inside a shell of thickness 2.1 nm around the surface of each nanostructure (see Supporting Information for more details). Figure 5.12a shows that the incoming electric field intensity is most strongly enhanced at the Q_{yz} resonance in the ordered nanoshell, and at the Q_{zz} resonance in the disordered nanoshell. In contrast, for the smooth nanoshell the maximum intensity occurs at the dipole resonance. The Raman enhancement factors (Figures 5.12b, 5.13 and 5.7), as determined based on Eq. 5.3.2, are stronger and broader in the disordered structure compared to those of the ordered structure and the smooth nanoshell. Additionally, unlike the smooth

nanoshell, in both ordered and disordered nanoshells the Raman enhancement factor is dominated by the quadrupole resonance rather than the dipole resonance. Furthermore, the maximum enhancement factors are at least 2 orders of magnitude higher than the enhancement factor in the smooth nanoshell. It is important to note that the real experimental enhancement factors may be even larger than these calculations because the real nanoshells have more sharp points, fine edges, long spikes, and other small-scale structures than the modeled particles, which would most likely further increase the QERS signal (see the Supporting Information for more details).

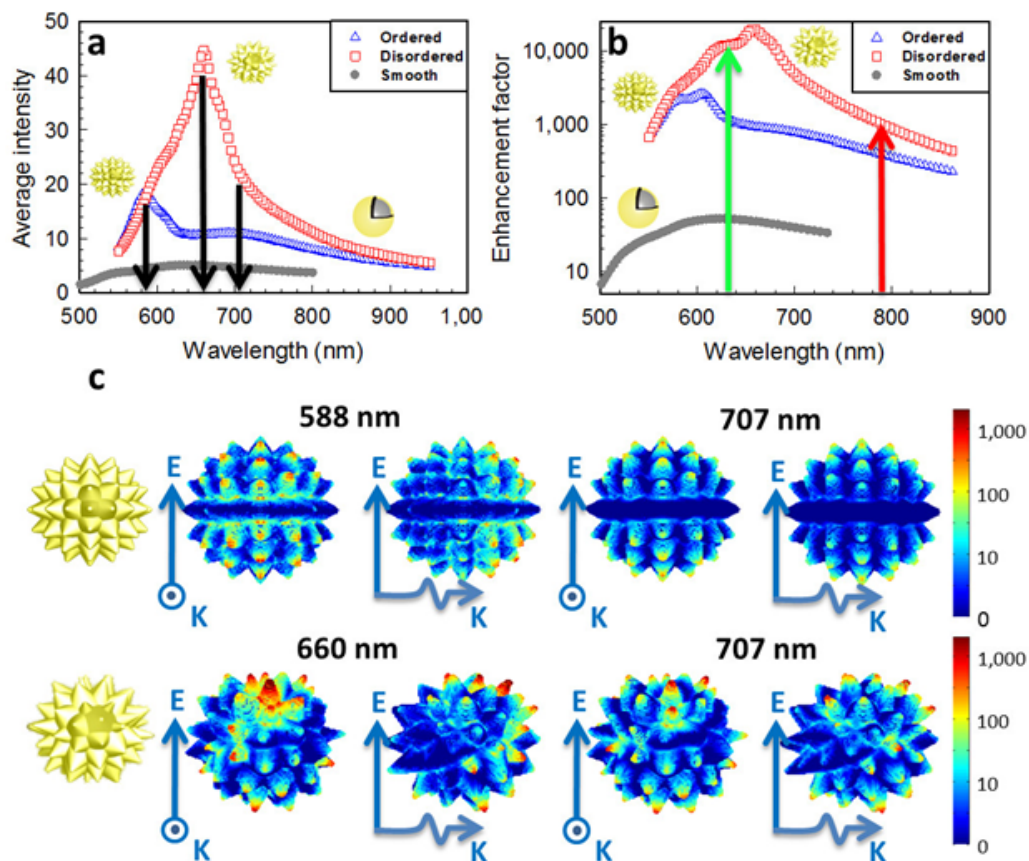


Figure 5.12: Simulated near-field enhancement of spiky nanoshells. (a) Integrated electric field intensity in a volume within 2.1 nm of the surface of the ordered (blue), the disordered (red), and the smooth nanoshells (gray), normalized to a unit incident electric field. (b) Raman enhancement factors calculated for the 1077 cm^{-1} Stokes line based on the near-field intensities. The green and red arrows show the laser excitation wavelengths. (c) Electric field intensity maps (log scale) of the ordered (top row) and disordered (bottom row) nanoshells. These maps were generated at the wavelength of the peak average intensity for each structure, 588 nm for the ordered nanoshell, and 660 nm for the disordered nanoshell and the dipole peak at 707 nm. Black arrows in a show the three wavelengths at which these plots are generated. Note that disorder delocalizes the hotspots. Reprinted with permission from Simon P. Hastings, Pattanawit Swanglap, Zhaoxia Qian, Ying Fang, So-Jung Park, Stephan Link, Nader Engheta, and Zahra Fakhraei. Quadrupole-Enhanced Raman Scattering. *ACS Nano*. 2014 8 (9), 9025-9034. Copyright 2014 American Chemical Society.

Figure 5.7 shows similar results for 10 different randomized structures and shows that the choice of the particular randomization does not affect these conclusions. Furthermore, this figure shows that while the addition of disorder significantly affects the detailed structure of the quadrupole resonances, the collective effect of all these resonances lead to an emerging enhancement factor with significantly smaller variations. Based on these calculations, the Raman enhancement due to near-field enhancement at 633 nm (green arrow in Figure 5.12b) is a factor of 11.2 larger than the Raman enhancement at 785 nm (red arrow in Figure 5.12b) for the disordered particle shown in Figure 5.12b. The average ratio of enhancement is 6.8 for the ensemble of particles shown in Figure 5.7b. It is necessary to also consider the λ^{-4} wavelength dependence of the Raman cross section [6], which contributes an additional factor of 2.5 to the total relative enhancement between the two excitation wavelengths. The combined relative enhancement factor is on average 17.0, which is in strong agreement with the experimental results of an average enhancement of 17.5 shown in Figure 5.4. Figure 5.14 shows the total relative enhancement factor, normalized to the Stokes shift at 633 nm enhancement, factoring in both the wavelength dependence and the near-field enhancement factors for the same structures as the one shown in Figure 5.12b. This result indicates that the strong and uniform Raman signal from spiky nanoshells is predominantly due to the QERS enhancement at 633 nm. Additionally, the variations of the signal at 633 nm are 15% smaller than those at 785 nm, which is also consistent with the experimental observations of QERS enhancement in single nanoshells as shown in Figure 5.4.

To understand the origin of the broad, heterogeneous spectral features, we examined the spatial distribution of the electric field intensity. Figure 5.12c presents electric field intensity maps at various wavelengths for both models (additional field

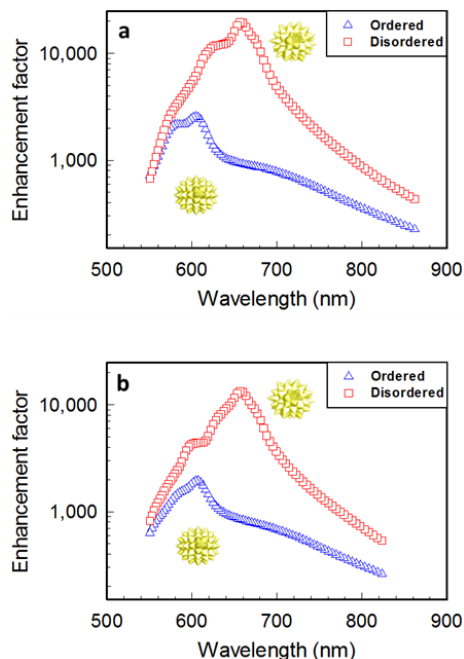


Figure 5.13: Enhancement factors for the ordered, blue, and disordered, red, models. These were calculated by integrating $I_{Exc} I_{Stokes}$ on a thin shell (2.1 nm thick) surrounding each particle, with appropriate wavelength shift for the excited line and a unit incident field. a, The enhancement factor calculated for the 1077 cm^{-1} line for both disordered and ordered models. b, The enhancement factor calculated for the 1585 cm^{-1} line for both disordered and ordered models. Reprinted with permission from Simon P. Hastings, Pattanawit Swanglap, Zhaoxia Qian, Ying Fang, So-Jung Park, Stephan Link, Nader Engheta, and Zahra Fakhraai. Quadrupole-Enhanced Raman Scattering. *ACS Nano*. 2014 8 (9), 9025-9034. Copyright 2014 American Chemical Society.

intensity maps for both structures can be found in Figure 5.15). These calculations show that the electric field intensity is mostly localized at the tip of the spikes and is spatially coupled with the strongest multipole resonance at a given frequency. They also show that the electric field at the tip of the spikes is stronger at the quadrupole resonance of each structure compared to the dipole resonance, explaining the effective increase in the Raman enhancement factors at the quadrupole resonance (Figure 5.12b). Furthermore, they reveal that the added heterogeneity in the disordered

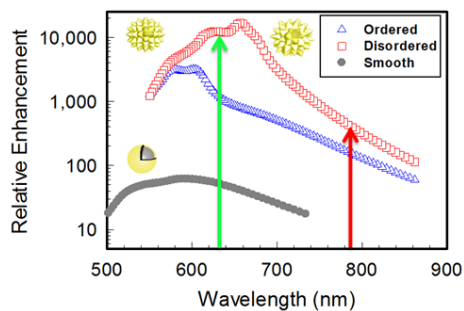


Figure 5.14: Relative Raman enhancement factors including both the near-field contribution to the enhancement, based on calculated near-field intensities (Figure 5.12), and the wavelength dependence of Raman scattering cross section, calculated for the 1077 cm^{-1} Stokes line. The relative contribution of Raman scattering cross section was calculated based on $(\lambda_{0,Stokes}^4/\lambda_{Stokes}^4)$ [6], where $\lambda_{0,Stokes}$ is the Stokes shift for the 633 nm excitation as a reference wavelength. The green and red arrows show the laser excitation wavelengths. Reprinted with permission from Simon P. Hastings, Pattanawit Swanglap, Zhaoxia Qian, Ying Fang, So-Jung Park, Stephan Link, Nader Engheta, and Zahra Fakhraei. Quadrupole-Enhanced Raman Scattering. *ACS Nano*. 2014 8 (9), 9025-9034. Copyright 2014 American Chemical Society.

structure spatially delocalizes the field by exciting spikes in previously dark places with stronger intensities than are present in the ordered structure. This is crucial in uniform QERS enhancement observed on a single particle level, because it shows that the specific position and orientation of the analyte is not crucial in coupling with a randomly oriented hotspot. This is in strong contrast with most hotspot based nanostructures, where the direction of detection and the position and orientation of the particle can have a strong influence on the SERS enhancement and specific gap size and shape.

To demonstrate that the hotspots observed in Figure 5.12c are the result of the quadrupole resonance and not any higher order resonances, spherical harmonic components, which can be directly related to the multipole modes, were calculated on the surface of a sphere just outside of the model nanoshell (more details in Supporting

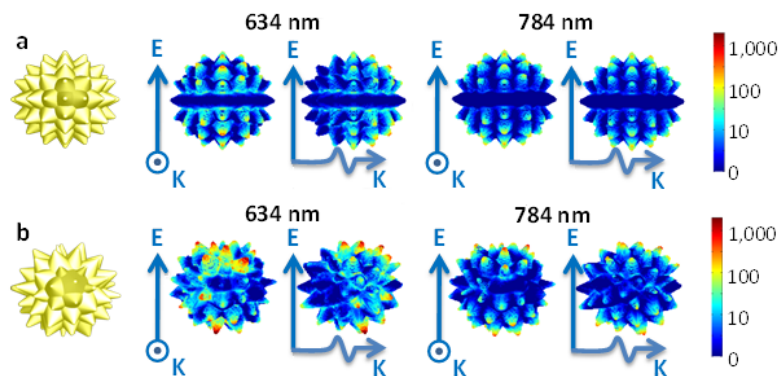


Figure 5.15: Average electric intensity (log scale) at the two Raman excitation frequencies 634 nm on the left and 784 nm on the right. The structures are viewed from two perspectives - one looking back at the source, and one in line with the source magnetic field. The intensities are determined by projecting the intensities in the thin shell used for calculating the enhancement factor onto the metal surface. For both models the quadrupole pattern is still seen at 634 nm compared to the dipole pattern at 784 nm, with correspondingly greater intensities. Additionally the disordered particle enhancement is substantially stronger than the ordered particle. Small mismatches in the wavelength of laser excitation to the above sample frequencies are due to simulation frequency discretization. a, Electric field intensity for the ordered structure at the Raman laser wavelengths. b, Electric field intensity for the disordered structure at the Raman laser wavelengths. Reprinted with permission from Simon P. Hastings, Pattanawit Swanglap, Zhaoxia Qian, Ying Fang, So-Jung Park, Stephan Link, Nader Engheta, and Zahra Fakhraei. Quadrupole-Enhanced Raman Scattering. *ACS Nano*. 2014 8 (9), 9025-9034. Copyright 2014 American Chemical Society.

Information). Calculations of the higher order harmonics in Figure 5.16 show that although these higher-order harmonics contribute to the overall near-field intensity, these contributions are significantly smaller than the first two harmonics, the dipole and the quadrupole. The small intensity observed in higher-order harmonics are largely the result of hotspots locally modulating the electric-field, as shown in Figures 5.12c, 5.15 and 5.17. The higher-order harmonics also do not present any new resonances in these model nanoshells providing strong evidence that the dipole and quadrupole resonances dominate the near-field features of the electric field intensity.

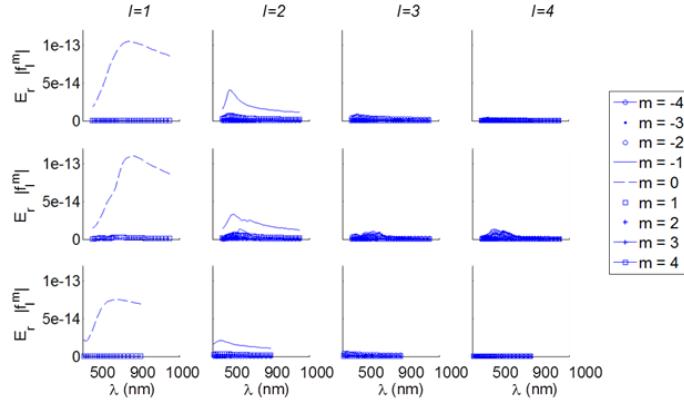


Figure 5.16: Modulus of the f_l^m components for the first four spherical harmonics of the radial component of the electric field in each shell. The top, middle and bottom rows are the ordered, disordered and smooth shells respectively. The radial component of the electric field is measured on the surface of a mathematical sphere with radius $r = 115$ nm. All m components are shown simultaneously for each l . As expected, at this distance the dipole-like terms ($l = 1$) are strongest over all, but the quadrupole-like mode ($l = 2$) comes second and dominates all subsequent modes. Reprinted with permission from Simon P. Hastings, Pattanawit Swanglap, Zhaoxia Qian, Ying Fang, So-Jung Park, Stephan Link, Nader Engheta, and Zahra Fakhraei. Quadrupole-Enhanced Raman Scattering. *ACS Nano*. 2014 8 (9), 9025-9034. Copyright 2014 American Chemical Society.

We can demonstrate the effect of the quadrupole in the exceptional enhancement of the electric field using a simplified model of the spiky nanoshell, as described in an earlier publication [107]. In this structure the spikes were only placed on a planar geometry as shown in Figure 5.18. In this model, it is possible to turn the far-field coupling to the quadrupole mode on and off by switching the propagation direction of light with respect to the plane of the spikes, while the dipole moment remains exactly the same in both orientations. Figure 5.18d shows an increased enhancement due to the quadrupole mode with no corresponding change to the far-field scattering spectrum of the particle. Additionally, Figure 5.18f shows that the high near-fields present at the spike tips are due to the coupling of the quadrupole resonance with the electric field at the tip of the spikes, and do not represent a separate electromag-

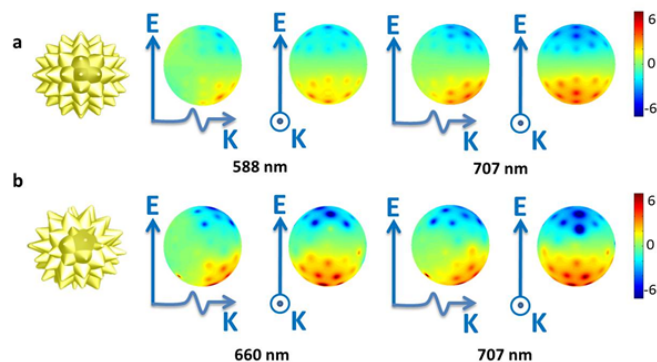


Figure 5.17: Projections of the real part of the radial component of the electric field surrounding the models onto a mathematical sphere of radius 115 nm. Note that at this distance (about 2 nm from the largest disordered models spikes, 9 nm from the ordered particles spikes) the dipole has already over-whelmed the quadrupole due to its slower fall off with distance. a, Electric field intensity on a mathematical sphere surrounding the ordered particle. b, Electric field intensity on a mathematical sphere surrounding the disordered particle. Reprinted with permission from Simon P. Hastings, Pattanawit Swanglap, Zhaoxia Qian, Ying Fang, So-Jung Park, Stephan Link, Nader Engheta, and Zahra Fakhraei. Quadrupole-Enhanced Raman Scattering. *ACS Nano*. 2014 8 (9), 9025-9034. Copyright 2014 American Chemical Society.

netic resonance. This coupling of a core mode to a tip-mode has been theoretically predicted in the gold nanostar system [35].

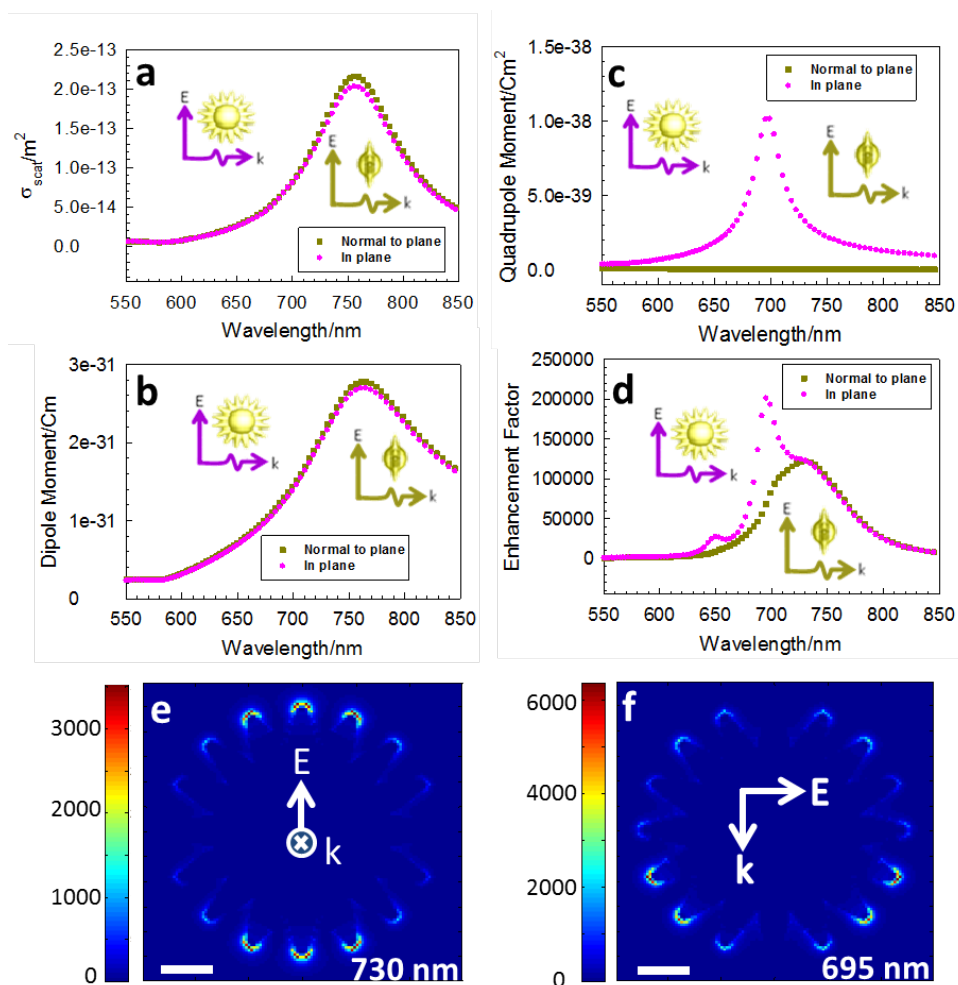


Figure 5.18: A simplified model of spikes only placed on a donut-like pattern to illustrate the importance of quadrupole in QERS. A core shell structure (inner radius 28 nm, outer radius 48 nm) with 16 cones (tip radius 4 nm, length 56.6 nm, and cone angle 30.4 degrees) is illuminated from two directions: k vector in plane (pink circles), and k vector perpendicular to the cone plane (yellow squares). a, Scattering cross section for the two structures. b, calculated dipole moments for the two incident angles. c, The corresponding strongest quadrupole moments for each orientation of the incident wave (Q_{xz} for incident normal to the plane of the nanoshell and Q_{xy} for the in-plane incidence). d, The QERS enhancement factor at 1077 cm^{-1} . e, electric field intensity at 730 nm (peak enhancement) for the incident angle normal to the plane of the nanoshell. f, Electric field intensity at 695 nm (peak enhancement) for the in-plane incident. The scale bars are 50 nm wide and the inset vectors indicate the polarization and propagation directions. Reprinted with permission from Simon P. Hastings, Pattanawit Swanglap, Zhaoxia Qian, Ying Fang, So-Jung Park, Stephan Link, Nader Engheta, and Zahra Fakhraei. Quadrupole-Enhanced Raman Scattering. *ACS Nano*. 2014 8 (9), 9025-9034. Copyright 2014 American Chemical Society.

As shown in our previous work [107], the synthesis applied to produce spiky nanoshells allows production of highly tunable surface morphologies with tunable far-field scattering cross sections. This tunability can be expanded to the QERS cross section. Figure 5.19a shows three model structures based on experimentally relevant values of the spiky nanoshells as reported in our previous publication [107], with randomness added in the spike parameters to enhance the QERS effect as explained above. To explore tunability without undue bias a set of 10 simulations with randomized parameters were performed for each of these three structures (Structural details can be found in the Supporting Information. The medium size structure is the same as presented in Figures 5.7 and 5.11) [107]. As shown in Figure 5.19b, the far-field scattering peak in air can be tuned over a range of about 200 nm, with the cross section moderately increasing with the overall size of the particle. Figure 5.19c shows that as the spike length, number, and aspect ratio are increased, the quadrupole moments increase in both strength and breadth. Consistent with our discussions above, larger quadrupole moments result in increased enhancement factors at 1077 cm^{-1} as shown in Figure 5.19d. Individual data for the scattering, enhancement, and quadrupole moments are shown in Figure 5.7 for the medium-sized structure. Figure 5.11 shows the average of all 6 quadrupole moments, including the weaker $Q_{\alpha\beta}$ modes for the medium-sized structure. These simulations suggest that the optimum QERS cross section can be tailored for particular applications. The combination of tunability with the reproducibility of the QERS enhancement can be extremely useful in biological and sensing applications.

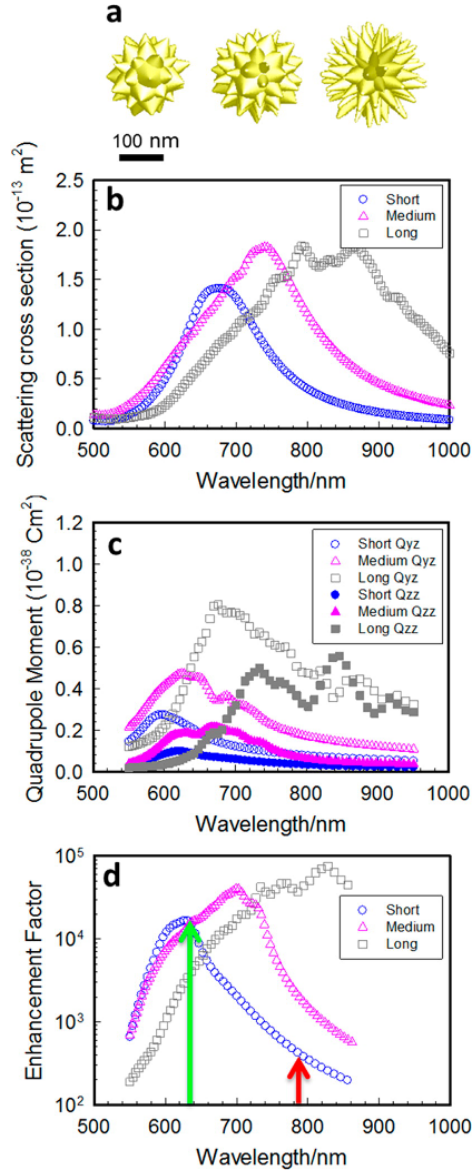


Figure 5.19: Ensemble-averaged behavior of three families of nanoshells, based on experimentally accessible structures. (a) Representative shapes of three synthesizable nanoshells produced based on our previous work [107] produced by randomizing the spike parameters (see Supporting Information for details). (b) Average far-field scattering cross section of 10 different realization of each structure. (c) Average Q_{yz} and Q_{zz} quadrupoles for each structure. (d) The average enhancement factor at 1077 cm^{-1} . Reprinted with permission from Simon P. Hastings, Pattanawit Swanglap, Zhaoxia Qian, Ying Fang, So-Jung Park, Stephan Link, Nader Engheta, and Zahra Fakhraei. Quadrupole-Enhanced Raman Scattering. *ACS Nano*. 2014 8 (9), 9025-9034. Copyright 2014 American Chemical Society.

5.3.4 Conclusion

These calculations show that heterogeneous substructure in disordered nanoshells is essential to the generation of strong dark quadrupole resonances that are both spectrally and spatially broad. The spectral breadth of the quadrupole resonances allows for effective coupling to both the excitation and the Stokes scattering modes, which results in increased QERS enhancement. Despite the large variations of the value of individual quadrupole moments of disordered nanoshells, the broadening of multiple quadrupoles lead to the emergence of highly reliable Raman enhancement in these nanoshells. This emerging property from added disorder is novel and merits further investigation in other nanoparticle systems. These results show that spiky nanoshells do not need to be perfectly ordered, or sized to be efficient QERS enhancers. In fact, as long as a continuous shell is maintained [108, 107], the added disorder increases the Raman scattering cross section. Furthermore, the disorder-induced spatial breadth allows omnidirectional sensing and effective coupling of many Raman analytes to the local electric field, which is critical in achieving a uniform Raman signal on a single nanoshell level. This differs from most designed dark plasmonic structures, which need to be precisely configured to achieve high enhancement factors [13], providing a new paradigm for materials design.

5.3.5 Acknowledgments

S.P.H and Z.F. greatly acknowledge Prof. H. Giessens helpful discussions and C. Lis contribution to the discussions. This work was supported by the startup funds from the University of Pennsylvania (for Z.F) and partial support from the MRSEC program of the National Science Foundation under award no. DMR-11-20901 at the University of Pennsylvania. S.L. thanks the Robert A. Welch Foundation (Grant C-1664), ACS-PRF (50191-DNI6) and NSF (CHE-0955286) for financial support of this work. N.E. acknowledges partial support from the US Air Force Office of Scientific Research (AFOSR) Grant number FA9550-10-1-0408. P.S. acknowledges support from the Royal Thai Government. S.-J.P. acknowledges the support from the Dreyfus teacher scholar award program.

5.3.6 Methods

Spiky nanoshells were synthesized using a recently reported procedure [106, 108, 107]. The structure of the nanoshells is shown in Figure 5.1a. Synthesized nanoshells were placed on a transparent substrate at a concentration suitable for single particle Raman and backscattering measurements. 4-Mercaptobenzoic acid (Figure 5.1b) was immobilized on the nanoshells as the Raman analyte. A total of 71 individual spiky nanoshells were investigated using an inverted microscope geometry as illustrated in Figure 5.1c [115]. After all optical measurements, the samples were imaged by SEM (Figure 5.1e) and compared with backscattering images (Figure 5.1d) to ensure that only single particle data was included in the analysis. A brief description of the synthesis, sample preparation, single particle backscattering and Raman experiments can be found in the Supporting Information.

Using transmission electron microscopy and scanning electron microscopy (Figure

5.1a) images of spiky nanoshells, two model nanoshells were generated for Finite-Difference Time Domain (FDTD) simulations, as described in our previous publications. The added disorder increases the Raman scattering cross section. Furthermore, the disorder-induced spatial breadth allows omnidirectional scattering. FDTD simulations were performed using Lumerical Solutions, Inc.'s FDTD Solutions software package (versions 8.6 and 8.7). On the basis of experimental variables, two representative structures were modeled (Figure 5.5a): an ordered nanoshell, with identical spikes placed symmetrically; and a disordered nanoshell, with randomized spike positions, sizes and shapes. The height, cone angle, and tip diameter of all of the spikes are identical in the ordered model and are 58 nm, 60 degrees, and 10 nm, respectively. For the short models, 40 spikes with lengths between 38 and 53 nm, cone angles between 45 and 85 degrees and tips between 2 and 6 nm were used. The disordered model and the medium models were as described above: 60 spikes with randomly chosen spike heights between 50 and 65 nm, tip radii between 2 and 6 nm and cone angles of 30 and 75 degrees. The long models were chosen to have 80 spikes with length 58 to 73 nm, cone angle 15 to 45 degrees, and tips between 2 and 6 nm in radius. All models have the same 95 nm core size. The parameters for these models were chosen to be consistent with the experimental data. The smooth shell was modeled as gold on polystyrene with inner and outer diameters of 98 nm and 172 nm, respectively. This produces a gold volume in the smooth shell equal to that in the disordered model. Further simulation details can be found in the Supporting Information.

5.4 Supporting Information

5.4.1 Particle Synthesis and Nanoparticle Characterization

The spiky nanoshells were synthesized by a templated surfactant-assisted seed growth method following our recently published procedure [106, 108, 107]. The seed-decorated polymer beads were prepared by sodium borohydride reduction of silver ions pre-absorbed onto the negatively charged polymer template. The growth solution was prepared by mixing 10 mL of 0.1 M CTAB, 421 μL of 0.01 M HAuCl_4 , 64 μL of 0.01 M AgNO_3 and 67 μL of 0.1 M ascorbic acid sequentially. The 20 μL of the seed-decorated bead solution was then added to the above growth solution followed by a gentle mixing for a few seconds. The spiky nanoshells were washed twice for characterization by centrifugation after 2 hours of reaction. A JEOL 1400 instrument operating at 120 kV accelerating voltage was used to record the transmission electron microscopy (TEM) images. A Quanta 600 FEG Mark II instrument at 15 kV accelerating voltage was used to record the scanning electron microscope (SEM) images. An Agilent 8453 UV-visible spectrophotometer was used to measure the extinction spectra of an aqueous solution of nanoshells.

5.4.2 Sample Preparation for Correlated Single Particle

Optical and Electron Microscopy Studies

The sample preparation for the correlated optical (surface enhanced Raman scattering (SERS) and dark-field spectroscopy) and scanning electron microscopy (SEM) characterization of individual spiky nanoshells involved first the drop-casting of an appropriately diluted colloidal solution of spiky nanoshells on cleaned glass coverslips on which an indexed gold pattern had been evaporated. The glass coverslips with the

spiky nanoshells were immersed in a solution of 4-mercaptobenzoic acid (0.0002 g/ml) over night and then rinsed with ethanol and dried under a flow of nitrogen. Samples were characterized by optical methods within one day of preparation. A total of 71 individual spiky nanoshells were investigated from three independently prepared samples from the same batch of colloidal spiky nanoshells by first measuring SERS spectra, then dark-field scattering spectra, and finally SEM images to confirm that only single nanoshells were included in the analysis. SEM was carried out last to avoid sample damage by the electron beam.

5.4.3 Single Particle Optical Studies

SERS and dark-field spectroscopy measurements were performed using a home-built microscope setup by directing two lasers, a 633 nm He-Ne laser (JSD Uniphase) and a 785 nm diode laser (Power Technology) into the microscope and focusing them to spot sizes of 600 nm and 500 nm (FWHM), respectively. These spot sizes were determined from image of fluorescent dye beads at 633 nm and images of gold nanorods at 785 nm, where in the latter case laser scattering was used as the signal in the sample scanned image. A 50X/0.8 objective (Zeiss Epiplan Neofluar) was used to focus the lasers at the sample with powers measured after the objective of 8 W and 17 W for 633 nm and 785 nm, respectively. The back-reflected SERS scattering was collected by the same objective and directed to a CCD camera (Princeton Instruments PIXIS 400BR) connected to a spectrograph (Princeton Instruments Acton SP2150i) after passing through appropriate notch filters and 645 nm and 800 nm long pass filters for 633 nm and 785 nm excitation, respectively. Typically, SERS measurements with 785 nm excitation were carried out first.

Dark-field scattering spectra were obtained after the SERS measurements using

an integration time of 2 seconds and a grating with 150 grooves/mm centered at 800 nm. To avoid second-order reflections, a 515 nm long-pass filter was added to the detection path. Single particle scattering spectra were corrected by subtracting background and dark counts as well as taking the spectral response of the lamp and other optical components into account using a white light reflectivity standard (Labsphere SRS-99-010).

The reported SERS intensities were calculated using the following procedure: First, the SERS peaks for all spectra were each fitted to Lorentzian functions to remove the background signal and to obtain the amplitudes of only the peaks. These amplitudes were then corrected for the CCD camera sensitivity, laser powers, and spot sizes for both excitation wavelengths according to:

$$I_{sers} = \frac{A}{C \times P \times \pi R^2} \quad (5.4.1)$$

In this equation I_{SERS} is the corrected SERS intensity as reported in Figure 5.4 and Figure 5.2, A is the background-corrected amplitude of the SERS peaks as obtained from the Lorentzian fits, C is a correction factor accounting for the sensitivity of the CCD camera, P is the laser power incident at the sample, and R is a spot size (FWHM) of the excitation beam. P and R were evaluated at the two excitation wavelengths of 633 nm and 785 nm. The correction factor C was obtained by collecting a bright-field spectrum on the same microscope using a calibration lamp (LS-1-CAL, Ocean Optics) with a known spectral output. C values were calculated for each excitation wavelength at the two SERS peaks at 1077 cm^{-1} and 1585 cm^{-1} .

5.4.4 Finite-Difference Time-Domain (FDTD) Simulations

FDTD simulations were performed using the Lumerical Solutions Inc. FDTD Solutions package (versions 8.6 and 8.7). As in previous work [108, 107], simulations were performed by placing rounded cones on a polystyrene core with a diameter of about 95 nm. The core is slightly expanded in order to fill in small gaps in the interface between gold and polystyrene. These gaps did not affect the results of the simulation. Spiky nanoshells were simulated in dielectrics modeling air ($n=1$) and water ($n=1.333$).

The geometry of the spiky shell was estimated by examining TEM and SEM images of the particles. We note that using this approach we are not able to extract a true cross-sectional image of the particle, but rather we can extract the perimeter of the projection of the particles. There are potential errors associated with estimating the parameters this way. For example, the lowest valley of a particle may be obscured by a spike closer to the viewer than the valley, and large spikes will obscure small ones, making an estimate of the distribution of spike heights very difficult. As a result, an exact duplication isn't possible.

We can, however, produce useful bounds on the typical spike size. Our analysis method provides that the average radius of the particles is less than 105.6 nm. With a core diameter of about 95 nm, the shell thickness should then be on average less than 58.1 nm. Likewise, the average largest spike on the particles examined is estimated to be 82 nm, and among the sampled particles the smallest observed largest spike on a single particle is 68 nm. This does not mean that a typical spike is 68 nm, but rather that a typical spike should be less than 68 nm. The lowest valley typically has an upper bound of 39 nm. Experimentally we estimate that there is about 2.99×10^6 nm³ gold in a typical shell.

It is clear from this that there are large outliers in the shape, and that it will be very difficult to produce a completely accurate shape. Since not all spiky nanoparticles contained large outlier spikes, and the results of the Raman scattering were very consistent, we believe that the largest outlier spikes are not dominant in the behavior of the particles. We therefore kept our variation below this level in order to make the modeling simpler. With that in mind, we sought to produce a model which qualitatively captured the behavior of the system, with a reasonable volume of gold. Sharp features are also most likely underestimated as they are numerically difficult to simulate and the spikes were rounded in order to remove artificially sharp points. Within these constraints, our models were selected to reproduce the far field scattering and extinction behavior observed on average from the particles in both air and water.

The ordered structure was constructed by hand in order to have a desirable level of symmetry for ease of computational analysis. The ordered particle was modeled as 66 spikes with a 58 nm height, a 5 nm tip radius and a 60 nm cone angle. This shape occupies $2.04 \times 10^6 \text{ nm}^3$ gold, making it a bit smaller than a typical experimental shell, but still in reasonable agreement. The difference in gold volume is partially due to the decision not to model the large outlier spikes. Given the high level of reproducibility in experimental results, the models should still capture all of the behavior of the spiky nanoshells.

To produce the disordered structure we used a force algorithm [15], where the cone locations were evenly distributed on the surface of the core by a r^{-2} repulsion force. This repulsion force results in asymmetric but evenly placed seed positions once the seeds reach equilibrium. Additionally, variations in the cone parameters were introduced to the disordered model. The disordered particle was modeled as 60 spikes with randomly chosen spike heights between 50-65 nm, tip radii between 2-6

nm and cone angles of 30-75 degrees. All random distributions were uniform on the range described. While this model more closely represents the experimental variations in the nanoshell shape and size, we expect our predictions of the field enhancement to be lower than the experimental field enhancement due to lack of sharp corners, edges, and defects that are present in the real nanoshells. This shape occupies $2.14 \times 10^6 \text{ nm}^3$ gold, making it 27% smaller than a typical experimental shell, but still in reasonable agreement given the choice to not include large outlier spikes in the model. Using the same amount of gold, the smooth shell was modeled as gold on polystyrene with an inner diameter of 98 nm and a resulting outer diameter of 172 nm respectively. The slightly different core diameter is due to the gold cones in the ordered and disordered model occupying the outer few nanometers of the core, thereby replacing it with gold. This was done to prevent any pockets of air from potentially influencing the simulation.

In order to validate the models, calculated backscattering spectra in air (background $n=1$) (Figure 5.5b) was compared to the experimental dark field spectrum and the calculated extinction cross section with $n=1.333$ was compared to the experimentally measured extinction in aqueous conditions (Figure 5.6). Both of these are seen to be a reasonable match. Additionally, studies found that the addition of a dielectric substrate near the particle had little effect on the scattering, and as a result the glass slide used during experimental measurements was not necessary to model. From those studies, the substrate would have at most resulted in a very small red shift. We conclude from their matching the average spectrum in Figure 5.6 and Figure 5.5b, and from the spread of the distribution of the LSPR in Figure 5.4, that these models represent typical particles in the experimental spectrum. In the course of these studies, several randomized versions of the disordered particle were produced

as discussed below, and although the exact spectrum differed the resulting conclusions were shared: the yz and zz quadrupoles result in spectrally broad and strong QERS, with similar ratios of Raman signal at 633 nm and 785 nm excitation.

The additional families of disordered structures were produced using previously reported parameters [107] for spikes as the mid points for randomization. Each data set was produced by generating new spike positions and re-randomizing the spike parameters ten times. Breadth was set to be approximately consistent with the breadth chosen for the original disordered model. For the short models, 40 spikes with lengths between 38 and 53 nm, cone angles between 45 and 85 degrees and tips between 2 and 6 nm were used. The medium models was as described above: 60 spikes with randomly chosen spike heights between 50-65 nm, tip radii between 2-6 nm and cone angles of 30-75 degrees. The long models were chosen to have 80 spikes with length 58 to 73 nm, cone angle 15 to 45 degrees, and tips between 2 and 6 nm in radius.

The electric field was monitored during the simulations and used to measure the near field parameters including both electric field enhancement and polarization current. To estimate enhancement the index of refraction at each point in space was sampled and an isosurface of refractive index produced surrounding the gold. The distance from that surface to every field sample was then computed, and anything outside of the surface and less than 2.1 nm from that surface was included as a sample point. The sample points have then formed a thin shell of 2.1 nm surrounding the nanoshell. Sample points were then multiplied in order to produce the appropriate enhancement (taking into account both enhancement frequency and Stokes frequency). Field maps as shown in Figure 5.12 were produced by projecting the thin shell used for integration onto the surface of the structure. In particular, each position on the

surface of the nanoshell, as determined by a Matlab isosurface, was assigned a field value by interpolation from the near field shell used earlier using a nearest neighbor method. For Figure 5.5b, and Figure 5.6, backscattering cross section refers specifically to the component of the electric field projected along k , *i.e.*, directly backwards. In contrast, the extinction, absorption, and regular scattering measurements include the field in all directions.

Mesh settings in Lumerical play an important role in the validity of these simulations. During simulation, mesh refinement was not used near the metal surface. Index assignment on the mesh introduces sharp artifacts along the edge of the metallic structure, but these most likely are still an underestimate of the true disorder of the structure and should not affect the validity of the simulation. The mesh spacing in the region around the particle (the override region in FDTD Solutions) was set to 2 nm, the shortest distance possible with our current computational constraints. This limits the near field measurement to a single layer of pixels surrounding the object. This will cause an underestimation in the field as the field drops strongly away from the metal surface, while in Raman experiments the analyte molecule is expected to be closer to the surface than this distance.

5.4.5 Scattering Mode Formalism

The induced Raman dipole moment of an analyte is given by [18]:

$$\mu_{\alpha} = \alpha_{\alpha\beta}E_{\beta} + \frac{1}{3}A_{\alpha\beta\gamma}E_{\beta\gamma} + \dots \tag{5.4.2}$$

where $\alpha_{\alpha\beta}$ and $A_{\alpha\beta\gamma}$ are the dipole and quadrupole polarizability tensors of the molecule, E_{β} is the electric field, and $E_{\beta\gamma}$ is the electric field gradient with respect to γ , where α , β , and γ denote the coordinates. Higher order terms and magnetic

coupling terms are assumed to be small and are dropped. In this work the localized electric field at the quadrupolar resonance of the nanoshell couples with the dipolar polarizability of the analyte as both observed Raman bands in the experiments are dipolar in nature. The local fields of the particle can be described as an expansion of the electric multipole moments about the origin. The magnetic dipole moment is small in this case, and higher-order multipoles decay sharply as shown in Figure 5.16, so we can only consider the contributions of the dipole and quadrupole field (labeled with subscripts p and Q):

$$E_{\beta} = E_{\beta,p} + E_{\beta,Q} \quad (5.4.3)$$

Combining these two expressions produces 4 terms:

$$\mu_{\alpha} = \alpha_{\alpha\beta}(E_{\beta,p} + E_{\beta,Q}) + \frac{1}{3}A_{\alpha\beta\gamma}(E_{\beta\gamma,p} + E_{\beta\gamma,Q}) + \dots \quad (5.4.4)$$

$$\mu_{\alpha} = \alpha_{\alpha\beta}E_{\beta,p} + \alpha_{\alpha\beta}E_{\beta,Q} + \frac{1}{3}A_{\alpha\beta\gamma}E_{\beta\gamma,p} + \frac{1}{3}A_{\alpha\beta\gamma}E_{\beta\gamma,Q} + \dots \quad (5.4.5)$$

Because the analyte used in these experiments does not have a quadrupolar vibrational mode at either of the two lines analyzed, we can discount the 3rd and 4th terms:

$$\mu_{\alpha} = \alpha_{\alpha\beta}E_{\beta,p} + \alpha_{\alpha\beta}E_{\beta,Q} \quad (5.4.6)$$

Thus, the Raman dipole is excited by the coupling of the nanoshells electric dipole and quadrupole to the analytes dipole. In practice the fundamental modes of the particle are only pure spherical multimodes in a spherically symmetric object, which is not the case for spiky nanoshells. The sharp tips of spikes locally perturb the

electric fields around them and enhance the field. This perturbation is large in the near-field, but decays rapidly in the far-field. However, as shown in Figure 5.18, the quadrupole and dipole modes still act as envelope functions for the spike excitation and are responsible for the field enhancement at those features. Figure 5.16 shows that the existence of these local perturbations does not result in additional resonance modes in these nanoparticles.

5.4.6 Spherical Harmonic Formalism

It is possible to express any function defined on a mathematical sphere as an expansion of the spherical harmonic functions which form an orthogonal complete basis. By expressing the spherical components of our electric field in three separate expansions we can assess the relative contributions of any given order of the expansion. By symmetry, all dipolar components of the electric field must be present only in the $l = 1$ terms of the spherical harmonics, while the quadrupole components are present only in the $l = 2$ terms and so on. While there is no direct one to one correspondence between each multipole mode with a given spherical harmonic mode, we can numerically determine which order moment dominates at a particular distance by looking at the corresponding spherical harmonic at that distance. We accomplish this as follows. For the radial component of the electric field we have:

$$E_r(r_0, \theta, \phi) = \sum_l \sum_m f_l^m Y_l^m(\theta, \phi) \quad (5.4.7)$$

And as a result we can find our coefficients by integrating over the normalized spherical harmonic conjugate:

$$f_l^m(r_0) = \int \int E_r(r_0, \theta, \phi) Y_l^{m*}(\theta, \phi) r_0^2 \sin(\theta) d\theta d\phi \quad (5.4.8)$$

We can then compare each set of terms, as the modulus squared of f_l^m is directly related to the electric field intensity. The absolute values for the ordered model, the disordered model, and a shell with equal gold to the disordered model are shown in Figure 5.16, for a sphere of radius nm (less than 5 nm outside the longest spike of the disordered structure). Similar expressions exist for the angular components of the electric field, but for the electric multipoles it is sufficient to calculate just the radial component [97]. It is important to note that one must include the imaginary components of the electric field and the sign of those components when calculating these coefficients. This can be clearly seen by looking at the field projections onto a sphere, as shown in Figure 5.17.

5.4.7 Calculations of the Scattering Cross section

Based on a vector spherical harmonic expansion similar to the one in the last section, Tsang *et al.* 2000 [123] provides a comprehensive set of equations to describe the scattering cross section, given the knowledge of a transfer matrix (T-matrix) for the particle:

$$\vec{a}_s = \mathbf{T}\vec{a}_i \quad (5.4.9)$$

Where the incident components of the incoming wave, a_i , are transformed by the matrix T (the “T-matrix”) to the outgoing scattered components, a_s . The T-matrix is purely diagonal if one can assume that no mode mixing can occur in the structure (this assumption will be explored in more detail in an upcoming paper). In this simplified case, the diagonal of the T-matrix is simply the ratio of the known incident components to the calculated projections, which can be inferred from the radial electric field components as described in the previous section. The results of

these calculations for the disordered particle are shown in Figure 5.9. One could also infer the scattering cross sections by using the scattered power of the dipole moment as shown below, divided by the intensity of the incident light [31]:

$$Power = \frac{\mu_0 |P|^2 \omega^4}{12\pi c} \quad (5.4.10)$$

However, as seen in Figure 5.20, such an approach results in a moderate over estimate of the dipole in the Lumerical FDTD package. This inconsistency between the currents and the cross section could be explained by an error of about 4% in the magnitude of the currents, calculated based on the electric field values reported by FDTD. We have not been able to identify the exact origin of this discrepancy, which only occurs in simulations of large nanoparticles. However we believe it may be the result of the discretization of the currents near metallic surfaces. Given the size of this discrepancy, this should not significantly affect the conclusions of this work, and from analysis of other particles we have determined that it affects all modes approximately equally, so it should not change any of the conclusions presented here. Nonetheless, we have chosen to present the field based analysis of the cross sections as it is directly self-consistent with the FDTD simulation results.

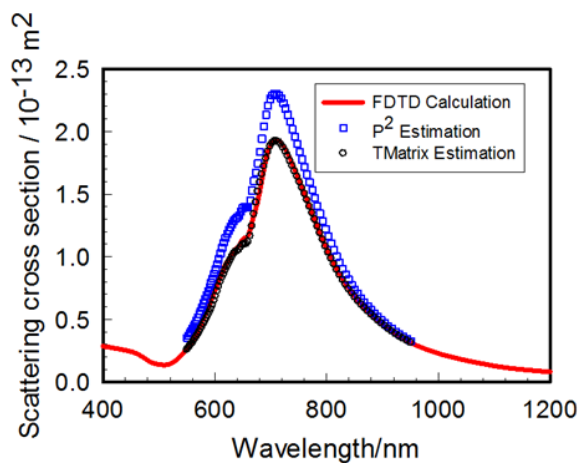


Figure 5.20: The dipole scattering cross section is estimated based on a standard scattering power formula in supplemental Eq. 5.4.10 (blue open squares) compared to the direct FDTD total scattering cross section provided by Lumerical (red line) and the T-matrix method estimate (black open circles) based on supplemental Eq. 5.4.9. Reprinted with permission from Simon P. Hastings, Pattanawit Swanglap, Zhaoxia Qian, Ying Fang, So-Jung Park, Stephan Link, Nader Engheta, and Zahra Fakhraei. Quadrupole-Enhanced Raman Scattering. *ACS Nano*. 2014 8 (9), 9025-9034. Copyright 2014 American Chemical Society.

Chapter 6

Nanoparticle Modal interference

6.1 Introduction

In the previous two chapters, the far-field has been assumed to be dominated by the electric dipole. In chapter 5, several things indicated that this was not necessarily the case. First, in the experimental measurements, a dip was observed in the scattering spectrum of some of the nanoparticles. Although this could be explained by two different dipole resonances, it could also indicate destructive interference. The FDTD models of disordered nanoshells reproduced this effect, opening up an avenue to explore this effect in principle. In the FDTD modeling, the quadrupole peaks were observed to sometimes peak when the dipole dipped. Additionally, all six quadrupole moments were activated, implying that mode mixing was occurring at some level (although it is not clear which modes are involved). Here, we present a novel method for calculating the T-matrix of an arbitrary particle using the FDTD method as input for a least squares fitting system. Unlike in other methods which are generally monochromatic, this allows the determination of the T-matrix at hundreds of frequencies simultaneously. With this method, the peaks in the far-field spectra are shown to

indeed be the result of quadrupole modes interfering with the dipole. As a necessary consequence of the symmetry of the T-matrix, this implies that the dipole must also be able to induce quadrupole modes, explaining the broadening and excitation of the six quadrupole moments.

6.2 Context

This work was performed in collaboration with a number of other researchers: the particle synthesis was performed by Zhaoxia Qian supervised by So-Jung Park, the dark field measurements were performed by Pattanawit Swanglap, supervised by Stephan Link. The author was responsible for the structural modeling, FDTD simulations, T-matrix algorithm development, and (collaboratively) writing the manuscript, supervised by Zahra Fakhraai and co-supervised by Nader Engheta.

6.3 Modal Interference in Spiky Nanoshells

Modal Interference in Spiky Nanoshells, Simon P. Hastings, Pattanawit Swanglap, Zhaoxia Qian, So-Jung Park, Stephan Link, Nader Engheta, and Zahra Fakhraai. Manuscript in preparation.

6.3.1 Abstract

Near-field enhancement of the electric field by metallic nanostructures is important in non-linear optical applications such as surface enhanced Raman scattering. One approach to producing strong localization of the electric field is to couple a dark, non-radiating plasmonic mode with a broad dipolar resonator that is detectable in the far-field. However, characterizing or predicting the degree of the coupling between

these modes for a complicated nanostructure is not always easy. Here we develop a method to solve the T-matrix, the matrix that predicts the scattered electric fields of the incident light, based on finite-difference time-domain (FDTD) simulations and least square fitting algorithms. This method allows us to simultaneously calculate the T-matrix for a broad spectral range. Using this method the coupling between the electric dipole and quadrupole modes of spiky nanoshells were evaluated. It is shown that the built-in disorder in the structure of these nanoshells allows for coupling between the dipole modes of various orientations as well as coupling between the dipole and quadrupole modes. A coupling strength of about 5% between these modes can explain the apparent interference features observed in the single particle scattering spectrum. This effect is experimentally verified by single particle backscattering measurements of spiky nanoshells. The modal interference in disordered spiky nanoshells can explain the origin of the spectrally broad quadrupole resonance which results in strong Quadrupole Enhanced Raman Scattering (QERS) in these nanoparticles.

6.3.2 Introduction

Plasmonic nanoparticles and nanostructures enable manipulation and enhancement of the electric field of light in the optical frequency range for applications such as surface enhanced Raman scattering [119], nanoscale imaging [111], biological detection [46, 104] and drug delivery applications [117]. The Localized Surface Plasmon Resonance (LSPR) usually refers to dipolar resonance of charge oscillations on a nanoparticle. Depending on the shape of the nanoparticle[87] or the nanostructure[43], higher order oscillations can also occur as either bright [125, 65] or dark modes [138] and can be in resonance with light in optical frequencies. While the excitation of the fundamental resonance modes are important in the above mentioned applications, recent

attention has been focused on the role of modal interferences in further enhancing the localization of the electric field [133]. Interference effects such as Fano-like resonances [72] can couple dark and bright resonances, and allow the far-field detection of dark modes [118, 86, 132].

Both constructive or destructive interference can occur if two oscillators overlap both spatially and spectrally [70]. This interference can affect localized electric fields and may have potential applications in index sensing [71, 62] and surface enhanced Raman spectroscopy (SERS) [135]. Destructive interference can result in reduced scattering cross sections and generate strongly localized electric fields in the gap between the oscillators [137], while constructive interference can result in super-radiant modes with enhanced scattering [118]. In spherically symmetric objects, such as gold nanoparticles and nanoshells, the multipole modes are orthogonal and interference can not be observed between any two modes in the total scattering cross section [76, 72]. In order to design modal interferences, asymmetry can be introduced in the design of the nanoparticle or the nanostructure. Examples include dipolar resonances that are shifted from the center of the object, in nanoclusters [26] or fanoshells [86], and structures that are not spherically symmetric such as nanorods [70], nanorice [71], and nanobelts [71].

In non-spherically symmetric nanoparticles, a generalized form of Mie theory called the T-matrix method [123, 129] can be used to estimate the coupling between multipole modes and their effects on both directional and total scattering cross sections. The main advantage of the T-matrix method is that, once determined, it allows rapid computation of scattering and extinction cross sections of a particle in any orientation. However, it is generally challenging to determine the T-matrix for complex shapes. In particular, shapes with sharp corners [55] and high aspect ratios [60] have

been shown to be numerically difficult to solve with surface integration methods such as the point matching [90] and Extended Boundary Condition (EBCM) methods [129]. Volume integration methods, including the discrete dipole approximation [73, 67] and the finite-difference frequency-domain method [68], have been modified to determine the T-matrix for more complex geometries. However, a separate calculation must be performed for each frequency of interest. Here, we have developed an algorithm which uses the finite-difference time-domain (FDTD) simulations to calculate the T-matrix simultaneously for a broad spectral range for complex structures. In this approach, the same particle is illuminated with a broadband plane-wave from many different directions. By decomposing the incident and scattered fields from each illumination into vector spherical harmonic wave functions [123], an over-determined equation for the T-matrix is produced. The most probable T-matrix is then calculated using the pseudo-inverse matrix based on the least square method.

Using this method, the T-matrix for a spiky nanoshell was calculated in order to investigate modal interference in these nanoparticles. These nanoshells are composed of numerous randomly sized sharp gold spikes that decorate the surface of a polystyrene core [106], and have tunable dipolar resonances in the visible and near-IR range [106, 108, 107]. It has been recently demonstrated that the disorder in these nanoshells generates spectrally and spatially broad dark quadrupole modes that enable highly efficient and reproducible Quadrupole Enhanced Raman Scattering(QERS) on a single particle level [38]. Single particle backscattering measurements of these nanoshells show interference patterns in the far-field scattering spectra [38]. Here, FDTD based T-matrix calculations allows us to investigate the origin of these interference patterns and its relationship to QERS enhancement. We show that both dipole-dipole and quadrupole-dipole (*i.e.*, incident quadrupole waves scattered as dipole waves) mode

mixing contributes to these interference patterns with a coupling strength of about 5% at the dipole resonance frequency. Furthermore, mode mixing is not only observed in backscattering and directional scattering but is also present in the total scattering cross section. Comparisons between a disordered nanoshell and a more ordered spiky nanoshell model, with spikes of the same size and shape, show that the disorder contributes strongly to the modal interference and allows efficient coupling of the dipole and the dark quadrupole modes, which can contribute to the strong QERS enhancements measured these nanoshells.

6.3.3 Methods

Synthesis and Dark Field Microscopy

As described in our previous publications [38, 106, 108, 107], spiky nanoshells were produced using a surfactant-assisted seed growth method. The nanoshells synthesized for this study have a polystyrene core with a diameter of 95 nm with spikes estimated to be less than 68 nm in length. The morphology of the synthesized nanoshells was studied using scanning electron microscopy (SEM) (Quanta 600 FEG Mark II operating at 15 kV). The inset of Figure 6.1A and Figure 6.2 show SEM images of the spiky nanoshells used in this work. Substantial disorder in the size, length and shape of the spikes are evident in these images. Particles were then drop cast onto clean glass slides and characterized for single particle backscattering measurements as described in detail in our previous publication [38] and in the supplementary online information (SOI). The combination of backscattering and SEM imaging ensures that only single particle spectra are reported here. In total, 71 single particle spectra were collected. As shown in Figure 6.1A, a characteristic double peak was observed in about 10% of the single particle backscattering spectra. More examples with and

without the double peak are shown in Figures 6.3 and 6.4.

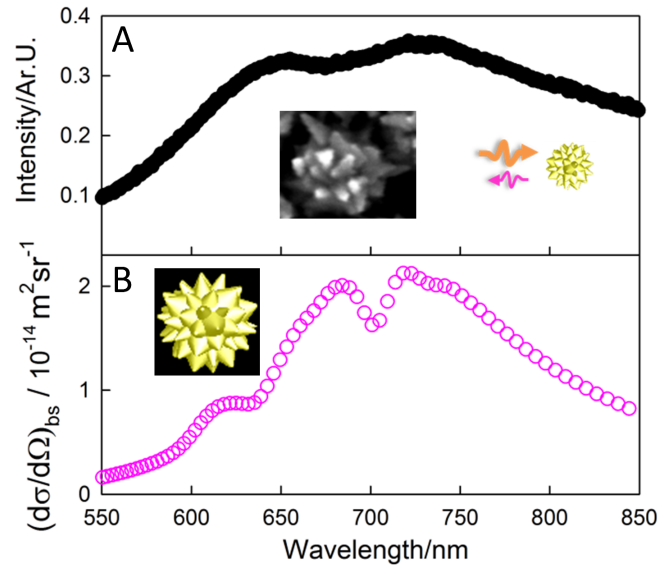


Figure 6.1: (A) Experimentally measured backscattering spectrum of a single spiky nanoshell with a characteristic double peak feature. The inset shows an SEM image of a typical spiky nanoshell (note that this spectrum does not correspond to this particle). (B) The backscattering cross section of a model disordered spiky nanoshell (inset) simulated using FDTD. In this orientation, the simulated spectrum also shows a double peak feature.

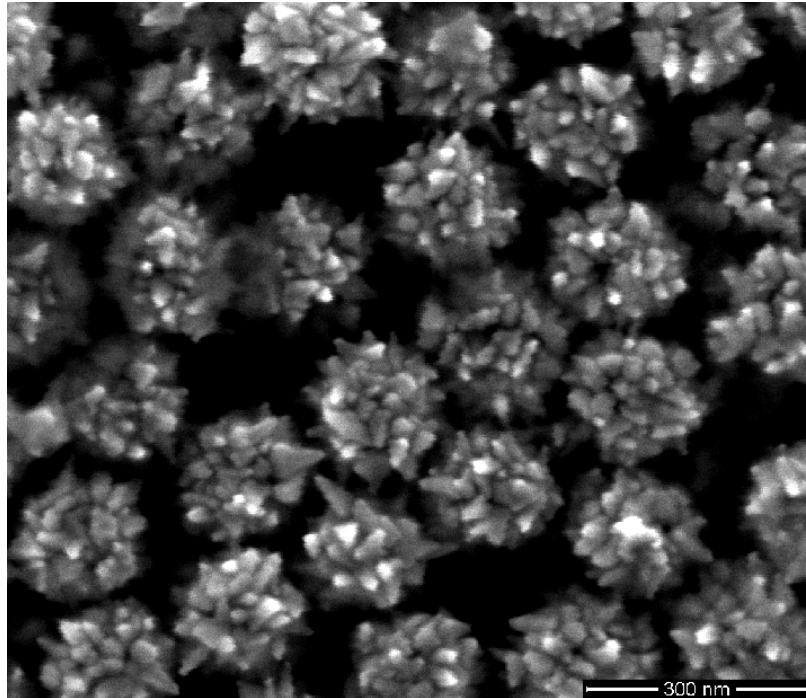


Figure 6.2: SEM images of the nanoparticles used in this study.

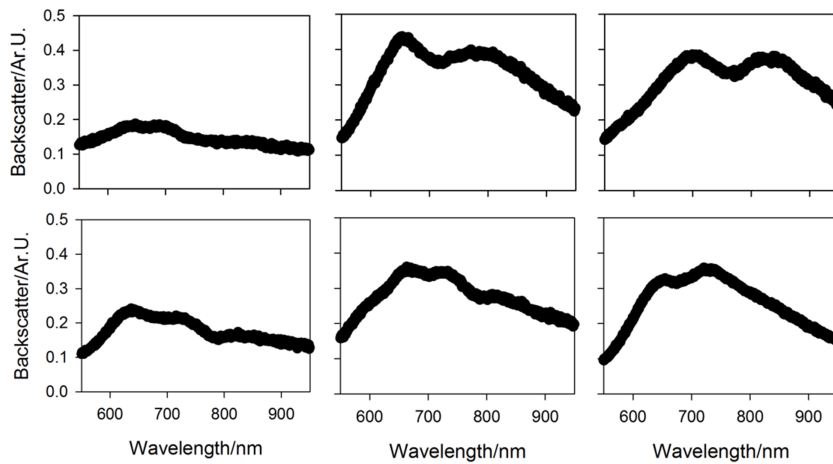


Figure 6.3: Dark-field backscattering measurements of a selection of single particle spiky nanoshells with a characteristic double peak feature.

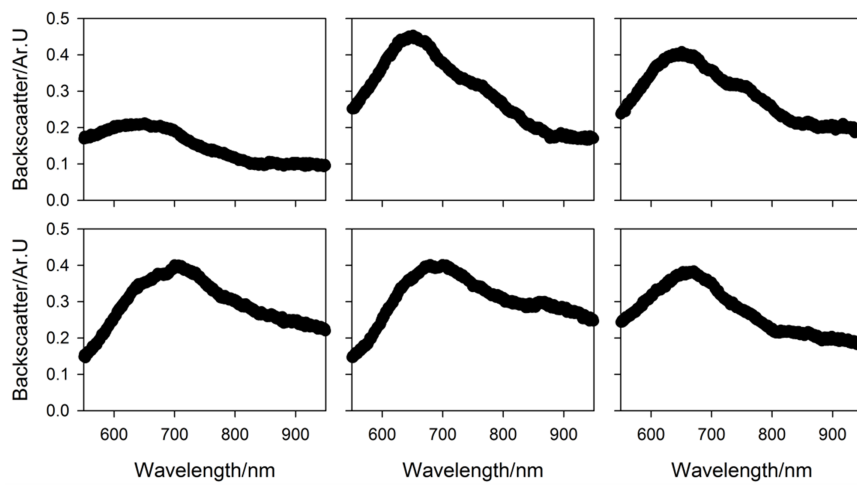


Figure 6.4: Dark-field backscattering measurements of a selection of single particle spiky nanoshells without a characteristic double peak feature.

Finite Difference Time Domain (FDTD) Simulations

FDTD Simulations were performed using Lumerical Solutions inc.'s FDTD package. As described in our previous work [38], disordered nanoshells were modeled as a polystyrene core of radius 48 nm decorated with 60 rounded cones. The height, tip diameter, and cone angles were randomized with ranges 50 nm - 65 nm, 2 nm - 6 nm, and 30° - 75° , respectively. In total, eleven randomized spiky nanoshells were produced and modeled using FDTD simulations. All models showed similar spectral features as shown by their total cross section in Figure 6.5. One particle was chosen for closer inspection. The structure of this particle is shown in the inset of Figure 6.1B with the corresponding simulated backscattering spectra. The simulated backscattering spectrum shows an apparent double peak, similar to the one observed experimentally. Similar patterns are also observed in some of the other simulated spectra shown in Figure 6.5. A total of 28 simulations were performed on this model with varying orientations with regards to the incident field. These simulations were used to solve the T-matrix for this structure. In order to compare the data with more ordered structures, ten simulations of various orientation of a simple gold nanosphere and 28 simulations of various orientations of an ordered spiky nanoshell with 60 spikes of 57 nm length, 4 nm tip radius, and 47 degree cone angle, were also produced and their corresponding matrices were calculated.

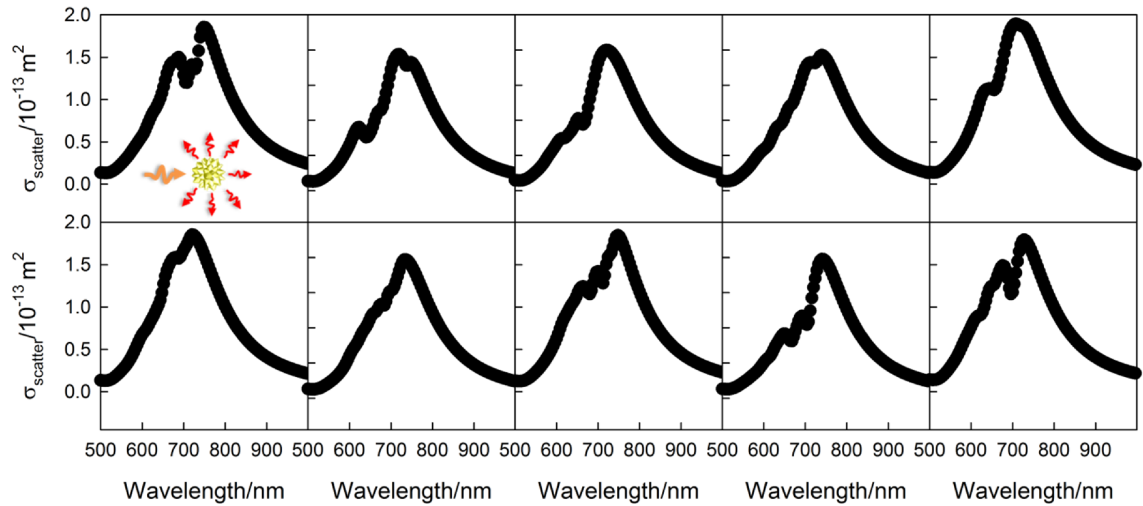


Figure 6.5: Total scattering cross sections of ten random modeled spiky nanoshells with a polystyrene core of radius 48 nm covered with 60 spiky cones. The height, tip diameter and the cone angles were randomly varied between 50 nm and 65 nm, between 2 nm and 6 nm, and between 30 and 75 degrees, respectively. In two of the ten simulations a prominent double peak is observed, while all of them have smaller features which are due to modal interference. This data set was previously used in Reference [38], and additional structural details and optical properties in the near-field can be found there.

T-Matrix Formalism

In Mie theory, the total scattering cross section and the differential backscattering cross section are described by the following equations [16]:

$$\sigma_{scatter} = \frac{\lambda^2}{2\pi} \sum_{n=1}^{\infty} (2n+1) (|a_n|^2 + |b_n|^2) \quad (6.3.1)$$

$$\left(\frac{d\sigma}{d\Omega} \right)_{bs} = \frac{\lambda^2}{16\pi^2} \left| \sum_{n=1}^{\infty} (2n+1) (-1)^n [a_n - b_n] \right|^2 \quad (6.3.2)$$

Where a_n and b_n are the scattering coefficients for the electric and magnetic modes of order n . As can be seen in Eq. 6.3.1, every term in the total scattering cross section is positive-definite. As a result, interference between different terms (*i.e.* modes) is only possible in directional scattering, such as in the differential backscattering cross section, $(d\sigma/d\Omega)_{bs}$, in Eq. 6.3.2. T-Matrix theory, a more general form of Mie theory, allows modal interference in structures that are not spherically symmetric. Here, the incident electric field, $E^i(\vec{r})$, and the scattered electric field, $E^s(\vec{r})$, are expanded as infinite sums of incoming and outgoing vector spherical harmonic wave functions (VSHWF):

$$\vec{E}^i(\vec{r}) = \sum_{m,n} \left[a_{mn}^{i(M)} Rg\vec{M}_{mn}(kr, \theta, \phi) + a_{mn}^{i(N)} Rg\vec{N}_{mn}(kr, \theta, \phi) \right] \quad (6.3.3)$$

$$\vec{E}^s(\vec{r}) = \sum_{m,n} \left[a_{mn}^{s(M)} \vec{M}_{mn}(kr, \theta, \phi) + a_{mn}^{s(N)} \vec{N}_{mn}(kr, \theta, \phi) \right] \quad (6.3.4)$$

where \vec{M} , \vec{N} , $Rg\vec{M}$ and $Rg\vec{N}$ are the VSHWF functions described in Reference

[123]. Here The incident electric and magnetic mode wave functions ($Rg\vec{N}$ and $Rg\vec{M}$ respectively) have been regularized at the origin by using spherical Bessel functions while the outgoing \vec{N} and \vec{M} wave functions employ spherical Hankel functions of the first kind. The coefficients $a_{mn}^{i(N)}$, $a_{mn}^{i(M)}$, $a_{mn}^{s(N)}$, and $a_{mn}^{s(M)}$ define the strength of each electric and magnetic mode of the incoming and scattered light, respectively. Here n indicates the order of the mode ($n = 1$ implies a dipole, $n = 2$ a quadrupole, *etc.*), while m indicates the specific submode in use and is an integer between $-n$ and n . The scattering of a particle is described by a matrix, \mathbf{T} (the ‘‘T-matrix’’), which maps the coefficients of the incident field to those of the scattered field:

$$\vec{a}^s = \mathbf{T}\vec{a}^i \tag{6.3.5}$$

Here, \vec{a}^s and \vec{a}^i include the electric and magnetic modes in that order. In this study the T-matrix was truncated to include dipole and quadrupole terms for both electric and magnetic modes as octopole and higher modes are substantially weaker [38]. As a result, the T-matrix has 16 rows, where we have chosen to order the modes as electric and then magnetic. We also assume that mode mixing can occur between electrical components and between magnetic components, but that inter-mixing of magnetic and electric modes are negligible, *i.e.*, the T-matrix is block diagonal. This results in separate matrices for the electric, $\mathbf{T}^{(EE)}$, and magnetic, $\mathbf{T}^{(MM)}$, mode mixing. This assumption is justified as mixing between the electric and magnetic modes (termed here as $\mathbf{T}^{(ME)}$ and $\mathbf{T}^{(EM)}$) requires a chiral structure which is not the case for the spiky nanoshells. Therefore we can removed the $\mathbf{T}^{(ME)}$ and $\mathbf{T}^{(EM)}$ mixing contributions in all following equations. The total scattering cross section is then given by [123]:

$$\begin{aligned}
\sigma_{scatter, \hat{\beta}}(\phi_i, \theta_i) &= \frac{16\pi^2}{k^2} \sum_{n,m} \\
&\left\{ \left| \sum_{m'n'} i^{n'} (-1)^{m'} \gamma_{-m'n'} T_{mnm'n'}^{(MM)} \vec{C}_{-m'n'}(\theta_i, \phi_i) \cdot \hat{\beta} \right|^2 \right. \\
&\quad \left. + \left| \sum_{m'n'} i^{n'} (-1)^{m'} \gamma_{-m'n'} T_{mnm'n'}^{(EE)} \frac{\vec{B}_{-m'n'}(\theta_i, \phi_i)}{i} \cdot \hat{\beta} \right|^2 \right\} \quad (6.3.6)
\end{aligned}$$

Here γ is a normalizing constant, \vec{C}_{mn} and \vec{B}_{mn} are vector spherical harmonics [123], $\hat{\beta}$ is the polarization vector, and θ_i and ϕ_i indicate the angle of incidence of the incident plane wave. Calculations of \vec{C}_{mn} and \vec{B}_{mn} were carried out using the Optical Tweezer Toolbox [91]. Additional details are provided in the appendix. Similarly, the differential backscattering cross section, the intensity of light reflected directly backwards, can be calculated as:

$$\begin{aligned}
\frac{\sigma_{bs, \beta}(\phi_i, \theta_i)}{d\Omega} &= \frac{16\pi^2}{k^2} \left| \sum_{nmm'n'} (-1)^{m'+n} i^{n'-n-1} \gamma_{mn} \gamma_{-m'n'} \left\{ \right. \right. \\
&\quad \left. \vec{C}_{mn}(\theta_i, \phi_i) T_{mnm'n'}^{(MM)} \left[\vec{C}_{-m'n'}(\theta_i, \phi_i) \cdot \hat{\beta} \right] \right. \\
&\quad \left. \left. - \vec{B}_{mn}(\theta_i, \phi_i) T_{mnm'n'}^{(EE)} \left[\vec{B}_{-m'n'}(\theta_i, \phi_i) \cdot \hat{\beta} \right] \right\} \right|^2 \quad (6.3.7)
\end{aligned}$$

To calculate the T-matrix, a least squares method (LSM) was developed. In this approach, a single particle was simulated in many different orientations with regards to the incident electric field. Both the incident electric and magnetic field, and the scattered electric and magnetic field can be extracted from the FDTD simulation using the built-in total-field scattered-field (TFSF) source in FDTD Solutions (more details in the SOI). The incident and the scattered electric fields were expanded in

VSHWF functions to obtain a set of a^i and a^s vectors. Using these vectors, a linear algebra problem was constructed to solve the T-matrix:

$$\mathbf{A}^s = \mathbf{T}\mathbf{A}^i \quad (6.3.8)$$

Where \mathbf{A}^s and \mathbf{A}^i are rectangular matrices composed of the \vec{a}^s and \vec{a}^i vectors. The T-matrix was then calculated using the Moore-Penrose least square method [4]. More details of the method, including the least squares inversion procedure used to invert Eq. 6.3.8 are provided in the SOI. The method was validated by computing the T-matrix and cross sections of a gold nanosphere. The results are shown in Figure 6.14.

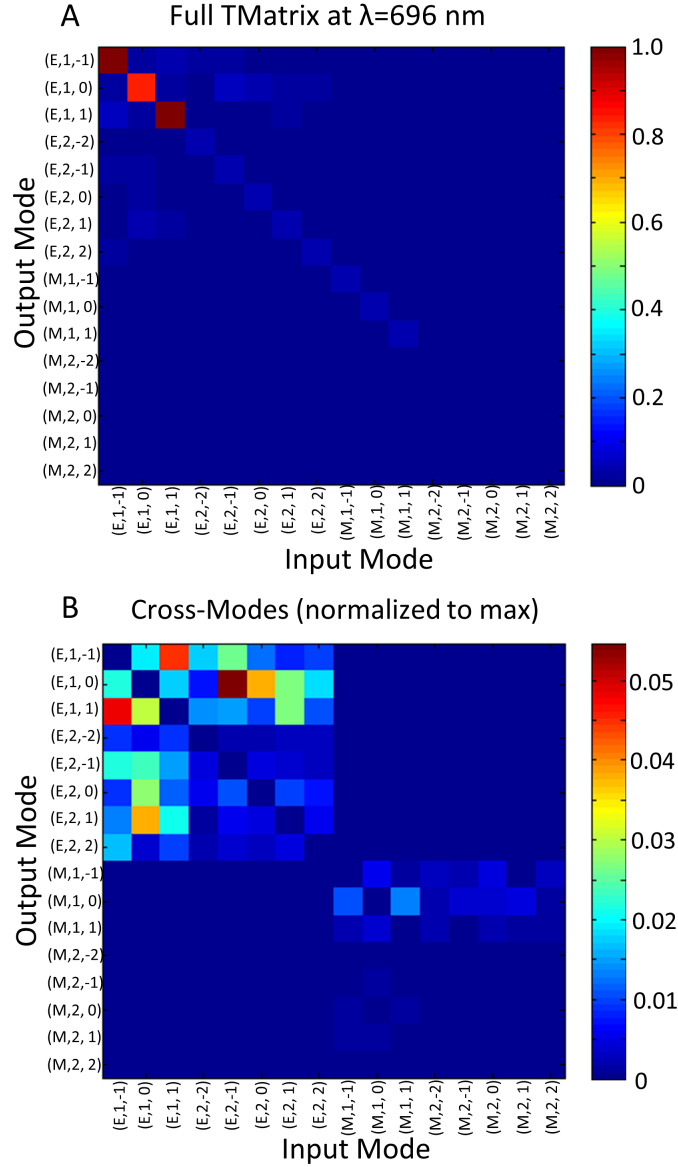


Figure 6.6: (A) The T-matrix at $\lambda = 696$ nm, the wavelength of the maximum dip in the backscattering peak. Here the $\mathbf{T}^{(EE)}$ quadrant is shown in the top left corner while $\mathbf{T}^{(MM)}$ is in the bottom right. (B) Off-diagonal terms of the same T-matrix, normalized to the T-matrix entry with the highest absolute value. Each position in both A and B denotes the absolute value of that T-matrix entry.

6.3.4 Results

Using the method described above, the T-matrix of the disordered-spiky nanoshell model shown in Figure 6.1 was calculated at 75 different wavelengths, spaced between $\lambda = 550$ nm and $\lambda = 850$ nm. Figure 6.6A shows the T-matrix at a wavelength of $\lambda = 696$ nm, which is the wavelength of the dip in the scattering cross section shown in Figure 6.1B. It can be seen that the diagonal terms, in particular the electric dipoles, are the strongest contributors to the scattering cross section, as expected [107]. Both the diagonal magnetic dipoles the diagonal electric quadrupoles are predominantly dark modes at this frequency(see Figure 6.11), with the magnetic dipoles non-resonant and contributing only a broad background. Figure 6.6B shows the same T-matrix, with the diagonal terms removed to highlight the contribution of the off-diagonal terms to the scattering cross section. At this frequency, each of the electric dipole-dipole and the electric quadrupole-dipole modes contribute up to about 5% to the scattering coefficient of the dipole mode.

6.3.5 Discussion

The T-matrix shown in Figure 6.6 indicates that the values of different diagonal modes of the same order multipole are not equal. This modal splitting implies that the scattering cross section is orientation-dependent. Furthermore, the off-diagonal coupling strengths are also not the same at different orientations, suggesting that the interference patterns observed both experimentally and in simulations are also orientation-dependent. This effect is demonstrated in Figure 6.7, where the interference feature appears and disappears in the total scattering cross section, depending on the angle of incidence. This suggests that although the interference patterns were observed in ten percent of the nanoshells examined experimentally, it may in fact

be present in many more of them when viewed at different orientations. This behavior is a consequence of broken symmetry in these nanoparticles. In spherically symmetric objects (Eq. 6.3.1) the total scattering cross section can not show interference effects or be orientation dependent. The broken symmetry implies that the true eigenmodes of this structure are not the vector spherical harmonic wave functions, but rather slightly perturbed mixtures of them. When these modes are viewed in the far-field, the dipole waveform still dominates, but is perturbed by the dipole-dipole and quadrupole-dipole mode mixing.

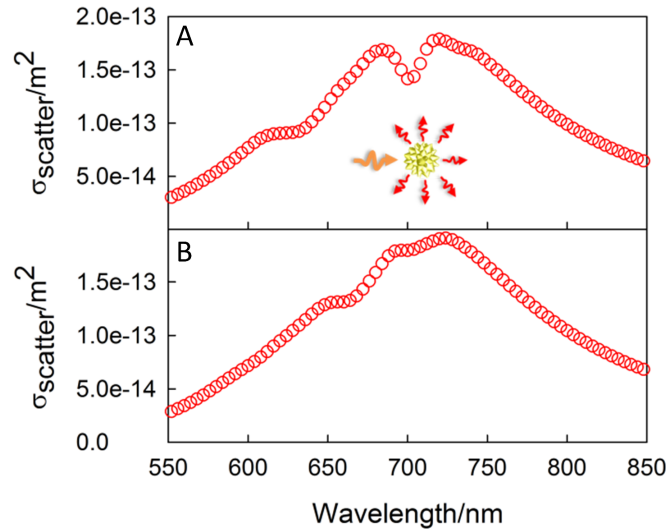


Figure 6.7: (A) Total scattering cross section, $\sigma_{scatter}$, of the model spiky nanoshell of Fig 6.1B with the same orientation as in Fig 6.1B. (B) Total scattering cross section, $\sigma_{scatter}$, of the same nanoshell at a different orientation with regards to the incident field. At this orientation the interference pattern is less evident.

In order to further examine the effects of the mode mixing in generating the interference patterns in the total scattering and backscattering spectra, we can calculate the T-matrix assuming that it is diagonal and all off-diagonal terms are zero. For a diagonal T-matrix, the maximum likelihood solution using standard Gaussian

probabilities results in the following solution:

$$T_{nmnm} = \frac{\sum_i a_{nm,i}^s a_{nm,i}^i}{\sum_i (a_{nm,i}^i)^2} \quad (6.3.9)$$

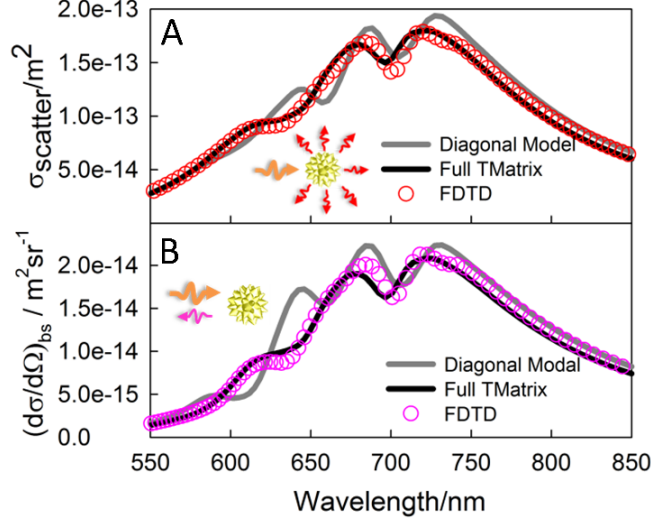


Figure 6.8: (A) Total scattering cross section calculated using FDTD (red circles), compared with the total scattering cross section spectra calculated using the full T-matrix solution (black solid lines) and a diagonal T-matrix (gray solid lines) solution. (B) Backscattering cross section calculated using FDTD (purple circles), compared with the total scattering cross section spectra calculated using the full T-matrix solution (black solid lines) and a diagonal T-matrix (gray solid lines) solution.

Figure 6.8 shows a comparison between the diagonal T-matrix and a full T-matrix solution in predicting the total scattering and backscattering cross section spectra of the model spiky nanoshell. While the diagonal T-matrix correctly predicts the approximate shape of each curve, it is unable to match the simulated data near apparent interference patterns. Only with the addition of the off-diagonal (mode mixing) terms, is the T-matrix solution able to model the amplitude of the scattering cross section near the interference features, both at $\lambda = 695$ nm where a dip is observed in the spectrum, and at $\lambda \approx 630$ nm where a plateau is observed near the dark quadrupole

resonance of this structure (See Figures 6.11 and 6.15). Therefore, even though each mode mixing contributes at most 5% to the scattered coefficients, it is crucial in describing the modal interference in these nanoshells. Additionally, we can show that mode mixing between the electric dipole modes alone is also not enough to describe the observed interferences and electric quadrupole-dipole mixing is crucial in obtaining the correct T-matrix. In order to do this, the T-matrix solution was calculated by only allowing dipole-dipole mode mixing and assuming that the dipole-quadrupole, quadrupole-dipole, and quadrupole-quadrupole mode mixing terms are zero. Figure 6.9 shows a comparison between the three T-matrix solutions discussed above in predicting the extinction cross section. Neither the diagonal T-matrix, nor the T-matrix with electrical dipole mode mixing are able to predict the extinction cross section, which includes information about the relative phases of these modes. The extinction cross section is only correctly modeled by including cross terms between the dipoles and quadrupoles in the full T-matrix solution. Figure 6.10 shows further comparisons between these three solutions in predicting the total scattering cross section and the extinction cross sections at another orientation of the particles with regards to the incident electric field. These results indicate that the simplest model which is capable of explaining the simulation results requires modal interferences in the dipole-dipole and quadrupole-dipole modes. In particular, the interference observed close to the dipole resonance peak, $\lambda = 695$ nm, is only explainable with the introduction of quadrupole-dipole interference. We also note that the diagonal T-matrix solution shown in Figure 6.8 gives rise to interference-like patterns, which do not represent real interferences. Therefore the observation of such patterns in a hypothetical nanoparticle structure is not enough to predict a modal interference without knowing the coupling strength or a full T-matrix solution for that structure.

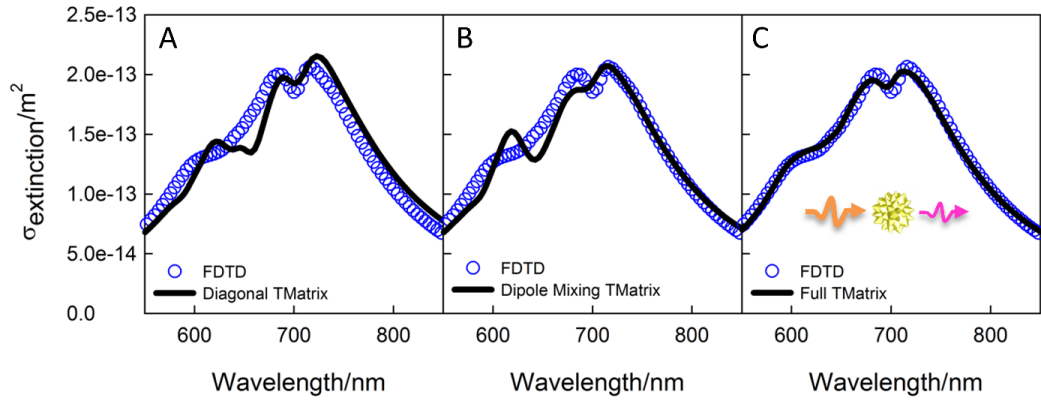


Figure 6.9: The extinction cross section at the same orientations as the data shown in Figure 6.8. (A) The T-matrix solution for a strictly diagonal T-matrix. (B) The T-matrix solution where mode mixing is allowed only between the electric dipole modes, but is diagonal in all other modes. (C) The T-matrix solution for the block-diagonal matrix with mode mixing between all electrical modes and between all magnetic modes. It is evident that quadrupole-dipole mixing is required to fully capture the behavior of the system. In each case the line represents the values calculated using the T-matrix and the circles represent the simulated cross section.

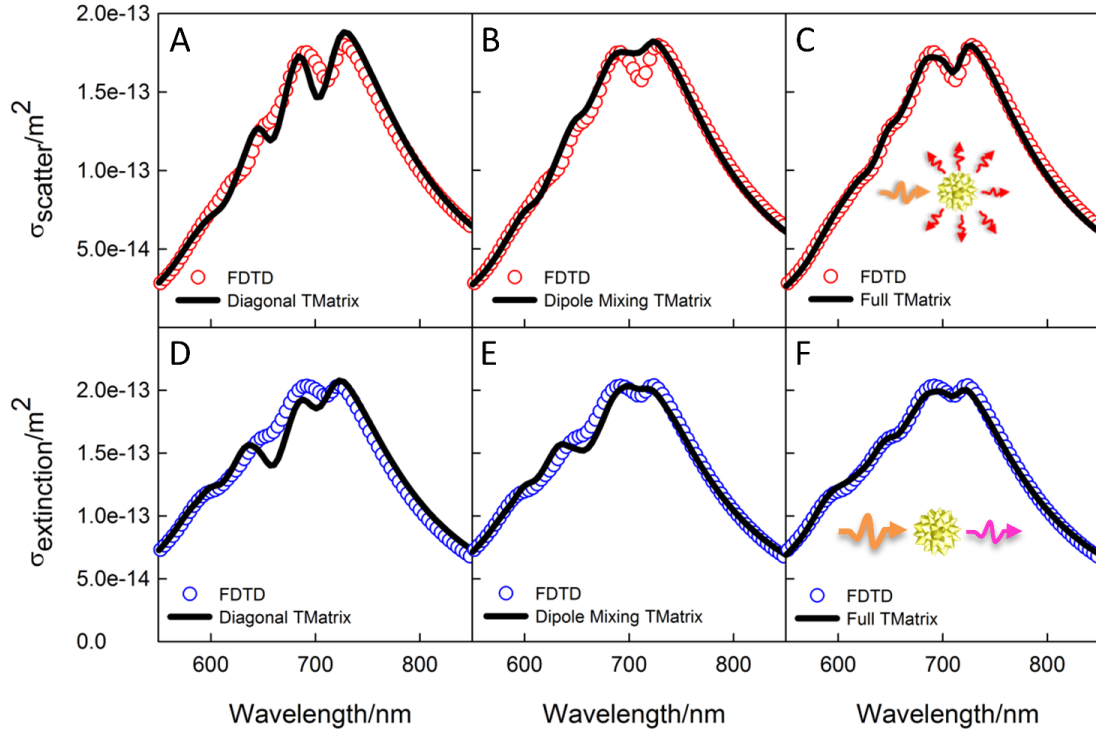


Figure 6.10: The scattering (A-C) and extinction (D-F) cross sections for a different orientation than the one shown in Figure 6.8 in the paper. (A,D) show the solutions for a strictly diagonal T-matrix model. (B,E) show the T-matrix solution when mode mixing is allowed between the electric dipole modes, but the matrix is diagonal in all others modes. (C,F) The full T-matrix solution with block-diagonal mode mixing. It is evident that quadrupole-dipole mode mixing is required to fully capture the behavior of the system. From the results above, we can see that without this mixing, it is not possible to account for the phase or orientation dependence of the modal mixing. In each case the line represents the model values and the circles represent the simulated cross section.

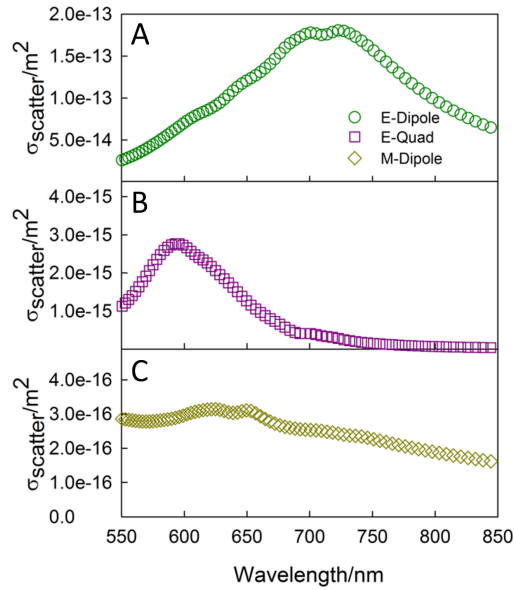


Figure 6.11: The cross sections associated with only the diagonal terms of the full T-matrix for the orientation and particle shown in Figure 6.1B. (A) The diagonal electric dipole cross section. (B) The diagonal electric quadrupole cross section, exhibiting substantial breadth but greatly suppressed scattering. (C) The diagonal magnetic dipole cross section exhibits no clear peak and is nearly two orders of magnitude weaker than the electric dipole. The magnetic dipole contributes only a background to the particle cross section.

As discussed above, the off-diagonal T-matrix terms are critical in explaining this result. We can understand the exact origin of this effect by examining the Eq. 6.3.6 in more detail. When the components inside the absolute value terms in Eq. 6.3.6 have differing complex phases, it is possible to have destructive interference, while in phase components will result in constructive interference. Near the dipole resonance, these phases can change rapidly with frequency, resulting in sharp features in the total scattering cross section spectrum. The detailed role of the off-diagonal terms in the observed interference patterns can be examined by calculating the magnitudes of different terms in the sum in Eq. 6.3.6. The sum over the diagonal components is given by:

$$\sigma_{scatter,\beta}^{Diagonal}(\phi_i, \theta_i) = \frac{16\pi^2}{k^2} \sum_{n,m} \left\{ \left| i^n (-1)^m \gamma_{-mn} T_{mnmn}^{(MM)} \vec{C}_{-mn}(\theta_i, \phi_i) \cdot \hat{\beta} \right|^2 + \left| i^n (-1)^m \gamma_{-mn} T_{mnmn}^{(EE)} \frac{\vec{B}_{-mn}(\theta_i, \phi_i)}{i} \cdot \hat{\beta} \right|^2 \right\} \quad (6.3.10)$$

A residual function can be obtained by subtracting the total scattering cross section from the sum of the contributions of all diagonal terms.

$$Residual = \sigma_{scatter,\beta}(\phi_i, \theta_i) - \sigma_{scatter,\beta}^{Diagonal}(\phi_i, \theta_i) \quad (6.3.11)$$

The residual is shown as a function of wavelength in Figure 6.12A. Similarly, the contributions of various off-diagonal terms in the total scattering cross section can be estimated by looking at the magnitudes of just those terms. These are defined for the electric dipole-dipole and electric quadrupole-dipole mixing as:

$$\sigma_{scatter,\beta}^{dipole,dipole}(\phi_i, \theta_i) = \frac{16\pi^2}{k^2} \sum_{n=1,m} \left| \sum_{n'=1, m' \neq m} i(-1)^{m'} \gamma_{-m'1} T_{m1m'1}^{(EE)} \frac{\vec{B}_{-m'1}(\theta_i, \phi_i)}{i} \cdot \hat{\beta} \right|^2 \quad (6.3.12)$$

$$\sigma_{scatter,\beta}^{quad,dipole}(\phi_i, \theta_i) = \frac{16\pi^2}{k^2} \sum_{n=1,m} \left| \sum_{n'=2, m'} (-1)^{m'+1} \gamma_{-m'2} T_{m1m'2}^{(EE)} \frac{\vec{B}_{-m',2}(\theta_i, \phi_i)}{i} \cdot \hat{\beta} \right|^2 \quad (6.3.13)$$

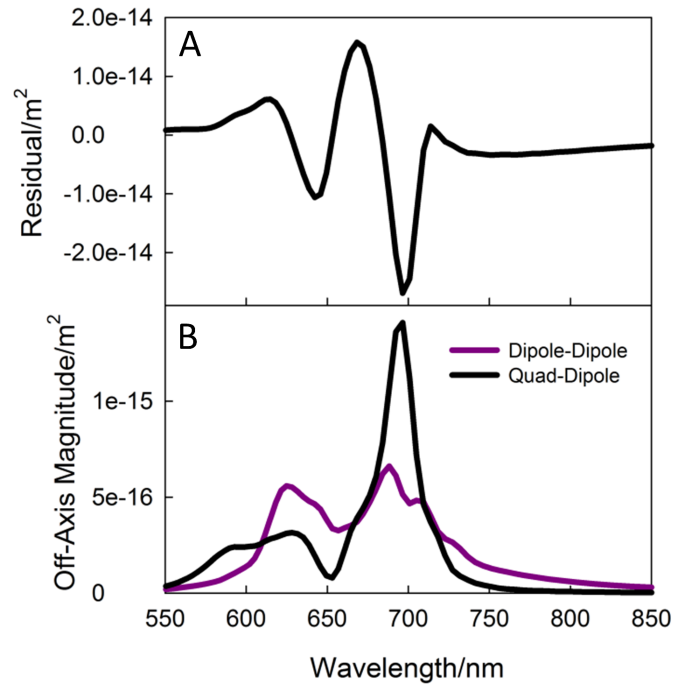


Figure 6.12: (A) The residual function of the scattering cross section as described in Eq. 6.3.11. (B) The magnitude of the off diagonal terms corresponding to mode mixing between dipole-dipole (purple) and dipole-quadrupole(black) modes as described in Eqs. 6.3.12 and 6.3.13.

The contribution of each type of mode mixing is shown in Figure 6.12B. Interestingly, the residual function shown in Figure 6.12A shows both constructive and destructive interferences. Despite the fact that the quadrupoles themselves scatter very weakly and are dark modes (as shown in Figure 6.11), they produce about half of the interference effects observed in the total scattering cross section. The dipole-dipole and quadrupole-dipole mode mixing together produce a total scattering cross section change of just under 20% of the total cross section, while the dipole-quadrupole and quadrupole-quadrupole modes produce almost no change at all. From Eq. 6.3.6, changes to the scattered dipole are magnified by the squaring operation due to the existing scattered dipole, while the quadrupole modes are not. This allows the quadrupole modes to couple with the bright far-field scattering mode and therefore be observed in the far-field as interferences. This effect is similar to the Fano resonances observed in previous studies [86, 118, 72]. However, we note that the complexity of this structure requires the full T-matrix solution to explain the interferences observed here and a simple coupling between one electric quadrupole and one electric dipole is not enough to fully explain the extent and complexity of the effect. When observed at a different orientation, the apparent coupling strength may vary between the dipole-dipole and quadrupole-dipole modes (both bright), and dipole-quadrupole (dark) modes. This is due to the heterogeneous nature of these nanoshells.

To further examine the role of the disorder in these observations, the T-matrix of a more ordered spiky nanoshell was also calculated. This ordered structure is very similar to the disordered structure, but all of the spikes decorating the polystyrene cores have the same height, length and tip angles. As shown in Figure 6.13, the T-matrix for the ordered model is predominantly diagonal with off-diagonal terms at

least an order of magnitude smaller than those observed in the disordered nanosell. No interference pattern is observed in the total scattering or backscattering spectra in the ordered nanoshell. This indicates that disorder is required to achieve substantial mode mixing in these structures.

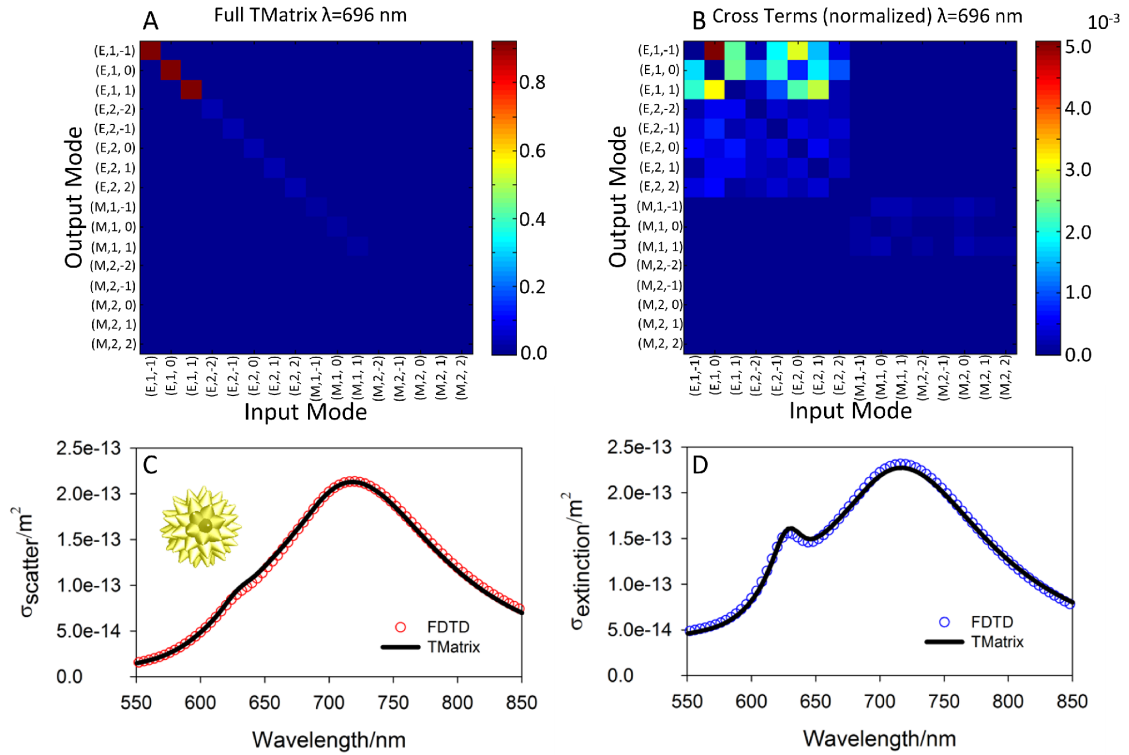


Figure 6.13: The T-matrix calculated for an ordered version of the model spiky nanoshell, with the same number of cones(60), but identical cone sizes and shapes. The cones have 57 nm height, cone angle 47 degrees, and tip radius 4 nm. These represent the average values used in the disordered nanoshells. (A) The full T-matrix solution for this structure at 696 nm. The diagonal dipole modes are the dominant terms and all nearly equal, which indicates that this structure is mostly isotropic in the far-field. (B)The off-axis terms. These terms are a factor of 10 smaller than those observed in the disordered structure and a factor of 200 smaller than the strength of the dipole modes. (C) Scattering cross section of the ordered nanoshell as calculated by FDTD (open symbols) compared with the cross section calculated using the T-matrix (solid line). (D) Extinction cross section of the ordered nanoshell as calculated by FDTD (open symbols) compared with the cross section calculated using the T-matrix (solid line). Both the scattering and the extinction cross sections are independent of direction of illumination within the accuracy of these calculations. This is further evidence that this particle is isotropic in the far-field, while the disordered structure is not.

The mode mixing discussed above can also strongly affect the electric near-field intensity in these disordered nanoshells and result in the recently observed strong Quadrupole Enhanced Raman Scattering (QERS) in these systems [38]. This effect is due to the T-matrix symmetry condition [123]:

$$T_{-m'n'(-m)n}^{(ij)} = (-1)^{m'+m} T_{mnm'n'}^{(ji)} \quad (6.3.14)$$

where i, j are either electric, E , or magnetic, M , modes. When using the LSM we did not explicitly enforce this requirement, however the T-matrix shown in Figure 6.6 still contains patterns which reflect this symmetry. Therefore, the quadrupole-dipole mixing shown in Figure 6.12B as a function of wavelength will also lead to a reciprocal dipole-quadrupole mixing and interference in the dark quadrupole modes. As shown in Figure 6.11 and in our previous work [38], this results in broadened quadrupole modes in the disordered spiky nanoshell and extends the modes towards the near-IR region of the spectrum. The dipole-quadrupole mode mixing results in spectral overlap between the dipole and quadrupole modes near the dipole resonance of this structure. As seen in Figure 6.11, the quadrupole dark modes scatter very little as they approach the dipole peak. However, from Figure 6.15 and our previous work [38], the near-field quadrupole moments are strongly excited across a broad range of wavelengths (see SOI). In our previous work it was shown that the dark quadrupole modes dominate the near-field intensity of light in these structures [38]. As a result, the dipole induced quadrupole broadening dramatically enhances the near-field intensity of the electric field, strengthening the QERS enhancement [38].

6.3.6 Conclusion

In this work we developed a novel method to calculate the T-matrix of a complicated nanoparticle using FDTD simulations and a least square matrix inversion algorithm. This is a general method that can be applied on a wide range of nanostructures to investigate the coupling between various modes and quantify the strength of modal interference in a classical electrodynamical framework. Using this method we demonstrated that modal interferences with complicated spectral shapes can explain both the far-field interference patterns in spiky nanoshells as well as their ability to efficiently enhance the near-field intensity of the electric field and produce strong QERS signals. We showed that in disordered spiky nanoshells, modal interference can be observed in the backscattering cross sections as well as the total scattering cross section and strongly depends on the orientation of the nanoshell with respect to the angle of incidence of light. The modal interference has non-trivial participation of both bright dipole-dipole and otherwise dark quadrupole-dipole modes with both constructive and destructive interferences. The mode coupling and modal interference directly results from the built-in disorder in these nanoshells which is intrinsically robust to error in construction, generating reliable coupling of the dark quadrupole modes to the far-field. In a reciprocal process, the coupling results in the broadening of the quadrupole modes due to the dipole-quadrupole coupling and allows strong enhancement of the near-field intensity.

This work provides a general recipe for analyzing modal interferences of arbitrary nanoparticles using existing commercially available software. With the advent of faster computers, this method should be able to generate a T-matrix for almost any particle, providing an analytical framework for studying modal interference in nanoparticles. Furthermore we demonstrated that in principle the observation of a

dip or increase in the backscattering spectrum alone is insufficient to describe the patterns as interferences, as shown in the scattering spectrum of a diagonal T-matrix solution, which indicates the importance of obtaining the full T-matrix solution to verify the existence of modal interferences in a complicated structure.

6.3.7 Appendix

The scattering behavior of a particle can be derived from the scattering dyad [123]:

$$\begin{aligned}
\mathbf{F}(\theta, \phi; \theta', \phi') = & \frac{4\pi}{k} \sum_{n,m,n',m'} (-1)^{m'} i^{n'-n-1} \times \\
& \left\{ \left[T_{nmm'n'}^{(MM)} \gamma_{mn} \vec{C}_{mn}(\theta, \phi) + T_{nmm'n'}^{(EM)} i \gamma_{mn} \vec{B}_{mn}(\theta, \phi) \right] \right. \\
& \quad \cdot \gamma_{-m'n'} \vec{C}_{-m'n'}(\theta', \phi') \\
& + \left[T_{nmm'n'}^{(ME)} \gamma_{mn} \vec{C}_{mn}(\theta, \phi) + T_{nmm'n'}^{(EE)} i \gamma_{mn} \vec{B}_{mn}(\theta, \phi) \right] \\
& \quad \left. \cdot \gamma_{-m'n'} \frac{\vec{B}_{-m'n'}(\theta', \phi')}{i} \right\}
\end{aligned} \tag{6.3.15}$$

Where \vec{B}_{-mn} and \vec{C}_{-mn} are vector spherical harmonics [123], θ' and ϕ' represent the direction of the incident light, while θ and ϕ represent the direction of scattering and k is the scalar wave number being considered. Here we have chosen to reverse the standard order of the T-matrix so that electric modes are in the top left quadrant of the T-matrix, while magnetic modes are in the bottom right. In this work, cross terms between electric and magnetic modes (labeled $\mathbf{T}^{(EM)}$ and $\mathbf{T}^{(ME)}$) were assumed to be zero. These terms will be dropped in all subsequent expressions. The factor γ has been used to normalize the waves:

$$\gamma_{nm} = \sqrt{\frac{(2n+1)(n-m)!}{4\pi n(n+1)(n+m)!}} \quad (6.3.16)$$

By integrating over all outward angles and summing the intensity of vertically and horizontally polarized components, we can calculate the total scattering cross section of a plane wave with incident polarization $\hat{\beta}$ [123]:

$$\begin{aligned} \sigma_{scatter\hat{\beta}}(\phi_i, \theta_i) &= \int_{4\pi} d\Omega \left[|f_{v\hat{\beta}}(\theta, \phi; \theta_i, \phi_i)|^2 + |f_{h\hat{\beta}}(\theta, \phi; \theta_i, \phi_i)|^2 \right] = \\ &= \frac{16\pi^2}{k^2} \sum_{n,m} \left\{ \left| \sum_{m'n'} i^{n'} (-1)^{m'} \gamma_{-m'n'} T_{mnm'n'}^{(MM)} \vec{C}_{-m'n'}(\theta_i, \phi_i) \cdot \hat{\beta} \right|^2 \right. \\ &\quad \left. + \left| \sum_{m'n'} i^{n'} (-1)^{m'} \gamma_{-m'n'} T_{mnm'n'}^{(EE)} \frac{\vec{B}_{-m'n'}(\theta_i, \phi_i)}{i} \cdot \hat{\beta} \right|^2 \right\} \quad (6.3.17) \end{aligned}$$

where $f_{v\hat{\beta}}$ and $f_{h\hat{\beta}}$ are the horizontal and vertical components of the \mathbf{F} dyad acting on the incident polarization. The extinction cross section is given by the optical theorem(neglecting the electric to magnetic mode mixing):

$$\begin{aligned} \sigma_{e\beta} &= \frac{4\pi}{k} Im [\hat{\beta} \cdot \mathbf{F}(\theta_i, \phi_i, \theta_i, \phi_i) \cdot \hat{\beta}] = \frac{16\pi^2}{k^2} Im \left[\sum_{nmm'n'} \right. \\ &\quad \left. (-1)^{m'} i^{n'-n-1} \gamma_{mn} \gamma_{-m'n'} \left\{ [\hat{\beta} \cdot \vec{C}_{mn}(\theta_i, \phi_i)] T_{mnm'n'}^{(MM)} [\vec{C}_{-m'n'}(\theta_i, \phi_i) \cdot \hat{\beta}] + \right. \right. \\ &\quad \left. \left. [\hat{\beta} \cdot \vec{B}_{mn}(\theta_i, \phi_i)] T_{mnm'n'}^{(EE)} [\vec{B}_{-m'n'}(\theta_i, \phi_i) \cdot \hat{\beta}] \right\} \right] \quad (6.3.18) \end{aligned}$$

And the differential backscattering cross section is simply the amount of light reflected directly backwards with either polarization(again neglecting electric to magnetic mode mixing):

$$\begin{aligned}
\frac{\sigma_{bs, \hat{\beta}}(\phi_i, \theta_i)}{d\Omega} &= \left\| F(\pi - \theta_i, \pi + \phi_i, \theta_i, \phi_i) \cdot \hat{\beta} \right\|^2 = \frac{16\pi^2}{k^2} \left\| \sum_{mmm'n'} \right. \\
&\quad (-1)^{m'+n} i^{n'-n-1} \gamma_{mn} \gamma_{-m'n'} \left\{ \vec{C}_{mn}(\theta_i, \phi_i) T_{mmm'n'}^{(MM)} \left[\vec{C}_{-m'n'}(\theta_i, \phi_i) \cdot \hat{\beta} \right] \right. \\
&\quad \left. \left. - \vec{B}_{mn}(\theta_i, \phi_i) T_{mmm'n'}^{(EE)} \left[\vec{B}_{-m'n'}(\theta_i, \phi_i) \cdot \hat{\beta} \right] \right\} \right\|^2 \quad (6.3.19)
\end{aligned}$$

6.3.8 Acknowledgments

S.P.H and Z.F. acknowledge C. Li's helpful contributions to the discussions. This work was supported by the startup funds from the University of Pennsylvania (for Z.F) and partial support from the MRSEC program of the National Science Foundation under award no. DMR-11-20901 at the University of Pennsylvania. S.L. thanks the Robert A. Welch Foundation (Grant C-1664), ACS-PRF (50191-DNI6) and NSF (CHE-0955286) for financial support of this work. N.E. acknowledges partial support from the US Air Force Office of Scientific Research (AFOSR) Grant number FA9550-10-1-0408. P.S. acknowledges support from the Royal Thai Government. S.-J.P. acknowledges the support from the Dreyfus teacher scholar award program.

6.3.9 Supplemental Information

Dark field measurements

Spiky nanoshells were deposited on clean glass cover slips with an evaporated indexed gold pattern. Since these nanoshells were simultaneously used for surface enhanced Raman spectroscopy (SERS) studies, discussed in our recent work [38], the spiky nanoshells were immersed in a solution of 4-mercaptobenzoic acid (0.0002 g/ml) over night, cleaned with ethanol, and allowed to dry under nitrogen. Three sets of mea-

measurements from one synthesized batch of spiky nanoshells were performed for a total of 71 particles. Single particle SERS measurements were performed first, followed by dark-field backscattering measurements and then last SEM measurements to ensure that only isolated nanoparticles were used. In this work only the dark-field backscattering data are presented.

Dark-field backscattering measurements were performed with an integration period of two seconds using a 150 grooves/mm grating centered on 800 nm. A 515 nm long-pass filter was used to remove second order reflections. Background and dark counts were removed from the single particle scattering spectra, and the spectrum of the lamp and the spectral response of other optical components were calibrated with a white light reflectivity standard (Labsphere SRS-99-010). Measurements were performed using a Princeton Instruments Acton SP2150i spectrograph.

Finite-Difference Time Domain Simulations

The FDTD Solutions package from Lumerical Solutions Inc. (versions 8.6 and 8.7) was used to simulate the spiky nanoshells as previously reported [108, 107, 38]. The spiky nanoshell was modeled as a polystyrene core of about 95 nm surrounded by 60 spikes. The spike parameters were randomized for the disordered particle analyzed in the text so that the cone angles, the height, and the tip diameter, were in the ranges 30° - 75° , 50 nm - 65 nm, and 2 nm - 6 nm, respectively. Additionally, a gold nanosphere of radius 52 nm and an ordered spiky nanoshell with cones of 47 degree cone angle, 57 nm length, and 4 nm tip radius, were also simulated. The material properties of gold originated from the CRC Handbook [41], while an ellipsometry measurement was used to determine the optical properties of polystyrene, as in previous work [107, 38]. The boundary conditions were set to Perfectly Matched Layers (PML), and a Total-Field

Scattered-Field (TFSF) source was used to inject a plane wave into the simulation.

In these simulations, the TFSF source surrounds the scattering object, creating a cubic volume. Inside the TFSF source volume, a plane wave is incident upon the scatterer. At the boundaries of this volume, the TFSF source subtracts the original wave such that the scattered component of the light escapes the volume, but the original wave does not. Outside the TFSF source, only the scattered fields are present. The fields in a cubic volume are collected and used to decompose the scattered wave into its components. This cubic monitor must be at least $\sqrt{3}$ larger on a side than the source in order to define a spherical surface for the vector spherical harmonic decomposition which does not include any of the source region. In order to illuminate the structure from different angles, the spiky nanoshell itself is rotated. After data collection, this rotation is reversed to the original coordinate system such that the light source has rotated in the opposite direction to the particle.

Calculation of the T-Matrix

A simple, effective, and stable approach to solve the T-matrix for a nanostructure is to reformulate the problem as a matrix inversion problem. In particular, since the T-matrix predicts the scattering coefficients at any given angle, sampling of the scattering function at various angles of the incident field can determine the truncated T-matrix, using a pseudo-inverse approach. As more terms are included in the T-matrix, more angles of illumination are required. Here, FDTD simulations were used to produce a set of input and output values, by rotating the structure randomly up to 180 degrees around each axis, which is equivalent to rotating the incident direction of light in the opposite fashion. The matrix inversion problem is then expressed as follows:

$$\begin{bmatrix} | & | & | & | \\ a_{s,1} & a_{s,2} & \dots & a_{s,N} \\ | & | & | & | \end{bmatrix} = \mathbf{T} \begin{bmatrix} | & | & | & | \\ a_{i,1} & a_{i,2} & \dots & a_{i,N} \\ | & | & | & | \end{bmatrix}$$

$$\mathbf{A}^s = \mathbf{T}\mathbf{A}^i \quad (6.3.20)$$

Where the n^{th} column of \mathbf{A}^s is the coefficients of the scattered field after exposure at a particular angle with an incident field described by the coefficients in the n^{th} column of \mathbf{A}^i . The elements of the a^i and a^s vectors are the coefficients of the spherical harmonics for each field. The far-field scattered light was isolated from the incident field by using the built-in Total Field-Scattered Field (TFSF) source function in the Lumerical software. Once isolated, the radial component of the scattered field can be decomposed using the spherical harmonics in order to determine the scattered coefficients.

One could then simply invert the incident \mathbf{A}^i matrix, assuming that sufficiently random sampling has been performed such that it is full rank and square:

$$\mathbf{T} = \mathbf{A}^s[\mathbf{A}^i]^{-1} \quad (6.3.21)$$

In this approach, one requires one illumination angle per row of the T-matrix. Since we assume that the electric and magnetic modes are decoupled, half that number of measurements are needed. However, due to numeric instability in the FDTD algorithm and the T-matrix truncation, the inversion of \mathbf{A}^i in the above approach is numerically unstable and will result in an inaccurate T-matrix calculation. Instead, by over sampling one can construct an over-determined least squares problem for each row of the T-matrix:

$$\mathbf{A}^s = \mathbf{T}\mathbf{A}^i \quad (6.3.22)$$

Where \mathbf{A}^s and \mathbf{A}^i are now rectangular matrices formed by the column vectors of the \vec{a}^s and \vec{a}^i coefficients extracted from each simulation. In order to find the most probable T-matrix in a least squares sense, the problem must be slightly reformulated. The standard form for a least squares inversion of this type is:

$$\vec{y} = \mathbf{M}\vec{x} \quad (6.3.23)$$

Where vector \vec{y} and matrix \mathbf{M} are known and the problem is over-determined in the sense that \mathbf{M} is not square. The minimization problem is then solved by the pseudo-inverse, *pinv*:

$$\min_{\vec{x}} |\mathbf{M}\vec{x} - \vec{y}| = \text{pinv}(\mathbf{M})\vec{y} \quad (6.3.24)$$

Equation 6.3.22 can be put into this form by taking the transpose:

$$(\mathbf{A}^s)^T = (\mathbf{A}^i)^T(\mathbf{T})^T \quad (6.3.25)$$

Where superscript T denotes transpose. The n th column of $(\mathbf{T})^T$ and the n th column of $(\mathbf{A}^s)^T$ are now in the correct form, so the solution of the n th row of the T-matrix is simply given by:

$$(T_{n^{th} \text{ row}})^T = \text{pinv}((A^i)^T)[A_{n^{th} \text{ row}}^s]^T \quad (6.3.26)$$

A built-in function in Matlab(TM) was used to calculate the pseudo-inverse using the Moore-Penrose method [4]. To accommodate the decoupling of the electric and

the magnetic modes, Eq. 6.3.26 was employed separately for the $\mathbf{T}^{(EE)}$ and $\mathbf{T}^{(MM)}$ quadrants of the T-matrix, and the $\mathbf{T}^{(EM)}$ and $\mathbf{T}^{(ME)}$ quadrants were assumed to be zero.

In choosing the dimension of the T-matrix in this work, we have assumed that octupoles and higher order modes as well as their coupling to the dipole mode are negligible. In principle there may be contributions from higher order modes, but these modes are weaker, and due to their smaller angular extent are more prone to noise from digitization. Additionally, by including the octupole, 14 new rows need to be added to the T-matrix, dramatically increasing the number of free fit parameters. This can result in over-fitting and instability in the pseudoinverse function. As a structure becomes larger, these modes will scatter more light and will be less prone to over-fitting.

In order to verify the validity of this approach, we calculated the T-matrix for a simple gold sphere with radius 52 nm without applying additional constraints due to symmetry. Figure 6.14A, shows that the calculated T-matrix is almost perfectly diagonal, with off diagonal terms several orders of magnitude smaller than the corresponding diagonal terms of the same rank. This T-matrix can be used to calculate the total scattering (Figure 6.14B), backscattering (Figure 6.14C) and extinction (Figure 6.14D) cross sections. These results are in excellent agreement with the corresponding cross sections directly calculated using FDTD and those calculated using Mie theory. The accurate prediction of the extinction and backscattering cross section values demonstrate that the phase of the T-matrix elements are also accurately predicted. It is important to note that this approach allows simultaneous calculation of the T-matrix for a broad spectral range.

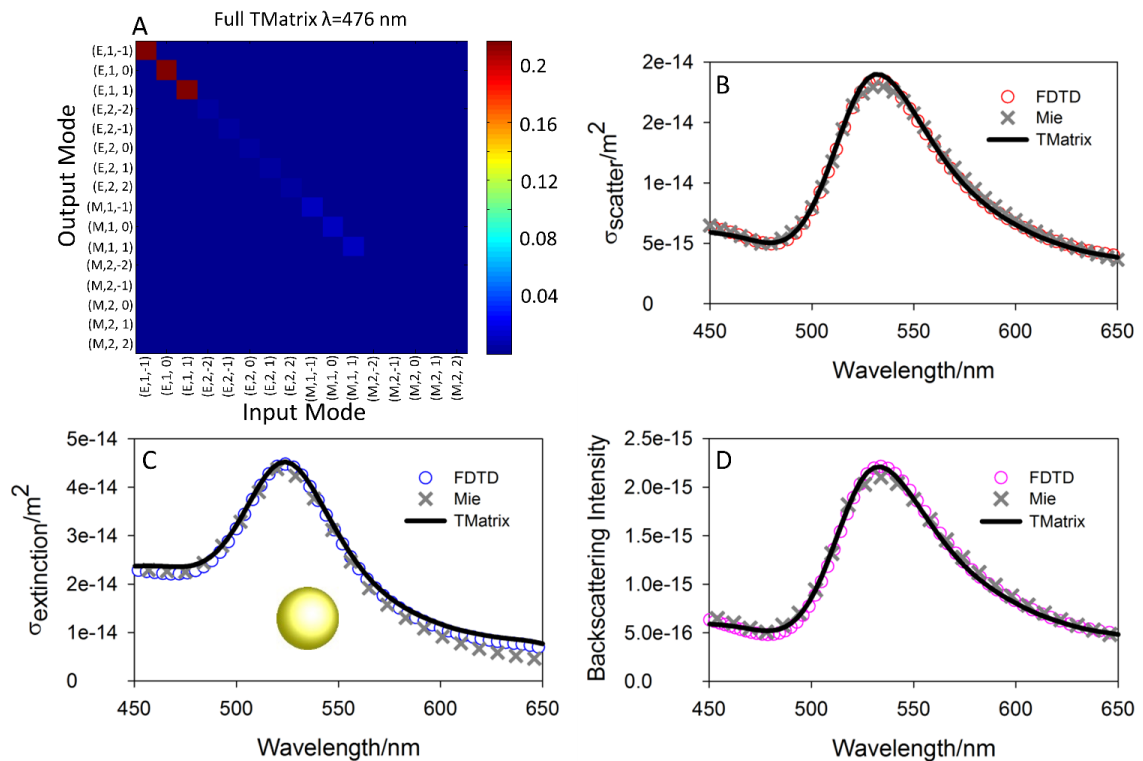


Figure 6.14: The T-matrix of a gold sphere with radius 52 nm. (A) The T-matrix at 476 nm. The strongest terms are diagonal terms for the dipole modes. Due to the spherical symmetry, all modes have equal values (although this was not enforced at any point). The matrix is nearly diagonal as expected. (B-D) The scattering and extinction cross sections and backscattering differential cross section from FDTD simulations (circles), compared with the values predicted by the T-matrix (solid line), and the Mie theory prediction (crosses).

Calculation of the Quadrupole Moments

While the scattering cross sections is useful for studying the far-field, it poorly describes the dark quadrupole modes due to their extremely small scattering. In our previous work [38], the quadrupole moments of a typical orientation of this particle were included (see Figure 6.15). This allows modal activity to be measured independently of scattering efficiency, although it still depends on the ability of the mode to couple to the incident field. These are calculated using the polarization current by applying the equation [97]:

$$Q_{\alpha\beta} = \frac{i}{\omega} \int \vec{J}_\alpha(\vec{r}') r'_{\beta} + \vec{J}_\beta(\vec{r}') r'_{\alpha} dV' \quad (6.3.27)$$

Where \vec{J}_α is the polarization current, r'_{β} is the position, α and β denote coordinate axis and the integral is over all space. While Figure 6.11 shows a distinct decrease in scattering from the quadrupole modes as the wavelength approaches the electric dipole resonance, the quadrupole moments themselves remain strong (Figure 6.15). This is because the quadrupole moments are a description of how well the far-field couples to the quadrupole currents, while the quadrupole scattering(Figure 6.11) measures both how well the far-field couples to the quadrupole moment, and how well the dark quadrupoles can scatter that power as a function of wavelength.

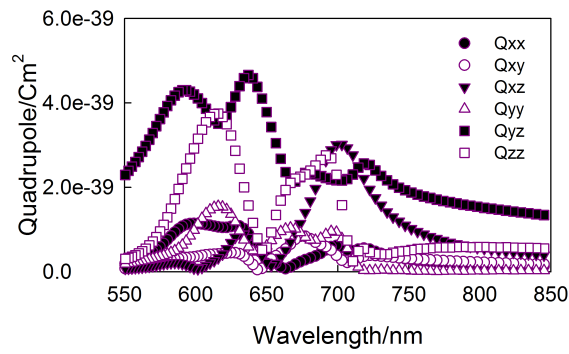


Figure 6.15: Quadrupole moment broadening for a typical orientation of the disordered particle in Figure 6.1B. For this illumination, light propagated in the \hat{y} direction and was polarized along \hat{z} . In the absence of disorder, the only excited quadrupole is in the yz plane, and forms a narrow peak around 630 nm. This data appeared in our previous studies of this particle [38]

Chapter 7

Future Directions and Conclusion

7.1 Future Studies of the Spiky Nanoshell

The far-field dipolar behavior of spiky nanoshells has been extensively studied in chapters 4 and 6. At this point, the most important unanswered question relates to the morphology variations present in the spikes. The studies in all previous chapters focused on particles where the simulated spike lengths were constrained to substantially less than the largest experimentally observed values, and the simulated spikes were simple cones with none of the sharp edges seen experimentally in SEM images. This was done largely due to memory and computational constraints. Outlier spikes would require a larger simulation, and characterizing additional morphology such as edges and angled spikes would require many more simulations due to the increased parameter space. With either the acquisition of a cluster or the next RAM architecture release, it should be possible to model these structures accurately as well. These questions are interesting for a few reasons. First, the Quadrupole Enhanced Raman Spectroscopy (QERS) effect is not fully understood, and by examining the effect of spike morphology (both sharpness and additional edges) this relationship might be

better understood. Second, the studies in chapter 6 assumed that the spiky nanoshells would have no mixing as they have no substantial chirality. This is certainly true in the simulation models used in those studies, however the addition of angled spikes could introduce mixing between these modes if there is incidental mismatches between the number of clockwise and counter-clockwise angled spikes.

While the near-field of the spiky nanoshell has been studied theoretically in substantial depth, it has not been examined in detail experimentally. The studies in chapter 5 for instance only sampled two excitation wavelength positions for SERS measurements (although these were measured across many particles). Performing single particle SERS measurements at more excitation wavelengths would enable a direct measurement of the enhancement factors, and provide an avenue for studying QERS in more detail. Other approaches of examining the near-field could also prove fruitful. One approach mentioned chapter 1 is EELS (electron energy-loss spectroscopy), which measures the amount of energy loss an electron beam experiences as a function of position near the particle. The resulting high resolution maps have been used to gain insight into the near-field behavior of bimetallic spiked particles [99], and could potentially provide the same information for the spiky nanoshells. These measurements may also provide additional supporting data for the QERS theory described in chapter 5.

In many respects the spiky nanoshell is ready to be tried for different applications. In addition to SERS, other techniques such as surface enhanced florescence [130] and surface enhanced resonant Raman spectroscopy [130] (SERRS) could also be attempted. SERRS is particularly interesting here because of the distribution of the enhancement volume around the spiky nanoshell. In particular, extremely large enhancement should occur near the spikes themselves. Combined with the extra

enhancement due to the resonant analyte, this may be sufficient to perform single molecule measurements [58, 89].

7.2 Future Studies of the Raspberry-Like Meta-molecules

The Raspberry-like Meta Molecule (Raspberry-MM) discussed briefly in chapter 3 is an extremely interesting particle, and should be given additional attention. As shown in Figure 7.1, this particle is composed of a 184 nm polystyrene core surrounded by a large number of dielectric coated gold beads. The dielectric coating insulates the beads from one another, and therefore the particle cannot support a strong global electric dipole. However, by forming a loop of beads around the core, a magnetic dipole mode can be sustained. This is described in detail in a manuscript in preparation.¹ The molecular dynamics techniques in chapter 3 were used to construct a realistic model of these particles to study their scattering behavior. Using the T-matrix technique for a single exposure described in chapter 3 (which assumed that there is no mode mixing), the multipolar scattering components were determined from an FDTD simulation. As shown in Figure 7.2, for a large Raspberry-MM, the magnetic dipole scattering is several times stronger than the electric dipole scattering, and there is an appreciable contribution from both the electric and magnetic quadrupole modes.

While it is straight forward to decompose the contributions of different scattering modes theoretically, doing it experimentally is more difficult. Given that the particle should only have strong dipole and quadrupole modes, the experimental design can

¹Synthetic Approach to Raspberry-like Metamolecules Exhibiting Strong Magnetic Resonances, Zhaoxia Qian, Simon P. Hastings, Chen Li, Brian Edward, Christine K McGinn, Nader Engheta, Zahra Fakhraai, So-Jung Park

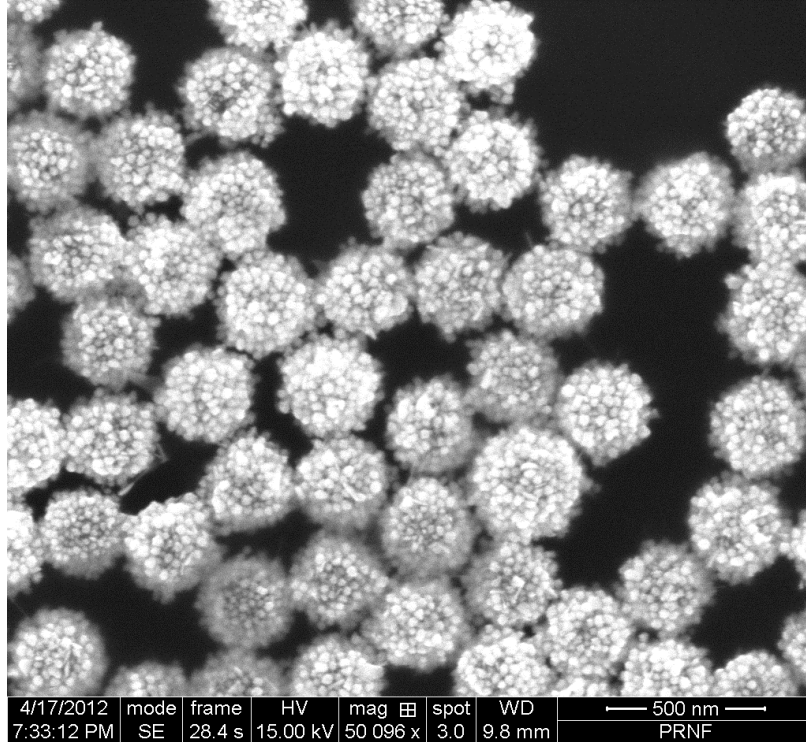


Figure 7.1: An SEM image of Raspberry-MM constructed around a 184 nm core. Image was generated by Zhaoxia Qian.

be simplified to take only those modes into account. In particular, in right-angle scattering (*i.e.*, 90 degree scattering), only the electric and magnetic dipoles should be present. However, while both dipole modes scatter at 90 degrees relative to the wave vector, for a linearly polarized light source they will also scatter perpendicularity to each other. This introduces a geometric separation which can be used to measure the contributions of each mode. Additionally, the polarization of the light scattered at 90 degrees will be determined based on the initial polarization. This provides a mechanism to measure background processes contributing to scattering which should not respect the polarizations required by these modes when they scatter. The strengths of these modes were explored experimentally with a home-built right-angle scattering spectrometer (shown in Figure 7.3).

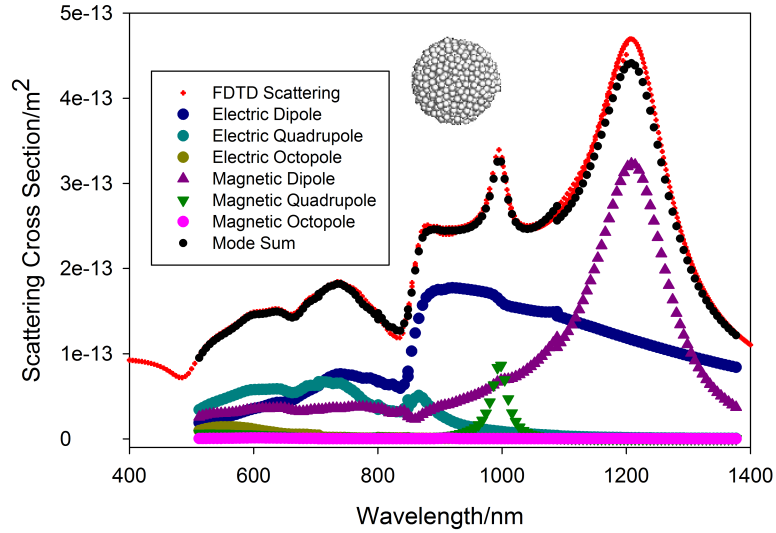


Figure 7.2: Mode decomposition for a large Raspberry-MM showing the relative strengths of each scattering mode. Data were generated with the assistance of Chen Li.

Using this system, the amount of light scattered at 90 degrees was measured as a function of wavelength and polarization. By comparing the four combinations of input and output linear polarization (input/output below), it was possible to measure the amount of magnetic and electric dipole scattering (shown in Figure 7.4). In these experiments, the 0/0 degree polarization configuration corresponds to electric dipole scattering, while the 90/90 degree polarization configuration corresponds to magnetic dipole scattering. In theory the mixed polarization measurements with 0/90 and 90/0 should be zero. However, several effects have been ignored in this analysis, including multiple-scattering and the small amounts of disorder-induced chirality in the structures. The cross-polarization configuration was used to estimate the background from these processes.

In order to establish that the spectrometer was working correctly, three control samples were measured that do not have strong magnetic dipole moments:

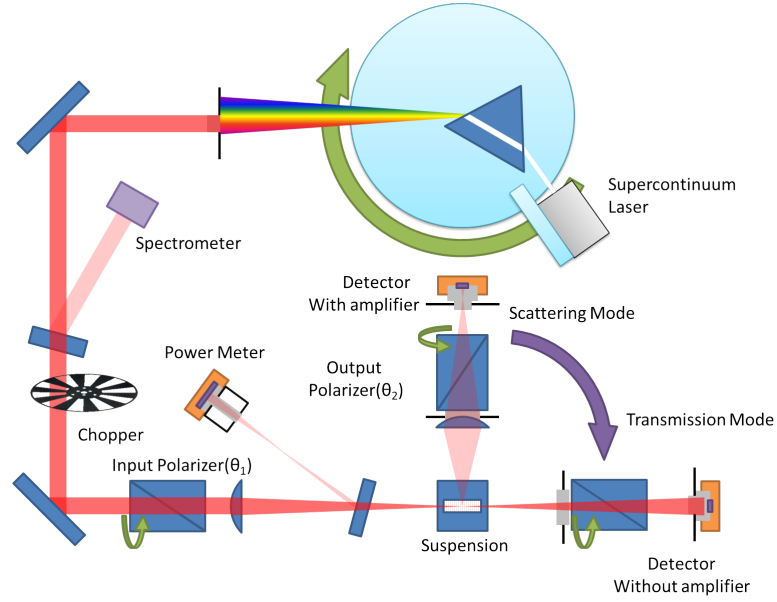


Figure 7.3: Simplified diagram of the optical configuration used to take the scattering measurements. A supercontinuum laser is fed into a prism which can rotate to select a narrow band of wavelengths. This signal is monitored with a spectrometer to determine the wavelength. The signal is chopped in order to modulate it at 1 kHz, allowing very sensitive measurements using a fast Fourier transform. The beam is then polarized to an angle θ_1 , passes through a lens, and a power meter is used to normalize the results to the incident power, taking into account any beam polarization. The beam then passes through the sample. Depending on the configuration of the measurement stage, light is measured at 90 degrees or at 0 degrees, and in those positions the level of magnification and amplification is tuned to avoid saturating the detector. This diagram was prepared with the assistance of Brian Edwards.

gold nanospheres, gold nanoshells, and polystyrene nanospheres. The polystyrene nanospheres are made of a dielectric material and are small compared to the wavelength. As a result, they should undergo Rayleigh scattering with the characteristic λ^{-4} cross section dependence, clearly visible in the data. Three different Raspberry-MM particles were measured, as shown in Figure 7.4D-F. While in Figure 7.4D, 56 nm core particles are shown to have very little (although still measurable) levels of magnetic dipole scattering, Figure 7.4E (95 nm core Raspberry-MM) and Figure 7.4F (184 nm core Raspberry-MM) both show substantial magnetic dipole activity. These

results indicate that the magnetic dipole position and strength are tuneable, with larger particles having stronger magnetic dipole scattering modes further into the near-IR. Importantly, the largest Raspberry-MM has a magnetic dipole scattering mode which is stronger than the electric scattering mode, opening up avenues for additional investigation. This is despite the fact that the wavelength range measured is on the shoulder of the magnetic dipole according to the FDTD model, and suggests that the true magnetic dipole is dramatically stronger than the electric dipole at peak scattering.

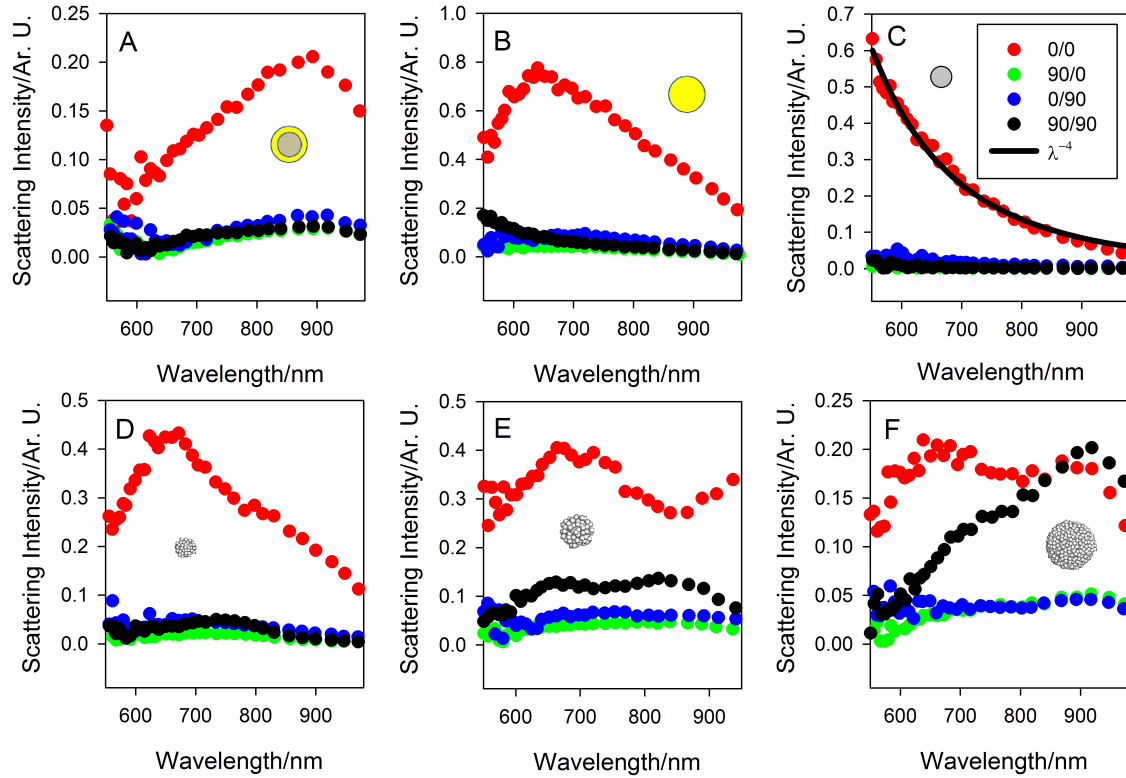


Figure 7.4: Right-angle scattering for four different polarization combinations, where the first polarization number refers to the incident polarization and the second to the receiving polarization filter. 90 degrees indicates that the polarization is in the plane of the optics table, while 0 degrees indicates that it is perpendicular to the optics table. A. Gold nanospheres, B. gold nanoshells, C. polystyrene nanospheres with λ^{-4} curve for comparison, D. 56 nm core Raspberry-MM, E. 95 nm core Raspberry-MM, F. 184 nm core Raspberry-MM. Insets show a diagram of the particle and are not to scale. The 0/0 configuration measures the amount of electric dipole scattering, while the 90/90 configuration measures the amount of magnetic dipole scattering.

Moving forward, there is a substantial amount of refinement possible for these measurements. The polystyrene scattering study provides quantitative confirmation that the spectrometer is not introducing spectral features while the nanosphere and nanoshell provide solid evidence that the signal to noise ratio is sufficient in these measurements. In order to characterize this spectrometer fully, it is necessary to perform repeated measurements on a single sample. This will measure the magnitude of random uncertainty in this device. Transmission measurements of the samples suggested that it is possible that there is a slight spectral offset being introduced at some stage, and this should be investigated. Due to settling of the particles, it may be necessary to change the experimental protocols - during the existing measurements, it was necessary to agitate the largest particle sample every 15 minutes in order to maintain consistent concentrations. It is not clear what effect this may have had on the experiment and protocols to minimize this would be desirable.

It may also be interesting to explore the effects of other tunable parameters on the magnetic scattering. Does the number of beads affect the scattering peak? Do larger beads make the particles more absorbent? What effect does the local dielectric environment have on the scattering behavior?

Simulation studies have also suggested that the Raspberry-MM may possess a magnetic quadrupole scattering mode, supporting multiple loops of out of phase current. This possibility can be investigated by performing angular resolved scattering measurements. Christine McGinn² and Brian Edwards³ have designed and implemented a spectrometer for this purpose. An index matched cylindrical cuvette was prepared, allowing the scattering detector to be rotated to a desired angle during

²Christine McGinn is a student participating in the Research Experiences for Undergraduates program (REU, NSF MRSEC grant DMR-1120901) at the Department of Electrical and Systems Engineering in the University of Pennsylvania. She is affiliated with the Department of Engineering, Swarthmore College, Swarthmore, Pennsylvania.

³Department of Electrical and Systems Engineering, University of Pennsylvania

these measurement. Preliminary proof of concept measurements were performed by Christine McGinn, as shown in Figure 7.5 for a 400 nm diameter gold sphere. The asymmetry and shape mismatch should improve with additional experimental refinement.

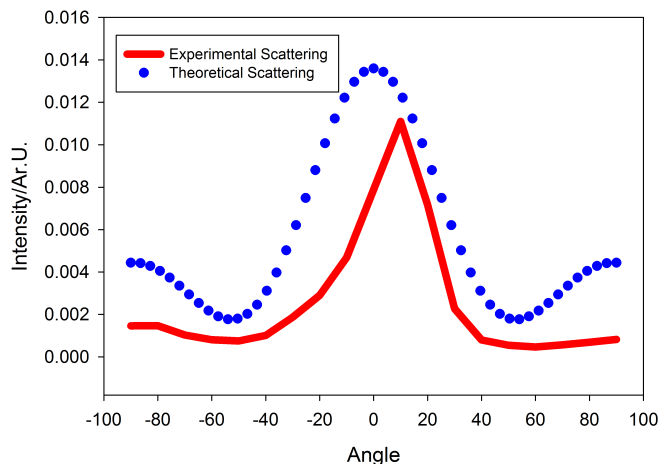


Figure 7.5: Theoretical and experimental angular resolved scattering for the 0/0 degree polarization setting, performed on 400 nm gold spheres at 950 nm incident wavelength. Data courtesy of Christine McGinn.

With the capability to analyze the angular dependence on the scattering cross section of a sample of particles, it may be worth measuring the angular dependence of spiky nanoshells in water. Due to the use of a chopper and Fourier analysis in the spectrometer, even very weak signals from the quadrupole may be detectable. If this is not the case, the quadrupole scattering could be strengthened by switching to solvents with a higher refractive index.

The Raspberry-MMs open up a number of possibilities for applications. Perhaps the most interesting is the ability to make a meta-material with a negative value of μ . From a future work perspective, this has several different aspects. First, the theoretical toolset for determining the effective μ and ϵ of a material must be established.

The first step in this process is determining the electric polarizability α_e and magnetic polarizability, α_m of the particle. This can be accomplished based on the definition of polarizability: $\alpha_m = \frac{m_h}{H_0(0)}$ [9], where m_h is the magnetic dipole induced by an incident magnetic field, $H_0(0)$ (and likewise for electric polarizability, α_e). These parameters are available as a function of frequency from simulation already. As discussed in chapter 5, the dipoles estimated from the currents in the simulation may be an overestimate due to a systematic simulation error. An alternative approach would be to use the total cross section determined by the methods in chapters 5 or 6 to calculate the effective dipole moment directly. From either of these approaches, it is fairly easy to determine the effective material parameters of the medium [9]:

$$\mu_{eff}^{(r)} = \mu_0 \left(1 + \frac{1}{N_d^{-1} \alpha_m^{-1} - 1/3} \right) \quad (7.2.1)$$

$$\mu_{eff}^{(p)} = \mu_0 \left(1 + \frac{1}{N_d^{-1} [\alpha_m^{-1} + i(k_b^3/6\pi)] - 1/3} \right) \quad (7.2.2)$$

$$\varepsilon_{eff}^{(r)} = \varepsilon_0 \left(1 + \frac{1}{\varepsilon_0 N_d^{-1} \alpha_e^{-1} - 1/3} \right) \quad (7.2.3)$$

$$\varepsilon_{eff}^{(p)} = \varepsilon_0 \left(1 + \frac{1}{\varepsilon_0 N_d^{-1} [\alpha_e^{-1} + i(k_b^3/6\pi\varepsilon_0)] - 1/3} \right) \quad (7.2.4)$$

Where k_b is the background wave number, and N_d is the number density of resonators. The effective medium parameters labeled with (r) correspond to randomly placed particles, while those labeled with (p) have a periodic lattice. In this fashion, the effective permeability of a suspension of the Raspberry-MMs can be determined, and potentially a region of unusual permittivity or permeability will be found. Theoretical studies can be followed up by experimental studies where a sample of such

exotic material could be made and characterized by UV-vis spectroscopy and ellipsometry.

7.3 Future Studies on Reconstructing the T-Matrix with FDTD

The algorithm for determining the T-matrix described in chapter 6 is under-characterized. For instance, the convergence behavior as the number of simulations is increased is currently unknown, and likewise it is unclear how this behavior changes with the size of the T-matrix employed. Another interesting question is the relationship between the grid spacing used for numeric integration and the error achieved, which should increase with multipole order.

In addition to characterizing the algorithm better, a number of simple modifications suggest themselves. For ease of calculation the pseudoinverse was used to invert the over-determined matrix problem line by line, but this approach loses some information. In particular, the T-matrix has a symmetry constraint [123]:

$$T_{-m'n'(-m)n}^{(ij)} = (-1)^{m'+m} T_{mnm'n'}^{(ji)} \quad (7.3.1)$$

For $i, j = 1$ or 2 . Enforcing this constraint decreases the number of free parameters to be determined substantially. Additionally, the T-matrix is physically constrained to conserve energy, and the fitting algorithm should enforce this. This is particularly useful as it provides magnitude constraints of the fitting parameters, which will substantially reduce over-fitting.

One interesting extension to this algorithm would relate the far-field parameters to the near-field values observed in simulation. At any given point on the structure,

the effect of each mode on the local electric field could be determined by assuming that the field at that point is a linear function of the incident waves:

$$\vec{E}(\vec{r}, \omega) = \sum_{n,m}^{N_{max}} a_{m,n}^I f(r, \omega)_{m,n} \quad (7.3.2)$$

Where $f(r, \omega)_{m,n}$ is determined by solving a linear algebra problem at each point in space similar to the T-matrix inversion described in chapter 6 and $a_{m,n}^I$ are the incident plane wave VSHWF coefficients. This approach automatically includes hybridization effects by using lower order modes as a ‘marker’ for the higher order modes. This is equivalent to solving for the net field of an entire column of the T-matrix, and is a somewhat simpler calculation as a result. The field/mode mapping function $f(r, \omega)_{m,n}$ is then extremely useful for understanding the behavior of the particle, as it is possible to plot it separately for each mode, and thereby determine the relative strengths and spatial distributions of different order hybrid multipoles. By using this approach with FDTD in particular, the near and far-field behavior of an arbitrary particle can be understood in the VSHWF basis space.

7.4 Summary and Conclusion

This dissertation presents detailed studies exploring the optical properties of spiky gold nanoshells. In chapter 4, the effects of the synthesis parameters on the particle morphology and extinction were measured. The relationship between the morphology and the extinction was explored using FDTD modeling. Spike length was determined to be the single most important determining factor in the LSPR position, and modeling indicated that a complete conductive shell must be present to explain observed extinction spectrum. These studies established that the spiky nanoshell could be

tailor-made for scattering activity from the red-visible region to the NIR region.

Chapter 5 explored the near-field behavior of the spiky nanoshell using SERS. These results established that the near-field behavior of the spiky nanoshell is dominated by the quadrupole resonance, providing the first demonstration of the QERS phenomenon - a dark quadrupole inducing substantial enhancement to the Raman cross section. As important, this work explored the effect of disorder on the modes present in this particle. Disorder among a large number of spikes was shown to result in surprisingly strong and consistent near-field behavior. Part of this consistency is geometric - in a disordered structure, the quadrupole is able to induce fields on many spikes, some of which were forbidden to be excited in the ordered structure. Additionally, while an individual quadrupole moment spectrum is quite noisy, the disorder has enabled all six quadrupole moments to be induced by the far-field, allowing the variations between the moments to be averaged out.

Chapter 6 developed an extremely general FDTD-based method of determining the T-matrix which describes the scattering behavior of the spiky nanoshell. Due to the heterogeneity in the structure, incident components of one mode are able to be scattered as other modes. In particular, the excitation of all quadrupole moments seen in chapter 5 can now be understood to be the result of several different types of mode mixing. Not only does the incident quadrupole field induce other quadrupolar modes, but the incident dipole is able to induce quadrupolar excitation, explaining the red shift in the quadrupole moments seen in chapter 5. Further, the incident quadrupole modes are scattered partially as outgoing dipoles, which induces an interference pattern observed in about 10% of the sampled particles both experimentally and theoretically.

This work has benefited from two over-arching philosophies. First, when possible,

the simulation and analysis of a nanostructure should be automated. This allows the parameter space for a structure to be fully explored. Second, a structure should be modeled with as much of the complexity present in nature as possible. By simplifying the structure in stages (as was done with individual cones in chapter 4 and the donut model in chapter 5), it is possible to identify which characteristics of the structure are responsible for its behavior. Together, these two approaches allow in depth characterization of almost any particle family.

This approach was very successful when applied to the spiky gold nanoshells. Spiky nanoshells at first glance appear very difficult to study. By producing realistic structures which encompass the range of morphologies seen experimentally, even these very disordered structures can be understood. Because the disorder occurs over many spikes simultaneously, the resulting structure is not sensitive to perturbations in geometry, but rather depends on the average value. Structural heterogeneity inducing electrical homogeneity is a surprising and non-intuitive result, which may have substantial impact on the future design of nanostructures. Although the far-field behavior depends on the average values of these parameters, the resulting particle is not equivalent to a structure composed with those average values due to mode mixing. This emergent behavior provides an unusually robust mechanism for exotic particle behavior and is applicable to many other systems.

Appendix A

Glossary of Terms

- BDAC - Benzyltrimethylhexadecylammoniumchloride, a surfactant used in nanoparticle synthesis
- CTAB - Hexadecyltrimethylammonium bromide, a surfactant used in nanoparticle synthesis
- DDA - The discrete dipole approximation method for determining the scattering of light from a discrete nanoparticle.
- EBCM - Extended boundary condition method, a surface integration approach to determining the T-matrix
- EELS - Electron energy-loss spectroscopy, a Transmission Electron Microscopy (TEM) technique which measures electron energy loss as a function of position around the particle
- FDFD - Finite-difference frequency-domain, a discrete technique for simulating Maxwell's equations in the vicinity of a nanoparticle in frequency space.

- FDTD - Finite-difference time-domain simulations, a discrete technique for simulating Maxwell's equations in the vicinity of a nanoparticle by advancing time, used here to predict the interaction of an incident light wave with a nanoparticle.
- FEM - The finite element method for determining the scattering of light at a single frequency from a nanoparticle.
- IEBCM - An iterative version of the extended boundary condition method for determining the T-matrix.
- LSM - Least squares method, the Finite-difference time-domain based method for determining the T-matrix described in chapter six.
- LSPR - Localized surface plasmon resonance, resonant excitation of charge in a discrete nanoparticle.
- NIR - Near infrared, the light wavelength region between approximately 750 nm and 2500 nm.
- PEC - Perfect electrical conductor, a theoretical material with infinite conductivity.
- PMM - The point matching method for determining the T-matrix by matching coefficients on either side of a surface boundary in a least-squares sense.
- QERS - Quadrupole enhanced Raman scattering, surface enhanced Raman scattering performed using a dark quadrupole mode, as described in chapter 5.
- Raspberry-MM - Raspberry-like magnetic meta-molecules, a class of nanoparticle composed of a large number of insulated spheres surrounding a dielectric core, as described in chapters 3 and 7.

- SEM - Scanning electron microscopy, a technique which images samples by moving an electron beam across the surface and examining the resulting signals.
- SERRS - Surface enhanced resonant Raman scattering, a spectroscopic technique where Surface enhanced Raman scattering is performed on a resonant analyte, resulting in several additional orders of magnitude of enhancement.
- SERS - Surface enhanced Raman scattering, a spectroscopic technique where Raman scattering is greatly enhanced due to the presence of a plasmonic surface.
- SPR - Surface plasmon resonance, used here to represent resonant excitation of charge in a discrete nanoparticle.
- T-matrix - the matrix mapping the incident vector spherical harmonic wave function coefficients to the outgoing wave function coefficients.
- TEM - Transmission electron microscopy, an imaging technique where electrons pass through a sample and the electrons which are transmitted are used to image the sample.
- TFSF Source - Total-field scattered-field source, a finite-difference time-domain specific light source where the injected light wave is constrained to the interior of a volume such that only the scattered field occurs outside the volume while the total field is present within the volume.
- UV-vis(-NIR) - absorption spectroscopy done in the ultraviolet, visible, and near-infrared regions
- VSHWF - Vector spherical harmonic wave functions, the spherical traveling wave solutions to Maxwell's equations for a spherically symmetric system.

Bibliography

- [1] Delaunay Triangulation - MATLAB & Simulink.
<http://www.mathworks.com/help/matlab/math/delaunay-triangulation.html>
Viewed on August 28, 2014.
- [2] Lumerical Solutions, Inc. — Innovative Photonic Design Tools.
<https://www.lumerical.com/> Viewed on August 28, 2014.
- [3] MATLAB Central. Thread Subject: 3D sphere defined by equally spaced points.
https://www.mathworks.com/matlabcentral/newsreader/view_thread/21747
Viewed on August 28, 2014.
- [4] Moore-Penrose pseudoinverse of matrix - MATLAB pinv. <http://www.mathworks.com/help/matlab/ref/pinv.html>, Viewed on August 30, 2014.
- [5] Aftab Ahmed and Reuven Gordon. Directivity enhanced Raman spectroscopy using nanoantennas. *Nano letters*, 11(4):1800–3, April 2011.
- [6] A. C. Albrecht and M.C. Hutley. On the Dependence of Vibrational Raman Intensity on the Wavelength of Incident Light. *The Journal of Chemical Physics*, 55(9):4438–4443, 1971.

- [7] M.G. Albrecht and J.A. Creighton. Anomalously Intense Raman Spectra of Pyridine at a Silver Electrode. *Journal of the American Chemical Society*, 99(15):5215–5217, 1977.
- [8] Paula Aldeanueva-Potel, Enrique Carbó-Argibay, Nicolás Pazos-Pérez, Silvia Barbosa, Isabel Pastoriza-Santos, Ramón A. Alvarez-Puebla, and Luis M. Liz-Marzán. Spiked Gold Beads as Substrates for Single-Particle SERS. *Chemphyschem : a European journal of chemical physics and physical chemistry*, 13(10):2561–5, July 2012.
- [9] A. Alù, A. Salandrino, and N. Engheta. Negative effective permeability and left-handed materials at optical frequencies. *Optics express*, 14(4):1557–67, February 2006.
- [10] Christos Argyropoulos, Pai-Yen Chen, Francesco Monticone, Giuseppe D’Aguanno, and Andrea Alù. Nonlinear Plasmonic Cloaks to Realize Giant All-Optical Scattering Switching. *Physical Review Letters*, 108(26):263905, June 2012.
- [11] J.S. Asvestas, J.J. Bowman, P.L. Christiansen, O. Einarsson, R.E. Kleinman, D.L. Sengupta, T.B.A. Senior, F.B. Sleator, P.L.E. Uslenghi, and N.R. Zitron. *Electromagnetic and Acoustic Scattering by Simple Shapes*. Hemisphere Publishing Corporation, 1987.
- [12] Leslie Au, Xianmao Lu, and Younan Xia. A Comparative Study of Galvanic Replacement Reactions Involving Ag Nanocubes and AuCl_2^- or AuCl_4^- . *Advanced materials*, 20(13):2517–2522, January 2008.

- [13] Matthew J. Banholzer, Jill E. Millstone, Lidong Qin, and Chad A. Mirkin. Rationally designed nanostructures for surface-enhanced Raman spectroscopy. *Chemical Society reviews*, 37(5):885–97, May 2008.
- [14] Rizia Bardhan, Surbhi Lal, Amit Joshi, and Naomi J. Halas. Theranostic Nanoshells: From Probe Design to Imaging and Treatment of Cancer. *Accounts of chemical research*, 44(10):936–946, 2011.
- [15] E. Bendito, A. Carmona, A. M. Encinas, J. M. Gesto, A. Gómez, C. Mouriño, and M.T. Sánchez. Computational cost of the Fekete problem I: The Forces Method on the 2-sphere. *Journal of Computational Physics*, 228(9):3288–3306, May 2009.
- [16] Craig F. Bohren and Donald R. Huffman. *Absorption and Scattering of Light by Small Particles*. WILEY-VCH Verlag GmbH & Co. KGaA, Weinheim, 2004.
- [17] Bruce E. Brinson, J. Britt Lassiter, Carly S. Levin, Rizia Bardhan, Nikolay Mirin, and Naomi J. Halas. Nanoshells Made Easy: Improving Au Layer Growth on Nanoparticle Surfaces. *Langmuir*, 24(24):14166–71, December 2008.
- [18] A.D. Buckingham. Permanent and Induced Molecular Moments and Long-Range Intermolecular Forces. *Advances In Chemical Physics*, 12:107–142, 1967.
- [19] Jon P. Camden, Jon A. Dieringer, Yingmin Wang, David J. Masiello, Lawrence D. Marks, George C. Schatz, and Richard P. Van Duyne. Probing the Structure of Single-Molecule Surface-Enhanced Raman Scattering Hot Spots. *Journal of the American Chemical Society*, 130(38):12616–7, September 2008.

- [20] Nicole Cathcart and Vladimir Kitaev. Multifaceted prismatic silver nanoparticles: synthesis by chloride-directed selective growth from thiolate-protected clusters and SERS properties. *Nanoscale*, 4(22):6981–9, November 2012.
- [21] Sehoon Chang, Hyunhyub Ko, Srikanth Singamaneni, Ray Gunawidjaja, and Vladimir V. Tsukruk. Nanoporous Membranes with Mixed Nanoclusters for Raman-Based Label-Free Monitoring of Peroxide Compounds. *Analytical chemistry*, 81(14):5740–8, July 2009.
- [22] Xi-Jun Chen, Brenda L. Sanchez-Gaytan, Zhaoxia Qian, and So-Jung Park. Noble metal nanoparticles in DNA detection and delivery. *WIREs Nanomed Nanobiotechnol*, 4(3):273–90, 2012.
- [23] Toon Coenen, Felipe Bernal Arango, A. Femius Koenderink, and Albert Polman. Directional emission from a single plasmonic scatterer. *Nature communications*, 5:3250, January 2014.
- [24] Samuel S. R. Dasary, Anant Kumar Singh, Dulal Senapati, Hongtao Yu, and Paresh Chandra Ray. Gold Nanoparticle Based Label-Free SERS Probe for Ultrasensitive and Selective Detection of Trinitrotoluene. *Journal of the American Chemical Society*, 131(38):13806–12, September 2009.
- [25] Joseph S. Duchene, Wenxin Niu, John M. Abendroth, Qi Sun, Wenbo Zhao, Fengwei Huo, and W. David Wei. Halide Anions as Shape-Directing Agents for Obtaining High-Quality Anisotropic Gold Nanostructures. *Chemistry of Materials*, 25:1392–1399, 2013.
- [26] Jonathan A. Fan, Kui Bao, Chihhui Wu, Jiming Bao, Rizia Bardhan, Naomi J. Halas, Vinothan N. Manoharan, Gennady Shvets, Peter Nordlander, and Fed-

- erico Capasso. Fano-like Interference in Self-Assembled Plasmonic Quadrumer Clusters. *Nano letters*, 10(11):4680–5, November 2010.
- [27] John R. Ferraro, Kazuo Nakamoto, and Chris W. Brown. *Introductory Raman Spectroscopy*. Academic Press, San Diego, 2nd edition, 2003.
- [28] A. Filankembo, S. Giorgio, I. Lisiecki, and M. P. Pileni. Is the Anion the Major Parameter in the Shape Control of Nanocrystals? *Journal of physical chemistry B*, 107:7492–7500, 2003.
- [29] Niti Garg, Clark Scholl, Ashok Mohanty, and Rongchao Jin. The role of Bromide Ions in Seeding Growth of Au Nanorods. *Langmuir*, 26(12):10271–6, June 2010.
- [30] Rebecca S. Golightly, William E. Doering, and Michael J. Natan. Surface-Enhanced Raman Spectroscopy and Homeland Security: a Perfect Match? *ACS nano*, 3(10):2859–69, October 2009.
- [31] David J. Griffiths. *Introduction to Electrodynamics*. Prentice-Hall, 3rd edition, 1999.
- [32] Andrés Guerrero-Martínez, Silvia Barbosa, Isabel Pastoriza-Santos, and Luis M. Liz-Marzán. Nanostars shine bright for you. *Current Opinion in Colloid & Interface Science*, 16(2):118–127, April 2011.
- [33] Tai Hwan Ha, Hee-Joon Koo, and Bong Hyun Chung. Shape-Controlled Syntheses of Gold Nanoprisms and Nanorods Influenced by Specific Adsorption of Halide Ions. *The Journal of Physical Chemistry C*, 111:1123–1130, 2007.
- [34] Encai Hao, Ryan C. Bailey, George C. Schatz, Joseph T. Hupp, and Shuyou Li. Synthesis and Optical Properties of “Branched” Gold Nanocrystals. *Nano Letters*, 4(2):327–330, February 2004.

- [35] Feng Hao, Colleen L. Nehl, Jason H. Hafner, and Peter Nordlander. Plasmon Resonances of a Gold Nanostar. *Nano letters*, 7(3):729–32, March 2007.
- [36] Feng Hao, Peter Nordlander, Yannick Sonnefraud, Pol Van Dorpe, and Stefan A. Maier. Tunability of Subradiant Dipolar and Fano-Type Plasmon Resonances in Metallic Ring/Disk Cavities: Implications for Nanoscale Optical Sensing. *ACS nano*, 3(3):643–52, March 2009.
- [37] Feng Hao, Yannick Sonnefraud, Pol Van Dorpe, Stefan A. Maier, Naomi J. Halas, and Peter Nordlander. Symmetry Breaking in Plasmonic Nanocavities: Subradiant LSPR Sensing and a Tunable Fano Resonance. *Nano letters*, 8(11):3983–8, November 2008.
- [38] Simon P. Hastings, Pattanawit Swanglap, Zhaoxia Qian, Ying Fang, So-Jung Park, Stephan Link, Nader Engheta, and Zahra Fakhraai. Quadrupole-Enhanced Raman Scattering. *ACS Nano*, 8(9):9025–9034, 2014.
- [39] Christy L. Haynes, Adam D. McFarland, and Richard P. Van Duyne. Surface-Enhanced Raman Spectroscopy. *Analytical chemistry*, 77(17):338–346, 2005.
- [40] Christy L. Haynes and Richard P. Van Duyne. Plasmon-Sampled Surface-Enhanced Raman Excitation Spectroscopy. *The Journal of Physical Chemistry B*, 107(30):7426–7433, July 2003.
- [41] W.M. Haynes, editor. *CRC Handbook of Chemistry and Physics*. CRC Press/Taylor and Francis, Boca Raton, FL, (internet version 2015) 95th edition.
- [42] W. Hermoso, T. V. Alves, F. R. Ornellas, and P. H. C. Camargo. Comparative study on the far-field spectra and near-field amplitudes for silver and gold

- nanocubes irradiated at 514, 633 and 785 nm as a function of the edge length. *The European Physical Journal D*, 66(5):1–11, May 2012.
- [43] Joseph B. Herzog, Mark W. Knight, Yajing Li, Kenneth M. Evans, Naomi J. Halas, and Douglas Natelson. Dark Plasmons in Hot Spot Generation and Polarization in Interelectrode Nanoscale Junctions. *Nano letters*, 13(3):1359–64, March 2013.
- [44] Leon R. Hirsch, Andre M. Gobin, Amanda R. Lowery, Felicia. Tam, Rebekah A. Drezek, Naomi J. Halas, and Jennifer L. West. Metal Nanoshells. *Annals of biomedical engineering*, 34(1):15–22, January 2006.
- [45] Seongmin Hong and Xiao Li. Optimal Size of Gold Nanoparticles for Surface-Enhanced Raman Spectroscopy under Different Conditions. *Journal of Nanomaterials*, 2013:1–9, 2013.
- [46] Ping-Ji Huang, Li-Lin Tay, Jamshid Tanha, Shannon Ryan, and Lai-Kwan Chau. Single-Domain Antibody-Conjugated Nanoaggregate-Embedded Beads for Targeted Detection of Pathogenic Bacteria. *Chemistry A European Journal*, 15(37):9330–4, September 2009.
- [47] Xiaohua Huang, Prashant K. Jain, Ivan H. El-Sayed, and Mostafa A. El-Sayed. Plasmonic photothermal therapy (PPTT) using gold nanoparticles. *Lasers in medical science*, 23(3):217–28, July 2008.
- [48] L.B. Hunt. The True Story of Purple of Cassius. *Gold Bulletin*, 9(4):134–139, 1976.
- [49] Umran S. Inan and Robert A. Marshall. *Numerical Electromagnetics The FDTD Method*. Cambridge University Press, New York, 2011.

- [50] Magdy F. Iskander, Akhlesh Lakhtakia, and Carl H. Durney. A New Procedure for Improving the Solution Stability and Extending the Frequency Range of the EBCM. *IEEE Transactions on Antennas and Propagation*, AP-31(2):317–324, 1983.
- [51] J. B. Jackson and N. J. Halas. Silver Nanoshells: Variations in Morphologies and Optical Properties. *The Journal of Physical Chemistry B*, 105(14):2743–2746, April 2001.
- [52] Nikhil R. Jana, Latha Gearheart, and Catherine J. Murphy. Wet Chemical Synthesis of High Aspect Ratio Cylindrical Gold Nanorods. *Journal of physical chemistry B*, 105:4065–4067, 2001.
- [53] David L. Jeanmaire and Richard P. Van Duyne. Surface Raman spectroelectrochemistry: Part I. Heterocyclic, aromatic, and aliphatic amines adsorbed on the anodized silver electrode. *Journal of Electroanalytical Chemistry and Interfacial Electrochemistry*, 84:1–20, 1977.
- [54] Virginia Joseph, Andrea Matschulat, Jörg Polte, Simone Rolf, Franziska Emerling, and Janina Kneipp. SERS enhancement of gold nanospheres of defined size. *Journal of Raman Spectroscopy*, 42(9):1736–1742, September 2011.
- [55] F. Michael Kahnert, Jakob J. Stamnes, and Knut Stamnes. Application of the extended boundary condition method to particles with sharp edges: a comparison of two surface integration approaches. *Applied Optics*, 40(18):3101–3109, 2001.
- [56] Samuel L. Kleinman, Bhavya Sharma, Martin G. Blaber, Anne-Isabelle Henry, Nicholas Valley, R. Griffith Freeman, Michael J. Natan, George C. Schatz, and

- Richard P. Van Duyne. Structure Enhancement Factor Relationships in Single Gold Nanoantennas by Surface-Enhanced Raman Excitation Spectroscopy. *Journal of the American Chemical Society*, 135(1):301–8, January 2013.
- [57] Janina Kneipp, Harald Kneipp, Burghardt Wittig, and Katrin Kneipp. Following the Dynamics of pH in Endosomes of Live Cells with SERS Nanosensors. *The Journal of Physical Chemistry C*, 114(16):7421–7426, April 2010.
- [58] Katrin Kneipp, Yang Wang, Harald Kneipp, Lev Perelman, Irving Itzkan, Ramachandra Dasari, and Michael Feld. Single Molecule Detection Using Surface-Enhanced Raman Scattering (SERS). *Physical Review Letters*, 78(9):1667–1670, 1997.
- [59] Amar S. Kumbhar, Mark K. Kinnan, and George Chumanov. Multipole Plasmon Resonances of Submicron Silver Particles. *Journal of the American Chemical Society*, 127(36):12444–5, September 2005.
- [60] Akhlesh Lakhtakia. Iterative extended boundary condition method for scattering by objects of high aspect ratios. *J. Acoust. Soc. Am.*, 76(September 1984):906–912, 1984.
- [61] Surbhi Lal, Susan E. Clare, and Naomi J. Halas. Nanoshell-Enabled Photothermal Cancer Therapy: Impending Clinical Impact. *Accounts of chemical research*, 41(12):1842–1851, 2008.
- [62] J. Britt Lassiter, Heidar Sobhani, Jonathan A. Fan, Janardan Kundu, Federico Capasso, Peter Nordlander, and Naomi J. Halas. Fano Resonances in Plasmonic Nanoclusters: Geometrical and Chemical Tunability. *Nano letters*, 10(8):3184–9, August 2010.

- [63] Eunice S. P. Leong, Yan Jun Liu, Bing Wang, and Jinghua Teng. Effect of Surface Morphology on the Optical Properties in Metal-Dielectric-Metal Thin Film Systems. *ACS applied materials & interfaces*, 3(4):1148–53, April 2011.
- [64] Carly S. Levin, Janardan Kundu, Aoune Barhoumi, and Naomi J. Halas. Nanoshell-based substrates for surface enhanced spectroscopic detection of biomolecules. *The Analyst*, 134(9):1745–50, September 2009.
- [65] Hongyan Liang, Zhipeng Li, Wenzhong Wang, Youshi Wu, and Hongxing Xu. Highly Surface-roughened “Flower-like” Silver Nanoparticles for Extremely Sensitive Substrates of Surface-enhanced Raman Scattering. *Advanced Materials*, 21(45):4614–4618, December 2009.
- [66] Dong-Kwon Lim, Ki-Seok Jeon, Jae-Ho Hwang, Hyoki Kim, Sunghoon Kwon, Yung Doug Suh, and Jwa-Min Nam. Highly uniform and reproducible surface-enhanced Raman scattering from DNA-tailorable nanoparticles with 1-nm interior gap. *Nature nanotechnology*, 6(7):452–60, July 2011.
- [67] Vincent L.Y. Loke, Timo A. Nieminen, Norman R. Heckenberg, and Halina Rubinsztein-Dunlop. T-Matrix calculation via discrete dipole approximation, point matching and exploiting symmetry. *Journal of Quantitative Spectroscopy and Radiative Transfer*, 110(14-16):1460–1471, September 2009.
- [68] Vincent L.Y. Loke, Timo A. Nieminen, Simon J. Parkin, Norman R. Heckenberg, and Halina Rubinsztein-Dunlop. FDFD/T-matrix hybrid method. *Journal of Quantitative Spectroscopy and Radiative Transfer*, 106(1-3):274–284, July 2007.

- [69] John. R. Lombardi and Ronald. L. Birke. A Unified Approach to Surface-Enhanced Raman Spectroscopy. *Journal of Physical Chemistry C*, 112(14):5605–5617, April 2008.
- [70] F López-Tejeira, R Paniagua-Domínguez, R Rodríguez-Oliveros, and J A Sánchez-Gil. Fano-like interference of plasmon resonances at a single rod-shaped nanoantenna. *New Journal of Physics*, 14(2):023035, February 2012.
- [71] Fernando López-Tejeira, Ramón Paniagua-Domínguez, and José A. Sánchez-Gil. High-Performance Nanosensors Based on Plasmonic Fano-like Interference: Probing Refractive Index with Individual Nanorice and Nanobelts. *ACS nano*, 6(10):8989–96, October 2012.
- [72] Boris Luk'yanchuk, Nikolay I. Zheludev, Stefan A. Maier, Naomi J. Halas, Peter Nordlander, Harald Giessen, and Chong Tow Chong. The Fano resonance in plasmonic nanostructures and metamaterials. *Nature materials*, 9(9):707–15, September 2010.
- [73] Daniel W. Mackowski. Discrete dipole moment method for calculation of the T matrix for nonspherical particles. *Journal of the Optical Society of America. A, Optics, image science, and vision*, 19(5):881–93, May 2002.
- [74] O. M. Magnussen. Ordered Anion Adlayers on Metal Electrode Surfaces. *Chemical reviews*, 102(3):679–725, March 2002.
- [75] Barbara J. Messinger, K. Ulrich Von Raben, Richard K. Chang, and Peter W. Barber. Local fields at the surface of noble-metal microspheres. *Physical Review B*, 24(2):649–657, 1981.

- [76] Gustav Mie. Beiträge zur Optik trüber Medien, speziell kolloidaler Metallösungen. *Annalen der Physik*, 330(3):377–445, 1908.
- [77] J. J. Mikulski and E. L. Murphy. The Computation of Electromagnetic Scattering from Concentric Spherical Structures. *IEEE Transactions on Antennas and Propagation*, 11(2):169–177, 1963.
- [78] Molly M. Miller and Anne A. Lazarides. Sensitivity of Metal Nanoparticle Surface Plasmon Resonance to the Dielectric Environment. *The journal of physical chemistry. B*, 109(46):21556–65, November 2005.
- [79] Jill E. Millstone, Sungho Park, Kevin L. Shuford, Lidong Qin, George C. Schatz, and Chad A. Mirkin. Observation of a Quadrupole Plasmon Mode for a Colloidal Solution of Gold Nanoprisms. *Journal of the American Chemical Society*, 127(15):5312–3, April 2005.
- [80] Jill E. Millstone, Wei Wei, Matthew R. Jones, Hyojong Yoo, and Chad A. Mirkin. Iodide Ions Control Seed-Mediated Growth of Anisotropic Gold Nanoparticles. *Nano letters*, 8(8):2526–2529, 2008.
- [81] Nikolay A. Mirin and Naomi J. Halas. Light-Bending Nanoparticles. *Nano letters*, 9(3):1255–1259, 2009.
- [82] Andrey E. Miroshnichenko, Sergej Flach, and Yuri S. Kivshar. Fano resonances in nanoscale structures. *Reviews of Modern Physics*, 82(3):2257–2298, August 2010.
- [83] F. Monticone, C. Argyropoulos, and A. Alù. Layered plasmonic cloaks to tailor the optical scattering at the nanoscale. *Scientific reports*, 2:912, January 2012.

- [84] Francesco Monticone, Christos Argyropoulos, and Andrea Alù. Multilayered Plasmonic Covers for Comblike Scattering Response and Optical Tagging. *Physical Review Letters*, 110(11):113901, March 2013.
- [85] Martin Moskovits. Surface-enhanced Raman spectroscopy: a brief retrospective. *Journal of Raman Spectroscopy*, 36(6-7):485–496, June 2005.
- [86] Shaunak Mukherjee, Heidar Sobhani, J. Britt Lassiter, Rizia Bardhan, Peter Nordlander, and Naomi J. Halas. Fano shells: Nanoparticles with Built-in Fano Resonances. *Nano letters*, 10(7):2694–701, July 2010.
- [87] Colleen L. Nehl, Nathaniel K. Grady, Glenn P. Goodrich, Felicia Tam, Naomi J. Halas, and Jason H. Hafner. Scattering Spectra of Single Gold Nanoshells. *Nano Letters*, 4(12):2355–2359, December 2004.
- [88] Colleen L. Nehl, Hongwei Liao, and Jason H. Hafner. Optical Properties of Star-Shaped Gold Nanoparticles. *Nano letters*, 6(4):683–8, April 2006.
- [89] Shuming Nie and Steven R. Emory. Probing Single Molecules and Single Nanoparticles by Surface-Enhanced Raman Scattering. *Science*, 275(5303):1102–1106, February 1997.
- [90] T.A. Nieminen, H. Rubinsztein-Dunlop, and N.R. Heckenberg. Calculation of the T-matrix: general considerations and application of the point-matching method. *Journal of Quantitative Spectroscopy and Radiative Transfer*, 79-80:1019–1029, June 2003.
- [91] Timo A. Nieminen, Vincent L. Y. Loke, Alexander B. Stilgoe, Gregor Knöner, Agata M. Braczyk, Norman R. Heckenberg, and Halina Rubinsztein-Dunlop.

- Optical tweezers computational toolbox. *Journal of Optics A*, 9:S196–S202, 2007.
- [92] Babak Nikoobakht and Mostafa A. El-Sayed. Preparation and Growth Mechanism of Gold Nanorods (NRs) Using Seed-Mediated Growth Method. *Chemistry of Materials*, 15(10):1957–1962, 2003.
- [93] S. J. Oldenburg, J. B. Jackson, S. L. Westcott, and N. J. Halas. Infrared extinction properties of gold nanoshells. *Applied Physics Letters*, 75(19):2897, 1999.
- [94] S.J. Oldenburg, R.D. Averitt, S.L. Westcott, and N.J. Halas. Nanoengineering of optical resonances. *Chemical Physics Letters*, 288(2-4):243–247, May 1998.
- [95] Steven J. Oldenburg, Sarah L. Westcott, Richard D. Averitt, and Naomi J. Halas. Surface enhanced Raman scattering in the near infrared using metal nanoshell substrates. *The Journal of Chemical Physics*, 111(10):4729, 1999.
- [96] D. W. Oxtoby, H. P. Gillis, and A. Campion. *Principles of Modern Chemistry*. Thomson Learning, Inc: Stamford, CT, 6th edition, 2008.
- [97] Charles Herach Papas. *Theory of Electromagnetic Wave Propagation*. Dover Publications, Inc., New York, 1988.
- [98] Emma Kathryn Payne, Kevin L. Shuford, Sungho Park, George C. Schatz, and Chad A. Mirkin. Multipole Plasmon Resonances in Gold Nanorods. *The journal of physical chemistry. B*, 110(5):2150–4, February 2006.
- [99] Srikanth Pedireddy, Anran Li, Michel Bosman, In Yee Phang, Shuzhou Li, and Xing Yi Ling. Synthesis of Spiky Ag-Au Octahedral Nanoparticles and

- Their Tunable Optical Properties. *The Journal of Physical Chemistry C*, 117(32):16640–16649, August 2013.
- [100] E. Prodan, C. Radloff, N. J. Halas, and P. Nordlander. A Hybridization Model for the Plasmon Response of Complex Nanostructures. *Science*, 302(5644):419–22, October 2003.
- [101] X.-M. Qian and S. M. Nie. Single-molecule and single-nanoparticle SERS: from fundamental mechanisms to biomedical applications. *Chemical Society reviews*, 37(5):912–20, May 2008.
- [102] Ximei Qian, Xiang-Hong Peng, Dominic O. Ansari, Qiqin Yin-Goen, Georgia Z. Chen, Dong M. Shin, Lily Yang, Andrew N. Young, May D. Wang, and Shuming Nie. *In vivo* tumor targeting and spectroscopic detection with surface-enhanced Raman nanoparticle tags. *Nature biotechnology*, 26(1):83–90, January 2008.
- [103] Jessica Rodríguez-Fernández, Carolina Novo, Viktor Myroshnychenko, Alison M. Funston, Ana Sánchez-Iglesias, Isabel Pastoriza-Santos, Jorge Pérez-Juste, F. Javier García de Abajo, Luis M. Liz-Marzán, and Paul Mulvaney. Spectroscopy, Imaging, and Modeling of Individual Gold Decahedra. *The Journal of Physical Chemistry C*, 113(43):18623–18631, October 2009.
- [104] Krista L Rule and Peter J Vikesland. Surface-Enhanced Resonance Raman Spectroscopy for the Rapid Detection of *Cryptosporidium parvum* and *Giardia lamblia*. *Environmental Science & Technology*, 43(4):1147–1152, February 2009.
- [105] Krishnendu Saha, Sarit S. Agasti, Chaekyu Kim, Xiaoning Li, and Vincent M. Rotello. Gold Nanoparticles in Chemical and Biological Sensing. *Chemical reviews*, 112(5):2739–79, May 2012.

- [106] Brenda L. Sanchez-Gaytan and So-Jung Park. Spiky Gold Nanoshells. *Langmuir : the ACS journal of surfaces and colloids*, 26(24):19170–4, December 2010.
- [107] Brenda L. Sanchez-Gaytan, Zhaoxia Qian, Simon P. Hastings, Michael L. Reza, Zahra Fakhraai, and So-Jung Park. Controlling the Topography and Surface Plasmon Resonance of Gold Nanoshells by a Templated Surfactant-Assisted Seed Growth Method. *The Journal of Physical Chemistry C*, 117(17):8916–8923, May 2013.
- [108] Brenda L. Sanchez-Gaytan, Pattanawit Swanglap, Thomas J. Lamkin, Robert J. Hickey, Zahra Fakhraai, Stephan Link, and So-Jung Park. Spiky Gold Nanoshells: Synthesis and Enhanced Scattering Properties. *The Journal of Physical Chemistry C*, 116(18):10318–10324, May 2012.
- [109] Tapan K. Sau and Andrey L. Rogach. Nonspherical Noble Metal Nanoparticles: Colloid-Chemical Synthesis and Morphology Control. *Advanced materials*, 22(16):1781–804, April 2010.
- [110] Pandian Senthil Kumar, Isabel Pastoriza-Santos, Benito Rodríguez-González, F Javier García de Abajo, and Luis M Liz-Marzán. High-yield synthesis and optical response of gold nanostars. *Nanotechnology*, 19(1):015606, January 2008.
- [111] Bhavya Sharma, Renee R. Frontiera, Anne-Isabelle Henry, Emilie Ringe, and Richard P. Van Duyne. SERS: Materials, applications, and the future. *Materials Today*, 15(1-2):16–25, January 2012.
- [112] Vivek Sharma, Kyoungweon Park, and Mohan Srinivasarao. Colloidal dispersion of gold nanorods: Historical background, optical properties, seed-mediated

- synthesis, shape separation and self-assembly. *Materials Science and Engineering: R*, 65(1-3):1–38, May 2009.
- [113] Leif J. Sherry, Shih-Hui Chang, George C. Schatz, Richard P. Van Duyne, Benjamin J. Wiley, and Younan Xia. Localized Surface Plasmon Resonance Spectroscopy of Single Silver Nanocubes. *Nano letters*, 5(10):2034–8, October 2005.
- [114] Sara E. Skrabalak, Jingyi Chen, Yugang Sun, Xianmao Lu, Leslie Au, Claire M. Cobley, and Younan Xia. Gold Nanocages: Synthesis, Properties and Applications. *Accounts of chemical research*, 41(12):1587–1595, 2008.
- [115] Liane Slaughter, Wei-Shun Chang, and Stephan Link. Characterizing Plasmons in Nanoparticles and Their Assemblies with Single Particle Spectroscopy. *The Journal of Physical Chemistry Letters*, 2(16):2015–2023, August 2011.
- [116] Danielle K. Smith, Nathan R. Miller, and Brian A. Korgel. Iodide in CTAB Prevents Gold Nanorod Formation. *Langmuir : the ACS journal of surfaces and colloids*, 25(16):9518–24, August 2009.
- [117] Jibin Song, Zheng Fang, Chenxu Wang, Jiajing Zhou, Bo Duan, Lu Pu, and Hongwei Duan. Photolabile plasmonic vesicles assembled from amphiphilic gold nanoparticles for remote-controlled traceable drug delivery. *Nanoscale*, 5(13):5816–24, July 2013.
- [118] Yannick Sonnefraud, Niels Verellen, Heidar Sobhani, Guy A.E. Vandenbosch, Victor V. Moshchalkov, Pol Van Dorpe, Peter Nordlander, and Stefan A. Maier. Experimental Realization of Subradiant, Superradiant, and Fano Resonances in Ring/Disk Plasmonic Nanocavities. *ACS Nano*, 4(3):1664–1670, 2010.

- [119] Paul L. Stiles, Jon A. Dieringer, Nilam C. Shah, and Richard P. Van Duyne. Surface-Enhanced Raman Spectroscopy. *Annual review of analytical chemistry*, 1:601–26, January 2008.
- [120] Chad E. Talley, Joseph B. Jackson, Chris Oubre, Nathaniel K. Grady, Christopher W. Hollars, Stephen M. Lane, Thomas R. Huser, Peter Nordlander, and Naomi J. Halas. Surface-Enhanced Raman Scattering from Individual Au Nanoparticles and Nanoparticle Dimer Substrates. *Nano letters*, 5(8):1569–74, August 2005.
- [121] Andrea Tao, Prasert Sinsersuksakul, and Peidong Yang. Polyhedral Silver Nanocrystals with Distinct Scattering Signatures. *Angewandte Chemie (International ed. in English)*, 45(28):4597–601, July 2006.
- [122] Michael I. Tribelsky, Sergej Flach, Andrey E. Miroshnichenko, Andrey V. Gorbach, and Yuri S. Kivshar. Light Scattering by a Finite Obstacle and Fano Resonances. *Physical Review Letters*, 100(4):043903, January 2008.
- [123] Leung Tsang, Jin Au Kong, and Kung-Hau Ding. *Scattering of Electromagnetic Waves: Theories and Applications*. Wiley-Interscience, 2000.
- [124] H. Wang, K. Fu, R.A. Drezek, and N.J. Halas. Light scattering from spherical plasmonic nanoantennas: effects of nanoscale roughness. *Applied Physics B*, 84(1-2):191–195, May 2006.
- [125] H. Wang and N. J. Halas. Mesoscopic Au “Meatball” Particles. *Advanced Materials*, 20(4):820–825, February 2008.
- [126] Hui Wang, Glenn P. Goodrich, Felicia Tam, Chris Oubre, Peter Nordlander, and Naomi J. Halas. Controlled Texturing Modifies the Surface Topography

- and Plasmonic Properties of Au Nanoshells. *The journal of physical chemistry. B*, 109(22):11083–7, June 2005.
- [127] Hui Wang, Felicia Tam, Nathaniel K. Grady, and Naomi J. Halas. Cu Nanoshells: Effects of Interband Transitions on the Nanoparticle Plasmon Resonance. *The journal of physical chemistry. B*, 109(39):18218–22, October 2005.
- [128] Z.L. Wang, R.P. Gao, B. Nikoobakht, and M. A. El-Sayed. Surface Reconstruction of the Unstable {110} Surface in Gold Nanorods. *The Journal of Physical Chemistry B*, 104(23):5417–5420, 2000.
- [129] P.C. Waterman. Matrix formulation of electromagnetic scattering. *Proceedings of the IEEE*, 53(8):805–812, 1965.
- [130] D. A. Weitz, S. Garoff, J.I. Gersten, and A. Nitzan. The enhancement of Raman scattering, resonance Raman scattering, and fluorescence from molecules adsorbed on a rough silver surface. *The Journal of Chemical Physics*, 78(9):5324–5338, 1983.
- [131] D.A. Weitz, S. Garoff, and T.J. Gramila. Excitation spectra of surface-enhanced Raman scattering on silver-island films. *Optics letters*, 7(4):168–70, April 1982.
- [132] Chihhui Wu, Alexander B. Khanikaev, Ronen Adato, Nihal Arju, Ahmet Ali Yanik, Hatice Altug, and Gennady Shvets. Fano-resonant asymmetric metamaterials for ultrasensitive spectroscopy and identification of molecular monolayers. *Nature materials*, 11(1):69–75, January 2012.
- [133] Kristin L. Wustholz, Anne-Isabelle Henry, Jeffrey M. McMahon, R. Griffith Freeman, Nicholas Valley, Marcelo E. Piotti, Michael J. Natan, George C. Schatz, and Richard P. Van Duyne. Structure-Activity Relationships in Gold

- Nanoparticle Dimers and Trimers for Surface-Enhanced Raman Spectroscopy. *Journal of the American Chemical Society*, 132(31):10903–10, August 2010.
- [134] Hongxing Xu and Mikael Käll. Polarization-Dependent Surface-Enhanced Raman Spectroscopy of Isolated Silver Nanoaggregates. *Chemphyschem : a European journal of chemical physics and physical chemistry*, 4(9):1001–5, September 2003.
- [135] Jian Ye, Fangfang Wen, Heidar Sobhani, J. Britt Lassiter, Pol Van Dorpe, Peter Nordlander, and Naomi J. Halas. Plasmonic Nanoclusters: Near Field Properties of the Fano Resonance Interrogated with SERS. *Nano letters*, 12(3):1660–7, March 2012.
- [136] Kane S. Yee. Numerical Solution of Initial Boundary Value Problems Involving Maxwell’s Equations in Isotropic Media. *IEEE Transactions on Antennas and Propagation*, 14(3):302–307, 1966.
- [137] Li-Yan Yin, Yun-Huan Huang, Xia Wang, Si-Tong Ning, and Shao-Ding Liu. Double Fano resonances in nanoring cavity dimers: The effect of plasmon hybridization between dark subradiant modes. *AIP Advances*, 4(7):077113, July 2014.
- [138] Shunping Zhang, Kui Bao, Naomi J. Halas, Hongxing Xu, and Peter Nordlander. Substrate-Induced Fano Resonances of a Plasmonic Nanocube: a Route to Increased-Sensitivity Localized Surface Plasmon Resonance Sensors Revealed. *Nano letters*, 11(4):1657–63, April 2011.
- [139] Fei Zhou, Zhi-Yuan Li, Ye Liu, and Younan Xia. Quantitative Analysis of Dipole and Quadrupole Excitation in the Surface Plasmon Resonance of Metal

Nanoparticles. *The Journal of Physical Chemistry C*, 112(51):20233–20240, December 2008.

- [140] Alyssa B. Zrimsek, Anne-Isabelle Henry, and Richard P. Van Duyne. Single Molecule Surface-Enhanced Raman Spectroscopy without Nanogaps. *The Journal of Physical Chemistry Letters*, 4(19):3206–3210, October 2013.